UNIVERSITÀ
DEGLI STUDI
FIRENZE

Università degli Studi di Firenze
Dipartimento di Ingegneria dell'Informazione (DINFO)
Corso di Dottorato in Ingegneria dell'Informazione
Curriculum: Control, Optimization and Complex Systems

Cooperative effects and long range interactions: How form shapes the substance

Candidate
Alessia Valzelli

Supervisors
Prof. G. L. Celardo
Prof. F. Bagnoli
Prof. D. Fanelli

Advisors
Prof. S. Ricci
Prof. F. Schoen

ciclo XXXVIII, 2022-2025

Università degli Studi di Firenze, Dipartimento di Ingegneria
dell'Informazione (DINFO).

To my parents,
for always teaching me to look
at the world with curiosity.

Abstract

Understanding the complex behavior of systems made of a large multitude of interacting constituents is a challenging and non-trivial task. Research in the complex systems framework aims to address this issue, seeking to uncover the relationship between structure and functionality, one of its central goals. Our daily-life provides many examples of systems where the interactions between the constituents can determine a collective and cooperative response, that differs significantly from the response of the isolated constituents. Such examples span from social networks and human societies (e.g., the spreading of pandemics, interactions among workers or students) to modern telecommunications and financial markets, all of which can be regarded as complex systems. The study of complex systems is not limited only to macroscopic communities of constituents, but similar cooperative behaviors can be observed at the atomic and nanoscale. The first attempt to study the laws governing the microscopic world was made in the early 1930s by the newborn quantum mechanics. Immediately scientists discovered the power of this discipline in describing the behavior of natural and artificial systems composed of interacting particles at the nanoscale. Among all the many remarkable quantum phenomena, one of the most striking is the Bose-Einstein condensation (BEC). BEC occurs when a gas of identical boson particles is cooled to extremely low temperatures, causing many particles to occupy the same quantum ground state. This collective transition determines the emergence of a macroscopic coherent state where particles behave as a new quantum entity, whose properties cannot be understood simply as the sum of individual behaviors. A few decades later, another milestone was achieved with the BCS theory of superconductivity (1957). BCS theory explains superconductivity as an emergent quantum state formed when electrons pair up into Cooper pairs through lattice-mediated interactions. These pairs behave cooperatively like bosons, condensing into a coherent ground state that allows resistance-free electrical flow. At the same time the theory of superradiance, proposed by Robert H. Dicke (1954), provided

another remarkable example of quantum cooperativity. Superradiance describes how ensembles of quantum emitters can radiate coherently as a single entity, amplifying their collective emission. In his work, Dicke predicted that when N emitters act coherently, their collective radiative response increases dramatically, scaling as N^2. In Dicke's theory of superradiance all the emitters are in their excited state. An even more interesting kind of radiation speedup can occur when a single photon is stored uniformly in a cloud of N emitters. In their 2009 Science article "The Super of Superradiance", Scully and Svidzinsky explored the cooperative single-photon emission, also called "single-photon superradiance" from an ensemble of emitters. If only one excitation is present in the emitter ensemble, you might expect the decay rate to be the one of the single emitter. However, if the emitters are symmetrically organized, the decay rate scales as N. Single-photon superradiance has become a subject of current interest, in particular, this cooperative effect has been found in many physical systems, such as perovskite quantum dots, molecular aggregates and crystals, cold atoms and nitrogen vacancies in nanodiamonds. In this thesis we investigate the emergence of cooperativity in molecular aggregates of bacteriochlorophyll molecules in light-harvesting complexes of Green sulfur and Purple bacteria. These systems, which can be considered as a network of bacteriochlorophyll molecules that exhibit a pattern of strong a weak couplings, are characterized by an efficient ability in performing absorption from sunlight and energy transfer to the reaction centers, that relies in the emergence of cooperative effects, such as superradiance and supertransfer coupling. Nowadays the growing field of quantum biology aims to understand the relationship between structure and functionality in biological systems, exploring how quantum coherence and cooperativity contribute to biological efficiency. Within this context, the present work seeks to provide insight into possible mechanisms underlying these effects. Finally, potential applications are briefly mentioned, including bio-inspired sunlight-pumped lasers, pointing toward clean and efficient light-harvesting technologies.

Acknowledgments

This thesis is the result of my research activity at the University of Florence, which started three years ago. Driven by a strong passion for science and quantum physics and motivated to harness and expand my "little" knowledge, in November 2022 I moved from my hometown, Brescia, to Florence to achieve this goal. Finding a link between architecture and functionality in light-harvesting systems was the main question that I tried to address a possible answer every day. The path was not always straightforward, in fact, it was often full of unexpected challenges, but in the end it brought many achievements, valuable learning and living experiences. Accounting for the many people that I met here in Florence and during my stay abroad, I can finally affirm that my experience has been a complex system in its own right, even before delving into the subject matter. I would have never been able to conclude this experience by myself and various acknowledgments are more than deserved.

I would like to acknowledge the efforts and input of my supervisor, Prof. G. L. Celardo, who guided me through the wide field of quantum biology and for all the opportunities offered to me. In particular, I am grateful to him for involving me in the APACE project and for giving me the chance to experience what it truly means to be part of an international research collaboration. I really enjoyed our stimulating and fruitful discussions and collaboration, which taught me a lot and broadened my perspective. Especially, I have benefited from the strong collaborations arisen in our early research group: my acknowledgment goes to F. S. Lonzano-Negro and T. Fillion, who shared with me part of the research during the last year of my PhD, extending my knowledge to other research fields. I enjoyed our weekly meetings, as well as the pleasant moments of leisure we spent together.

During this journey I have also greatly benefited from the teachings of Prof. F. Borgonovi (Catholic University). Thank you for introducing me to the field of quantum biology and showing me a methodical approach for conducting research.

I also thank my co-supervisors, Prof. F. Bagnoli and D. Fanelli, and the Heads of the PhD School of Information Engineering, Prof. S. Ricci and Prof. F. Schoen, for directing the PhD program. In particular, I am grateful to Prof. F. Schoen and his research group, who warmly welcomed me at the Engineering School of S. Marta and hosted me in their GOL lab during my

brief stay. Further thanks go to S. Altamura for her expertise in handling administrative matters and her kind assistance. Here at the University of Florence I also have the great opportunity to join the lab of Prof. R. Torre. I want to thank him and A. Boschetti (LENS and INRiM) for the hospitality in their lab, because this experience has improved my experimental skills and made my approach to theory more conscious. Being a theoretician, it has been extremely valuable for me to spend some time dealing with experimental issues to better understand the theoretical models to be developed. In particular, I want to acknowledge A. Boschetti for having guided me through the experimental part and for our fruitful collaboration. During my stay in Florence I have also benefited from interesting discussions with Prof. F. Martelli, Prof. S. Cavalieri and Prof. F. Piazza of the Dept. of Physics and with Prof. G. Battistelli of the Dept. of Information Engineering. I also want to thank L. Pattelli and G. Mazzamuto of LENS for their help in running high-performance computational simulations.

During the second year of my PhD I had the great opportunity to join the Quantum Theory Team (QTT) led by Prof. E. M. Gauger at Heriot-Watt University (HWU) in Edinburgh (Scotland). I would like to thank Prof. E. M. Gauger for hosting me in his group for almost eight months. It was a very productive stay and I have benefited from the knowledge in his group, learning and understanding new techniques and methods. It was a great pleasure and privilege to have this opportunity for both career and personal growth. During my stay in the QTT I have also met new young researches and PhD students from all over the world in a open-minded and friendly environment. In particular, I would like to acknowledge J. Wiercinski, A. Burgess, H. Hajek , P. Banerjee, K. Damezin for our interesting discussions and also for the enjoyable moments we shared together.

Another shorter stay of two weeks took place during my second year of PhD at Max Planck Institute for the science of light in Erlangen (Germany). Joining the group led by H. Fattahi was a shorter but nonetheless interesting and fruitful opportunity for me. I would like to thank H. Fattahi for the hospitality in her group and M. Kueblboeck for sharing with me the knowledge and expertise on sunlight pumped lasers.

Finally, I don't want to forget valuable discussions with Prof. J. Cao (MIT), M. Trotta and S. Doria (CNR), Prof. A. Painelli, Prof. F. Terenziani and D. Giavazzi of the University of Parma and A. Sherniyozov (KIT). Thanks to all of you for your contribution to my project and for giving me a

fresh perspective on conducting the research. In particular, I have benefited from interesting and extremely useful discussions with F. Mattiotti (University of Saarland). I want to thank him for his strong collaboration and for the help in running high-performance computational simulations.

During these three years, I spent most of my time at the Dept. of Physics of Florence in the Complex Systems Group, which has become my 'second family' throughout this journey. Here I had the great pleasure to meet fantastic people, even those not directly involved in my research, who were nonetheless equally important to me. My acknowledgment goes to Giovanna, a true reference point. From my first day at the department, she welcomed me and supported me in overcoming all the challenges I faced, while also sharing all the successes and satisfactions that a PhD program can offer. I also want to thank all the other current and former members of the Complex Systems Group: Valentina, L. Chicchi, L. Giambagli, L. Buffoni, Raffaele, Michele, Giuliano, Diego, Feliciano, Gianluca, Luca, Francesca and all the master students who joint our group.

Infine ringrazio tutti gli amici e i famigliari che mi hanno sempre sostenuto in questo percorso. In particolare mi rivolgo ai miei genitori, Ausilia e Roberto, ai quali dedico questa tesi. Anche se in questi tre anni ho trascorso la maggior parte del tempo lontano da casa, la mia famiglia è sempre stata un punto di riferimento per me e la ringrazio per il sostegno che mi ha dimostrato in tutte le mie scelte e soprattutto nei momenti più impegnativi di questo percorso di dottorato.

Contents

Chapter 1

Introduction

Quantum biology is a research field that studies the role of quantum mechanics in biological systems. Recent research suggests that biological phenomena such as photosynthesis, enzyme catalysis, avian navigator or olfaction make use of a number of non-trivial features of quantum mechanics, such as coherence, tunneling and quantum entanglement [1–6]. One of the most relevant examples of the role of quantum mechanics in biological systems is the long-lived coherence observed in the excitation energy transport during photosynthesis [7, 8]. In Refs. [9, 10] some important experimental proofs that demonstrate the crucial role of quantum coherence for ensuring efficient excitonic energy transfer in the photosynthetic light-harvesting apparatus of Green sulfur bacteria (GSB) and Purple bacteria (PB) have been given. In literature there is evidence that coherence and efficient energy transfer are strictly related to the geometry of the system [11, 12], and that the models found in nature can support macroscopic coherent states robust to static disorder and thermal noise comparable to room temperature energy [13–16]. Nowadays this topic is still an open question and with this thesis we aim for giving a possible and reasonable explanation of the relationship between structure and functionality in photosynthetic antennae, that we usually model as an ensemble of interacting emitters coupled to a thermal bath and to the incoming sunlight.

Let us start from the origin of this incredible process which is **photosynthesis**. Photosynthesis is a biological process exploited by plants, algae and some bacteria initiated by the Sun's energy. The Sun produces a broad spectrum of light output ranging from gamma rays to radio waves. However the availability of energy current density measured on the Earth surface is

reduced by scattering events, absorption from molecules forming the atmosphere and it depends on geographical position and weather conditions. The solar irradiance on Earth is about 1000 $\mathrm{W/m^2}$. During the early stage of photosynthesis solar energy is captured and stored by specific organelles present in photosynthetic organisms. These organelles, also called chloroplast, are able to convert the incoming solar radiation into chemical energy.

Photosynthesis is carried out by a wide variety of organisms, however in this thesis we account only for **Green sulfur and Purple bacteria light-harvesting systems**, because they are among the most efficient antennae able to exploit this process with high efficiency, even if they live under low light conditions where only a few photons per seconds can be absorbed [17, 18]. The early processes of photosynthesis are performed by **bacteriochlorophyll molecules** (BChl *a*-*g*), also called pigments, that usually aggregate into antenna complexes. Individual BChl molecules show two main absorption bands, one in the blue or near UV-region (Soret bands) and one in the red or near IR-region (Q_x and Q_y bands) [19], see Fig. (1.1). BChl molecules are often treated as two-level systems (TLSs) with excitation energy e_0 and a transition dipole moment (TDM) $\vec{\mu}$, corresponding to the Q_y transition.

Spectroscopic methods, such as infrared and resonance Raman studies, solid state NMR and cryo-EM, have revealed that BChl molecules are usually arranged in supramolecular complexes, also called **antennae**. These systems are characterized by a high degree of order and symmetry that concerns both position and dipole orientations in the space [20–26], see Fig. (1.2). In particular in PB and GSB antennae BChls are organized into vesicle and cylindrical structures, respectively. These aggregates can reach $60-70$ nm in diameter and contain ~ 5000 BChls *a* for PB complexes while for GSB BChls *c*-*d*-*e* form tubular aggregates containing hundred of thousands molecules and $100-200$ nm in length with widths and depths varying between 60 and 100 nm [18, 27, 28]. The role of the antenna structure is to capture and funnel the incoming solar energy to the reaction centers (RCs), where the process of charge separation takes place and drives all the next chemical reactions in order to convert the excitation into chemical energy.

Why we need antennae? The answer comes from a consideration of the Sun's intensity and the absorption properties of BChls. In Chapt. 5 we show that each BChl under natural sunlight intensity can absorb on average 10 photons per second. So the absorption rate is a tenth of a second, an eter-

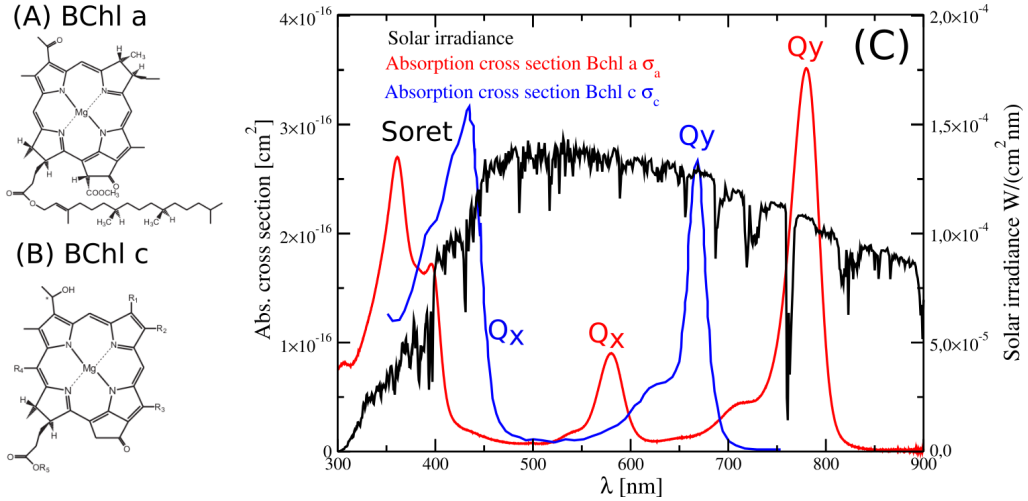

Figure 1.1: *Spectral properties of BChl a and c.* Panels (A-B): chemical structures of bacteriochlorophylls a and c taken from [19]. Panel (C): solar irradiance (black line) and absorption cross section of BChl a (red line) and BChl c (blue line). Soret bands, Q_y and Q_x transitions are shown for BChl a and BChl c. Since the Q_y transition is the most relevant for the calculations of this thesis, a two-level model adequately describes such systems. Note that, while BChl a is typical of PB antennae, for GSB BChl c is considered. Absorption cross sections have been taken from Refs. [24, 29–32].

nity compared to molecular timescales. This would obviously be wasteful. However nature has found an ingenious solution to overcome this issue. If all the pigments are close enough to interact each others, a **cooperative response** can be achieved, giving rise to an enhanced absorption TDM at a specific wavelength. In GSB and PB systems the average nearest-neighbor distance between pigments is ~ 1Å, so a hierarchical pattern of tight packing is displaced. Strong electron interactions arise from the most coupled groups of pigments, that share the excitation coherently. On the other hand between groups of pigments which are weakly coupled excitation is shared incoherently and it is spread through multi-chromophoric Förster resonance energy transfer (**MC-FRET**) from a donor unit made of n_D molecules to an acceptor unit with n_A molecules. MC-FRET rate given in Eq. (7.18) in Chapt. 7 generalizes the well known Förster resonance energy transfer (FRET) rate $K_{n,m} = \dfrac{2\pi|\Omega_{nm}|^2}{\hbar} J_{nm}$, where $|\Omega_{nm}|$ is the coupling between the m^{th} eigenstate of the donor unit and the n^{th} eigenstate of the acceptor,

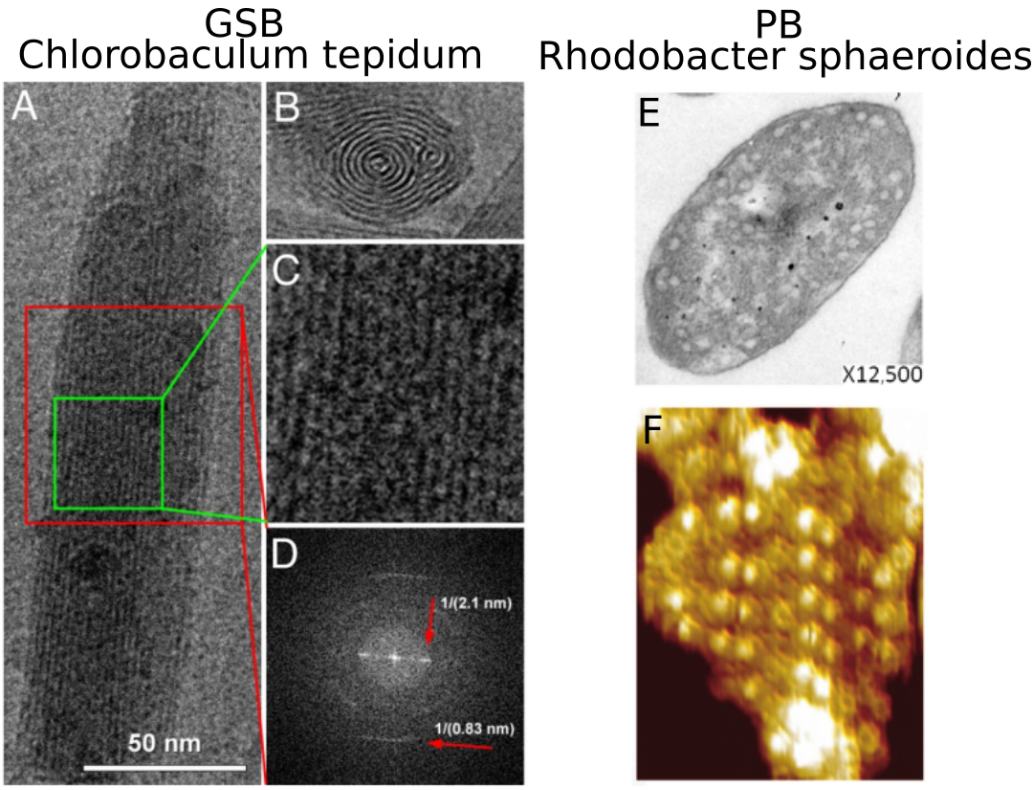

Figure 1.2: *Antenna complexes in GSB and PB.* Panels (A-D): GSB *C. Tepidum bchQRU* mutant architecture taken from Ref. [28]. Here the structure of the GSB antenna complexes made of concentric cylindrical aggregates of BChl molecules is shown. Panels (A-B) CryoEM images of isolated chlorosomes seen in side-on view (A) and in end-on view (B). Panel (C): enlarged region of the side-on view indicated by the green box in panel (A). Panel (D): Fourier transform of the red box in panel (A). The red arrows indicate reflections from a 2.1 nm spacing between BChl layers and a 0.83 nm spacing along the layers. Panels (E-F): PB *Rhodobacte sphaeroides* architercure. Panel (A): TEM of the wild type model found in Ref. [33]. The figure shows a section of a cell of PB, where the spherical antenna complexes, also called chromatophores, can be easily identified. Panel (F): AFM image from Ref. [27] used to identify the arrangement of pigment-protein complexes on a portion of the chromatophore.

while J_{nm} is the overlap integral between the absorption and emission lineshapes [15–17, 34, 35]. **Quantum coherence** arises from strongly coupled

pigments ($\Omega_{NN} \sim 500$ cm^{-1}) and from the overall architecture of the antenna and it is responsible for the higher efficiency associated to the energy transfer process. Due to the coherent excitonic coupling MC-FRET rates become fast enough to ensure that almost all the absorbed energy is funneled to the RCs within 100 ps before radiative and non-radiative processes occur, achieving a high internal efficiency [18, 36–39]. A proof of principle has been proposed in Fig. (1.3), where the MC-FRET rate has been computed between two aggregates made of 27 BChl *a*, the LH2 rings typical of the PB antennae, and two individual BChl *a* molecules as a function of the distance.

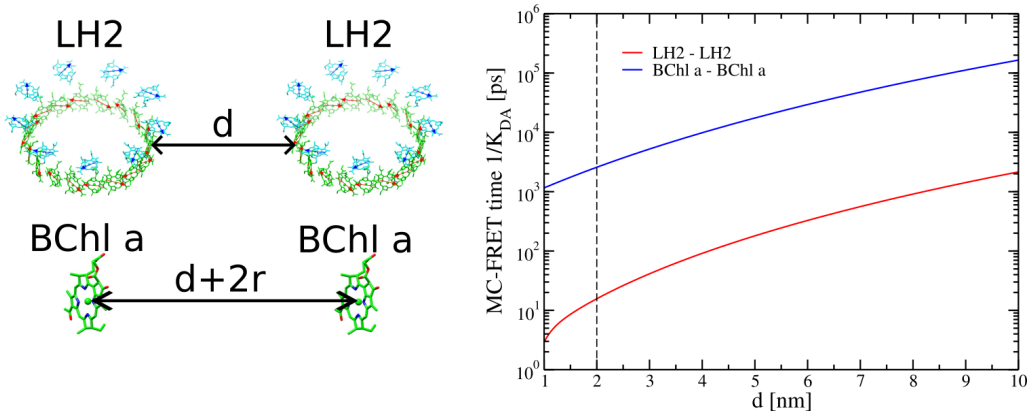

Figure 1.3: *MC-FRET time between PB antenna complexes and BChl a molecules.* The figure shows the comparison between the MC-FRET time computed with Eqs. (7.18) given in Chapt. 7 between two identical aggregates of BChl *a* molecules (see the red line) and the FRET time given by the inverse of $\frac{2|\Omega|^2}{\Gamma_\Phi \hbar}$ between two BChl molecules (see the blue line). Here d represents the edge to edge distance between the two LH2 rings, while $\Gamma_\Phi = 1000$ cm^{-1} has been chosen as the dephasing linewidth. The black dashed line represents the value found in natural systems for the edge to edge distance between LH2 antenna complexes, which is ~ 2 nm. The dephasing linewidth has been tuned in order to find a MC-FRET time of about 10 ps when the two rings are 2 nm apart. On the left a picture of the two configurations has been shown. LH2-LH2 configuration: two adjacent ring-shaped aggregates with radius $r \sim 3$ nm at a given edge to edge distance d, with 27 TDMs (see red and blue arrows) each. BChl *a* - BChl *a* configuration: two BChl molecules have been considered instead of the two rings at a distance given by $d + 2r$.

In this thesis the photosynthetic apparatus of GSB and PB has been widely investigated and modeled. The interaction between all the BChl molecules, trated as TLSs, has been considered and the process of fluorescence from an ensemble of emitters has been taken into account through a radiative non-hermitian Hamiltonian approach, that goes beyond the widely used model of the Frenkel Hamiltonian, that fails when the system is no longer in the small volume limit. The main results of Chapts. 2, 3 and 4 show that in both PB and GSB systems cooperativity leads to the emergence of a few red-shifted **superradiant states**, that radiate much faster than the single emitter. For the first time we performed large scale simulations of the entire light- harvesting complexes, showing that the superradiant response is present not only in smaller portions but also in the entire antennae and it increases with the system size, which is far from being trivial. Fig. (1.4) shows how the superradiant decay rate scales with the system size in PB and GSB antennae. For a detailed discussion about the antenna complexes used for GSB and PB see Chapt. 2. Furthermore, the effects of static disorder and thermal noise comparable to room temperature energy have been considered, proving that the cooperative response is still present. In our previous work [13], we have given a detailed explanation of the origin of this large coherence length and we have proved that the architecture of the system is responsible for the emergence of such behavior, which is lost in other mathematical models.

How quantum coherence affects the energy transfer process? Is there a relationship between optimal energy transfer and geometry of the system? These are the two main questions this thesis wants to give an answer. We have tried to find a conceivable explanation by comparing **excitation energy transfer process** in natural antennae and in mathematical models (see Chapt. 7). We have developed incoherent rate equations to describe the dynamics of the population of the GSB light-harvesting apparatus under natural sunlight and in presence of a thermal bath (see Chapt. 6). A pictorial representation of the system is given in Fig. (1.5), where different aggregates of BChl molecules (chlorosome, baseplate and RCs) are considered and the excitation funneling from the chlorosomes to the RC is represented. Sunlight spectrum has been widely analyzed and modeled through the black-body radiation theory (see Chapt. 5), while incoherent generalized MC-FRET rates between different aggregates has been considered. Our analysis reveals that the fastest rates are those ones connecting natural aggregates, while for all

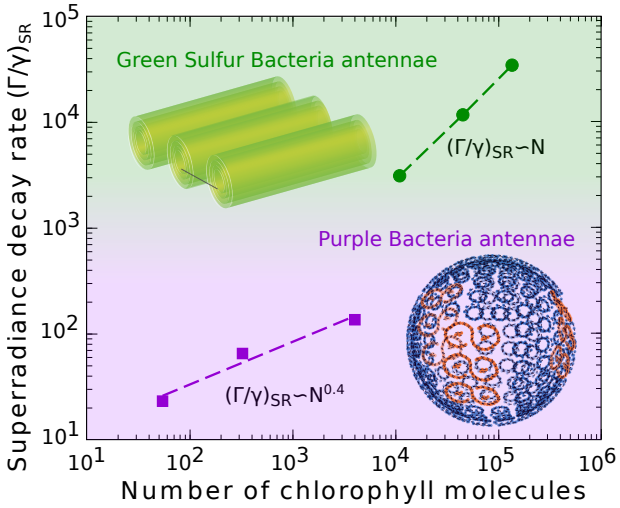

Figure 1.4: *Superradiance in GSB and PB antenna complexes.* This figure shows how the superradiant decay rate increases with the size of the aggregates, here represented by the total number of BChl molecules. For GSB complexes (see green dots) we considered one single cylinder, four concentric cylinders and the entire chlorosome, the largest system close to natural size made of three adjacent concentric cylinders with $N \sim 10^5$ BChl *c*. For PB complexes (see purple squares) we considered a single s-shaped LHI+2RCs, s-shaped LHI+2RCs surrounded by 10 LHII and the chromatophore ($N \sim 5000$ BChl *a*). See Chapt. 2 for a detailed explanation of the PB and GSB complexes. Figure taken from Ref. [14].

the other mathematical models a slower MC-FRET rate has been found, see Chapt. 7 for a detailed analysis of the mathematical models that we studied. As found in the literature [18,36,37], our calculations for GSB antennae have shown an internal efficiency that ranges between $70 - 85\%$ and a value of the trapped current per RC which matches the closure rate of the RC. At this point a digression on the RC dynamics is worth. Each RC contains a pair of strongly coupled BChl *a* molecules, also called the special pair, that can undergo charge separation after the absorption of an excitation. After charge separation the RC can no longer absorb any other excitation and it goes in a closed state. The time RC needs to be opened again is defined as the closure time and determines the maximal amount of excitations that the RC can process [40–42].

A similar study has been conducted also for the PB antennae using net-

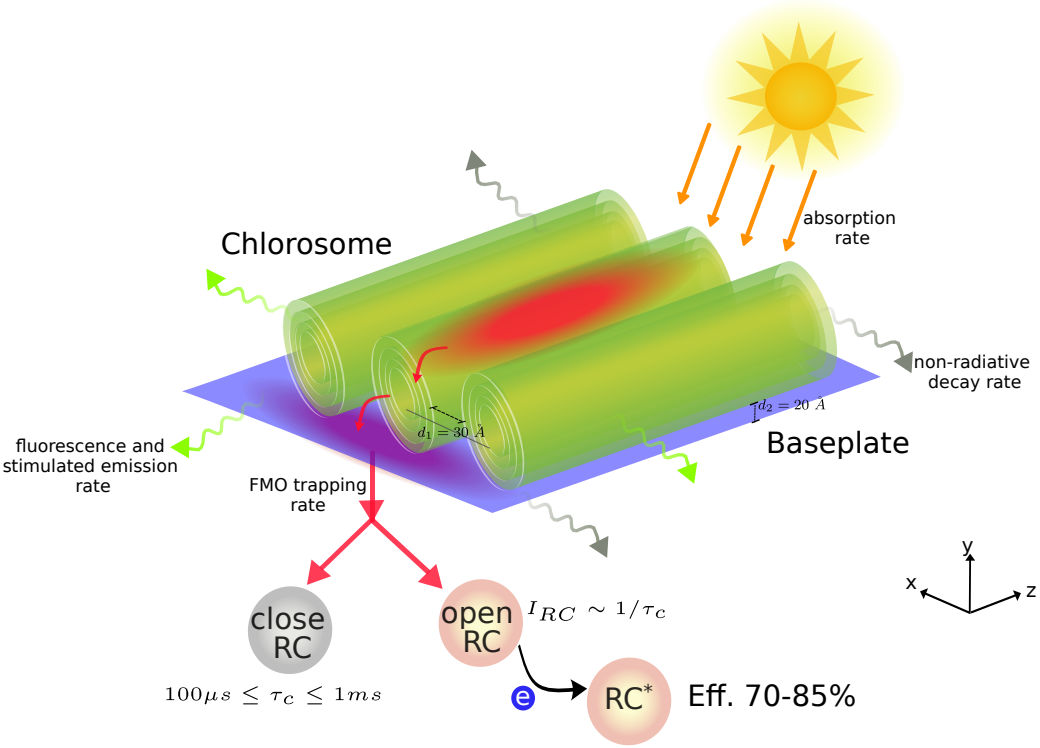

Figure 1.5: *Study of the EET in GSB light-harvesting apparatus.* The figure represents the process of excitation energy transfer in the entire light-harvesting apparatus of GSB, formed by the chlorosome, the baseplate (two-dimensional aggregate placed below the chlorosome), the FMO complexes and the RCs. Once sunlight radiation is absorbed by a single BChl molecule (single excitation regime) in the chlorosome, it is shared coherently between the molecules within the aggregate, forming the so called excitons. Excitation is funneled to the baseplate and finally trapped to the RCs by the FMO trapping rate. This model is known in literature for its large efficiency $(70 - 85\%)$, nevertheless radiative and non-radiative losses can occur. RCs can exist in an open state and thus they can absorb the excitation and undergo charge separation, that drives all the next chemical reactions. If an RC is already in a charge separated state, it can no longer absorb excitation and it is therefore considered closed. The closure rate refers to the rate at which the RC returns to the opened state, and in these systems it corresponds to the current flowing in each RC. Figure taken from Ref. [43].

work theory (see Chapt. 8), but it is still currently ongoing. In this case the process of energy transfer between different aggregates has been modeled by using stochastic and deterministic approaches and an analysis of the dynamics under different illumination conditions has been addressed. The network-based theory is a powerful tool to study these systems for its notable aptitude for addressing issues related to the system's geometry. In fact, this approach allows us to determine the optimal geometry for energy transfer and opens new perspectives towards the development of possible applications for light-harvesting quantum devices that mimic natural systems.

What are the **potential applications** that may arise from this investigation? Among all the topics studied by quantum biology, nowadays some possible application for light-harvesting have been considered [44–47]. The main idea behind the realization of these devices relays in mimicking the behavior and the geometry typical of natural systems. From our perspective, the efficient capability of the natural antennae to capture and funnel the excitation to the RCs is driving a new proposal of bio-inspired sunlight pumped lasers, a first attempt to reach lasing by using unconcentrated sunlight and the antenna complexes of PB for funneling the excitation to the lasing unit, relying on the results published in Ref. [46]. This is the goal of the **EIC pathfinder challenges APACE project** (Towards a bio-mimetic sunlight pumped laser based on photosynthetic antenna complexes), which I had the great opportunity to join during my PhD. It aims for developing an unprecedented **sunlight pumped laser** (SPL), based on nanoscale engineered photosynthetic antenna complexes, turning unconcentrated thermal sunlight into a coherent laser beam. Since sunlight is a very diluted source of energy, the lasing unit can't reach the lasing condition by itself. However we utilize the light-harvesting systems of PB as a nanoscope lens. By attaching them to the lasing unit, they can successfully concentrate sunlight and deliver the excitation energy needed to sustain lasing even with ambient natural light, see Fig. (1.6).

The APACE project has G. L. Celardo as the principal coordinator. He conceived the idea of bio-inspired solar lasers with E. M. Gauger and both of them lead the theory group and conduct the theoretical modeling of APACE solar pumped laser, with the strong support and expertise of H. Fattahi, A. Boschetti, F. Martelli and B. S. Richards. At the end of October 2025 the APACE consortium submitted an internal technical report that is kept confidential, as it includes highly sensitive data related to an ongoing patent

filing.

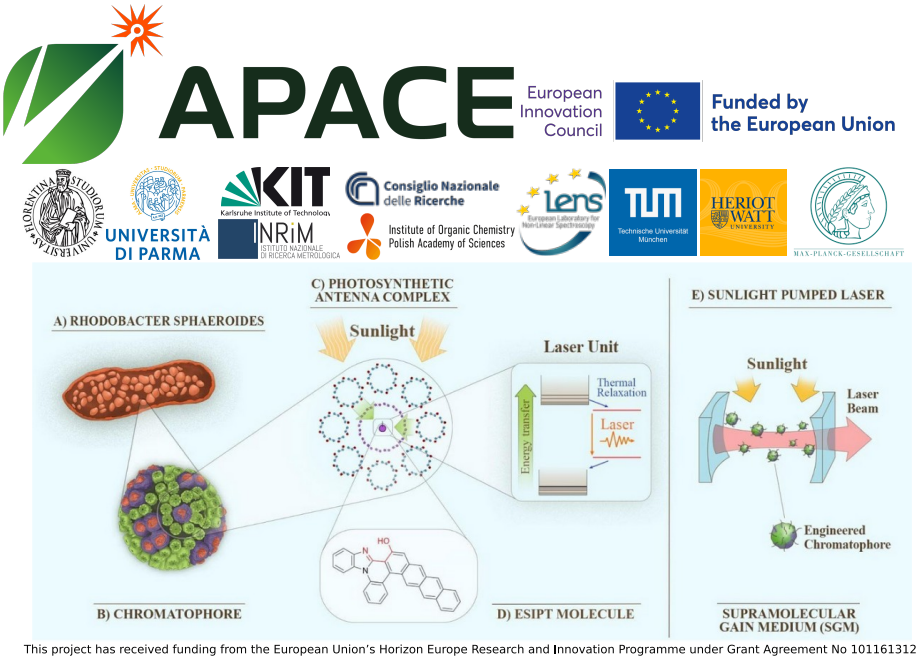

Figure 1.6: *Main idea of APACE: Towards a bio-mimetic sunlight pumped laser based on photosynthetic antenna complexes* The figure represents the general idea of the APACE project. Antenna complexes of PB (A-C) can act as nanoscale lenses due to their high efficiency in harvesting solar radiation and transferring the excitation to other aggregates. The supramolecular gain medium proposed by the APACE consortium consists of a lasing molecule (D) attached to the photosynthetic antenna complexes of PB. This architecture should ensure high efficient energy transfer of the solar energy from the antenna to the lasing unit (quasi three-level model), reaching the lasing condition even under natural sunlight. Panel (E) is a pictorial representation of the cavity geometry that we plan to develop. The figure also shows the logos of all the institutions involved in this project. This project has received funding from the European Union's Horizon Europe Research and Innovation Programme under Grant Agreement No. 101161312.

1.1 Thesis outline and contributions

This section provides a general outline of the thesis contents, along with a sincere acknowledgment of all individuals who contributed to the research.

- In **Chapters 2, 3 and 4** the main results of Ref. [14], published on The Journal of Physical Chemistry B, are discussed. Specifically in Chapt. 2 the geometry of the light-harvesting systems of PB and GSB has been shown, while in Chapt. 3 a wide explanation of the emergence of superradiance in PB and GSB light-harvesting complexes through a radiative non-hermitian Hamiltonian approach has been addressed. An explanation of the possible approximations that lead to hermitian and Frenkel Hamiltonians and their regime of validity have been given. Chapt. 4 shows an analysis of the robustness of coherence in presence of static disorder and thermal noise comparable to room temperature energy.

  This project has been supervised and conceived by prof. G.L. Celardo and prof. F. Borgonovi and it has been pursued in strong collaboration with F. Mattiotti, A. Boschetti, prof. A. Kargol and C. Green. I'm the main author of this publication and my contribution was to derive the geometry of the light-harvesting complexes, to perform the numerical simulations and to write and edit the original draft.

- In **Chapter 5**, after a description of the solar irradiance through the black body radiation theory, the study of the optical properties (absorption and fluorescence) of BChl *a* and *c* molecules has been given. The comparison between the absorption spectrum of the aggregate and the spectrum of a single BChl molecule is investigated, pointing out that the interaction between emitters in antennae usually leads to the formation of J-type or H-type aggregates with different spectroscopic properties. Finally a comparison with experimental data is given, showing the validity of our theoretical model.

  The writing of this chapter is the result of interesting and useful discussions with prof. A. Painelli, M. Trotta, A. Boschetti and S. Doria. M. Trotta also provided the experimental absorption spectrum of the PB antennae.

- In **Chapter 6** the theoretical derivation of the Lindblad master equation is provided. The interaction of an aggregate of emitters with a thermal bath at finite temperature is calculated. A Lindblad quantum master equation is derived under the Born-Markov and secular approximations. Neglecting the coherences, rate equations for the populations of the system have been computed and the thermal rates has been derived. Finally a discussion about the choice of the spectral density is provided. Note that the results of this chapter serve as the starting point of Chapt. 7.

  This chapter benefited from valuable discussions with F. Mattiotti and J. Wiercinski, who provided the numerical spectral density.

- In **Chapter 7** we have modeled the entire process of the exciton energy transfer, from sunlight absorption to exciton trapping in the reaction centers (RCs) in presence of a thermal bath in GSB light-harvesting apparatus. The energy transfer has been analyzed using the radiative non-hermitian Hamiltonian and solving the rate equations for the populations. Sunlight pumping has been modeled as black-body radiation at $T = 5800$ K, with an attenuation factor that takes the Sun-Earth distance into account. Cylindrical structures typical of GSB antenna complexes (chlorosomes), and the dimeric baseplate, a two dimensional aggregate made of BChl molecules lying between the cylinders and RCs, have been considered. An interesting comparison between the natural model and other mathematical models has been address in order to find a relationship between geometry and functionality in these systems.

  Prof. G.L. Celardo and prof. J. Cao conceived the main idea of the results of Chapter 7 and supervised the research work. I and F. Mattiotti are the first authors of the manuscript related to this chapter. We developed the theoretical background to model the theory of the generalized multi-chromophoric transfer rate (MC-FRET) between different light-harvesting complexes found in GSB antennae, we derived the geometry of the entire photosynthetic apparatus of Green sulfur bacteria, including both chlorosomes and baseplate, and we performed all the numerical simulations. We wrote and edited the original draft. This project is available as a preprint on arXiv, see Ref. [43].

  This chapter also benefited from valuable discussions with M. Trotta,

and R. A. Molina.

- In **Chapter 8** a novel theoretical model based on the network theory has been proposed to describe the dynamics of the antenna systems in PB. In this chapter the PB antenna has been modeled as a network, where excitation can be transferred from a node to another one. Network theory represents a new approach to study the dynamics in these systems, and it could be crucial to achieve the goal of this work: finding the best architecture that ensures optimal energy transfer.

  Prof. G.L. Celardo served as the principal investigator of this research line and he has drawn on the expertise in network theory of prof. F. Bagnoli, prof. D. Fanelli and prof. F. Piazza to oversee the research activities. This project is still ongoing and a draft with preliminary results will be included in the thesis with the purpose to submit a paper in the next months. My role in this project was to derive the network geometry of the Purple bacteria chromatohopore, to compute multichromphoric transfer rates between each pair of nodes and to model the absorption of the incoming sunlight, while the post-doc T. Fillion performed all the simulations of the dynamics of the system comparing the stochastic Gillespie algorithm with the deterministic approach.

Finally **Chapter 9** summarizes all the results shown previously, addressing the limits of validity of the model, and indicates some future perspectives.

Chapter 2

The models: antenna complexes in GSB and PB

In this chapter the geometry of the antenna complexes of two kinds of photosynthetic anaerobic bacteria has been analized. The Chlorobium Tepidum Green sulfur bacteria (GSB) and Rhodobacter sphaeroides Purple bacteria (PB), which are the systems we are interested in, are among the most efficient light-harvesting complexes able to exploit photosynthesis even under low light conditions due to their geometrical features. Here, after a general overview about GSB and PB geometrical description, our theoretical model to simulate the entire light-harvesting apparatus is explained in detail, starting from the main experimental data obtained by spectroscopic methods. The model we propose treats each BChl molecule as a two level system (TLS) with a transition dipole moment (TDM) characterized by a well defined position and orientation in the space. In this chapter we show the theoretical method we used in order to reproduce the chlorosome for the GSB and the chromatophore for the PB. The chlorosome is formed by adjacent aggregates that comprise more concentric cylindrical rolls made of BChl c, while the chromatophore is a vesicle where BChl a are arranged.

Here we investigate antenna complexes of photosynthetic anaerobic bacteria: the *Chlorobium Tepidum* Green sulfur bacteria (GSB) and *Rhodobacter sphaeroides* Purple bacteria (PB) which are among the most efficient

photosynthetic complexes in Nature [48]. Indeed these anaerobic bacteria have the ability to harvest sunlight in deep murky waters, where incident light levels are much reduced beyond the already dilute level on land [17,27]. For instance, Purple bacteria have the ability to exploit extremely weak light sources [17, 18, 27, 49] (less than 10 photons per molecule per second) and some species of Green sulfur bacteria even perform photosynthesis with geothermal radiation from deep-sea hydrothermal vents at about 400°C [50].

Photosynthetic antenna complexes of anaerobic bacteria [9, 17, 27, 51–57] are comprised of a network of Bacteriochlorophyll (Bchl) molecules which are typically modeled as two-level systems (2LS) capable of absorbing radiation and transferring the resulting electronic excitation to the reaction center (RC) where charge separation occurs, a process which precedes and drives all other photosynthetic steps. To each 2LS a transition dipole moment (TDM), corresponding to the Q_y transition, is associated which determines its coupling with both the electromagnetic field and with other chlorophyll molecules. While the two-level approximation offers a simplified framework for describing molecular interactions with an incoming electromagnetic field, its validity is generally restricted to those systems where more electronic energy levels are not considered and the decay into triplet states and the vibrational structure induced by the phonon bath are not explicitly treated. However, in this thesis, the two-level approach is maintained as it provides a clear physical intuition of the transition dynamics without loss of generality for the phenomena under investigation.

Owing to the low solar photon density, photosynthetic aggregates operate in the single-excitation regime, meaning that at most one excitation is present in the system at any time. Antenna complexes of photosynthetic bacteria have an internal efficiency of almost 90% (i.e. nearly each photon absorbed produces a charge separation event in the RC) [17, 18].

A possible origin of this incredible ability of bacterial photosynthetic systems to utilize weak sources of incoherent light and funnel the collected energy to specific molecular aggregates could be brought back to the high level of symmetry and hierarchical organization characterizing the antenna complexes of bacterial photosynthetic organisms [15, 16]. Photosynthesis in GSB involves chlorophyll pigments tightly packed in light-harvesting systems with cylindrical shapes, known as chlorosomes [19] and shown in Fig. (2.1). They are able to absorb the sunlight and transfer the electronic excitation to other fundamental units, such as the baseplate and the Fenna-Matthews-

Olson (FMO) trimer complex, and finally to the reaction centers (RCs), where the incoming energy is converted into a charged-separated state [17, 18]. Purple bacteria offer an alternative organization of the antenna system. The main photosynthetic units of Purple bacteria are the chromatophores ($\approx$ 60 nm in size) [27] which contain about 5000 BChl molecules [58,59], and are composed of different antenna complexes: LHI, LHII and the RC [20,27, 60]. LHI and LHII complexes show a very well ordered disposition of Bchl molecules which are arranged in ring and s-shaped structures. The energy collected by the chromatophore reaches the RC complex mainly through the LHI complex which surrounds it (see Fig. (2.2)).

The basic components of the photosynthetic antenna complexes of anaerobic bacteria have been widely studied both theoretically and experimentally in Refs [20–26].

2.1 Models

The positions and the orientations of the Bchl molecules in both GSB and PB, exhibit a high degree of hierarchical order and symmetry. However, the connection between these structures and their functionality remains an open question. Recent research, see Ref. [13], has demonstrated that the natural arrangement of Bchl molecules in GSB cylindrical structures ensures the presence of cooperative effects even at room temperature. In this chapter, we analyze much larger complexes containing an order of magnitude more Bchl molecules and thus more close to natural sizes.

Below we describe the specific complexes employed in this thesis.

2.1.1 Antenna complexes in Green sulfur bacteria (GSB)

The most common pigments found in the GSB antenna [18,61] are Bchls *c*, *d*, or *e*, along with carotenoids, and to a lesser extent, Bchls *a* [23,62,63], although Bchls *c* is the most abundant pigment [64,65]. Pigment organization and orientations of the GSB chlorosome have been studied by using various spectroscopic methods, such as infrared and resonance Raman studies, solid state NMR and cryo-EM, that have revealed that it can be formed by pigments assembling in rod-like (cylindrical) aggregates with lateral lamellae [23, 62, 63, 66–69]. The specific structure are strongly dependent on the growing and the environmental conditions [13, 70, 71]. In particular, *Chloro-*

bium Tepidum triple mutant antenna complexes present cylindrical structures that can contain between 50000 to 250000 Bchl*c*. These structures typically range in size from 100 to 200 nm in length with widths and depths varying between 60 and 100 nm [61, 72–74].

Although natural antennae of GSB exhibit considerable variation in size and in the types of Bchl aggregates present (such as lamellae and cylindrical structures), here we model the antenna using only cylindrical structures to capture the primary natural features. The cylindrical structures in GSB are made of concentric single wall cylinders, which are observed to lie adjacently to each other on the baseplate.

The model that we consider is shown in Fig. (2.1). It is inspired by the antenna complexes found in the Green sulfur bacterium *C. Tepidum* bchQRU triple mutant type, whose chlorosomes exhibit a much more regular geometry with respect to the wild type. Nevertheless, both types exhibit very similar optical properties and demonstrate similar cooperative effects [13,28]. Below, we describe, in order of hierarchical complexity, the geometry of three structures utilized in this study to model the cooperative effects occurring in the antenna systems of photosynthetic GSB.

Complex A - single cylinder. In Fig.(2.1 A) we present the model utilized for a single cylinder in the bchQRU triple mutant chlorosome. The cylinder comprises a stack of tightly-packed rings of Bchl *c* molecules. Each molecule is treated as a dipole with a squared dipole moment $|\vec{\mu}|^2 = 30$ D^2, possessing a well defined orientation and position in space [13]. Each ring has a radius $R = 6$ nm and contains 60 Bchl molecules separated by a nearest neighbour distance $d = 0.628$ nm. The rings are equally separated by a vertical distance $h = 0.83$ nm [13, 28, 62]. This choice of parameters for the geometry of the bchQRU triple mutant type is in agreement with Ref. [62], where the same cylindrical structure is obtained by wrapping the planar lattice under the rolling angle of $\delta = 0^\circ$ with respect to the vertical axis of the lattice. In our simulations the single cylinder complex can contain up to 10800Bchl *c* molecules, resulting in a maximum length $L_{\max} = 148.57$ nm, corresponding to a stack of 180 rings. Further details about the geometry of the bchQRU triple mutant concerning the positions and orientations can be found in Ref. [13].

Complex B - four concentric cylinders. Chlorosomes of GSB display a complex arrangement of molecules on a multi-wall structure [13, 18, 62, 63, 75]. Panel B of Fig. (2.1) depicts the model we developed, wherein Bchl *c*

molecules form four concentric cylinders. On each cylinder, the dipoles positions and orientations are consistent with those found in the single cylinder model of the bchQRU triple mutant, as explained in [13]. The innermost cylinder has a radius $R = 3\,\text{nm}$, while the distance from wall to wall is $d = 2.1$ nm [13, 71].

Complex C - three adjacent concentric cylinders. In panel C of Fig. (2.1) we show a more elaborate model formed by three adjacent structures, each comprising four concentric cylinders. The wall-to-wall distance between adjacent cylinders is set to 3 nm, a realistic value according to Ref. [23]. The maximum length considered here is $L_{\text{max}} = 148.57$ nm, corresponding to 180 vertical rings in each cylindrical structure. The largest system considered in our simulations contains 132840 Bchl *c* molecules, comparable with natural sizes. The positions and orientations of dipoles on each tubular wall are the same as in Complex A and B.

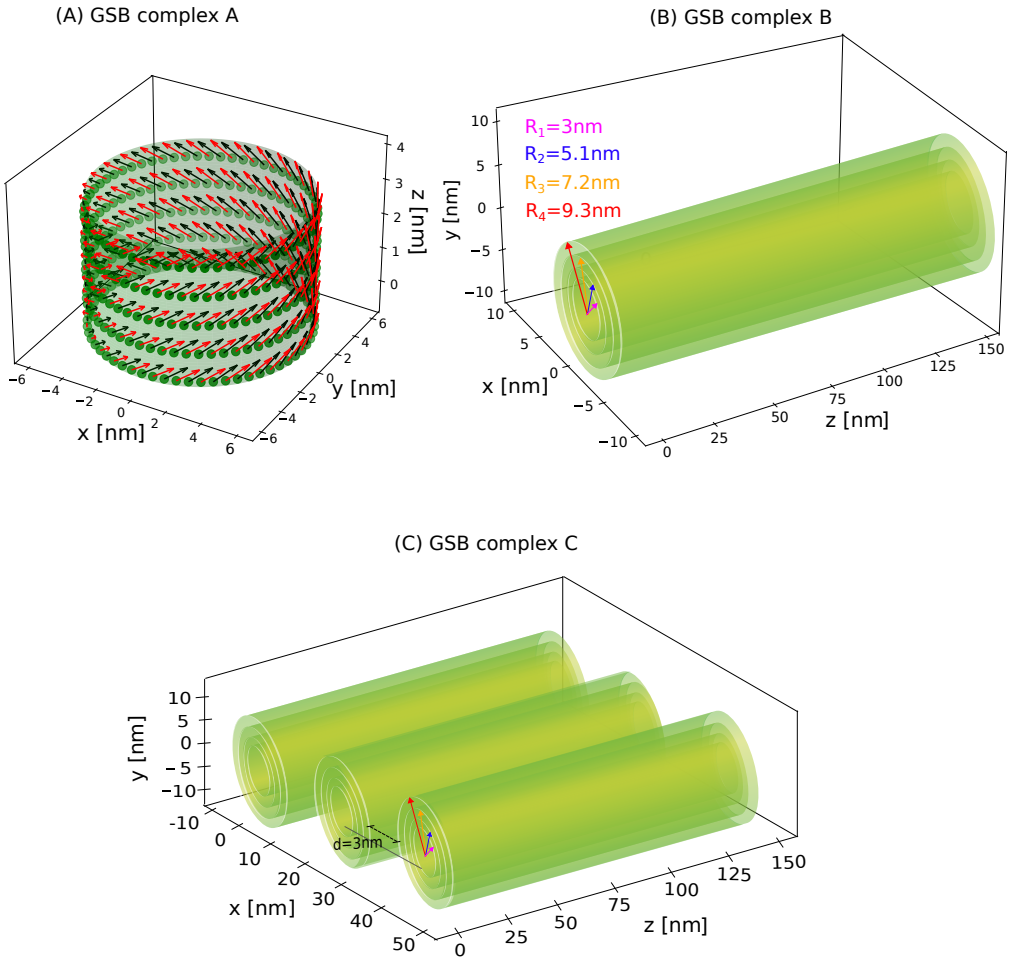

Figure 2.1: *Architecture of GSB light-harvesting complexes.* Cylindrical complexes representing the Green sulfur bacterium bchQRU triple mutant antenna system. (A) Complex A: a section of a single cylinder with a radius $R = 6$ nm and 5 rings is represented. Each Bchl molecule is associated to a transition dipole moment represented by an arrow with a well defined position and orientation. TDM belonging to the same ring are tilted by small alternating angles $\pm\alpha$ out of the lattice plane as a result of the syn-anti stacking [62, 76, 77]. This alternation is so small that optically it may be neglected [62]. In particular black (red) arrows on the same ring characterizes dipoles that point inward (outward) with respect to the tangent plane of the cylinder by a small angle $\alpha = \pm 4°$, for more details see Ref.s [13, 62]. (B) Complex B: representation of the structure with four concentric cylinders with radii of $3-5.1-7.2-9.3$ nm and containing respectively $30-51-72-93$ dipoles per ring. On each wall the positions and the orientations of the transition dipole moments are the same as in panel (A). (C) Complex C: model formed by three adjacent cylindrical aggregates with four concentric rolls each.

2.1.2 Antenna complexes in Purple bacteria (PB)

In Purple bacteria *Rhodobacter Sphaeroides*, the light-harvesting complexes are organized in thousands of spherical membrane-embedded protrusions, called chromatophores which typically measure around 60 nm in diameter. Depending on the light conditions, Purple bacteria can contain from 500 up to 2500 chromatophores made of ~ 5000 Bchl molecules each [27]. The major pigments in the chromatophores are the Bchl a [58, 59] which are organized on different complexes inside the chromatophores. Here we consider a portion of the chromatophore (complex A) and the whole chromatophore (complex B):

Complex A - light-harvesting system subunit. The RC is directly surrounded by the so-called light harvesting complex I (LHI). LHI is in turn surrounded by several smaller light harvesting complexes, the LHII complexes [27, 48, 78]. As shown in panel A of Fig. (2.2) two RCs are surrounded by the light-harvesting complex LHI B875, which is an s-shaped structure with 56 Bchl molecules. Then the LHI aggregate is surrounded by 10 LHII rings, each composed by 2 units, the B800 ring, composed by 9 Bchl molecules, and the B850 ring with 18 Bchl molecules. Both complexes LHI and LHII are J-aggregates. In particular LHI is a J-aggregate with two superradiant states close to the lowest excitonic state at 875 nm which are polarized in the ring plane. For the LHII aggregate, the B850 ring has two superradiant states at 850 nm, while the B800 ring has a main absorption peak at 800 nm. This hierarchical structure is able to absorb photons at different frequencies and to funnel the collected energy to the RC [15, 16, 27, 46, 79].

In our simulations we model the RC as an aggregate of four Bchls: two forming the tightly-coupled special pair and two accessory ones [16]. Even if other molecules are present in the RC, these four Bchl molecules are the most relevant for the interaction with the electromagnetic field [80].

Complex B: the chromatophore. We model the whole 3D structure of the chromatophore using data from Ref. [79] collected by AFM, cryo-EM, X-ray crystallography and NMR measurements. In panel B of Fig. (2.2) our model of the chromatophore is shown with different substructures: i) LHII (blue rings); ii) LHI (orange structures); iii) RC, placed at the center of the LHI structures. Chromatophores, see Fig. (2.2 B), are connected to the cell membrane at their south pole, therefore the southern polar region

is left empty (no molecular aggregates are placed there) to allow the contact with the cell membrane [81]. The chromatophore spherical vesicles are reproduced by mapping small planar regions onto spherical ones containing the LHI-RCs or an LHII complex with the area-preserving inverse-Mollweide transformations, see Fig. (A.1) in section A.1 of the Appendix A, used also in Ref. [79, 82, 83]. While in nature the ratio between LHII and LHI-RC depends on illumination and other conditions, here we consider a vesicle model that contains 9 s-shaped LHI-RCs and 131 LHII complexes. The overall Bchl/RC ratio used in our simulation (229) is within the natural range for these vesicles, which is between 108 and 248 and corresponds to low-light growth conditions [79] where these systems show the largest efficiency. The data for the LHI, LHII and RC are taken from Ref. [16, 27]. Even if it would be more realistic to add random rotations of LHII rings around the axis joining the center of the vesicle and the center of the LHII rings, we checked that the effect of such random rotations is small, see Fig. (A.9) of section A.6 of the Appendix A, and thus we did not include such rotations in our simulations.

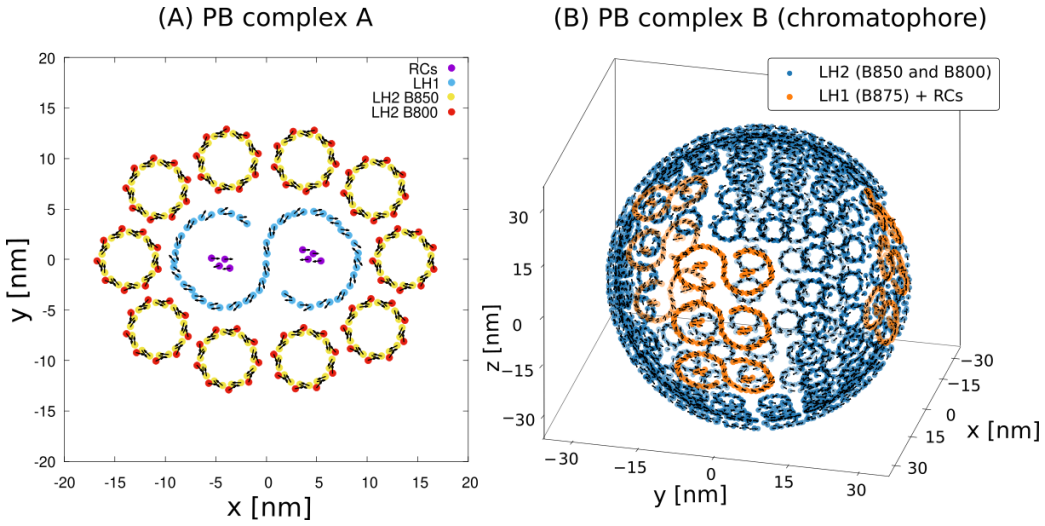

Figure 2.2: *Architecture of PB light-harvesting complexes.* The two complexes A and B of Purple bacteria *Rhodobacter sphaeroides* light-harvesting systems are shown. (A) Complex A: light-harvesting system including two reaction centers RCs (purple) surrounded by the antenna complex LHI B875 (cyan), which is surrounded by 10 LHII B850 and LHII B800 (respectively yellow and orange). Complex A light-harvesting system contains $N = 334$ Bchl molecules. Black arrows represent the positions and orientations of transition dipole moments associated to each Bchl$a$ molecule. (B) Complex B: the vesicle with a radius $R = 30$ nm contains 9 LHI+RC complexes (orange s-shaped complexes) and 131 LHII (B800 + B850) complexes (light blue circles). The total number of molecules is $N = 4113$ and the area of the empty spherical cap at the south pole is $A_{emp} = 39.17$ nm^2 (for more details about the geometry see [81]).

Chapter 3

Quantum theory of light-matter interaction and the emergence of superradiance

In this chapter the topic of light-matter interaction has been addressed. Many processes, including fluorescence, absorption and stimulated emission, occur in atoms and molecules. If absorption and stimulated emission can be treated with a quantum-classical description, where radiation is represented as a classical electromagnetic field and matter is quantized, fluorescence can no longer be explained by this approach, but it requires that both matter and radiation are quantized. In this chapter a quantum description of the interaction between matter and the vacuum of the EMF has been given by the radiative Hamiltonian approach. The radiative Hamiltonian describes the process of spontaneous emission, also called fluorescence, from an ensemble of emitters, assuming a single excitation is already present in the system. The origin of this process relies in the presence of vacuum fluctuations, that induce transitions known as spontaneous emission, even if no photon is present in the field. In this thesis we are interested in the study of light-matter interaction in molecular aggregates of photosynthetic bacteria, such as GSB and PB light-harvesting complexes, which are seen as an ensemble of emitters, that can support a coherent and cooperative response to the interaction with the vacuum of the EMF, called single-photon superradiance.

In Sec. 3.1 a detailed explanation of the radiative Hamiltonian and its approximations has been given, Sec. 3.2 gives a description of the collective phenomenon of superradiance in GSB and PB light-harvesting systems, while in Appendix D the derivation of the non-hermitian Hamiltonian is provided.

3.1 Radiative Hamiltonian and dipole-dipole Frenkel approximation

In this section the problem of an ensemble of emitters coupled to the vacuum of the EMF has been studied. Each emitter can be seen as a two-level system (TLS) with excitation energy e_0 and transition dipole moment (TDM) $\vec{\mu_0}$. The EMF is treated through the black body radiation theory, assuming the Sun is a source of radiation at finite temperature T_{BB} that can induce absorption and both spontaneous and stimulated emission. Ref. [46] have already been deal with this topic by using a Lindblad master equation approach. Here under Born-Markov and secular approximations the system-bath interaction is modeled. Moreover, other assumptions are needed to derive the radiative Hamiltonian: the black body is considered at thermal equilibrium, the single excitation regime is valid because sunlight radiation on the Earth is very diluted and and T_{BB} is vanishing. If all these conditions are considered, the master equation reduces to an effective radiative non-hermitian Hamiltonian, that explains the process of spontaneous emission from an ensemble of emitters and their mutual interaction mediated by the vacuum of the EMF. A well detailed derivation of this model can be found in Ref. [84].

Since the systems operate under natural sunlight, which is very dilute, the single-excitation approximation is used, so that only states containing a single excitation have been considered. Choosing the basis states in the single-excitation manifold, where $|i\rangle$ represents a state in which the i^{th} molecule is excited while all the others are in the ground state, the systems can be described through a radiative non-hermitian Hamiltonian which takes into account the interaction between the molecules mediated by the electromagnetic field (EMF) [54, 55, 85, 86]. The radiative Hamiltonian reads:

$$H_{NHH} = \sum_{i=1}^{N} e_0 |i\rangle\langle i| + \sum_{i \neq j} \Delta_{ij} |i\rangle\langle j| - \frac{\mathrm{i}}{2} \sum_{i,j=1}^{N} Q_{ij} |i\rangle\langle j| \ , \tag{3.1}$$

where e_0 is the excitation energy of single emitter (BChl molecule in our case). The terms Δ_{ij} and Q_{ij} have a diagonal part given by:

$$\Delta_{jj} = 0 \qquad \text{and} \qquad Q_{jj} = \frac{4}{3}\mu_0^2 k_0^3 = \gamma \tag{3.2}$$

with $\mu_0 = |\vec{\mu_0}|$ being the transition dipole moment (TDM) and $k_0 = \frac{2\pi}{\lambda_0}$, where λ_0 is the wavelength associated with the molecular transition. The off-diagonal part ($i \neq j$) is given by

$$\begin{aligned}\Delta_{ij} =& \frac{3\gamma}{4}\left[\left(-\frac{\cos(k_0 r_{ij})}{(k_0 r_{ij})} + \frac{\sin(k_0 r_{ij})}{(k_0 r_{ij})^2} + \frac{\cos(k_0 r_{ij})}{(k_0 r_{ij})^3}\right)\hat{\mu}_i \cdot \hat{\mu}_j \right. \\ & \left. - \left(-\frac{\cos(k_0 r_{ij})}{(k_0 r_{ij})} + 3\frac{\sin(k_0 r_{ij})}{(k_0 r_{ij})^2} + 3\frac{\cos(k_0 r_{ij})}{(k_0 r_{ij})^3}\right)(\hat{\mu}_i \cdot \hat{r}_{ij})\,(\hat{\mu}_j \cdot \hat{r}_{ij})\right],\end{aligned} \tag{3.3}$$

$$\begin{aligned}Q_{ij} =& \frac{3\gamma}{2}\left[\left(\frac{\sin(k_0 r_{ij})}{(k_0 r_{ij})} + \frac{\cos(k_0 r_{ij})}{(k_0 r_{ij})^2} - \frac{\sin(k_0 r_{ij})}{(k_0 r_{ij})^3}\right)\hat{\mu}_i \cdot \hat{\mu}_j \right. \\ & \left. - \left(\frac{\sin(k_0 r_{ij})}{(k_0 r_{ij})} + 3\frac{\cos(k_0 r_{ij})}{(k_0 r_{ij})^2} - 3\frac{\sin(k_0 r_{ij})}{(k_0 r_{ij})^3}\right)(\hat{\mu}_i \cdot \hat{r}_{ij})\,(\hat{\mu}_j \cdot \hat{r}_{ij})\right],\end{aligned} \tag{3.4}$$

where $\hat{\mu}_i := \vec{\mu}_i/\mu_0$ is the unit dipole moment of the i^{th} site and $\hat{r}_{ij} := \vec{r}_{ij}/r_{ij}$ is the unit vector joining the i^{th} and the j^{th} sites. See section A.2 of the Appendix A for the parameters we used for GSB and PB in the Hamiltonian and Appendix D for the derivation of the Δ_{ij} and Q_{ij} terms of the non-hermitian Hamiltonian.

Diagonalizing the Hamiltonian (3.1) we obtain the complex eigenvalues $\varepsilon_n = \mathrm{E}_n - \mathrm{i}\frac{\Gamma_n}{2}$ where Γ_n is the radiative decay of the n^{th} eigenstate. In general Γ_n differs from the radiative decay of the single molecule γ. In particular, when the ratio $\Gamma_n/\gamma \gg 1$ we will talk about a "superradiant state" (SRS) or bright state, otherwise when $\Gamma_n/\gamma \ll 1$ the state is called "subradiant" or dark. In other words, a SRS can radiate much faster than a single molecule, while a subradiant one radiates at a rate much slower than the single molecule radiative decay.

The non-hermitian part of the radiative Hamiltonian (3.1) can be treated as a perturbation whenever the decay widths are much smaller than the mean level spacing computed using the real part of the complex eigenvalues, see discussion in section A.3 of the Appendix A. When this criterion, known

as *resonance overlap criterion* [87], is valid, one can exclusively utilize the hermitian part of the Hamiltonian. This reduction in complexity accelerates calculations. The hermitian part of the Hamiltonian (3.1) is defined as follows:

$$\hat{H}_{HH} = \sum_{i=1}^{N} e_0 |i\rangle\langle i| + \sum_{i \neq j} \Delta_{ij} |i\rangle\langle j| \ , \tag{3.5}$$

where $\Delta_{i,j}$ is given in (3.3). In section A.3 of the Appendix A a comparison between the radiative decay widths computed with the NHH model and the perturbation theory has been provided for a single MT model cylinder (complex A). Assuming that we are in the perturbative regime, where the non-hermitian term Q_{ij} is much smaller than Δ_{ij}, the radiative decay widths have been estimated as the expectation value of Q_{ij} with the eigenstates of the hermitian Hamiltonian.

If the non-hermitian term Q_{ij} can be considered a small perturbation and the system size L is small compared to the wavelength associated with the optical transition of the molecules (small volume limit $L < \lambda_0$), the optical absorption of an eigenstate can be estimated in terms of its dipole strength, computed using only the hermitian part of the Hamiltonian (3.1). Denoting the n^{th} eigenstate of the hermitian part of the Hamiltonian (3.1) with $|E_n\rangle$, we can expand it on the site basis, so that

$$|E_n\rangle = \sum_{i=1}^{N} C_{ni} \, |i\rangle \ . \tag{3.6}$$

To each basis state $|i\rangle$, a dipole moment $\vec{\mu}_i$ is associated, corresponding to the TDM of the i^{th} molecule. If N is the total number of molecules, then we will express the TDM $\vec{D}_n$ associated with the n^{th} eigenstate as follows:

$$\vec{D}_n = \sum_{i=1}^{N} C_{ni} \, \hat{\mu}_i \ . \tag{3.7}$$

The dipole strength of the n^{th} eigenstate is defined by $|\vec{D}_n|^2$ (note that due to normalization $\sum_{n=1}^{N} |\vec{D}_n|^2 = N$ [88]).

Finally, we note that when resonances do not overlap and $k_0 r_{ij} \ll 1$, the hermitian part of the radiative Hamiltonian reduces to the standard dipole-dipole Frenkel Hamiltonian:

$$H_{DH} = \sum_{i=1}^{N} e_0 |i\rangle\langle i| + \sum_{i \neq j} \frac{\vec{\mu}_i \cdot \vec{\mu}_j - 3(\vec{\mu}_i \cdot \hat{r}_{ij})(\vec{\mu}_j \cdot \hat{r}_{ij})}{r_{ij}^3} |i\rangle\langle j| \ . \tag{3.8}$$

In the following, we will analyzed all complexes using the three different Hamiltonian models introduced in this section, namely:

1. NHH: non-hermitian radiative Hamiltonian Eq. (3.1),
2. HH: hermitian Hamiltonian Eq. (3.5) valid under the non-overlapping resonance criterion,
3. DH: Dipole Hamiltonian Eq. (3.8) valid under the non-overlapping resonance criterion and when the system size is small compared to the wavelength associated with the optical transition of the molecules.

3.2 The emergence of superradiance in GSB and PB antenna complexes

Cooperativity is a common feature in complex systems, since an ensemble of emitters generally behaves differently from its individual constituents when they interact coherently via a common light field. Spontaneous emission of photons occurs because of coupling between excited two-level systems (TLSs) and the vacuum modes of the electromagnetic field, effectively stimulated by its zero-point fluctuations. When an ensemble of emitters confined in a volume smaller than about λ_0^3 (where λ_0 is the corresponding emission wavelength of the TLS) a coherent and cooperative spontaneous emission, also called superradiance, emerges [89]. In 2009 two scientists, Scully and Svidzinsky, explored this cooperative single-photon emission described on the Science article "The Super of Superradiance", see Ref. [90]. This so-called superradiant emission results from the coherent coupling between individual TLS through the common vacuum modes, effectively leading to a single giant emitting dipole from all participating TLS.

Experimental evidences and theoretical models confirm the presence of superradiance (SR) in many physical systems, such as perovskite quantum dots [89], molecular aggregates and crystals [91, 92], cold atoms [93] and nitrogen vacancies in nanodiamonds [94]. In this thesis we are interested in

the study of the relationship between structure and cooperativity in molecular aggregates. There is evidence in the literature that both natural and artificial systems can support cooperative effects, such as superradiance in artificial nanotubes [95] and in natural light-harvesting systems of PB [10] and GSB [24].

In this thesis we perform large scale numerical simulations using the three Hamiltonian models described in the previous section in order to investigate the emergence of SR both in portions and in the entire light-harvesting systems of GSB and PB.

Here below we show the numerical results obtained for the antenna complexes of GSB and PB. The three Hamiltonian models explained in Sec. 3.1 (NHH, HH and DH) have been diagonalized for both GSB and PB complexes in order to study the interaction between the molecules mediated by the vacuum of the EMF and the emergence of superradiance, which is the collective emission of light from an ensemble of emitters due to the formation of coherent and extended exciton states.

The cooperative response to light of the entire photosynthetic antenna complexes has not been theoretically studied thus far. Indeed, whether the arrangement of the Bchl molecules in the entire GSB and PB antenna complexes is capable of supporting collective states brighter than the single subunits in the complex, is not a trivial question to address. On one side, it is not guaranteed that the symmetry of the entire antenna is capable of supporting a cooperative response larger than its sub-units. Moreover, the most widely used theoretical model, the Frenkel Hamiltonian [96] based on dipole-dipole interaction, becomes ineffective beyond the small volume limit, i.e. when the system size is comparable with the wavelength of the absorbed light. For this reason here we employ a radiative Hamiltonian model, well-established in quantum optics for several decades [13, 54]. The radiative Hamiltonian allows us to explore light-matter interaction of photosynthetic antennae beyond the small volume limit, where the Frenkel Hamiltonian cannot be used. The radiative Hamiltonian contains non-hermitian terms that account for photon losses due to spontaneous emission and accurately describes the effective interaction between molecules. Even if the non-hermitian part is usually considered in the frame of perturbation theory, this approximation breaks down in large systems when resonances overlap [87].

Note that in chapter 5 the absorption spectra derived using our model will be compared with the experimental results for GBS and PB, showing

a good agreement and proving that our model is a valid approximation for these systems.

3.2.1 Green Sulfur Bacteria complexes

Here, the complexes A, B, C of GSB described in Sec. 2.1.1 have been analyzed. In Fig. (3.1) the spectrum of the three complexes is shown for the maximal length considered, $L = 148.57$ nm, corresponding to cylindrical aggregates with 180 rings. Thus, for the three complexes we have $N = 10800$ (complex A), $N = 44280$ (complex B), $N = 132840$ (complex C) chlorophyll molecules. Panels (A-C) in Fig. (3.1) show that the structure of all complexes allow for the emergence of red-shifted superradiant states, close to the lowest excitonic states. Moreover the amount of maximal superradiance ($(\Gamma/\gamma)_{max}$) increases with the system size, see Fig. (3.2). The largest amount of superradiance is present in complex C which is the largest one and the closest to the natural size and structure of GSB antennae. Note that the fact that in larger aggregates superradiance is enhanced is far from being trivial. Indeed, if we would increase the system size by adding the molecules in the same positions but with randomized dipole directions, no superradiant enhancement would be present, as shown in section A.7 of the Appendix A.

By comparing the three Hamiltonians, see also discussion in section A.4 of the Appendix A, we note that for complex A, all of them give a good description of the superradiant states. For complex B a deviation between DH and the other two models (NHH and HH) is observed, while in complex C the three Hamiltonian models give different results. This shows that using the most accurate Hamiltonian, which is the NHH model, is essential to describe large photosynthetic antennae. The same behavior is also shown in Fig. (3.2). In each panel of Fig. (3.2) we show the maximal decay width for each complex as a function of the complex length. In each panel the maximal decay width has been computed using three different Hamiltonian models: DH, HH, NHH. For the DH and HH model we computed the maximal decay width using the dipole strength, while for the NHH model the maximal decay width has been computed using the imaginary part of the complex eigenvalues of the radiative non-hermitian Hamiltonian. As one can see in the largest complex Fig. (3.2 panel C) the three Hamiltonians give very different results.

The origin of the difference between the NHH and the other Hamiltonian

models can be explained by the overlapping resonance criterion [87], see panel D in Fig. (3.1). Indeed, when the decay width becomes comparable with the eigenmodes mean level spacing, the non-hermitian part of the Hamiltonian cannot be treated perturbatively and the dipole strength Eq. (3.7) does not describe anymore the decay widths of the eigenmodes.

Accounting for the results of Fig. (3.1) and those ones found in section A.3 of the Appendix A, we have demonstrated that for a single cylinder Q_{ij} can be considered a small perturbation and the same values for the radiative decay widths have been obtained using both the radiative non-hermitian Hamiltonian and the perturbation theory. These foundings have already been proved in Fig. (3.1, panels D-F), where the ratio between all the radiative decay widths Γ_n and the mean level spacing δ between the energies of the system has been computed for complexes A, B and C. The results shown in panels (D-F) revealed that for complex A the ratio is always smaller than 1, so the perturbative approach is still valid. For the entire chlorosome (complex C) the maximum value of the ratio, corresponding to the most SRS, is almost 10^2 and also other eigenstates show a ratio larger than 1, proving that for larger systems the perturbative regime and the HH model fail, while the NHH model is the only way to describe the radiative response of the system.

3.2.2 Purple Bacteria complexes

Here we analyze the whole chromatophore of the Purple bacteria antenna complex (complex B), see Fig. (2.2 B) containing 4113 chlorophyll molecules. As a comparison we will also analyze complex A, see Fig. (2.2 A).

Fig. (3.3) shows the spectra of the two complexes obtained by diagonalizing the three Hamiltonians models (HH, NHH and DH). Panels (A-B) of Fig. (3.3) demonstrate that both PB complexes allow the emergence of red-shifted superradiant states. Furthermore, the amount of superradiance is larger in the larger complex, the chromatophore. It is interesting to note that all Hamiltonian models (HH, NHH and DH) give very similar results in both the complexes considered. The HH model and the NHH model give similar results since, as it is shown in panel C of Fig. (3.3), the decay widths are always smaller than the eigenmodes mean level spacing, so that the non-hermitian part of the Hamiltonian can be treated perturbatively. The DH model is also a good approximation even for the whole chromatophore since $L/\lambda_0 \approx 0.1$ so that we are in the small volume limit.

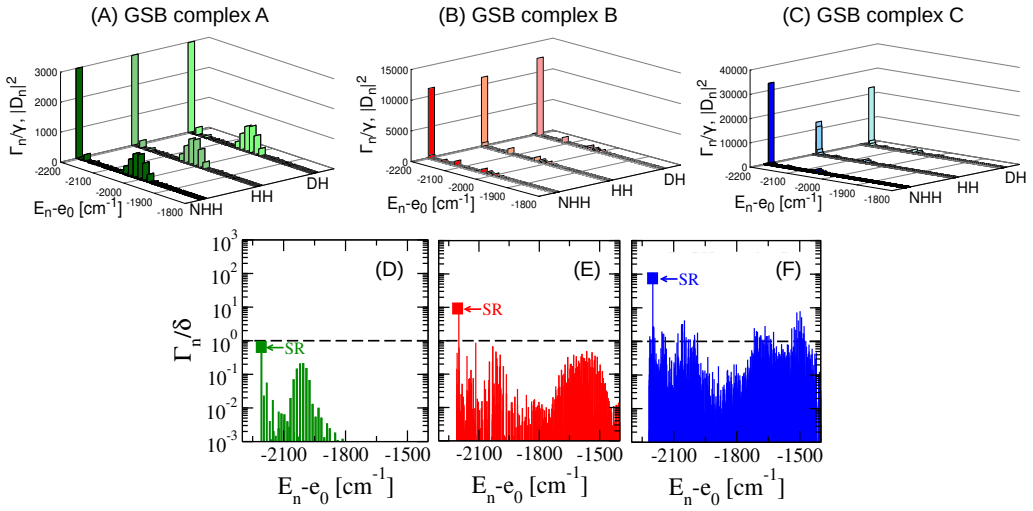

Figure 3.1: *Superradiant states in Green Sulfur Bacteria Antennae.* Complexes A (single cylinder, green), B (four concentric cylinders, red) and C (three adjacent concentric cylinders, blue) are shown in the respective panels (Panels A,B,C). Three different Hamiltonian models are compared for each complex using different shades of colour (NHH: non-hermitian Hamiltonian Eq. (3.1, dark), HH: hermitian Hamiltonian Eq. (3.5, medium shade), DH: Dipole Hamiltonian Eq. (3.8, light). The dipole strength $|\mathrm{D}_n|^2$, see Eq. (3.7), is shown for the HH and DH model, while the radiative decay width Γ_n/γ is shown for the NHH model as a function of the energy $E_n - e_0$. Panels (A-C) show only the lowest part of the energy spectrum where the most superradiant states are located. Results are computed by using a fixed length $L = 148.57$ nm for each aggregate, which corresponds to the maximal length analyzed (180 rings for each cylinder). (Panels D-F) Ratio between the decay width Γ_n obtained by diagonalizing the full radiative Hamiltonian (NHH model) in Eq. (3.1) and the mean level spacing δ as a function of the energy $E_n - e_0$ for complexes A (dark green), B (dark red), C (dark blue) with a fixed length $L = 148.57$ nm. The mean level spacing δ is computed as the ratio between the energy spectral width and the total number of eigenmodes for each complex. Green, blue and red squares indicate the positions in the energy spectra of the most superradiant state for each complex. The horizontal dashed line represents the value of the ratio $(\Gamma_n/\delta = 1)$ above which resonances overlap.

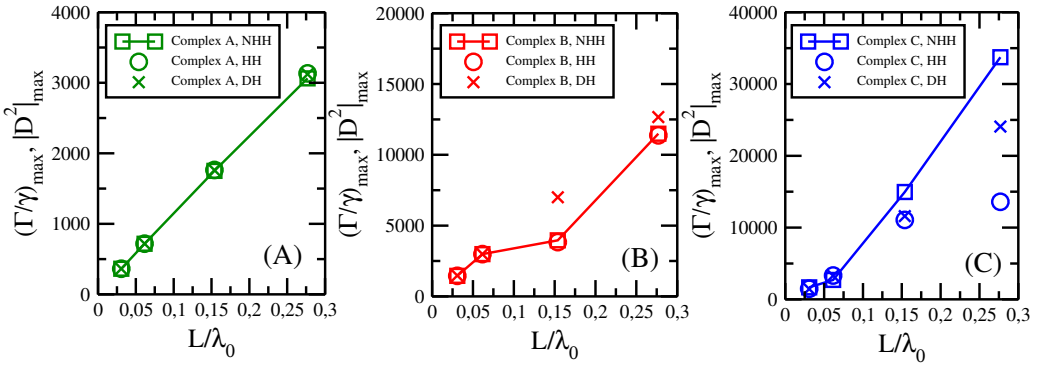

Figure 3.2: *Cooperativity in GSB complexes.* Panels A, B, C: the maximal decay width is shown for different complexes A (green symbols in panel A), B (red symbols in panel B), C (blue symbols in panel C) as a function of the length of the aggregates L, normalized to the transition wavelength of a single molecule λ_0, see Tab. (A.1) in section A.2 of the Appendix A. The maximal decay width has been obtained from the dipole strength $|D|^2_{max}$ for the DH model (crosses) and the HH model (circles) and from $(\Gamma/\gamma)_{max}$ for the NHH model (squares). For the NHH model, which is the most accurate model, symbols (squared) have been connected by lines. The maximal length we considered is $L = 148.57$ nm, that corresponds to aggregates made of cylinders with 180 rings.

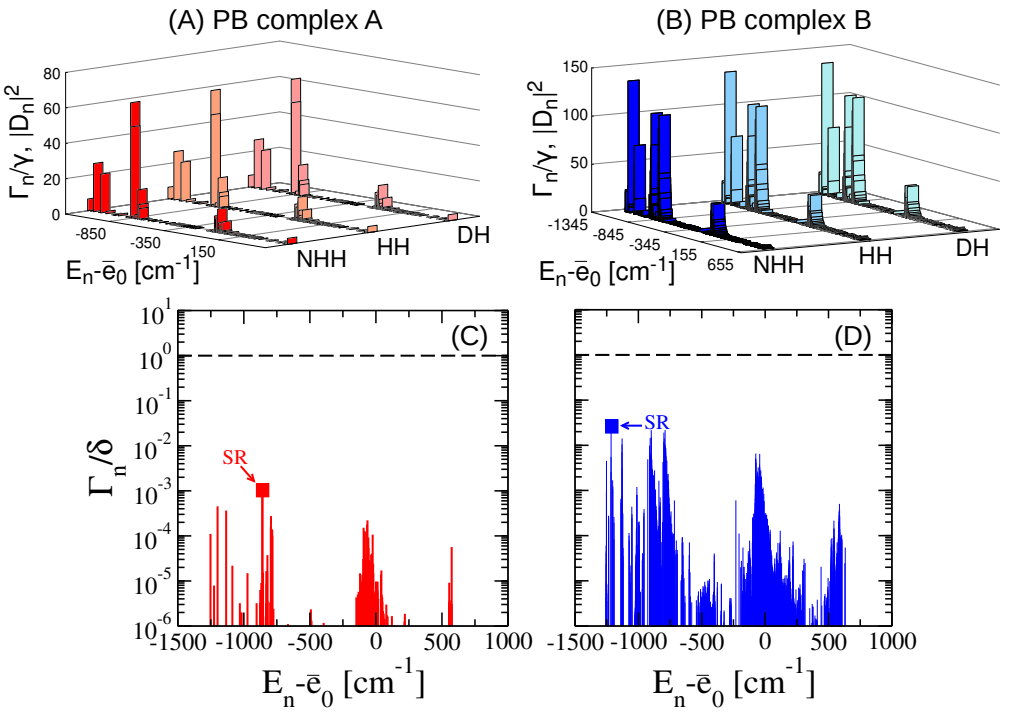

Figure 3.3: *Superradiant states and cooperativity in Purple bacteria Antennae.* (Panels A) Complex A (light-harvesting system with an LHI s-shaped system with 2 RCs surrounded by 10 LHII rings in red colour). (Panels B) Complex B (entire PB chromatophore in blue colour). Three different Hamiltonian models are compared for each complex using different shades of colour (NHH: non-hermitian Hamiltonian Eq. (3.1, in dark colours), HH: hermitian Hamiltonian Eq. (3.5, in medium shade of colours), DH: Dipole Hamiltonian Eq. (3.8, in light colours). In panels A-B, the dipole strength $|D_n|^2$, see Eq. (3.7), is shown for the HH and DH models, while the radiative decay width Γ_n/γ is shown for the NHH model as a function of the energy $E_n - \bar{e}_0$, where $\bar{e}_0$ is the average excitation energy of the Bchl molecules found in PB antennae complexes, see Tab. (A.2) in section A.2 of the Appendix A. Panels (A-B) show only the lowest part of the energy spectrum where the most superradiant states are located. Panels (C-D) show in log-scale the ratio between the decay width Γ_n, obtained by diagonalizing the full radiative Hamiltonian (NHH model) in Eq. (3.1), and the mean level spacing δ as a function of the energy $E_n - \bar{e}_0$ for complexes A (in dark red color) and B (in dark blue color). The mean level spacing δ is computed as the ratio between the energy spectral width and the total number of eigenmodes for each complex. Red and blue squares indicate the positions in the energy spectra of the most superradiant state for each complex. The horizontal dashed line represents the value $\Gamma_n/\delta = 1$ above which resonances overlap.

3.2.3 Cubic arrays of chromatophores in PB cells

Purple bacteria cells present an ellipsoidal shape with a length of about $1-2$ μm and a width of 0.8 μm that contain from 500 to 2500 chromatophores, depending on the lighting conditions. There are about 500 vesicles per cell in cultures grown under high-light intensities, while low-light cells can contain up to 2500 vesicles [97, 98]. A single cell of Purple bacteria has a volume of about $V_{cell} = \frac{4}{3}\pi abc = 6.7 \cdot 10^8$ nm^3, where $a = c = 0.4$ μm and $b = 1$ μm are the ellipsoid semi-axis [97]. A single chromatophore has a volume of about $V_{chrom.} = \frac{4}{3}\pi R^3 = 1.13 \cdot 10^5$ nm^3, where $R = 30$ nm is the radius of the vesicle. If the total number of vesicles varies from 500 to 2500, their concentration χ is between 750 chrom./μm^3 and 3730 chrom./μm^3.

In this section cubic arrays comprising 8 chromatophores with different concentrations have been taken into account in order to study whether a large concentration of the aggregates can enhance the superradiance. Fig. (3.4) shows the four different concentrations we have chosen for this study. The smallest value we have considered, $\chi_{min} = 0.2$ chrom/μm^3, corresponds to the minimum value of the concentration, also used by our experimental collaborators at CNR of Bari [97]. The other models are consistent with the realistic data, where χ is between 750 chrom./μm^3 and 3730 chrom./μm^3, as found in literature [98].

Here large scale simulations of systems comprising 8 PB chromatophores arranged in a cubic array at different concentrations has been done in order to understand if superradiance is enhanced with respect to the single vesicle. Fig. (3.5) shows how cooperative effects scales with the concentration of the system. In particular panels (A-B) represents how the superradiant decay width increases with the concentration of the system, reaching its maximum value for the largest concentration $\chi = 3730$ chrom./μm^3 we have considered. In this case superradiance is enhanced by 7 times with respect to the single vesicle, whose maximum decay width is represented by the blue dashed line. When chromatophores are very diluted ($\chi_{min} = 0.2$ chrom./μm^3), the most superradiant decay width is comparable to the one found for the single vesicle. These results demonstrate that closer the chromatophore, larger is the coupling strength between the aggregates, so that an enhanced cooperative response is obtained. For the most dilute system the edge to edge distance between chromatophores is so large that the coupling between molecules belonging to different aggregates is negligible and we obtain a spectrum which

is comparable to the one for the single vesicle.

Finally panel C shows the ratio between the decay width Γ_n/γ, obtained by diagonalizing the full radiative Hamiltonian, and the mean level spacing δ both for the single vesicle and the cubic arrays formed by 8 chromatophores at different concentrations. The results show that for the largest values of the concentration ($\chi = 750 - 2000 - 3730$ chrom./μm^3) the ratio is close to 1. This means that the radiative Hamiltonian is the most accurate approach to describe superradiance in such systems. These results confirm our decision to choose the NHH model to perform calculations, even if for the single vesicle both HH and DH models can be considered good approximations, as already demonstrated in panels B and D of Fig. (3.3).

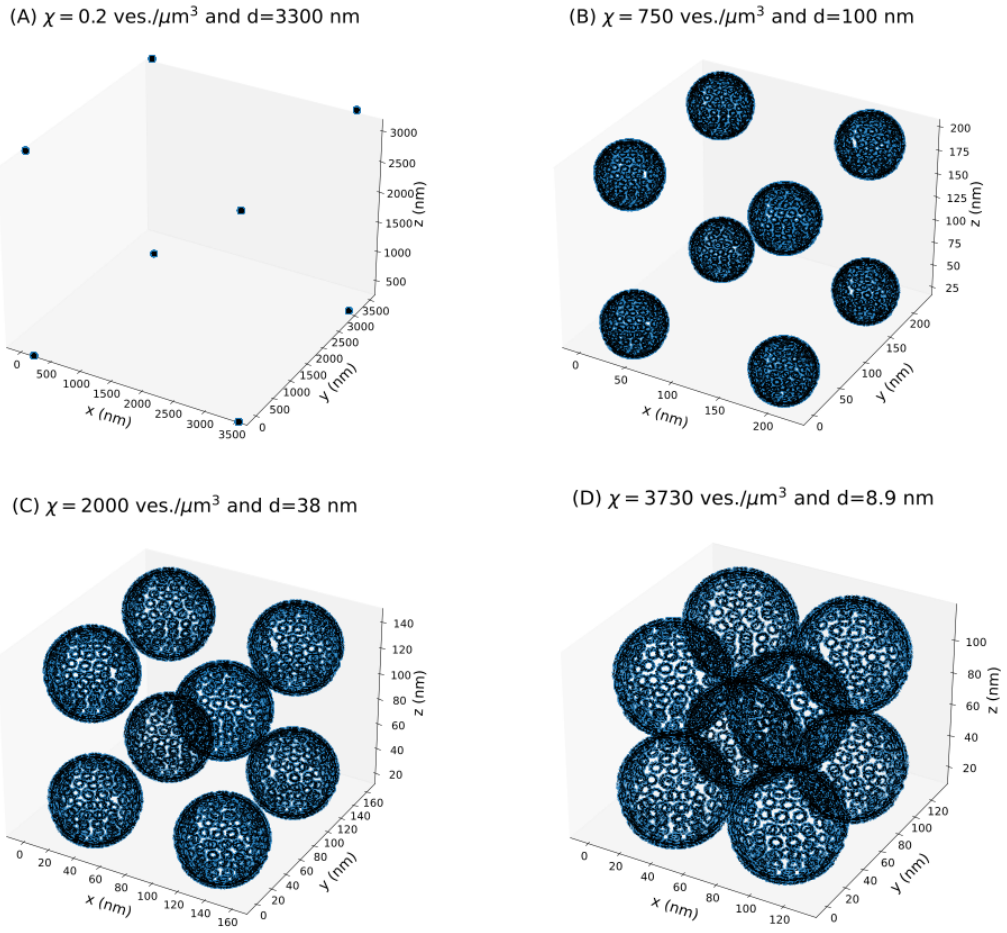

Figure 3.4: *Cubic arrays of 8 chromatophores at different concentrations.* Panels (A-D) model a solution of 8 chromatophores in a cubic array at different concentrations χ. Panel A shows the min. value of concentration ($\chi_{min} = 0.2$ chrom/μm^3), also used by our experimental collaborators at CNR of Bari [97]. Panels (B-D) represent the realistic values of concentration which are between 750 chrom/μm^3 and 3730 chrom/μm^3. Here the parameter d represents the edge to edge distance between chromatophores.

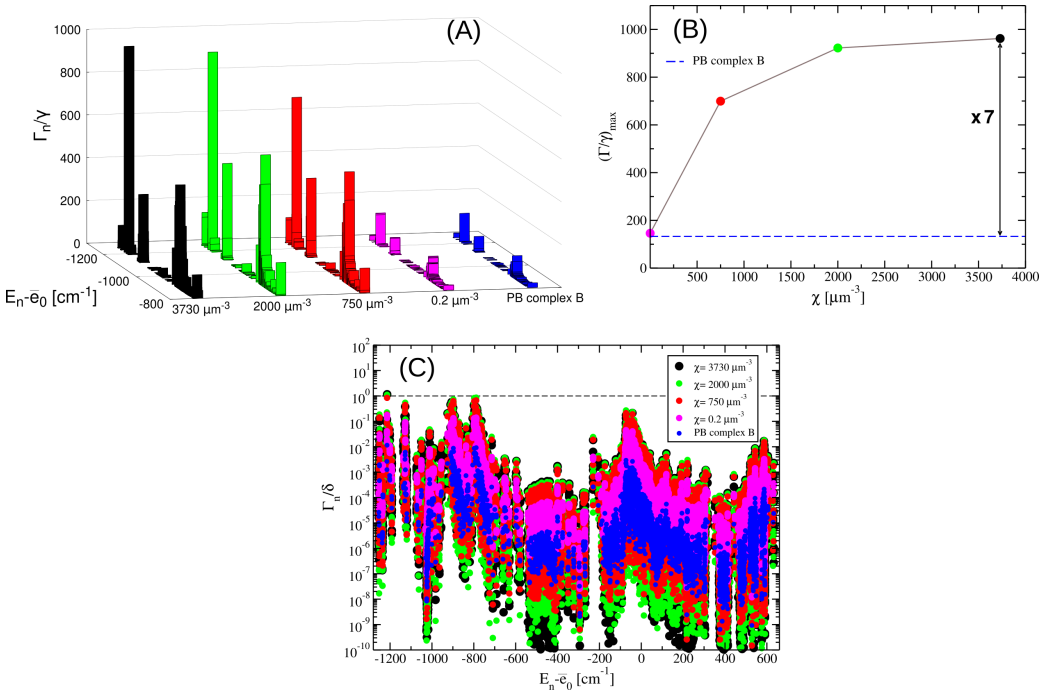

Figure 3.5: *Cooperativity in cubic arrays of PB chromatophores.* Panel A shows the lowest part of the energy spectrum obtained by using the full radiative Hamiltonian (NHH). Results of the decay width Γ_n/γ are compared both for a single PB chromatophore (blue color) and for a cubic array of 8 chromatophores with different concentrations χ (magenta, red, green and black colors for $\chi = 0.2 - 750 - 2000 - 3730$ μm^{-3} respectively). Panel B shows the largest value of the decay width as a function of the concentration. The blu dashed line represents the value obtained for a single PB chromatophore. Panel C represents in log-scale the ratio between the decay width Γ_n, obtained by diagonalizing the full radiative Hamiltonian (NHH model) in Eq. (3.1), and the mean level spacing δ as a function of the energy $E_n - \overline{e}_0$ for PB complex B (in dark blue color) and for arrays of chromatophore with different concentrations χ (magenta, red, green and black colors for $\chi = 0.2 - 750 - 2000 - 3730$ μm^{-3} respectively). The mean level spacing δ is computed as the ratio between the energy spectral width and the total number of eigenmodes for each complex. The horizontal dashed line represents the value $\Gamma_n/\delta = 1$ above which resonances overlap.

3.3 Conclusions

In this chapter large scale simulations of the whole antenna complexes of Green sulfur bacteria and Purple bacteria have been performed using a radiative non-hermitian Hamiltonian, which, at variance with the standard Frenkel dipole Hamiltonian, is valid beyond the small volume limit. The largest Green sulfur antenna complex considered was composed of 132840 Bchl$c$ molecules, arranged in three adjacent cylinders, each composed of 4 concentric cylinders of different radii. The size of the largest complex was 148.57 nm $\times$ 18.6 nm $\times$ 61.8 nm, comparable with the size of natural antenna complexes. For the Purple bacteria the whole chromatophore was considered, which is a spherical structure of 60 nm of diameter and composed of 4113 Bchl$a$ molecules. Finally cubic arrays made of 8 chromaptophores at different concentrations have been analyzed. According to literature [98], four values of the concentrations has been considered: $\chi = 0.2 - 750 - 2000 - 3730$ chrom./μm^3. The smallest value is consistent with experiments made by our collaborators at CNR of Bari, while the other values are in strong agreement with realistic data found in nature.

While smaller portions of these complexes have been widely analyzed in literature and superradiance has been found both theoretically and experimentally, an open question was whether superradiant effects will be enhanced in the whole complex. Our analysis has shown that the maximal superradiant decay width in the largest Green sulfur bacteria complex is ten times larger than in a single wall cylinder of the same length (see Fig. (4.2) panel A), while in the Purple bacteria chromatophore, it is about six times larger than in the single LHI complex and about ten times larger than the single LHII complex (see Fig. (4.3) panels A and B). Also the results obtained for the cubic arrays of PB chormatophores show that the maximal superradiant decay width increases with the concentration. For the system with the largest value of the concentration $\chi = 3730$ chrom./μm^3 the maximal superradiant decay width is seven times larger than in the single vesicle (see Fig. (3.5) panel B). This proves that the bare structure of the whole antenna complexes is able to support an enhanced superradiant response. This is not trivial since superradiance critically depends on the arrangement of the emitters and it can be easily quenched.

In analyzing different antenna complexes, we compared three distinct Hamiltonian models: the full radiative non-hermitian Hamiltonian model;

the hermitian Hamiltonian, valid when the decay widths are significantly smaller than the mean level spacing; and the Dipole Hamiltonian, applicable when resonances do not overlap and when $k_0 r_{ij} \ll 1$. For Purple bacteria chromatophores, all models (complex A and B) yield consistent results due to the system's small size (e.g., 60 nm) relative to the absorbed wavelength ($\lambda \approx 800$ nm) and the limited number of Bchl molecules present. However, for the largest complexes considered in Green sulfur bacteria and for cubic arrays of PB chromatophores, only the non-hermitian Hamiltonian model provides reliable results.

Indeed consistent differences have been found in the largest complex analyzed (GSB complex C). The origins of such differences are not trivial. Indeed, they are not due to the fact that the three Hamiltonian models considered (DH, HH, and NHH) are characterized by different coupling strengths between the chlorophyll molecules, see section A.8 of the Appendix A, but due to the fact that the decay widths in the largest system overlap leading to a different distribution of the dipole strengths among the eigenstates. This idea is supported by our analysis of the resonance overlap presented in this thesis. This shows that the full non-hermitian Hamiltonian is essential to analyze the light-matter interaction in molecular aggregates even in the small volume limit when resonances overlap.

The presence of very bright (superradiant) states in the whole photosynthetic antenna could shed new light in understanding the functionality of such complexes. In particular, the presence of superradiance and subradiance plays an important role for the efficiency of the energy transfer in these aggregates [16, 99]. Let us also remark that the system dynamics strongly depends on the choice of the initial state which is mainly determined by the most superradiant states, see section A.5 of the Appendix A for a more detailed discussion about the delocalization of superradiant states in PB and GSB antennae.

Our theoretical findings could inspire experimental validation of the extent of cooperative response in natural complexes predicted in this chapter. To address these experiments, spectroscopy methods can be employed to characterize the size dependence of the optical response, comparing different portions of the photosynthetic antennae extracted from Green and Purple bacteria, with the whole photosynthetic structures. In particular, the radiative decay widths obtained through time resolved fluorescence spectroscopy and the quantum yield obtained from spectrofluorimetric measurements con-

ducted at different temperatures (from 77 K to room temperature) could provide a clear signature of cooperative effects present in large photosynthetic aggregates.

Chapter 4

Robustness to static and thermal noise in GSB and PB

In this chapter the effect of static and thermal noise will be investigated. In the field of quantum biology modeling noise and disorder in light-harvesting systems is an important issue, because there is evidence that in presence of disorder and thermal noise the dynamics of the system can be affected considerably. The presence of disorder induces localization and an exponential suppression of transport efficiency. Here we ask if cooperativity can be sustained in natural systems even in presence of static and thermal noise comparable to natural conditions. In this chapter, due to the large size of the systems we are considering (PB and GSB light-harvesting systems), a minimal but solid model to include both static and thermal noise is developed. Here we provide a detailed analysis of the thermal coherence length, that indicates on how many molecules the excitation is spread coherently when the system is at thermal equilibrium with a thermal bath at a given temperature T, and superradiance in presence of static disorder. Results show that our systems are able to support cooperative effects and to maintain a large value of the thermal coherence length even in presence of static and thermal noises comparable to ambient conditions.

4.1 Static and thermal noise

Modeling the effect of noise and disorder in natural systems has been an important issue in the field of quantum biology. The environmental noise in the literature has been described with an open quantum system approach using an environment-system interaction even for non-markovian baths [100, 101]. Nevertheless due to the huge sizes considered in this thesis we will adopt a minimal but solid modeling of noise and disorder. Noise due to thermal fluctuations will be taken into account by considering a state at thermal equilibrium, while disorder will be modeled as space dependent and time independent fluctuations of the site energies, keeping the couplings between the molecules constant. Both approaches have been widely used in literature [10, 51, 55, 102]. They have the advantage to capture the main detrimental effects of noise and disorder even if a realistic modeling of the environment would require a much more sophisticated approach [26, 76, 77, 103, 104].

Given a quantum state specified by the density matrix $\hat{\rho}$ it is possible to define its coherence length in the single-excitation manifold defined by the basis states $|i\rangle$ [13, 105, 106] in the following way:

$$L_\rho = \frac{1}{N} \frac{\left(\sum_{ij} |\rho_{ij}|\right)^2}{\sum_{ij} |\rho_{ij}|^2} \ . \tag{4.1}$$

L_ρ in Eq. (4.1) measures how much a single excitation is spread coherently over the molecules composing the aggregate. To give an idea of its physical meaning let us consider three different simple cases.

- A pure localized state, $\hat{\rho} = |i\rangle\langle i|$; then it is easy to see that the coherence length defined in Eq. (4.1) is given by $L_\rho = 1/N$. This case represents the minimal value that L_ρ can get.

- A completely delocalized mixed state characterized by the density matrix

$$\hat{\rho} = (1/N) \sum_{i=1}^{N} |i\rangle\langle i|. \tag{4.2}$$

  In this case we have $L_\rho = 1$. This state is maximally delocalized in the basis, but it is completely incoherent.

- Lastly we consider the fully delocalized coherent state: $\hat{\rho} = (1/N)\sum_{i,j=1}^{N} |i\rangle\langle j|$. In this case we have $L_\rho = N$. Note that any pure state with constant amplitude $1/\sqrt{N}$ over the sites and arbitrary phases would give the same result.

It is easy to see that $1/N \leq L_\rho \leq N$. The closer L_ρ is to N, the higher a coherent delocalization can be assigned to our state. In the same way $L_\rho < 1$ indicates an incoherent localized state. States characterized by $L_\rho \sim 1$ have a little ambiguity (since both localization and coherence are measured on the same length scale).

For all models we have computed the thermal coherence length at room temperature ($T = 300$ K), defined for a state at the canonical equilibrium and whose matrix elements are given by:

$$\rho_{ij} = \sum_n \frac{e^{-\beta E_n}}{\mathrm{Tr}(e^{-\beta \hat{H}})} \langle i|E_n\rangle\langle E_n|j\rangle \ , \tag{4.3}$$

where $\beta = 1/k_B T$.

A very important question to be answered is how much the symmetrical arrangement of the molecules that produces superradiance, is also able to produce a large thermal coherence length at room temperature. Note that even if we consider the coherence length at thermal equilibrium, this does not mean that out-of-equilibrium processes are not important in molecular nanotubes. Indeed in Ref. [107] strong evidence of ultra-fast transport in natural structures with transfer times less than 100 fs have been discussed. Nevertheless thermal equilibrium can be considered as a worst case scenario for coherences. For this reason assuming thermal equilibrium can be considered a good starting point to assess the structural robustness of quantum coherence to thermal noise. In the following we calculate the coherence length L_ρ according to Eq. (4.1), using a thermal density matrix as in Eq. (4.3).

Natural complexes are not only affected by thermal noise but also by other sources of disorder due to the fluctuations in the local environment. In order to analyze the robustness to this kind of disorder, we have considered time-independent and space-dependent fluctuations of the excitation energy of the molecules in the aggregates. Specifically, we consider energy fluctuations which are uniformly distributed around the excitation energy of the molecules e_0, between $e_0 - W/2$ and $e_0 + W/2$, where W represents

the disorder strength. It is known that static disorder induces eigenmodes localization [108] and quenching of superradiance [102].

In order to analyze the robustness of natural models to static disorder and thermal noise we have chosen two figures of merit: the maximal dipole strength Eq. (3.7) and the thermal coherence length Eq. (4.1). Both quantities have been studied as a function of the static disorder strength W.

Fig. (4.1 A,B) shows the maximal dipole strength and the thermal coherence length for the case of a single cylinder (complex A of the GSB) for different cylinder lengths. For complex A we used the HH model to compute both figures of merits since the results obtained with the latter model do not differ substantially from those obtained with the NHH model while giving a substantial computational advantage.

In Fig. (4.1 A,B), one can see that both quantities increase with the system size, even if the thermal coherence length tends to saturate. Moreover, both figures of merits show that single cylinders are very robust to disorder and thermal noise. Indeed, their maximal value (for $W = 0$) remains mostly unchanged up to values of the disorder strength comparable with the thermal energy at room temperature ($W = k_B T$ for $T = 300$ K). Note that, in natural systems, the static disorder strength is usually of the same order of magnitude of the thermal energy. In Fig. (4.1 C,D) the maximal dipole strength (panel C) and the thermal coherence length (panel D) are shown at $W = 0$ and $W = k_B T$ for different cylinder length containing different number N of chlorophyll molecules. Interestingly the value of both figure of merits is the same for the two values of disorder strength considered, showing their extreme robustness to disorder. Moreover the maximal dipole strength (panel C) increases linearly with N which shows that such structures are extremely effective at preserving cooperative effects as a function of the system size. Indeed single excitation superradiance cannot increase faster than N. The thermal coherence also increases with the system size (panel D), even if it shows a tendency to saturate as N increases.

We now consider in Fig. (4.2), the three different complexes for a fixed length corresponding to 100 rings for each cylindrical aggregates (82.17 nm), smaller than the maximal system length considered in Fig. (3.1,3.2). Also in this case we used the HH model to compute both figures of merit since for this length scale the HH model is quite accurate for all complexes, see discussion in section A.4 of the Appendix A. While the maximal dipole strength decreases with disorder Fig. (4.2 A), it is still much larger than one even

for $W = k_B T$. On the other hand, the thermal coherence length shows a large robustness to disorder, Fig. (4.2 B) up to $W = k_B T$. In Fig. (4.2 C,D) the maximal dipole strength (panel C) and the thermal coherence length (panel D) are shown at $W = 0$ and $W = k_B T$ as a function of the number N of chlorophyll molecules present in the three different complexes A,B,C. The most important feature of both figures of merit is that they grow as a larger portion of the photosynthetic antenna is considered, showing that the structure of the GSB photosynthetic antenna as a whole is able to support excitonic coherences. Note that in presence of disorder, the maximal dipole strength grows slower with N compared with the case of zero disorder (panel C). On the other hand, the value of the coherence length is the same for the two values of disorder strength considered, showing its robustness to disorder (panel D), but as N increases it shows a tendency to saturate.

Finally, we analyze the robustness to static disorder and thermal noise in PB complexes (single LHI, complex a and B) using the average maximal dipole strength Eq. (3.7) and the average thermal coherence length Eq. (4.1) as figures of merit. Both of them have been computed using the HH model.

In Fig. (4.3) the average maximal dipole strength and thermal coherence length for both complexes A and B are shown as a function of the disorder strength W rescaled over the thermal energy $k_B T$ at room temperature, $T = 300$ K. For sake of comparison, we also add the data for the s-shaped LHI (green symbols), indicated by the cyan structure in Fig. (2.2 A), which is smaller than complex A and complex B.

As for the GSB complexes, the maximal dipole strength decreases with disorder Fig. (4.3 A), even if it is still much larger than one for $W = k_B T$. On the other hand, the thermal coherence length shows a large robustness to disorder, Fig. (4.3 B) up to $W = k_B T$. In Fig. (4.3 C,D) the maximal dipole strength (panel C) and the thermal coherence length (panel D) are shown at $W = 0$ and $W = k_B T$ as a function of the number N of chlorophyll molecules contained in the s-shaped LHI and complexes A and B.

Both figures of merit grow as a larger portion of the photosynthetic antenna is considered. Note that in presence of disorder, the maximal dipole strength grows slower with N compared with the case of zero disorder (panel C). On the hand, the value of the coherence length is the same for the two values of disorder strength considered, showing its robustness to disorder (panel D). Nevertheless, as N increases, it shows a tendency to saturate.

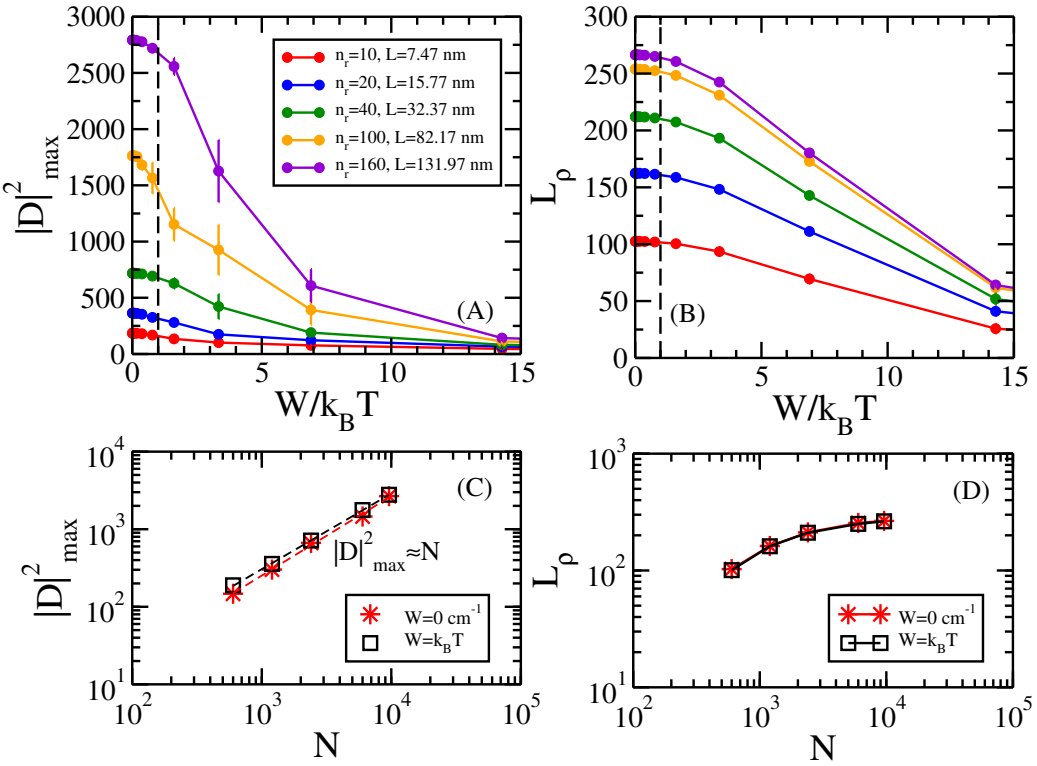

Figure 4.1: *GSB complex A: robustness to disorder and thermal noise.* The average maximal dipole strength (panel A) defined in Eq. (3.7) and the thermal coherence length (panel B) shown in Eq. (4.1) as a function of the normalized static disorder W/k_BT are shown for a GSB single wall cylinder (complex A) with different lengths L, comprising n_r rings. The thermal coherence length and the maximal dipole strength are computed using the HH model Eq. (3.5) and averaging over 10 disorder realizations. k_BT is the thermal energy at room temperature ($T = 300$ K). The vertical dashed line represents $W = k_BT$. Panels (C-D): average maximal dipole strength (panel C) and thermal coherence length (panel D) as a function of the number N of Bchl molecules at zero disorder (red stars) and at room temperature (black squares).

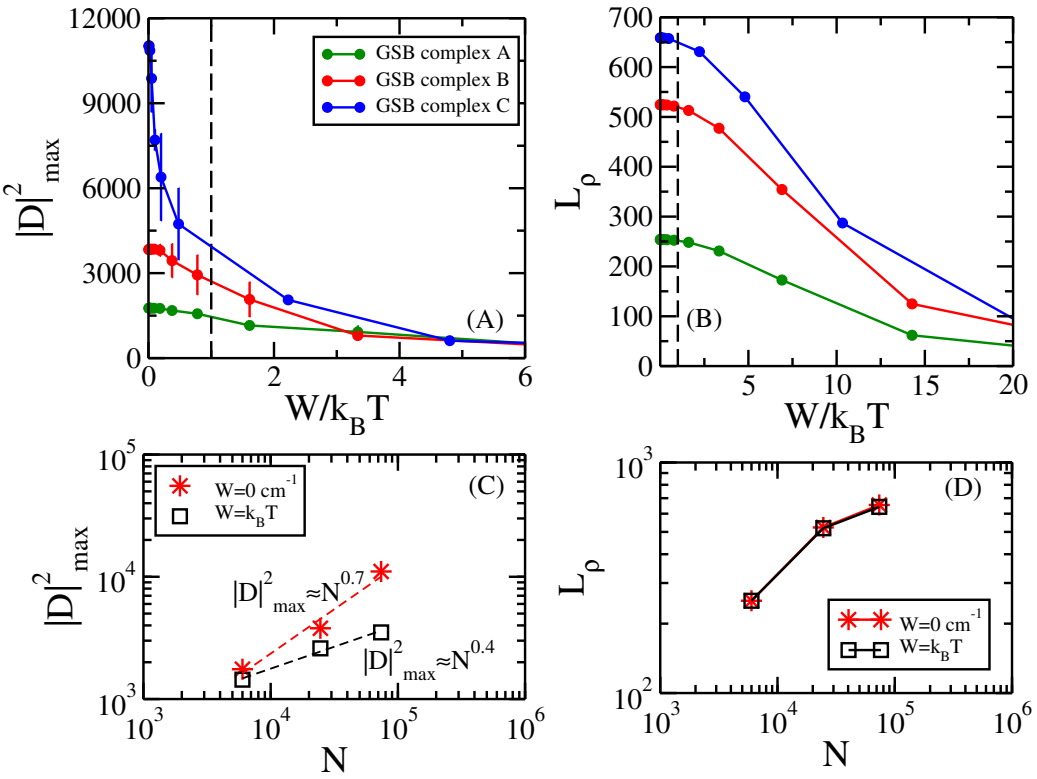

Figure 4.2: *Robustness to static disorder and thermal noise: comparison between GSB complexes A,B,C.* Comparison between aggregates with a single cylinder (complex A, green circles), four concentric rolls (complex B, red circles) and three adjacent aggregates (complex C, blue circles). The average thermal coherence length and the average maximal dipole strength have been computed using the HH model Eq. (3.5) and averaging over 10 disorder realizations for complexes A and B and 5 disorder realization for complex C. (Panel A) Average maximal dipole strength defined in Eq. (3.7) as a function of of the normalized static disorder. (Panel B) Average thermal coherence length, Eq. (4.1), as a function of the normalized static disorder. In both panels the complexes have the same length $L = 82.17$ nm that corresponds to $n_r = 100$ rings for each cylindrical aggregate. k_BT is the thermal energy at room temperature $T = 300$ K. The vertical dashed line represents $W = k_BT$. Panels (C-D): average maximal dipole strength (panel C) and thermal coherence length (panel D) as a function of the number N of Bchl molecules at zero disorder (red stars) and at room temperature (black squares).

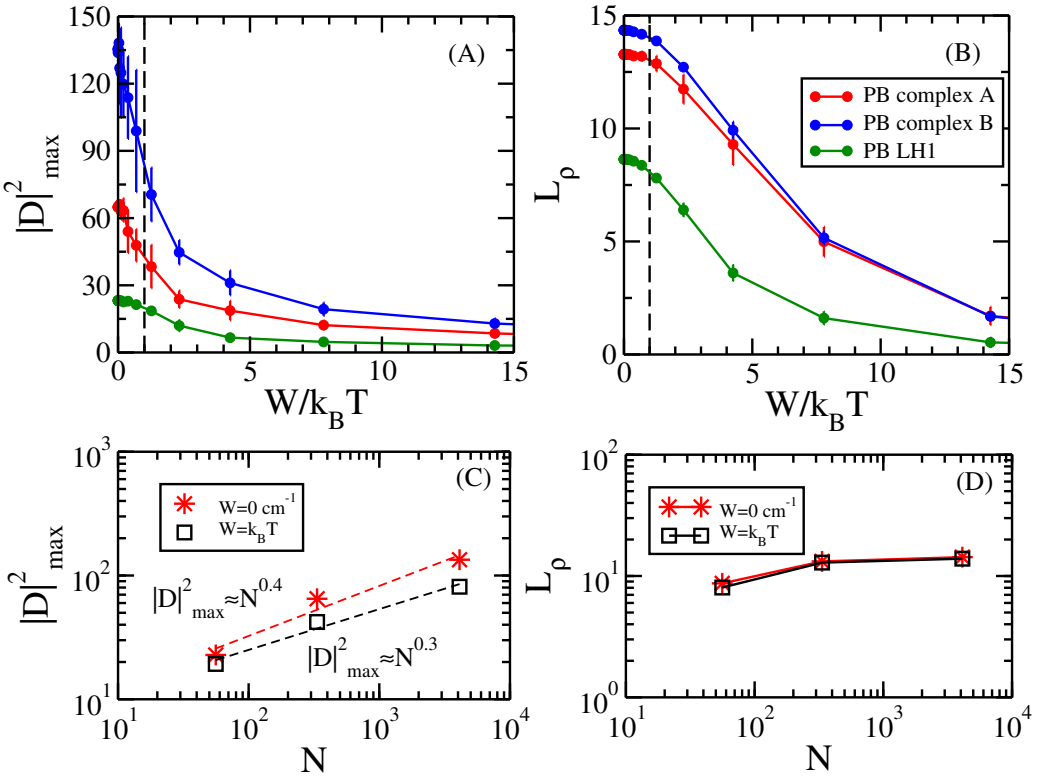

Figure 4.3: *Robustness to static disorder and thermal noise: comparison between PB complexes A,B and LHI system.* The average maximal dipole strength (panel A) and the average thermal coherence length (panel B) are shown as a function of the normalized static disorder W/k_BT for complexes A (red circles), B (blue circles) and a LHI s-shaped system with $N = 56$ (green circles). k_BT is the thermal energy at room temperature $T = 300$ K. The vertical dashed line represents $W = k_BT$. The average thermal coherence length and the maximal dipole strength defined respectively in Eq. (4.1) and Eq. (3.7) have been computed by using the HH model Eq. (3.5). For each value of the disorder strength we average the thermal coherence length and the maximal squared dipole strength over 10 disorder realizations. Panels (C-D): average maximal dipole strength (panel C) and thermal coherence length (panel D) as a function of the number N of Bchl molecules at zero disorder (red stars) and at room temperature (black squares).

4.2 Conclusions

In this chapter large scale simulations of the whole antenna complexes of Green sulfur bacteria and Purple bacteria have been performed including the effect of static and thermal noise. In order to analyze the robustness of natural models to static disorder and thermal noise we have chosen two figures of merit: the maximal dipole strength Eq. (3.7) and the thermal coherence length Eq. (4.1). Both quantities have been studied as a function of the static disorder strength W and an accurate analysis for both GSB antenna complexes (A, B and C) and PB antenna complexes (A, B and a single LHI) has been performed.

Here the largest Green sulfur antenna complex considered was composed of 73800 Bchl$c$ molecules, arranged in three adjacent cylinders, each composed of 4 concentric cylinders of different radii. The size of the largest complex was 82.17 nm $\times$ 18.6 nm $\times$ 61.8 nm, comparable with the size of natural antenna complexes. For the Purple bacteria the whole chromatophore was considered, which is a spherical structure of 60 nm of diameter and composed of 4113 Bchl$a$ molecules.

The results found in this chapter show that the thermal coherence length in the largest Green sulfur bacteria complex is between two and three times larger than in a single wall cylinder of the same length, see Fig. (4.2 panel B) while in the Purple bacteria chromatophore the thermal coherence length is approximately two times larger than in the single (s-shaped) LHI complex, see Fig. (4.3 panel B). On the other hand, the maximal dipole strength decreases with disorder, but it is still much larger than one for $W = k_BT$ at room temperature both in PB and GSB antenna complexes. Furthermore both figures of merit, the thermal coherence length and the maximal dipole strength, grow as a larger portion of the photosynthetic antenna is considered in PB and GSB complexes. Note that in presence of disorder, the maximal dipole strength grows slower with N compared with the case of zero disorder (panel C of Figs. (4.2,4.3)). On the hand, the value of the coherence length is the same for the two values of disorder strength considered ($W = 0$ and $W = k_BT$), showing its robustness to disorder (panel D of Figs. (4.2,4.3)). Nevertheless, as N increases, it shows a tendency to saturate.

This results confirm that both in the whole GSB and PB antenna complexes cooperative effects have been found to be robust even with disorder and noise levels comparable with ambient conditions.

Chapter 5

Emission and absorption properties in molecular aggregates of GSB and PB

Sunlight harvesting is the main feature for photosynthetic complexes in nature, in particular an efficient light absorption becomes relevant for those organisms which live under low light conditions. Among all the the photosynthetic organisms, PB and GSB present light-harvesting systems able to exploit photosynthesis efficiently, even if only a few photons per second can be absorbed. Their capability to absorb and transfer excitation to the reaction centers (RCs) has origin into the particular geometry of their antenna complexes, as already demonstrated in literature and in the previous chapters of this thesis. After a preliminary a study of the solar irradiance through the black body radiation theory, a description of the absorption in isolated BChl molecules and in the entire aggregates has been addressed. Here a theoretical explanation of the formation of H-type and J-type aggregates and their spectroscopic properties is provided. Finally the absorption and emission spectra of PB and GSB complexes have been compared to experimental results, finding good agreement and validating our theoretical model.

5.1 Solar irradiance

In this section a study of the solar irradiance has been given by using different approaches. The solar spectrum measured on the Earth is analyzed and compared with the Planck's law for a black body at a finite temperature $T_S = 5800$ K, typical of sunlight. Note that the solar spectrum is not exactly described by black-body radiation, as the photon experiences multiple scatterings upon arriving on the Earth. However, the sunlight spectrum is sufficiently broad compared to the absorption of light-harvesting complexes and our approximation holds [109].

From the black body theory, sunlight radiation is modeled as a photon bath at a given temperature T_S. Due to the fact that photons are boson particles, they can be studied with the Bose-Einstein statistics, that describes how a collection of non-interacting identical particles may occupy a set of available discrete energy levels at thermodynamic equilibrium. Here this approach has been used and the occupation number of photons at a given frequency ω and temperature has been determined. In this case the Bose-Einstein distribution $n_S(\omega)$ reads:

$$n_S(\omega) = \frac{1}{e^{\hbar\omega/(k_B T_S)} - 1} \ . \tag{5.1}$$

Fig. (5.1) shows the comparison between experimental and theoretical models for solar irradiance as a function of the wavelength. The function here represented by the black line is the well known Planck's law at finite temperature T_S multiplied by a coefficient Ω_S, see Eq. (5.2), that accounts for the angle under which the Sun can be seen from Earth. The Planck's law for a black body at a temperature T_S at a given wavelength λ reads:

$$g(\lambda, \Omega_S) = \Omega_S \frac{2hc^2}{\lambda^5} \frac{1}{\exp\left(\frac{hc}{k_B T_S \lambda}\right) - 1} \ , \tag{5.2}$$

where h is the Planck's constant, c the speed of light, k_B the Boltzman's constant and Ω_S the solid angle under which the Sun is seen from the Earth.

In Ref. [110] the concentration of the solar radiation on the Earth has already been computed. Viewed from the Earth, the Sun has an angular diameter of $\alpha_S = 0^\circ\ 32'$, corresponding to a solid angle Ω_S given by

$$\Omega_S = 2\pi \int_0^{\alpha_S/2} \sin(\theta)\, \mathrm{d}\theta = 6.8 \cdot 10^{-5} \ . \tag{5.3}$$

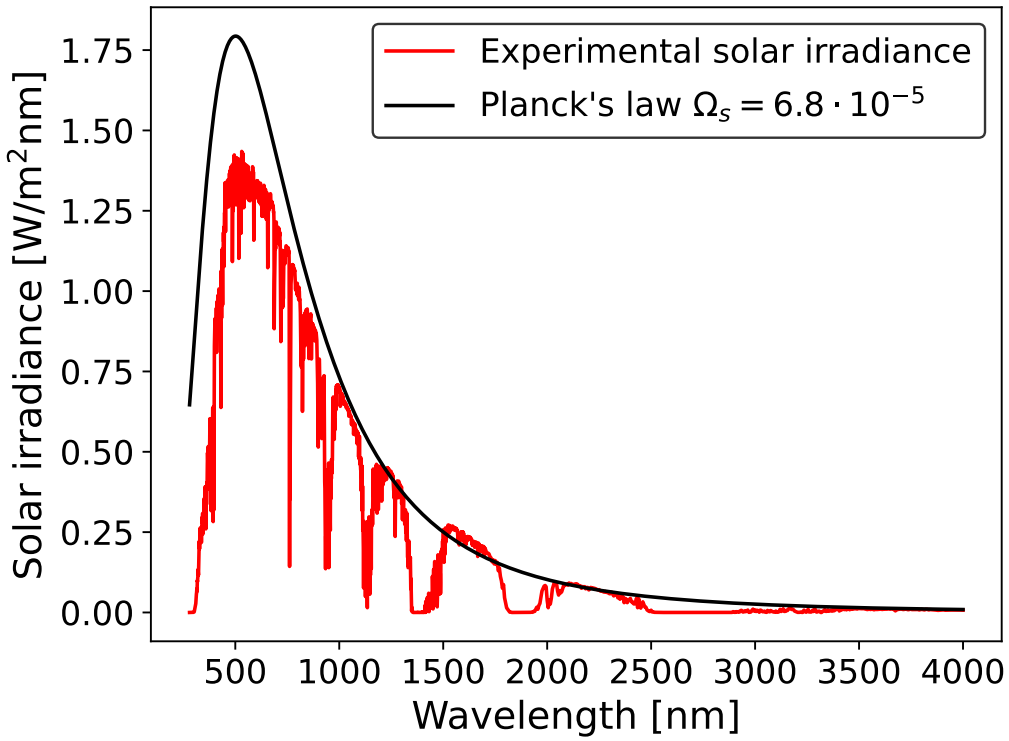

Figure 5.1: *Solar irradiance: comparison between experimental data measured on the Earth surface and black body theory.* Comparison between an experimental solar spectrum (red continuous line) and the Planck's law $g(\lambda, \Omega_S)$ (black continuous line, see Eq. (5.2)) for a black body at the Sun temperature $T_S = 5800$ K multiplied by the solid angle $\Omega_S = 6.8 \cdot 10^{-5}$, representing the solid angle under which Sun is seen from the Earth.

Because of the small value of the solid angle Ω_S, the sunlight energy current density measured on the Earth is reduced with respect to the total energy flux emitted by the Sun. Integrating the experimental solar irradiance $\Phi(\lambda)$ (red curve in Fig. (5.1)), we obtain $P_{Sun} = \int_{\lambda_i}^{\lambda_f} \Phi(\lambda) d\lambda = 901.24$ W/m^2 (with cut-offs $\lambda_i = 280$ nm and $\lambda_f = 4000$ nm), which is close to 1353 W/m^2 found in Ref. [110] referring to the solar irradiance measured outside the atmosphere. The small discrepancy between the two data is due to the Earth atmosphere and it strongly depends on the latitude, the weather conditions and the incident angle of sunlight with respect to the normal to the Earth surface.

Our findings show that modeling sunlight through the black body radia-

tion is a good approximation for sunlight. The spectrum computed using the black body theory can be compared to the experimental spectrum, minus a factor Ω_S that takes the Sun-Earth distance into account. This approach has already been done in literature. In Ref. [46] the Sun is seen as a black body at finite temperature T_S. The authors used the parameter f_S, which represents the fraction of solid angle under which Sun is seen from Earth, to compute the occupation number of photons at a given wavelength and temperature. f_S found in Ref. [46] is related to the solid angle Ω_S by the following relationship:

$$f_S = \Omega_S/4\pi = \frac{\pi r_s^2}{4\pi R_{ES}^2} = 5.4 \cdot 10^{-6} \ , \tag{5.4}$$

depending on the radius of the Sun r_s and the Sun-Earth distance R_{ES}.

5.2 Optical properties of BChl *a* and *c*

In this section the optical properties (emission and absorption) for BChl a and c molecules typical of GSB and PB light-harvesting complexes are computed by using different methods.

First a subsection for the emission rate is given. Then the absorption rate is computed through the black body approach, where each BChl molecule is seen as a TLS and only the main absorption transition frequency and its transition dipole moment are taken into account. Then a more accurate estimation of the absorption is given by integration of the overlap between the absorption cross section and the solar irradiance for all the transition frequencies.

5.2.1 Emission

The radiative decay rate of a molecule, modeled as a TLS, can be estimated as the inverse of the fluorescence lifetime τ_{fl} and reads:

$$\frac{\gamma}{\hbar} = \frac{1}{\tau_{fl}} = \frac{4\mu_0^2\omega_0^3}{3\hbar c^3} \ , \tag{5.5}$$

where $\omega_0 = \frac{2\pi c}{\lambda_0}$ is the transition frequency, while μ_0 is its corresponding transition dipole moment. Tab. (5.1) shows all the parameters for BChl a and c.

	BChl a	BChl c
TDM μ_0 [debye] [111]	10	5.6
Trans. wavelength λ_0 [nm]	780	670
$\gamma/\hbar$ [s^{-1}]	$7 \cdot 10^7$	$3.2 \cdot 10^7$
τ_{fl} [ns]	15	30

Table 5.1: *Emission in BChl molecules.* The table shows the emission parameters for BChl a and c molecules found in literature [13, 19, 23, 30].

5.2.2 Absorption

Black body theory Here we compute the absorption rate for BChl a and c through the black body theory and assuming that each BChl molecule

can be treated as a TLS with excitation energy e_0 and TDM $\vec{\mu_0}$, given in Tab. (5.1). We can express the absorption rate as follows,

$$P_{abs} = \frac{\gamma}{\hbar} n_S(\omega) f_S e_0 \ , \tag{5.6}$$

where $e_0 = 1/\lambda_0$ is the excitation energy of single BChl molecules (see Tab. (5.1) for the values of λ_0 for BChl a and c), $n_S(\omega)$ represents the occupancy of photons at the Sun temperature $T_S = 5800$ K for a given frequency ω (see Eq. (5.1)), while f_S is the fraction of solid angle from which sunlight is seen from the Earth.

Using the parameters shown in Tab. (5.1), the absorption rate for BChl a and c is computed, showing good agreement with the data found in literature [19]:

- BChl a: $P_{abs} = 4 \cdot 10^{-18}$ W, corresponding to $N_{abs} = 15.8$ s^{-1} photons per second;
- BChl c: $P_{abs} = 1.3 \cdot 10^{-18}$ W, corresponding to $N_{abs} = 4.6$ s^{-1} photons per second.

Absorption cross section Refs. [24, 29–32] report the extinction coefficient ϵ for BChl molecules in units of $\mathrm{M}^{-1}\mathrm{cm}^{-1}$. Through an easy calculation already found in Ref. [19], the absorption cross section in cm^2 can be obtained as

$$\sigma = \frac{\ln(10)\epsilon c_m}{n} = \frac{\ln(10)10^3\epsilon}{N_{av}} \ , \tag{5.7}$$

where c_m and n are respectively the concentration of the solution in molarity [M] and in [cm^{-3}], N_{av} is the Avogadro's number and $c_m = n\frac{10^3}{N_{av}}$ is the relationship between c_m and n.

Fig. (5.2) shows the solar irradiance $\Phi(\lambda)$ (black line) and the absorption cross section for both BChl a (σ_a in red line) and c (σ_c in blue line).

Finally the number of photons absorbed by each BChl has been computed by computing numerically the following integral:

$$N_{abs} = \int_{\lambda_i}^{\lambda_f} d\lambda \, \Phi(\lambda) \, \sigma_{a,c}(\lambda) \, \frac{\lambda}{hc} \ . \tag{5.8}$$

The number of photons absorbed by a BChl is given by

- $N_{abs} = 12.5$ s^{-1} for BChl a,

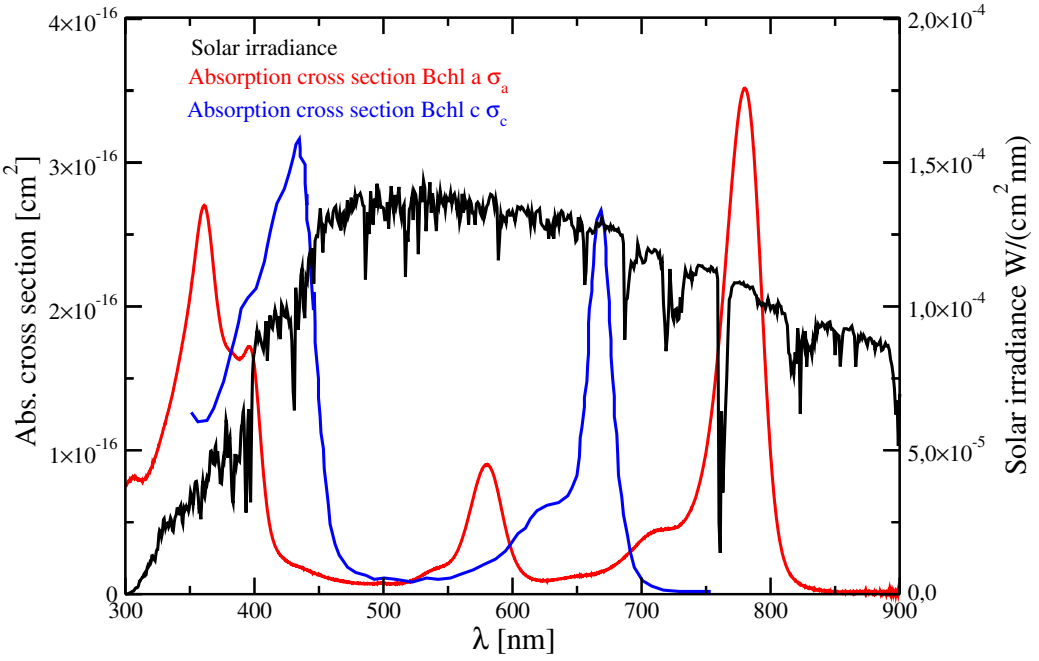

Figure 5.2: *Solar irradiance and absorption cross section for BChl a and c.* Solar irradiance (black line) and absorption cross section for BChl *a* (red line) and *c* (blue line) are represented as a function of the transition wavelength. The absorption cross section has been computed by Eq. (5.7) from experimental data of the extinction coefficient found in literature [24, 29–32].

- $N_{abs} = 8.6\ \mathrm{s}^{-1}$ for BChl c,

in good agreement with the previous calculations obtained by using the black body approach and the experimental data reported in literature [19].

5.3 Absorption and emission spectra in molecular aggregates

In this section we compute the absorption and emission spectra of PB and GSB antenna complexes comprising thousands of equivalent molecules, investigating how the absorption spectra of the aggregate change with respect to the spectrum of a single BChl molecule. The emergence of superradiant red-shifted and blue-shifted excitonic states has been studied, introducing the theory of H- and J-Molecular aggregates. After that, the absorption and emission spectra of PB and GSB antenna complexes have been compared with experimental results, showing good agreement.

5.3.1 Theory of absorption and emission spectra in H- and J-molecular aggregates

According to the Kasha theory [112], here we propose an exciton approach in order to derive the main features of the absorption and emission properties of molecular aggregates of BChl molecules in GSB and PB antenna complexes. This approach has already employed in literature [112–115], finding an enormous success in qualitatively accounting not only for the basic photophysics of the cyanine dye aggregates, but also for numerous other dye chromatophore assemblies. The purpose of this section is to draw attention to the fact that aggregation may lead to important changes in absorption and emission spectra.

Here we consider two interacting molecules, seen as TLSs, characterized by the same excitation energy e_0 and their associated TDMs $\vec{\mu}_1$ and $\vec{\mu}_2$ with the same magnitude and orientation in the space. We assume a regime where the Heitler-London approximation is valid, taking only the effect of intermolecular interactions among degenerate electronic state into account, and the coupling between molecules 1 and 2 is given by the point-dipole approximation J, see Eq. (3.8) in Chapter 3. Under these approximations

the coupling J between the two species reads:

$$J = \frac{\mu_0^2(1 - 3\cos^2\theta)}{r_{12}^3} \ , \tag{5.9}$$

where μ_0 represents the magnitude of the TDMs associated to molecules 1 and 2, $\vec{r}_{12}$ is the relative distance between them and θ is the relative angle between each TDM and the displacement vector $\vec{r}_{12}$, see Fig. (5.3). The coupling strength J is positive when $\theta_M < \theta \leq \pi/2$, while the coupling strength J becomes negative if $\theta < \theta_M$. $\theta_M = 54.7$ represents the magic angle for which J is zero.

Kasha initially identified two aggregation species, depending on the relative orientation of $\vec{\mu}_1$ and $\vec{\mu}_2$ with respect to the displacement vector connecting the two molecules, which is quantified by the the θ angle. Fig. (5.3) shows how the sign of the coupling leads to different kind of aggregates with different photophysical response for a molecular dimer. In particular the energy level diagrams show that the interaction between the two degenerate state $|1\rangle$ and $|2\rangle$, representing the state where only one molecule is in the excited state while the other one is in the GS, leads to the formation of two delocalized excited states split by $2|J|$. These states are an in- and out-of-phase linear superposition of $|1\rangle$ and $|2\rangle$. The in-phase state has a TDM enhanced relative to the monomer by a factor of $\sqrt{2}$ and it is radiatively coupled to the ground state. The out-of-phase state is not radiatively coupled to the ground state, due to the out-of-phase alignment of the dipoles.

Based on the θ angle that determines the sign of the coupling J, two scenarios emerges.

- **Case 1: J-aggregate formation.** When $\theta < \theta_M$, the coupling between the two molecules is negative $J < 0$. Panel (A) of Fig. (5.3) shows the case of a J-aggregate, where the two excited states consist of in- and out-of-phase linear combination of the two local excited states $|1\rangle$ and $|2\rangle$. For J-aggregates the in-phase excited state, characterized by an enhance TDM relative to the monomer, is red-shifted with respect to the excitation energy e_0. As a result, J-aggregates show a main enhanced red-shifted absorption and fluorescence peak compared to the monomer. In literature there is evidence of J-aggregate formation both in natural photosynthetic aggregates, such as GSB and PB light-harvesting systems [116–118], and artificial dye aggregates, such C8S3 nanotubes [95, 119, 120].

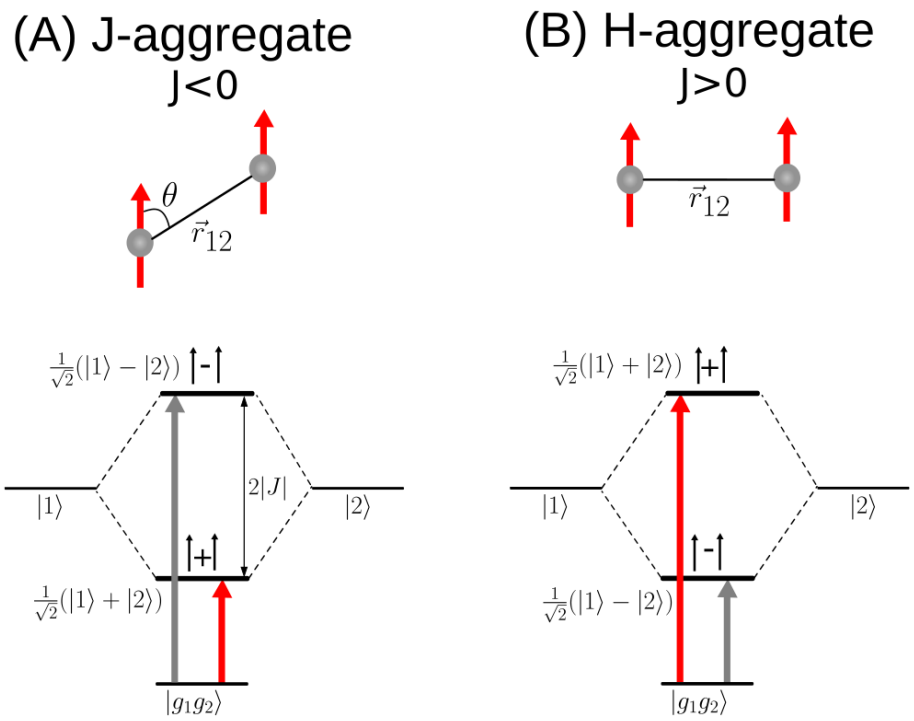

Figure 5.3: *H- and J-aggregates formation and energy level diagrams.* The figure shows two different configurations of dimeric systems with their energy level diagrams. The system comprises two identical molecules represented by their TDM which have a specific orientation with respect to the displacement vector $\vec{r}_{12}$. θ represents the angle between each TDM and $\vec{r}_{12}$. Panel (A) shows the configuration and the energy level diagram typical of J-aggregates. Due to the negative coupling between the two TDMs associated to molecules 1 and 2, the in-phase state is red-shifted with respect to the excitation energy of the monomer, leading to an enhanced absorption and radiative decay rate with respect to the monomer (see the red arrow from the ground state $|g_1g_2\rangle$ to the low energy in-phase state). Panel (B) represents the typical configuration and energy level diagram of H-aggregates. Due to the positive coupling between the two TDMs associated to molecules 1 and 2, the in-phase state is blue-shifted with respect to the excitation energy of the monomer. The dimer has the main absorption peak at high energy (see the red arrow from the ground state $|g_1g_2\rangle$ to the high energy in-phase state). In these systems fast thermal relaxation leads to the depletion of the high energy state, making the low energy out-of-phase state populated.

- **Case 2: H-aggregate formation.** When $\theta_M < \theta \leq \pi/2$, the coupling becomes positive $J > 0$ and H-aggregates emerge. Panel (B) of Fig. (5.3) shows that the in-phase state is blue-shifted, leading to the formation of an enhanced main absorption peak at high energy. In these systems there is likely rapid intraband relaxation subsequent to absorption, leading to efficient population of the lowest energy state that has no coupling to the ground state and cannot radiate. Literature shows that H-aggregates can emerge from aggregation of cyanine dyes, such as $DiSC_2(3)$ [121], or anionic thiacarbocyanine dye (TCC) [122].

Due to the fact that the squared TDM associated to the in-phase transition is enhanced relative to the monomer by a factor of 2, for an aggregate containing N-coupled molecules, the squared TDM is ehhanced by a factor of N, a phenomenon known as superradiance and already discussed in Chapter 3 of this thesis.

In Refs. [95, 119, 120, 123, 124] self-assembled light-harvesting nanotubes (LHNs) made of amphiphilic cyanine molecules (C8S3) in water-methanol mixture have been studied. These artificial light-harvesting nanotubes show a double-walled structure with diameters of ~ 63 and ~ 143 Å for the inner and outer walls respectively and longitudinal dimensions tens of micrometers in length [120, 123]. Linear spectroscopy measurements confirmed also by theoretical simulations have proved that these self-assembled nanotubes behave as J-aggregate, with two red-shifted absorption peaks with respect to the monomer. Fig. (5.4) shows the absorption and emission spectra both for the C8S3 nanotubes and the monomer.

The C8S3 monomer has an absorption band peaking at 580 THz, and a broad emission with a Stokes shift of 30 THz. Nanotube formation leads to a red-shift of 80 THz in the linear absorption spectrum, indicating the presence of J-type aggregation. The aggregate absorption spectrum presents two main peaks centered at 500 THz and 510 THz, which have been attributed to the inner and outer wall absorption. The pronounced narrowing of the absorption spectrum occurring upon aggregation is an indication of delocalized excitonic behavior. No Stokes shift is observed between the absorption and emission spectra of the nanotubes, suggesting weak coupling with the local environment and the almost complete absence of low-energy trap states. These observations reinforce the assumption of a very low disorder in the nanotube supramolecular structure [124].

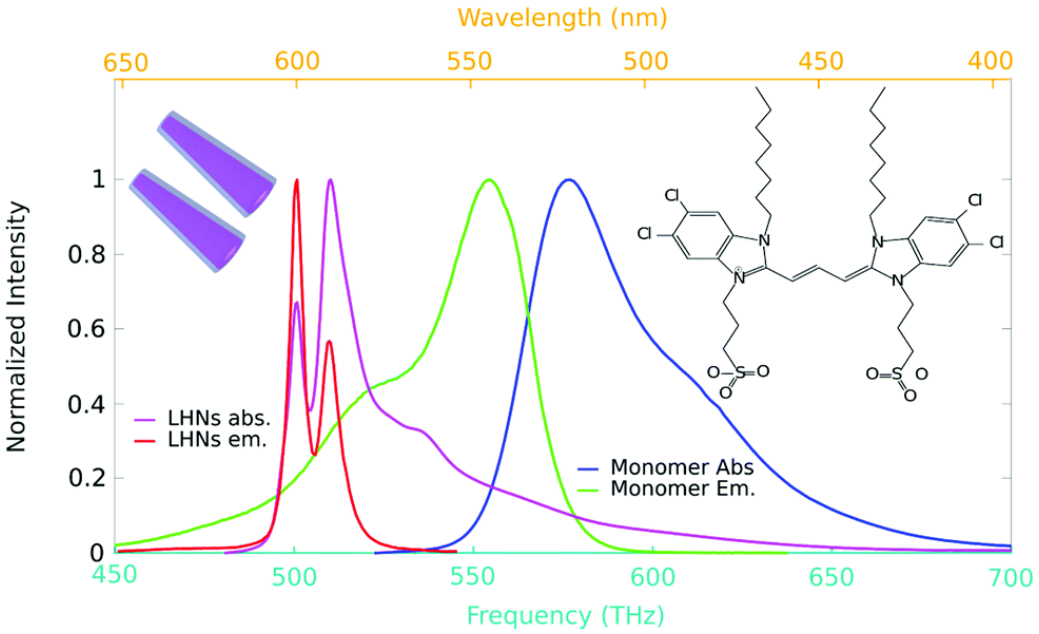

Figure 5.4: *Absorption and emission spectra in C8S3 monomers in methanol solution and double-walled tubular light-harvesting nanotubes in the sugar matrix.* Figure taken from Ref. [124]. On top the chemical structure of the monomer and a representation of the tubular structures have been represented. The figure shows the normalized absorption and emission spectra of both monomers and tubular structures.

5.3.2 Results: absorption spectra of GSB and PB

In this section a comparison between our models and the experimental results in both PB and GSB aggregates is considered. Figs. (5.5-5.6) show that our theoretical model reproduces the basic features of the experimental absorption and emission spectra. In addition it shows that the main absorption peak in both aggregates is red-shifted with respect to the single monomer (see Tab. (5.1) for the transition wavelength of BChl *a* and *c*), proving that both PB and GSB antenna complexes can be considered J-aggregates.

The absorption spectrum indicates the amount of incident electromagnetic radiation absorbed by the BChl chromophores in the aggregate, between a range of energies or frequencies [125]. Following Ref. [126], the linear absorption spectrum can be defined as the real part of the Fourier-Laplace transform of the dipole-dipole correlation function, also known as the lineshape function, which can be expressed as a function of the energy:

$$A(E) = K \sum_j \Gamma_j D_j(E) \ , \tag{5.10}$$

where Γ_j is the decay corresponding to each j^{th} eigenstate of the Hamiltonian, K is a normalization factor and $D_j(E)$ is the lineshape function. Here we assume only homogeneous broadening, so a Lorentzian lineshape function centred at E_j is considered:

$$D_j(E) = \frac{\sigma}{(E - E_j)^2 + \sigma^2} \ , \tag{5.11}$$

where the parameter σ is the strength of the homogeneous broadening.

Conversely, the fluorescence spectrum indicates the amount of electromagnetic radiation emitted by the molecules in the network. The expression for the fluorescence emission intensity is obtained by multiplying each lineshape by the corresponding Boltzmann factor

$$I(E) = K' \sum_j \frac{e^{-E_j/k_B T}}{Z} \Gamma_j D_j(E) \ , \tag{5.12}$$

where Z is the partition function, while K' is a different normalization factor. T is the temperature measured in Kelvin (K) and k_B is the Boltzmann's constant.

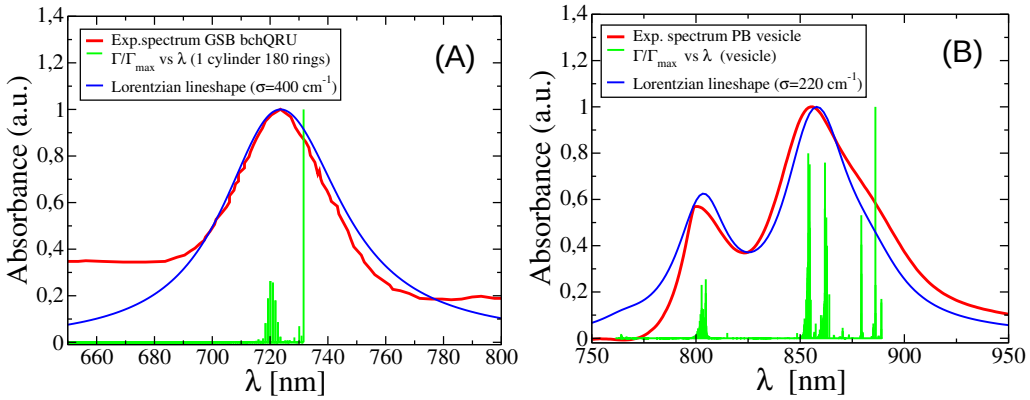

Figure 5.5: *Absorption spectra of GSB and PB complexes.* Experimental and numerical normalized absorption spectra for GSB bchQRU triple mutant and PB *Rhodobacter sphaeroides* are compared. Panel (A): the experimental absorption spectrum of whole cells of GSB bchQRU mutant (red solid line) taken from Ref. [22] is compared with the numerical spectrum for a single cylinder with 180 rings (blue solid line) obtained with Eq. (5.10), assuming a Lorentzian lineshape with homogeneous broadening $\sigma = 400$ cm^{-1}. The numerical spectrum has been shifted by 27 nm to the blue to match the position of the experimental absorption maximum. Panel (B): experimental data (red solid line) provided by Ref. [97] are compared with the numerical spectrum for a chromatophore (blue solid line) obtained with Eq. (5.10), assuming a Lorentzian lineshape with homogeneous broadening $\sigma = 220$ cm^{-1}. In both panels (A-B) the light green solid line represents the radiative decay rate as a function of the wavelength computed with the NHH model, see Eq. (3.1) in Chapt. 3.

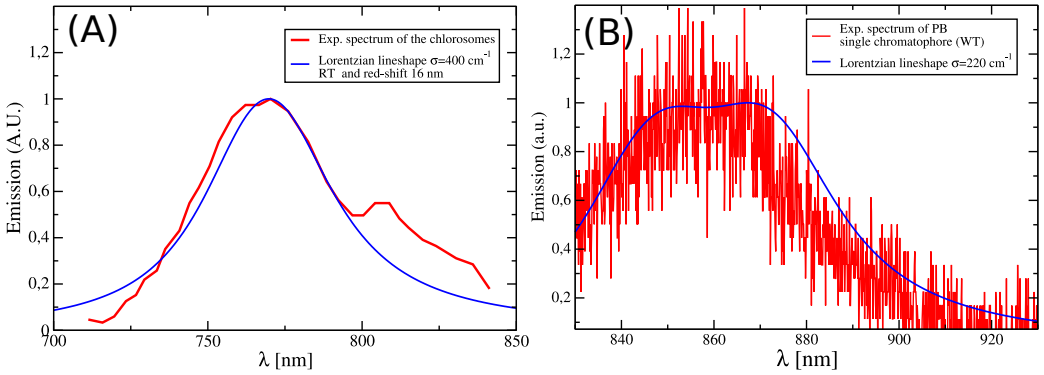

Figure 5.6: *Emission spectra of GSB and PB complexes.* Experimental and numerical normalized emission spectra for GSB and PB *Rhodobacter sphaeroides* are compared. Panel (A): the experimental emission spectrum of chlorosomes of GSB (red solid line) taken from Ref. [24] is compared with the numerical spectrum for a single cylinder with 180 rings (blue solid line) obtained with Eq. (5.12), assuming a Lorentzian lineshape with homogeneous broadening $\sigma = 400$ cm^{-1} and room temperature. The numerical spectrum has been shifted by 16 nm to the red to match the position of the experimental emission maximum. Panel (B): experimental data for single chromatophore (wild type) (red solid line) provided by Ref. [127] are compared with the numerical spectrum (blue solid line) obtained with Eq. (5.12), assuming a Lorentzian lineshape with homogeneous broadening $\sigma = 220$ cm^{-1} and room temperature. The numerical spectrum has been shifted by 12 nm to the blue to match the position of the experimental emission maximum.

5.4 Conclusions

In this chapter we have discussed the main photophysical properties of isolated BChl molecules (a and c) and aggregates. In particular after a preliminary study of the solar irradiance, we showed how absorption and emission properties change in molecular aggregates with respect to the single monomer. The formation of J- and H-aggregates has been explained and a computation of the absorption and emission spectra in PB and GSB light-harvesting systems has been done, finding good agreement with experimental results. From the results found in literature and our results, we can confirm that both PB and GSB behave as J-aggregates because their absorption spectra show a main red-shifted absorption peak with respect to the single monomer ($\lambda_a \sim 800$ nm and $\lambda_c \sim 650$ nm).

As future perspective, we aim to extend the theoretical study adding a source of static disorder, that plays a fundamental role in such aggregates. From the experimental point of view we aim for finding experimental evidence of superradiance in such aggregates in strong collaboration with experimental groups at LENS in Florence, CNR of Bari and University of Parma. In particular we plan to implement spectroscopic measurements even at low temperature in order to find experimentally the enhancement of the absorption peak with the system size, typical of superradiance behavior. These experiments will be carried out not only on the single aggregate but also on ensemble of light-harvesting complexes at different concentrations in order to show how superradiance is enhanced in large systems comparable to natural size. A preliminary theoretical prediction has already been given in Sec. 3.2.3 of Chapt. 3, where the superradiance enhancement has been proved for cubic array of 8 PB chromatophores.

Finally my research activity is now focused also on artificial light-harvesting complexes, in particular I'm investigating superradiance in C8S3 nanotubes in order to reproduce the experimental absorption and emission spectra in strong collaboration with the research group in Parma led by A. Painelli and S. Doria of CNR of Florence, the main author of Refs. [95, 124].

Chapter 6

General derivation of Lindblad master equations for independent phononic baths

Until now we have given a description of the system by a single wavefunction, here to go beyond this approach the density operator is introduced and it is used to treat the dynamics of the system when interacting with a macroscopic environment. In this chapter we introduce the description of decoherence dynamics in terms of so-called master equations. Such master equations yield the time evolution of the reduced density matrix for the open quantum system interacting with an environment. In particular here the problem of a system of N emitters weakly coupled to a thermal bath, seen as an ensemble of independent harmonic oscillators, is taken into account through a Lindblad master equation approach. A detailed derivation of the master equation in Lindblad form has been provided and under Born-Markov and secular approximations the rate equations for the time-dependent occupation probabilities of certain quantum states $|E_m\rangle$ of the systems have been obtained. These equations contain the rates for the transition from state $|E_m\rangle$ to $|E_n\rangle$ mediated by the presence of the thermal bath and describe the incoherent dynamics of the system. The interaction between the system and the thermal bath is described by the spectral density. Finally in Sec. 6.6 a study of the spectral density for BChl a molecules has been provided and

the choice of an ohmic environment has been justified.

6.1 Hamiltonian and master equation for the whole system

In this chapter a detailed derivation of the Lindblad master equation for the description of the dynamics of the reduced density matrix $\hat{\rho}_S$ of the system has been provided following Refs. [128, 129]. Let us consider a system made of N coupled sites representing the BChl molecules in the light-harvesting aggregates. All across this section for the sake of clarity we use indices i and j to indicate sites (BChls) and m and n for the eigenstates of the system, as already done in the previous chapters. Each site is connected to an independent thermal bath. The N baths have the same temperature and the same spectral density $J(\omega)$. The full Hamiltonian is

$$\hat{H} = \hat{H}_S + \hat{H}_B + \hat{H}_I \,. \tag{6.1}$$

Here $\hat{H}_S$ is the system Hamiltonian (DH or HH models) already described in chapter 3, while the Hamiltonian term for the N independent baths is

$$\hat{H}_B = \sum_{k,i} \hbar\omega_k \hat{b}^\dagger_{k,i} \hat{b}_{k,i} \;, \tag{6.2}$$

where the summation runs over the modes k of the baths and the sites $i = 1, \ldots, N$ and the creation/annihilation operators follow the commutation rules $[\hat{b}_{k,j}, \hat{b}^\dagger_{k',i}] = \delta_{k,k'}\delta_{j,i}$. Finally, the interaction is

$$\hat{H}_I = \sum_{k,i} \hbar g_k \left|i\right\rangle \left\langle i\right| \left(\hat{b}^\dagger_{k,i} + \hat{b}_{k,i}\right) \;, \tag{6.3}$$

where $\hbar g_k$ is the coupling between a site and the position of the k-th mode of the bath and $|i\rangle$ is a state in which the i^{th} molecule is excited while all the others are in the ground state. Note that the derivation presented in this section does not rely on the form of $\hat{H}_S$, but only on the form of the interaction $\hat{H}_I$.

The dynamics of the full system is described by the Liouville master equation which, in the interaction picture, reads

$$\frac{d\hat{\rho}(t)}{dt} = -\frac{i}{\hbar}\left[\hat{H}_I(t), \hat{\rho}(t)\right] \;, \tag{6.4}$$

where $\hat{\rho}(t)$ is the density matrix in the interaction picture and it is related to the density matrix in the Schrödinger picture $\hat{\rho}$ by

$$\hat{\rho}(t) = e^{i(\hat{H}_S+\hat{H}_B)t/\hbar}\,\hat{\rho}\,e^{-i(\hat{H}_S+\hat{H}_B)t/\hbar}\,. \tag{6.5}$$

Note that also the density matrix $\hat{\rho}$ is time-dependent both in the Schrödinger and in the interaction picture.

The interaction Hamiltonian in the interaction picture can be factorized as

$$\hat{H}_I(t) = \sum_{\omega}\sum_{i} e^{-i\omega t}\hat{A}_i(\omega)\otimes\hat{B}_i(t) \tag{6.6a}$$

$$= \sum_{\omega}\sum_{i} e^{i\omega t}\hat{A}_i^{\dagger}(\omega)\otimes\hat{B}_i(t)\ , \tag{6.6b}$$

where $\hat{A}_i(\omega)$ are operators acting on the system,

$$\hat{A}_i(\omega) = \sum_{\substack{m,n\\(E_n-E_m)/\hbar=\omega}} C_m^*(i)C_n(i)\,|E_m\rangle\,\langle E_n|\ , \qquad C_m(i) = \langle i|E_m\rangle \tag{6.7}$$

with $|E_m\rangle$ and $|E_n\rangle$ being eigenstates of the system hamiltonian ($\hat{H}_S\,|E_m\rangle = E_m\,|E_m\rangle$), and $\hat{B}_i(t)$ are hermitian operators acting only on the baths, given by

$$\hat{B}_i(t) = \sum_k \hbar g_k\left(\hat{b}_{k,i}^{\dagger}e^{i\omega_k t} + \hat{b}_{k,i}e^{-i\omega_k t}\right)\ . \tag{6.8}$$

6.2 Born and Markov approximations

Eq. (6.4) can be integrated from 0 to t to obtain

$$\hat{\rho}(t) = \hat{\rho}(0) - \frac{i}{\hbar}\int_0^t dt'\left[\hat{H}_I(t'),\hat{\rho}(t')\right]\ , \tag{6.9}$$

which, substituted back into (6.4), gives the integro-differential equation

$$\frac{d\hat{\rho}(t)}{dt} = -\frac{i}{\hbar}\left[\hat{H}_I(t),\hat{\rho}(0)\right] - \frac{1}{\hbar^2}\int_0^t dt'\left[\hat{H}_I(t),\left[\hat{H}_I(t'),\hat{\rho}(t')\right]\right]\ . \tag{6.10}$$

Now, let us perform the *Born approximation*: the interaction between the system and the bath is assumed to be weak, so that it does not change

relevantly the status of the bath. Formally, it translates in approximating the density matrix as

$$\hat{\rho}(t) \approx \hat{\rho}_S(t) \otimes \hat{\rho}_B \ , \tag{6.11}$$

where the bath part $\hat{\rho}_B$ is also assumed to be a steady state of the bath, i.e. $[\hat{H}_B, \hat{\rho}_B] = 0$. Making the change of variable $\tau = t - t'$ into the integral, tracing over the degrees of freedom of the bath and assuming that the average value of the positions of the bath oscillators vanish

$$\mathrm{tr}_B \left\{ \left[\hat{H}_I(t), \hat{\rho}(0) \right] \right\} = 0 \ , \tag{6.12}$$

we have

$$\frac{d\hat{\rho}_S(t)}{dt} = -\frac{1}{\hbar^2} \int_0^t d\tau \, \mathrm{tr}_B \left\{ \left[\hat{H}_I(t), \left[\hat{H}_I(t-\tau), \hat{\rho}_S(t-\tau) \otimes \hat{\rho}_B \right] \right] \right\} \ . \tag{6.13}$$

Now let us perform the *Markov approximation*: the memory effects between the system and the bath are neglected, i.e. we approximate the density matrix as

$$\hat{\rho}_S(t-\tau) \approx \hat{\rho}_S(t) \tag{6.14}$$

(first Markov approximation) and we extend the integration to ∞ (second Markov approximation). This gives the Redfield master equation

$$\frac{d\hat{\rho}_S(t)}{dt} = -\frac{1}{\hbar^2} \int_0^\infty d\tau \, \mathrm{tr}_B \left\{ \left[\hat{H}_I(t), \left[\hat{H}_I(t-\tau), \hat{\rho}_S(t) \otimes \hat{\rho}_B \right] \right] \right\} \ . \tag{6.15}$$

6.3 Secular approximation

Let us now rewrite Eq. (6.15) more explicitly. We use the notation

$$\left\langle \hat{C} \right\rangle_B = \mathrm{tr}_B \left\{ \hat{C} \hat{\rho}_B \right\} \tag{6.16}$$

to indicate average value of some operator $\hat{C}$ on the bath and h.c. for the hermitian conjugate. Thus, Eq. (6.15) becomes

$$\frac{d\hat{\rho}_S(t)}{dt} = \frac{1}{\hbar^2} \int_0^\infty d\tau \, \left[\left\langle \hat{H}_I(t-\tau) \hat{\rho}_S(t) \hat{H}_I(t) \right\rangle_B - \left\langle \hat{H}_I(t) \hat{H}_I(t-\tau) \hat{\rho}_S(t) \right\rangle_B \right] + \text{h.c.} \ . \tag{6.17}$$

Now we use Eq. (6.6) to write the interaction Hamiltonian explicitly as

$$\hat{H}_I(t) = \sum_{\omega'} \sum_j e^{i\omega' t} \hat{A}_j^\dagger(\omega') \otimes \hat{B}_j(t) \ , \tag{6.18a}$$

$$\hat{H}_I(t-\tau) = \sum_{\omega} \sum_i e^{-i\omega(t-\tau)} \hat{A}_i(\omega) \otimes \hat{B}_i(t-\tau) \tag{6.18b}$$

and, substituting into (6.17), we have

$$\frac{d\hat{\rho}_S(t)}{dt} = \sum_{\omega,\omega'} e^{i(\omega'-\omega)t} \sum_{j,i} \Gamma_{ji}(\omega, t) \left[\hat{A}_i(\omega)\hat{\rho}_S(t)\hat{A}_j^\dagger(\omega') \ - \hat{A}_j^\dagger(\omega')\hat{A}_i(\omega)\hat{\rho}_S(t) \right] + \text{h.c.} \ , \tag{6.19}$$

where we have defined the rates $\Gamma_{ji}(\omega, t)$ as the half-sided Fourier transformed correlators of the bath

$$\Gamma_{ji}(\omega, t) = \frac{1}{\hbar^2} \int_0^\infty d\tau \, e^{i\omega\tau} \left\langle \hat{B}_j(t)\hat{B}_i(t-\tau) \right\rangle_B \ . \tag{6.20}$$

Since we assumed $\hat{\rho}_B$ stationary, the rates $\Gamma_{ji}(\omega)$ are independent of time, namely

$$\Gamma_{ji}(\omega) = \frac{1}{\hbar^2} \int_0^\infty d\tau \, e^{i\omega\tau} \left\langle \hat{B}_j(\tau)\hat{B}_i(0) \right\rangle_B \ . \tag{6.21}$$

Now let us perform the *secular approximation*: we neglect the oscillating terms, assuming that the energy spacings between the system states induces Rabi oscillations which are faster than the relaxation time so that, in a coarse-grained time scale, these oscillations average to 0. So, keeping just the non-oscillating terms ($\omega = \omega'$), we get a master equation in the Lindblad form:

$$\frac{d\hat{\rho}_S(t)}{dt} = \sum_{\omega} \sum_{j,i} \Gamma_{ji}(\omega) \left[\hat{A}_i(\omega)\hat{\rho}_S(t)\hat{A}_j^\dagger(\omega) \ - \hat{A}_j^\dagger(\omega)\hat{A}_i(\omega)\hat{\rho}_S(t) \right] + \text{h.c.} \ . \tag{6.22}$$

It is important to stress that the positivity of populations is guaranteed only by the secular approximation. Redfield Eq. (6.15) can have solutions with negative populations.

6.4 Explicit calculation of the rates

Here we compute the rates $\Gamma_{ji}(\omega)$ for the specific case of identical independent thermal baths under consideration. Note that these rates appear both

in the Redfield master equation (6.19) and in the Lindblad master equation (6.22). By substituting the expressions (6.8) into (6.21) we have

$$\Gamma_{ji}(\omega) = \int_0^\infty d\tau\, e^{i\omega\tau} \sum_{k,j,k',i} g_k g_{k'} \Big[e^{-i\omega_k\tau} \left\langle \hat{b}_{k,j} \hat{b}_{k',i} \right\rangle_B + e^{-i\omega_k\tau} \left\langle \hat{b}_{k,j} \hat{b}^\dagger_{k',i} \right\rangle_B + e^{i\omega_k\tau} \left\langle \hat{b}^\dagger_{k,j} \hat{b}_{k',i} \right\rangle_B + e^{i\omega_k\tau} \left\langle \hat{b}^\dagger_{k,j} \hat{b}^\dagger_{k',i} \right\rangle_B \Big] \ . \tag{6.23}$$

Now we assume that the thermal baths are at thermal equilibrium, i.e.

$$\hat{\rho}_B = \frac{e^{-\beta \hat{H}_B}}{\mathrm{tr}_B \left\{ e^{-\beta \hat{H}_B} \right\}} \ , \tag{6.24}$$

where $\beta = 1/(k_B T)$ is the inverse temperature. In this case one can show that the correlators in (6.23) are

$$\left\langle \hat{b}_{k,j} \hat{b}_{k',i} \right\rangle_B = 0 \ , \tag{6.25a}$$

$$\left\langle \hat{b}^\dagger_{k,j} \hat{b}^\dagger_{k',i} \right\rangle_B = 0 \ , \tag{6.25b}$$

$$\left\langle \hat{b}_{k,j} \hat{b}^\dagger_{k',i} \right\rangle_B = \delta_{k,k'} \delta_{j,i} \left(1 + N_{BE}(\omega_k) \right) \ , \tag{6.25c}$$

$$\left\langle \hat{b}^\dagger_{k,m} \hat{b}_{k',n} \right\rangle_B = \delta_{k,k'} \delta_{j,i} N_{BE}(\omega_k) \ , \tag{6.25d}$$

where we have defined the Bose-Einstein function

$$N_{BE}(\omega_k) = \frac{1}{e^{\beta\hbar\omega_k} - 1} \, . \tag{6.26}$$

Thus we have

$$\Gamma_{ji}(\omega) = \delta_{j,i} \int_0^\infty d\tau\, e^{i\omega\tau} \sum_k g_k^2 \times \left[e^{-i\omega_k\tau} \left(1 + N_{BE}(\omega_k) \right) + e^{i\omega_k\tau} N_{BE}(\omega_k) \right] \ . \tag{6.27}$$

As regards the sum over k, we take the continuum limit

$$\sum_k g_k^2 f(\omega_k) \to \int_0^\infty d\omega_k \, J(\omega_k) f(\omega_k) \, , \tag{6.28}$$

where $J(\omega_k)$ is the spectral density and $f(\omega_k)$ is the function in the squared brackets.

Now we perform the integral over τ using the relation

$$\int_0^\infty d\tau\, e^{i\omega\tau} = \pi\delta(\omega) + i\mathrm{P}\frac{1}{\omega}\ , \tag{6.29}$$

where P is the Cauchy principal value. So, we can split the rates into their real and an imaginary parts,

$$\Gamma_{ji}(\omega) = \frac{1}{2}\gamma_{ji}(\omega) + iS_{ji}(\omega)\ , \tag{6.30}$$

which are, respectively,

$$\begin{aligned}
\gamma_{ji}(\omega) =& 2\pi\delta_{j,i}\int_0^\infty d\omega_k\, J(\omega_k)\left[\delta(\omega-\omega_k)\left(1+N_{BE}(\omega_k)\right)+\delta(\omega+\omega_k)N_{BE}(\omega_k)\right]\ ,\\
S_{ji}(\omega) =& \delta_{j,i}\mathrm{P}\int_0^\infty d\omega_k\, J(\omega_k)\left[\frac{1+N_{BE}(\omega_k)}{\omega-\omega_k}+\frac{N_{BE}(\omega_k)}{\omega+\omega_k}\right]\ .
\end{aligned} \tag{6.31a}$$

On integrating the $\delta(\omega\pm\omega_k)$ functions we have the real part of the rates

$$\begin{aligned}
\gamma_{ji}(\omega) &= 2\pi\delta_{j,i}\left[J(\omega)\left(1+N_{BE}(\omega)\right)+J(-\omega)N_{BE}(-\omega)\right] =\\
&= \gamma^{(p)}(\omega)\delta_{j,i}\,,
\end{aligned} \tag{6.32}$$

where we have defined the diagonal rate $\gamma^{(P)}(\omega)$ implicitly. The imaginary parts $S_{mn}(\omega)$ of the rates induce a constant renormalization of the site energies (Lamb-shift effect) and thus they can be neglected. The Lamb-shift contribution leads to a to a renormalization of the energy levels because the presence of the environment often perturbs the free Hamiltonian.

6.5 Lindblad master equations on the system eigenbasis

The Lindblad master equations may be written back to the Schrödinger picture as

$$\frac{d\hat{\rho}_S}{dt} = \underbrace{-\frac{i}{\hbar}\left[\hat{H}_S,\hat{\rho}_S\right]}_{\text{unitary evolution}} + \underbrace{\mathcal{L}_T[\hat{\rho}_S]}_{\text{decoherence}}\ , \tag{6.33}$$

where the dissipator $\mathcal{D}_L[\hat{\rho}_S]$ in the Lindblad case (6.19) is

$$\mathcal{L}_T[\hat{\rho}_S] = \sum_\omega \gamma^{(p)}(\omega)\sum_i\left[\hat{A}_i(\omega)\hat{\rho}_S\hat{A}_i^\dagger(\omega) - \frac{1}{2}\left\{\hat{A}_i^\dagger(\omega)\hat{A}_i(\omega),\hat{\rho}_S\right\}\right]\ . \tag{6.34}$$

Eq. (6.33) is a first-order differential equation that determines the time evolution of $\hat{\rho}_S$ and it is local in time. This means that the change of $\hat{\rho}_S$ at time t depends only on $\hat{\rho}_S$ evaluated at t but not at any other times $t' \neq t$. Eq. (6.33) can be decomposed into two parts: a unitary part, that is given by the Liouville-von Neumann commutator with the Hamiltonian of the system $\hat{H}_S$ (note that here we are neglecting the Lamb-shift contribution), and a non-unitary part given by $\mathcal{L}_T[\hat{\rho}_S]$ that represents decoherence due to the interaction of the system with the environment.

We now proceed to write the master equation on the eigenbasis of $\hat{H}_S$, i.e. we use the expression (6.7) to compute the terms $\langle E_m| \mathcal{L}_T |E_n\rangle$.

For simplicity, let us assume that the coefficients $C_m(i) = \langle i|E_m\rangle$ are all real numbers. Since $\hat{H}_S$ is hermitian, it is always possible to find an eigenbasis that satisfies this requirement.

The dynamics of the populations is given by

$$\langle E_m| \mathcal{L}_T |E_m\rangle = \sum_n \left(T_{mn}\rho_{nn} - T_{nm}\rho_{mm}\right) \ , \tag{6.35}$$

while for the coherences ($m \neq n$) we have

$$\langle E_m| \mathcal{L}_T |E_n\rangle = -\Gamma_{mn}\rho_{mn} \tag{6.36}$$

and

$$\langle 0| \mathcal{L}_T |E_m\rangle = -\Gamma_{0m}\rho_{0m} \, . \tag{6.37}$$

Defining the coefficients

$$\Lambda_{mn} = \sum_i |C_m(i)|^2 |C_n(i)|^2 \, , \tag{6.38}$$

we derive the relaxation rates for the populations, expressed as

$$T_{mn} = \gamma[(E_n - E_m)/\hbar]^{(p)} \Lambda_{mn} \ . \tag{6.39}$$

The Lindblad master equation for the Hamiltonian eigenstate populations reads explicitly:

$$\begin{aligned} \frac{d\rho_{mm}}{dt} = \sum_n \{ & 2\pi \left[J(\omega_n - \omega_m)\left(1 + N(\omega_n - \omega_m)\right) + J(\omega_m - \omega_n)N(\omega_m - \omega_n)\right] \Lambda_{mn}\rho_{nn} \\ & -2\pi \left[J(\omega_m - \omega_n)\left(1 + N(\omega_m - \omega_n)\right) + J(\omega_n - \omega_m)N(\omega_n - \omega_m)\right] \Lambda_{mn}\rho_{nn}\} \ , \end{aligned} \tag{6.40}$$

where we chose $J(\omega) = J(\omega_n - \omega_m) = k_{vib}\omega$ as the phonon spectral density.

6.6 Spectral density for BChl molecules

Eq. (6.40) is a rate equation for the the populations of the system eigenstates, where the relaxation rates are given by Eq. (6.39). The relaxation rates have a strong dependency on the so-called spectral density $J(\omega)$, that describes the effective coupling strength between the system and the environment. In modeling the environment, one often goes to a continuum limit for the environment in which the description in terms of individual oscillators with discrete frequencies ω_k is replaced by a spectral density $J(\omega)$ corresponding to a continuous spectrum of environmental frequencies ω. Usually, the frequency dependence of $J(\omega)$ is taken to follow a power-law dependence of the form $J(\omega) \propto \omega^{\alpha}$. The most common choice for the exponent α is $\alpha = 1$, such that $J(\omega)$ increases linearly with ω. This type of spectral density is called ohmic.

The aim of this section is to give evidence that the spectral density found for BChl *a* molecules in Ref. [130] can be approximated with an ohmic spectral density, taking only the most relevant vibrational mode frequencies found for our light-harvesting aggregates into account. Here below in panel (A) of Fig. (6.1) the numerical spectral density for BChls *a* has been shown (see the red curve) and compared to the measured spectral density (see the dashed blue curve). Ref. [130] has provided the vibrational mode frequencies and the associated reorganization energies used to compute the Drude Lorentz peaks. Finally Drude-Lorentz peaks and a Drude-Lorentz background have been convolved with a gaussian function in order to derive the numerical spectral density. Panel (B) in Fig. (6.1) shows the ohmic spectral density $J(\omega) = k_{vib}\omega$ with $k_{vib} = 0.3$ (see the black dashed line) that we used to fit the lowest part of the numerical spectral density. Since more than the 50% of the transition frequencies are between 0 and 1000 s^{-1} (see the histogram in panel (B)), which is the frequency range where the linear fit is a good approximation, the measured spectral density has been replaced by the linear one with $k_{vib} = 0.3$. The transition frequencies have been computed for a single cylindrical aggregate (MT model) made of 6000 BChl *c* molecules, see Sec. 2.1.1 in Chapt. 2 for a detailed discussion about the geometry of the system and Chapt. 3 for the hermitian Hamiltonian model used to compute the transition frequencies. In Chapter 7 the ohmic spectral density $J(\omega) = k_{vib}\omega$ has been used in order to derived the thermal rates between the eigenstates of the light-harvesting aggregates of GSB and the parameter $k_{vib} = 0.3$ has

been tuned in order to ensure thermalization in a few-picoseconds timescale, which is the typical value found for light-harvesting aggregates [46].

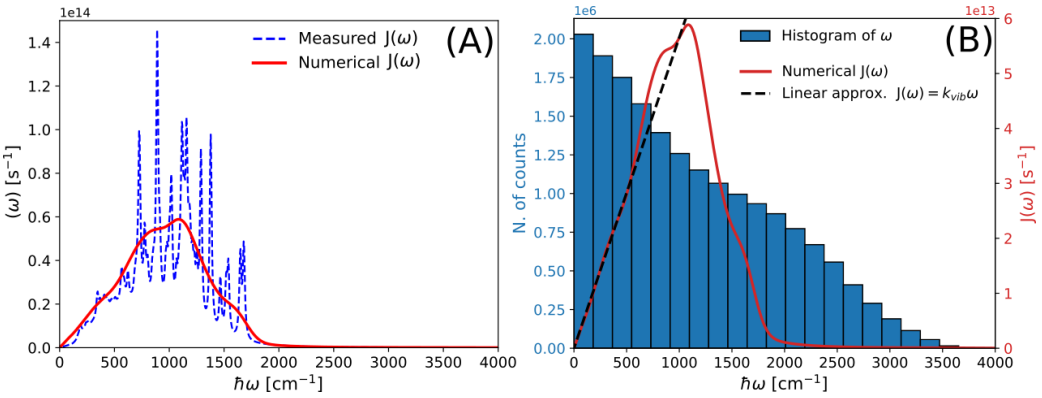

Figure 6.1: *Spectral density for BChls a: numerical calculation and ohmic approximation.* Panel (A) shows the measured spectral density (blue dashed curve) and the numerical one (red curve) as a function of the transition frequency ω. The numerical spectral density has been obtained by convolution of Drude-Lorentz peaks and a Drude-Lorentz background with a gaussian function. The measured data (transition frequencies and reorganization energies) have been taken from Ref. [130]. Panel (B): the numerical spectral density and the linear approximation (black dashed line) have been shown as a function of the transition frequency. Panel (B) also includes the histogram of the transition frequencies ω in order to see where most of them are placed compared to the spectral density. The transition frequencies have been computed for a single roll MT model (see chapter 2 for the geometry) with 6000 BChl *c*. The y axis on the right refers to the spectral density while the y axis on the left to the transition frequencies histogram).

Chapter 7

The role of symmetry in the photosynthetic antenna complex of GSB: efficiency under natural sunlight pumping

In this chapter large-scale simulations of light-matter interaction in natural photosynthetic antenna complexes of the Chlorobium Tepidum green sulfur bacteria (GSB) containing more than one hundred thousand chlorophyll molecules, comparable with natural size, have been performed. Here we have modeled the entire process of the exciton energy transfer, from sunlight absorption to exciton trapping in the reaction centers (RCs) in presence of a thermal bath. The energy transfer has been analyzed using the radiative non-hermitian Hamiltonian and solving the rate equations for the populations. Sunlight pumping has been modeled as black-body radiation at $T = 5800$ *K, with an attenuation factor that takes the Sun-Earth distance into account. Cylindrical structures typical of GSB antenna complexes, and the dimeric baseplate have been considered. The maximal antenna size, comparable to natural size, includes three adjacent, 4-walls concentric cylinders* 1485.7 *Å long arranged over a dimeric baseplate of dimensions* 3075 *Å* $\times$ 1148 *Å, for an overall number of molecules greater than* 10^5*. Our analysis shows that under natural sunlight, in photosynthetic antennae of GSB the number of exci-*

tations reaching the RC per unit time matches the RC closure rate and the internal efficiency shows values close to $\sim 80\%$*. We also considered cylindrical structures where the orientation of the dipoles does not reflect the natural one. Specifically, we vary continuously the angle of the transition dipole with respect to the cylinder main axis, focusing on the case where all dipoles are parallel to the cylinder axis. We also consider the important case where the dipoles are randomly oriented. In all cases the light-harvesting efficiency is lower than in the natural structure, showing the high sensitivity of light harvesting to the specific orientation of the dipole moments. Our results allow for a better understanding of the relationship between structure and functionality in natural photosynthetic antennae of Green sulfur bacteria and could drive the design of efficient light-harvesting devices.*

7.1 Introduction

Photosynthesis is a fundamental process able to capture sunlight and convert it into biochemical energy used to drive cellular processes [19]. In this chapter we model the process of sunlight absorption and energy transfer in the entire antenna complex of a species of photosynthetic anaerobic bacteria: the *Chlorobium Tepidum* green sulfur bacteria (GSB). GSB use sunlight as their main source of energy. They are among the most efficient systems able to harvest sunlight in deep murky waters, where incident light levels are reduced much beyond the already dilute level on land [17, 27]. They are even able to perform photosynthesis with geothermal radiation from deep-sea hydrothermal vents at about 400°C [50].

The GSB antenna complexes are composed of a network of bacteriochlorophyll molecules (BChls *a*, *c*, *d* or *e*) [22]. In GSB BChl molecules are typically modeled as two-level systems (2LS). To each 2LS a transition dipole moment (TDM) is associated, which determines its coupling with both the electromagnetic field and other chlorophyll molecules. Photosynthesis in GSB involves chlorophyll pigments tightly packed in light-harvesting systems with (mostly) cylindrical shapes, known as chlorosomes. In nature these structures typically range in size from 1000 to 2000 Å in length, with widths and depths varying between 600 and 1000 Å, and they can contain between 50000 and 250000 BChl *c* [61, 72, 74]. Sunlight absorbed by the chlorosome

is funneled to other complexes, such as the baseplate (BPL) and the Fenna-Matthews-Olson (FMO) trimer complexes, and finally to the reaction centers (RCs) [17,18], where charge separation occurs, a process which precedes and drives all other photosynthetic steps [9, 17, 27, 53–57]. Once the RC receives an excitation, it produces a charge-separated state and electron transport through the RC begins. A reaction center is said to be in an open state before the excitation reaches it. Once an excitation reaches it and charge separation occurs, the RC goes in a closed state. The time needed for the RC to be open again is called the closure time (from 100 μs to few milliseconds [40, 41]). The closure time defines the frequency at which each RC is able to process an excitation.

Fig. (7.1) shows the model we used to analyze the entire light-harvesting unit in GSB. The energy transfer process from the light-harvesting complex to the RC has a very high (near-80%) internal efficiency in these complexes [18, 36, 37]. A possible origin of this incredible ability to utilize weak sources of incoherent light and funnel the collected energy to specific molecular aggregates could be brought back to the high level of symmetry and hierarchical organization characterizing the antenna complexes of bacterial photosynthetic organisms [15, 16].

The basic components of the photosynthetic antenna complexes of anaerobic bacteria have been widely studied both theoretically and experimentally in Refs. [20–26]. Due to the symmetric arrangement of BChl molecules, these structures display bright (superradiant) and dark (subradiant) states in their single-excitation manifold [10, 17]. Bright states are characterized by a giant transition dipole moment (much larger than the single-molecule dipole moment), while dark states exhibit a significantly smaller transition dipole moment compared to that of a single molecule.

As already demonstrated in literature [79], bright states robust to disorder arise due to the strong coupling between BChl molecules within the aggregates. Within each aggregate (chlorosome and baseplate), excitations are spread coherently due to the small distances between nearest-neighbor BChl molecules (a few Ångstroms), while between pigment groups at a distance of about a few nanometers, electronic excitation is shared incoherently through multi-chromophoric Förster Resonance Energy Transfer (MC-FRET).

In this study, we thus conduct a large-scale analysis of sunlight absorption and exciton energy transfer in GSB photosynthetic complexes. Specifically, we examine a model of the GSB chlorosome comprising more than 10^5

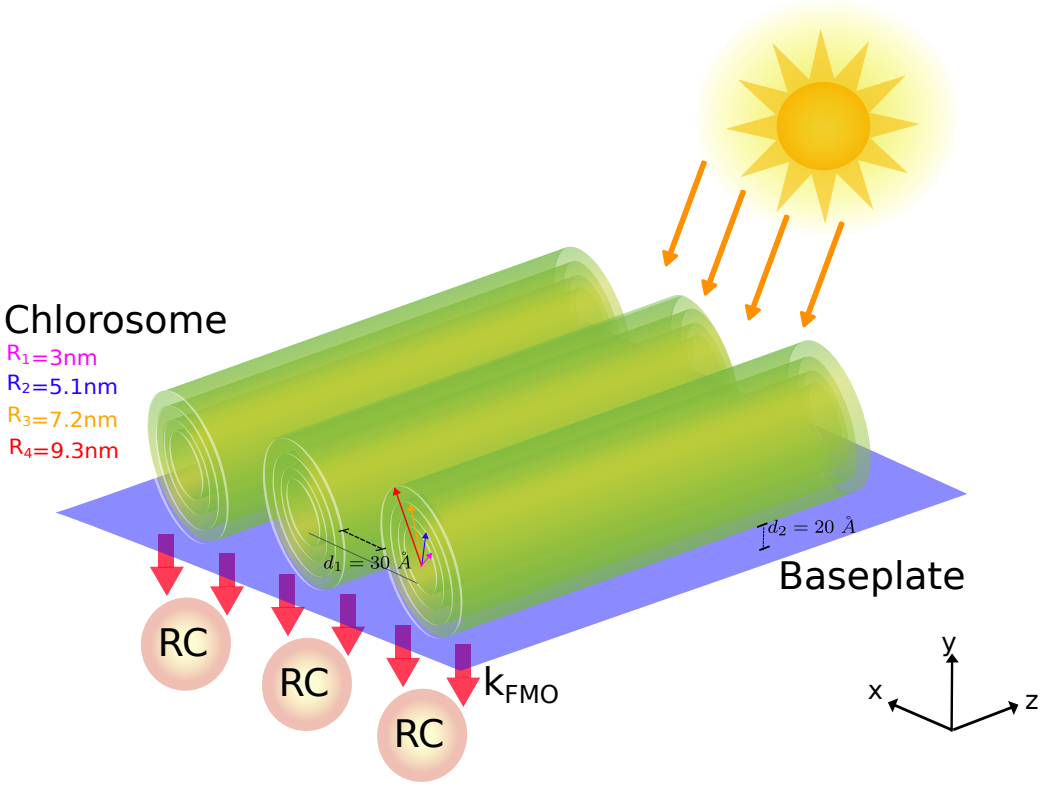

Figure 7.1: *Architecture of GSB light-harvesting unit under natural sunlight.* The chlorosome of GSB comprising three adjacent concentric cylinders and the dimeric baseplate (BPL) have been represented. Each aggregate is made of four concentric MT model cylinders with radii of 30, 51, 72 and 93 Å and containing, respectively, 30, 51, 72 and 93 dipoles per ring. The entire chlorosome contains 132840 BChl *c* with a length $L = 1485.7$ Å and the distance between two adjacent concentric cylinders is $d_1 = 30$ Å. Under the chlorosome a dimeric baseplate with dimesnsions 1147.5×3075.3 Å^2 and comprising 3350 BChl *a* has been represented. The distance between the cylinder and the baseplate is set to $d_2 = 20$ Å, according to Refs. [18, 23]. Finally the energy transfer from the baseplate to the RCs is mediated by the k_{FMO} rate, represented by red arrows connecting the baseplate to the RCs.

chlorophyll molecules arranged on three adjacent concentric cylinders (the chlorosome) above a two-dimensional dimeric baseplate. In order to understand the relation between shape and functionality, the orientations of BChl dipole moments in the cylindrical structures present in the chlorosome have

been modified. The light-harvesting efficiency of the natural geometry has been compared with the light-harvesting efficiency of these mathematical models. Our findings shed new light on how the natural structure of the chlorosome is able to support an efficient energy transfer, even in presence of thermal noise and static disorder.

7.2 Models: the geometry of the system

Here we analyze different models of the chlorosome. Together with the natural cylindrical structures present in the chlorosome, we also considered mathematical cylindrical structures where both positions and orientations of the chlorophyll transition dipole moment have been changed with respect to the natural system. Fig. (7.2) shows the three cylindrical models we analyze. The main difference between different models lies in the dipole orientation.

- *Chlorobium Tepidum* bchQRU triple mutant (MT). The MT model can be thought as organized into a stack of vertical rings [13, 62], each containing 60 BChl *c* molecules represented by dipoles. In panel A of Fig. (7.2) the alternation between the colors of two consecutive dipoles on the same ring (red and black) represents those dipoles pointing inward ($\alpha = +4^\circ$) and outward ($\alpha = -4^\circ$) with respect to the cylinder. See Ref. [13] for more details.

- Parallel dipoles cylinder (PD). The dipoles on the PD are arranged in circles, similarly to MT type, with their direction parallel to the cylinder main axis, see Fig. (7.2) panel (B).

- Random dipoles cylinder (RD). In the RD model, see Fig. (7.2) panel (C), the position of the dipoles are the same as in the PD model, while the dipole orientations are randomly chosen from the unit sphere.

The maximum number of molecules we consider in a single cylinder (MT, PD and RD) is $N = 6000$ BChl *c* with a maximum length of 821.7 Å. More information on the geometry of the MT, PD and RD cylinders can be found in Refs. [13, 14].

The structure of natural GSB light-harvesting systems can vary depending on growing conditions. In general the chlorosome is placed on the top of a two-dimesional dimeric baseplate. The chlorosome does not include

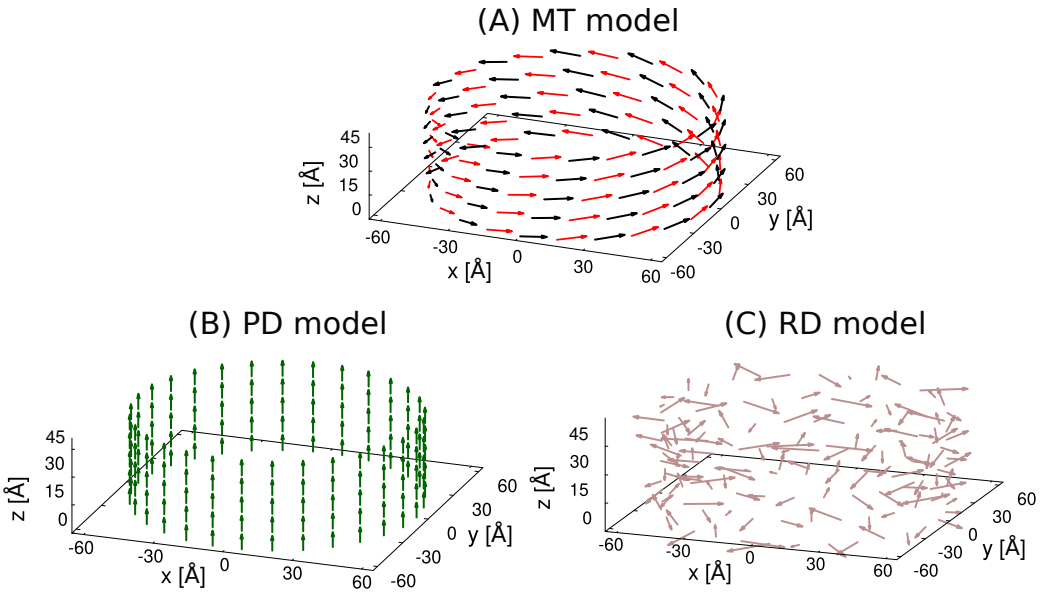

Figure 7.2: *Section of the different cylindrical models.* Panel (A) shows the MT model, the natural structure with a radius $R = 60$ Å. In panels (B) and (C) cylinders made of a stack of rings with the same radius $R = 60$ Å are presented. For the sake of clarity we show only 30 dipoles per ring instead of 60 as we consider in this paper. For more details about the geometry see Refs. [13, 14].

only one cylindrical structure as antenna complex, it can contain several multi-wall cylindrical structures (usually four concentric cylinders) placed adjacently above the baseplate, see Fig. (7.1). Also BChl molecules aggregated in lateral curved lamellae can be present, depending on the growing conditions [13, 14, 70, 71].

In this chapter, in order to model the entire light-harvesting unit, we considered a chlorosome composed by three adjacent cylindrical aggregates with four concentric rolls each, containing 132840 BChl *c* molecules and with a length of $L = 1485.7$ Å. Each aggregate is made of four concentric MT model cylinders with radii of 30, 51, 72 and 93 Å and containing, respectively, 30, 51, 72 and 93 dipoles per ring. The distance between two adjacent concentric cylinders is $d_1 = 30$ Å, according to Ref. [23].

Below the chlorosome, at a distance $d_2 = 20$ Å, there is the dimeric baseplate. The baseplate is a two-dimensional aggregate formed by BChl *a* molecules that connects the chlorosome pigments to the RCs through the

FMO proteins. It is located on the chlorosome envelope on the surface toward the cytoplasmic membranae [64] and in nature its dimensions were roughly estimated to be 500 Å × 2000 Å [23]. Two kind of baseplates are found in literature: monomeric and dimeric [23, 64]. The monomeric baseplate is typical of the FAP (filamentous anoxigenic phototrophs), represented by the *Chloroflexux aurantiacus*, that do not show the FMO complexes [64], while the dimeric baseplate is tipical of GSB [18, 23]. Even if the microscopic structure of the baseplate has not yet been experimentally verified, a model for the dimeric baseplate lattice found in GSB has already been proposed in Refs. [18, 64]. The lattice has two layers and two different transition dipole moments $\vec{\mu}_t$ and $\vec{\mu}_b$ are used for the top and bottom layers respectively. Panel A of Fig. (7.3) shows the arrangement of dimers in a portion of the baseplate, distinguishing between blue and red dipoles belonging respectively to the bottom and top layers, while panel B represents the dimeric unit cell comprising $\vec{\mu}_t$ and $\vec{\mu}_b$.

After the excitation is absorbed by the BChl molecules in the cylindrical structures or in the baseplate, it is driven to the RCs by the FMO complexes. In GSB light-harvesting systems we have 1 FMO trimer per 50 nm^2 [18] and 1 RC per 100 nm^2 , since we have one RC every two FMO complexes.

In order to describe the light-harvesting process in the entire photosynthetic complex, a system of incoherent rate equations has been derived, accounting for the interaction of the system with natural sunlight, exciton energy transfer, the interaction with a thermal bath and the presence of dissipation through radiative and non-radiative decay channels.

To this purpose, different levels of approximation have been considered. First, a Lindblad master equation approach has been developed for the populations of the eigenstates of the entire system (single cylinder + baseplate) assuming finite transfer time and finite thermalization time [15, 44, 46] (see Sec. 7.3). Then, two approximations (see Sec. 7.3.2 and Sec. 7.3.3), decreasing the computational costs, have been developed and compared to the Lindblad approach, finding good agreement.

Overview of the system Hamiltonian models. Before discussing these three approaches, see a detailed description of the Hamiltonian of the system in Chapt. 3. Here we compare the radiative decay widths of the eigenstates of different molecular aggregates computed with the three different Hamiltonian models introduced in Chapt. 3:

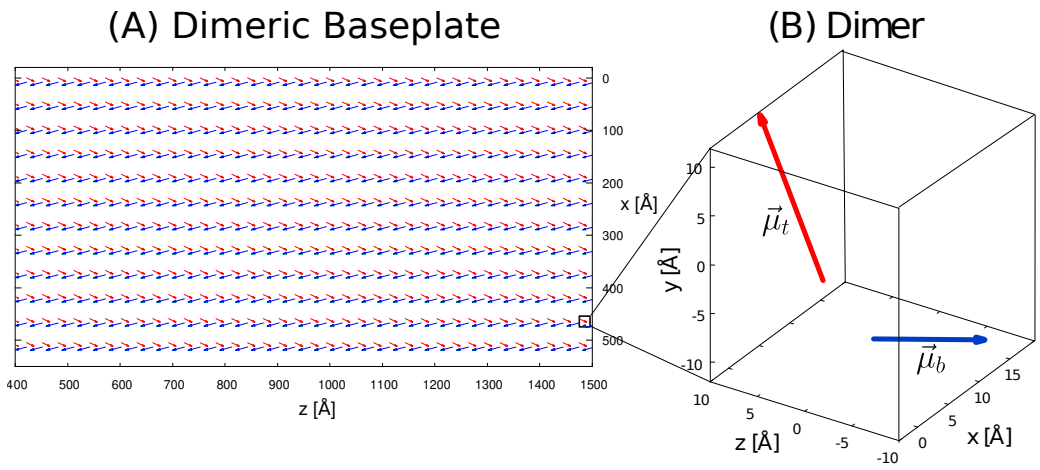

Figure 7.3: *Representation of the dimeric baseplate (BPL) in GSB light-harvesting unit.* Panel (A): top view of a portion of the dimeric baseplate, a planar structure in the xz-plane containing BChl *a* molecules. The blue and red arrows represent the TDM associated to each BChl *a* and belonging to the bottom and top layer respectively. Panel (B): zoomed-in view of the dimeric unit formed by a red arrow (μ_t) and a blue one (μ_b). Dipoles orientations have been found in Ref. [18] and the corresponding unit vectors are given by $\hat{\mu}_t = (0.2795, 0.7484, 0.5982)$ and $\hat{\mu}_b = (0.2533, 0.1607, -0.9533)$. The distance between two dipoles in the same dimeric unit cell is set to 12.8 Å , while the distance along consecutive BChl *a* on x and z axis are 45.9 Å and 30.1 Å respectively. For sake of clarity in panel B the dipole length is multiplied by a factor of 16.

1. NHH: non-hermitian radiative Hamiltonian (3.1).

2. HH: hermitian Hamiltonian (3.5) valid under the non-overlapping resonance criterion.

3. DH: Dipole Hamiltonian (3.8) valid under the non-overlapping resonance criterion and when the system size is small compared to the wavelength associated with the optical transition of the molecules.

In Fig. (7.4) the radiative decay widths of the eigenstates obtained by diagonalizing the NHH are compared with the dipole strength computed with the HH and DH models. Note that, both in the main text and in the Appendix B, all energy values are given in cm^{-1} units, *i.e.* they are divided by *hc*. Panel A of Fig. (7.4) shows that for the single cylinder, which is about

821.7 Å long, the three models give comparable results, because we are in the small-volume limit, defined as $L \ll \lambda_0$. For the whole chlorosome, see panel B of Fig. (7.4), made of three adjacent concentric cylinders covering an area of 3075.3×1147.5 Å^2 we are neither in the small-volume limit nor in the perturbative one, see discussion in Ref. [14] and in section A.3 of the Appendix A. Thus, the three Hamiltonians give very different results. For the baseplate, see panel C of Fig. (7.4), of size 2739.1×2739.1 Å^2, the NHH and the HH give very similar results, showing that we are in the perturbative limit with respect to the non-hermitian interaction. On the other hand, some differences between the DH and the NHH model can be observed. Nevertheless, the discrepancies in the largest dipole strength are just $\approx 14\%$, so that we can use the DH as a first approximation.

In the following we will use the DH model for the single cylinder and baseplate, while for the whole chlorosome the full NHH Hamiltonian will be used.

For the sake of clarity, in this chapter, the indices i, j are used to label the site basis (the BChl molecules), while the eigenstates are labeled by n and m.

Finally, three figures of merit have been chosen in order to estimate the efficiency of the energy transfer in the systems here considered: (1) the trapped current to the RCs defined as the number of excitation reaching the RC per unit time under natural sunlight, (2) the internal and (3) external efficiencies which means the number of excitation reaching the RC divided by the number of incoming photons (external efficiency) or by the number of absorbed photons (internal efficiency).

7.3 Master equation

The whole light-harvesting process can be described by the following master equation for the density matrix $\hat{\rho}_S$ [128]:

$$\frac{d\hat{\rho}_S}{dt} = -\frac{\mathrm{i}}{\hbar}[\hat{H}_S, \hat{\rho}_S] + \mathcal{L}_{fl}[\hat{\rho}_S] + \mathcal{L}_{Sun}[\hat{\rho}_S] + \mathcal{L}_T[\hat{\rho}_S] \tag{7.1}$$

that contains the following terms: $\hat{H}_S$ is the hermitian part of the Hamiltonian of the system (according to the aggregate considered we will use either $\hat{H}_{DH}$ or $\hat{H}_{NHH}$, see dicussion above); $\mathcal{L}_{fl}$, $\mathcal{L}_{Sun}$ and $\mathcal{L}_T$ are Lindblad dissipators derived under the Born-Markov and secular approximations [128].

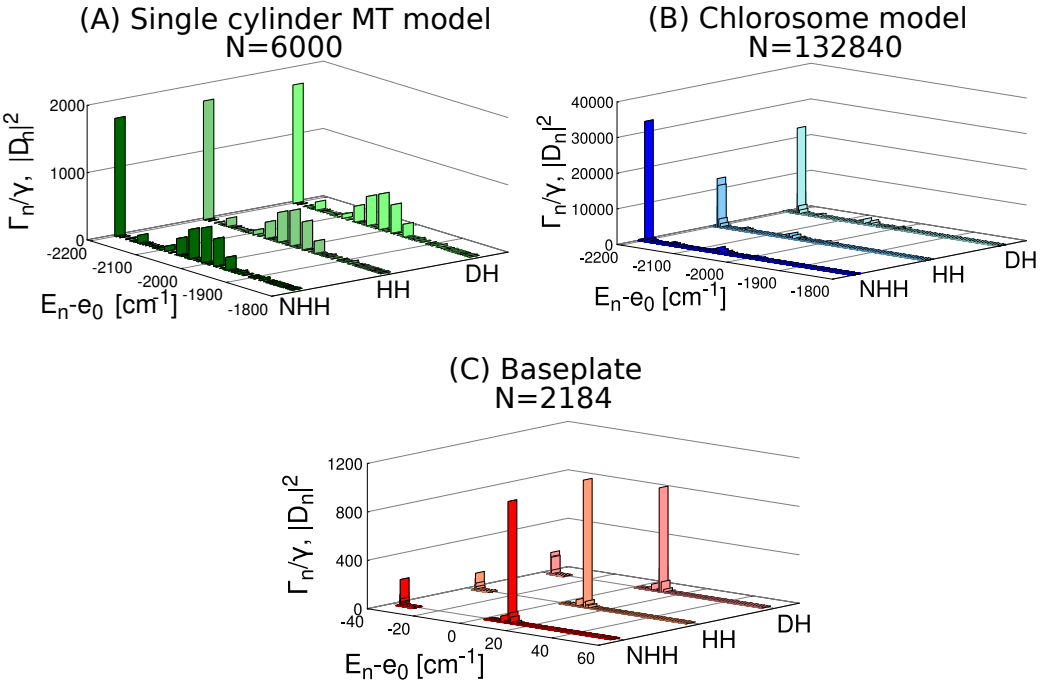

Figure 7.4: *Dipole strength $|D_n|^2$ (DH and HH models) and radiative decay rate Γ_n/γ (NHH model) in cylindrical aggregates and baseplate.* Comparison between the dipole strength (DH and HH models) and radiative decay rate (NHH model) for (A) a single MT cylinder, (B) the chlorosome and (C) the dimeric baseplate. Note that in Ref. [14] for a single MT cylinder (A) the ratio Γ_n/δ is always less than 1, while for the chlorosome (B) the maximum value of $(\Gamma_n/\delta)_{\max}$ is almost 10^2, proving that the perturbative regime for this aggregate fails and only the NHH model can be used to describe superradiance. The mean level spacing δ has been computed as the ratio between the energy spectral width and the total number of eigenmodes for each complex. For the geometry of the system, refer to Table B.2 of the Appendix B. Panels (A-B) show only the lowest part of the energy spectrum, while panel C represents the entire energy spectrum.

They describe respectively spontaneous emission ($\mathcal{L}_{fl}$) and absorption and stimulated emission induced by sunlight ($\mathcal{L}_{Sun}$), while $\mathcal{L}_T$ is the dissipator modeling thermal relaxation and decoherence in presence of a thermal bath [44, 46], see discussion in chapter 6.

The Lindblad dissipators read explicitly:

$$\mathcal{L}_{fl}[\hat{\rho}_S] = \sum_{ij} \frac{Q_{ij}}{\hbar} \left[\hat{a}_j \hat{\rho}_S \hat{a}_i^\dagger - \frac{1}{2}\{\hat{a}_i^\dagger \hat{a}_j, \hat{\rho}_S\} \right] , \tag{7.2a}$$

$$\mathcal{L}_{Sun}[\hat{\rho}_S] = \sum_{ij} f_s n_s \frac{Q_{ij}}{\hbar} \left[\hat{a}_j^\dagger \hat{\rho}_S \hat{a}_i - \frac{1}{2}\{\hat{a}_i \hat{a}_j^\dagger, \hat{\rho}_S\} \right] + \sum_{ij} f_s n_s \frac{Q_{ij}}{\hbar} \left[\hat{a}_j \hat{\rho}_S \hat{a}_i^\dagger - \frac{1}{2}\{\hat{a}_i^\dagger \hat{a}_j, \hat{\rho}_S\} \right] , \tag{7.2b}$$

where the sums over i, j run over all the system sites, $\hat{a}_i = |0\rangle \langle i|$ ($|0\rangle$ is the ground state with no excitation, while $\langle i|$ can be a cylinder or baseplate site), Q_{ij} is given in Eq. (3.4) and in the small-volume limit $Q_{ij} \approx \gamma \hat{\mu}_i \cdot \hat{\mu}_j$.

Note that the absorption of sunlight photons is non-markovian and leads to coherent oscillations, *i.e.* Fano coherence, even if the excitation is incoherent. The sunlight-induced coherence is particularly relevant as the dipole coupling in Eq. (3.4) is collective. As demonstrated in an early calculation, the sunlight-induced coherence may not affect light-harvesting efficiency, as dephasing is typically faster than energy transfer. Then, the Markov approximation assumed in the quantum master equation can be justified [109].

Finally $\mathcal{L}_T$ is

$$\mathcal{L}_T[\hat{\rho}_S] = \sum_{\omega} \gamma^{(p)}(\omega) \sum_i \left[\hat{A}_i(\omega) \hat{\rho}_S \hat{A}_i^\dagger(\omega) - \frac{1}{2} \left\{ \hat{A}_i^\dagger(\omega) \hat{A}_i(\omega), \hat{\rho}_S \right\} \right] , \tag{7.3}$$

where

$$\gamma^{(p)}(\omega) = 2\pi \left[J(\omega)(1 + n_{BE}(\omega)) + J(-\omega) n_{BE}(-\omega) \right] \tag{7.4}$$

are the thermal rates, depending of the spectral density $J(\omega)$ and on the Bose distribution $n_{BE}(\omega) = (e^{\hbar\omega/k_B T} - 1)^{-1}$ of the phonons at room temperature ($T = 300$ K) and

$$\hat{A}_i(\omega) = \sum_{E_m - E_n = \hbar\omega} C_m^*(i) C_n(i) \, |E_n\rangle \langle E_m| . \tag{7.5}$$

More details about the Lindblad dissipators can be found in Refs. [44, 46].

Eq. (7.1), in its Lindblad form, is derived under the secular approximation. Moreover, it can be largely simplified under a well-motivated assumption: the excitons are transferred incoherently between the cylinder eigenstates and baseplate eigenstates; this is consistent with the approach of some recent works [44, 46, 93, 131], where a similar model to describe exciton dynamics in GSB antenna complexes has been already employed. Under

these assumptions, the coupling with the thermal bath and natural sunlight are well approximated by rate equations for the populations of the cylinder eigenstates ($P_{n\in C}$) and the populations of the baseplate eigenstates ($P_{n\in B}$), as we show in the following.

7.3.1 Rate equations for the light-harvesting process: finite transfer time and finite thermalization time

The following set of full rate equations for the whole light-harvesting process have been derived starting from the master equation Eq. (7.1) (see also Chapt. 6). They read:

$$\begin{aligned}\frac{dP_0(t)}{dt} =& -\sum_n R_n P_0(t) + \sum_n (R_n + \Gamma_n/\hbar + \kappa_{NR}) P_n(t) \\ &+ \sum_{n\in B} \kappa P_n(t) \ , \end{aligned} \tag{7.6a}$$

$$\begin{aligned}\frac{dP_{n\in C}(t)}{dt} =& R_n P_0(t) - (R_n + \Gamma_n/\hbar + \kappa_{NR}) P_n(t) \\ &+ \sum_{m\in C} \left(T_{n,m} P_m(t) - T_{m,n} P_n(t)\right) \\ &+ \sum_{m\in B} \left(K_{n,m} P_m(t) - K_{m,n} P_n(t)\right) \ , \end{aligned} \tag{7.6b}$$

$$\begin{aligned}\frac{dP_{n\in B}(t)}{dt} =& R_n P_0(t) - (R_n + \Gamma_n/\hbar + \kappa_{NR} + \kappa) P_n(t) \\ &+ \sum_{m\in B} \left(T_{n,m} P_m(t) - T_{m,n} P_n(t)\right) \\ &+ \sum_{m\in C} \left(K_{n,m} P_m(t) - K_{m,n} P_n(t)\right) \ , \end{aligned} \tag{7.6c}$$

where the summations $\sum_{n\in C}$ include all the cylinder eigenstates, while $\sum_{n\in B}$ include all the baseplate eigenstates and $\sum_n$ include all the eigenstates (cylinder and baseplate).

The terms in Eq. (7.6) are explained in detail in the following.

Radiative decay The radiative decay $\Gamma_n/\hbar$ is given by the imaginary part of the NHH. When the DH is valid, it can be computed from the dipole strengths of the eigenstates as follows:

$$\frac{\Gamma_n}{\hbar} = \frac{4}{3}\frac{\mu^2 D_n^2 \omega_n^3}{\hbar c^3} \ , \tag{7.7}$$

where D_n is defined in (3.7) and $\omega_n = E_n/\hbar$ is the eigenstate transition frequency.

Absorption and stimulated emission induced by sunlight radiation Sunlight induces absorption and stimulated emission to each eigenstate $|E_n\rangle$ with rates given by

$$R_n = f_S n_S(\omega_n)\frac{\Gamma_n}{\hbar} \ , \tag{7.8}$$

where

$$n_S(\omega_n) = \frac{1}{e^{\hbar\omega_n/(k_B T_S)} - 1} \tag{7.9}$$

is the Bose occupation of photons at the black-body temperature of the Sun, $T_S = 5800$ K, while the factor

$$f_S = \frac{\pi r_S^2}{4\pi R_{ES}^2} = 5.4 \times 10^{-6} \tag{7.10}$$

models how the absorption (and stimulated emission) rate is reduced by the Sun-Earth distance [46]. Specifically, f_S is the fraction of the solid angle of the Sun as seen from the Earth, with r_S being the radius of the Sun and R_{ES} the Sun-Earth distance. See Sec. 5.1 of chapter 5 for a more detailed discussion about the validity of the approximation of the solar spectrum with the black-body radiation theory and Sec. 5.2 of chapter 5 of for a comparison between different approaches used to compute the absorption rates of BChl molecules. Note that the solar spectrum is not exactly described by black-body radiation, as the photon experiences multiple scatterings upon arriving on the Earth. However, the sunlight spectrum is sufficiently broad compared to the absorption of light-harvesting complexes and our approximation holds [109].

Non-radiative decay In addition to the radiative decay, we include non-radiative recombination processes on each n eigenstate by adding a non-radiative rate $\kappa_{NR} = 1$ ns^{-1} for each eigenstate [15].

Trapping to RC We also consider an additional decay channel due to excitation transfer from the baseplate to the reaction centers (RCs) through the FMO trimers. We model this by adding a decay rate κ on all the baseplate eigenstates. Specifically, the excitation is lost through the FMOs to the RCs with a rate $k_{FMO} \sim 0.023 - 0.044$ ps^{-1} [37]. k_{FMO} is the reciprocal

of the time required for an excitation to be lost in the RC through the FMO, and such time is the sum of four contributions,

$$k_{FMO}^{-1} = \tau_b + \tau_t + \tau_e + \tau_{cs} \ , \tag{7.11}$$

that represent explicitly:

- the transfer time τ_b *from the baseplate to the FMO*, which we estimate as the inverse of the FRET rate

  $$\tau_b = \frac{\hbar^2 \Gamma_\phi}{2J^2} \tag{7.12}$$

  between the two molecules closest to each other, one in the baseplate and one in the FMO complex; here, $\Gamma_\phi = 1000\ \mathrm{cm}^{-1}$, where $\Gamma_\phi/\hbar$ is the dephasing rate, estimated from the cylinder-baseplate transition rate, as explained in Sec. 7.3.2; $J \approx \mu^2/r^3$ is the dipole coupling between two BChl molecules (one belonging to the baseplate and the other one to the FMO), where $\mu \approx 6$ D is the transition dipole of a single BChl molecule and $r = 20$ Å is the distance; therefore we have $J \approx 23\ \mathrm{cm}^{-1}$, from which $\tau_b \approx 5$ ps;

- the time for an excitation to go *through the FMO* from edge to edge has been estimated in Ref. [132], and it is $\tau_t \approx 3$ ps, in good agreement with the experimental data found in Ref. [37] that report an energy relaxation within the FMO complex, which lies between 0.1 and 20 ps;

- the exit time τ_e *from FMO to RC*, which is ~ 17 ps [37];

- the *charge-separation* time τ_{cs} at which the excitation is irreversibly lost in the RC is $\tau_{cs} \approx 1$ ps [17, 37].

The sum of these three contributions gives the typical range 22.5 ps $< k_{FMO}^{-1} <$ 43 ps, in agreement with the estimation given above.

Finally the trapping rate to the RC κ can be estimated as follows. We have a molecular density of 1 molecule per 6.9 nm^2 in the baseplate and a density of 1 FMO trimer per 50 nm^2. [18]. Since we have one RC every two FMO trimers [40, 71, 133, 134], we have a density of 1 RC per 100 nm^2. Therefore, we have a ratio $N_{FMO}/N_{BPL} = 0.138$ between the number of FMO trimers and the number of baseplate molecules. So, we have modeled the FMO-RC trapping with a constant decay rate $\kappa = 0.138\ k_{FMO}$ from all the baseplate molecules (see Eqs. (7.6)).

Thermal relaxation and energy transfer Finally, we include thermal relaxation rates $T_{n,m}$ between each pair of eigenstates within the cylinder and the baseplate, and Förster energy transfer rates $K_{n,m}$ between the cylinder and the baseplate. More details on this are given below.

The transfer rates $T_{m,n}$ model thermal relaxation inside the aggregate, see chapter 6 for the derivation. They are detailed-balanced, namely

$$T_{m,n} = \frac{2\pi\Lambda_{mn} J[(E_m - E_n)/\hbar]}{1 - e^{-(E_m - E_n)/(k_B T)}} \ , \tag{7.13}$$

where $\Lambda_{mn} = \sum_i |C_m(i)|^2 |C_n(i)|^2$, the phonon temperature is $T = 300$ K and the spectral density is $J(\omega) = \kappa_{vib}\omega$. $\kappa_{vib} = 0.3$ ensures thermal relaxation in a few-picoseconds timescale [46]. On the other hand, the transfer rates between eigenstates of different aggregates are the incoherent Förster rates

$$K_{m,n} = \begin{cases} \frac{2\Omega_{m,n}^2 \Gamma_\phi}{\hbar\left[\Gamma_\phi^2 + (E_m - E_n)^2\right]} & E_n \geq E_m \\ \frac{2\Omega_{m,n}^2 \Gamma_\phi}{\hbar\left[\Gamma_\phi^2 + (E_m - E_n)^2\right]} e^{-(E_m - E_n)/(k_B T)} & E_n < E_m \end{cases} \tag{7.14}$$

where $\Omega_{m,n}$ is the dipole-dipole coupling (matrix element) between the eigenstates of different aggregates computed by using (3.8), while $\Gamma_\phi = 1000\ \mathrm{cm}^{-1}$, where $\Gamma_\phi/\hbar$ is the dephasing rate for every $m - n$ transition and E_n is the transition energy of the nth eigenstate. Note that the "energy-upwards" rates in Eq. (7.14) are multiplied by an exponential factor that ensures the detailed balance [16]. The parameter Γ_ϕ has been tuned to match the transfer rates between the MT cylinder and the baseplate (tens of picoseconds [18, 38, 39]) and it corresponds to the sum of the FWHM of the emission spectrum of the donor and the absorption spectrum of the acceptor. See section B.3 of the Appendix B for a detailed discussion about FRET and the choice of Γ_ϕ.

The rate equations (7.6) are linear and they can be solved at the steady state or as a function of time by numerical diagonalization, with a computational cost that increases as N^3, where N is the total number of molecules in the cylinder+baseplate. A scheme of Eqs. (7.6) is shown in Fig. (7.5).

From the steady-state solution of Eqs. (7.6) we obtain the current trapped in the RCs,

$$I_{RCs} = \kappa \sum_{n \in B} P_n^{SS} \ , \tag{7.15}$$

where P_n^{SS} are steady-state populations of the baseplate eigenstates, and we

also compute the internal efficiency [16],

$$\eta_{in} = \frac{\kappa \sum_{n\in B} P_n^{SS}}{\sum_n R_n P_0^{SS}} \ , \tag{7.16}$$

where P_0^{SS} is the steady-state population of the ground state and the sum in the denominator runs over all the cylinder and baseplate states.

Here we introduce another figure of merit, the external efficiency:

$$\eta_{ext} = \frac{I_{RCs}}{I_{Sun} \times A_{BPL}} = \eta_{abs} \times \eta_{in} \ , \tag{7.17}$$

where I_{Sun} is the photon flux coming from sunlight impinging the baseplate surface, I_{RCs} is the total current trapped in the RCs, η_{abs} and η_{in} are the absorption and internal efficiencies, respectively. An analytical expression for η_{in} has been given in Eq. (7.16), while the absorption efficiency η_{abs}, given by Eq. B.3 of the Appendix B, is the ratio between the power absorbed by the system and the solar irradiance. In section B.1 of the Appendix B a deeper study and detailed calculations of the absorption in the entire light-harvesting apparatus of GSB comprising the chlorosome and the baseplate are offered.

7.3.2 Thermal equilibrium within each aggregate

To simplify the rate equations (7.6), here we follow a widely used approach, presented *e.g.* in Refs. [34, 35] and in Ref. [17]. In this approach, thermal equilibrium is assumed inside each aggregate (a cylinder, or the baseplate). Note that light-harvesting systems are usually disordered and strongly coupled to protein environments, so the thermalization process may not lead to the Boltzmann distribution of the system Hamiltonian [135]. Instead, the light-harvesting system relaxes to non-canonical distribution due to the system-bath correlation and exhibit bath-induced coherence, which can affect fluorescence emission and Förster energy transfer. The master equation in Eq. (7.1) assumes the factorization of the system-bath density matrix and thus implies the system Boltzmann distribution. Possible corrections due to the system-bath correlation can be considered in the future.

Under the assumption of thermalization in each aggregate, the transfer rate from a donor aggregate "D" to an acceptor aggregate "A" is given by the generalized multi-chromophoric Förster resonance energy transfer rate

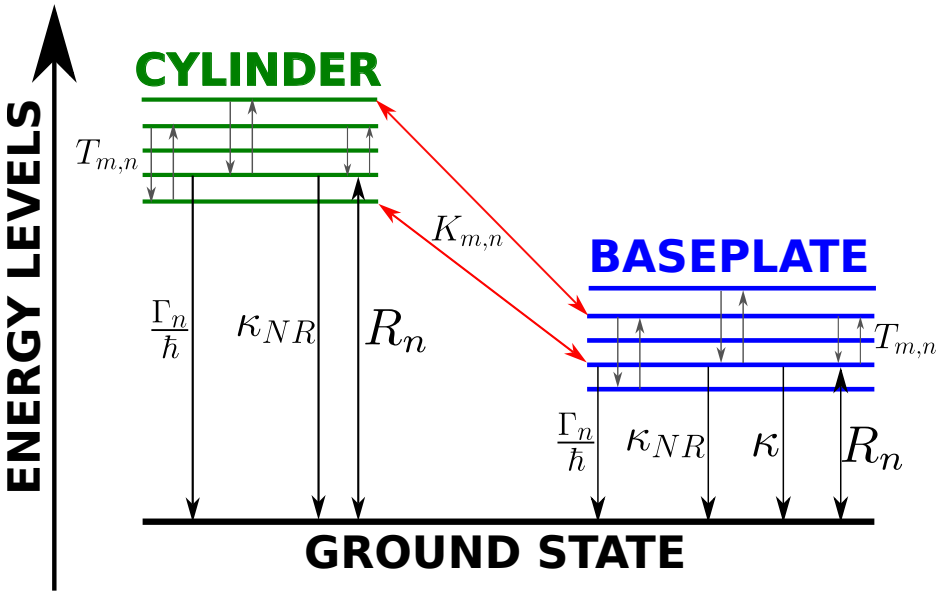

Figure 7.5: *Rate equation scheme.* Scheme of the rate equations, Eqs. (7.6). Here, $\Gamma_n/\hbar$ is the radiative recombination rate, κ_{NR} is the non-radiative recombination rate (equal for all levels), $R_n = f_S n_S(\omega_n)\frac{\Gamma_n}{\hbar}$ are the sunlight absorption and stimulated emission rates, $T_{m,n}$ are the thermalization rates within each aggregate, see Eq. (7.13), $K_{m,n}$ are the transfer rates between eigenstates of each aggregates, see Eq. (7.14), and κ is the trapping rate from the baseplate, through the FMOs, to the RC.

(MC-FRET)

$$K_{D,A} = \sum_{m\in D}\sum_{n\in A} \frac{e^{-E_m/(k_B T)}}{\sum_{l\in D} e^{-E_l/(k_B T)}} K_{n,m} \ , \tag{7.18}$$

where $K_{n,m}$ is the transfer rate from the donor eigenstate m to the acceptor eigenstate n, see Eq. (7.14). In section B.3 of the Appendix B a more detailed explanation of the MC-FRET is given. Similarly, we assume thermal equilibrium within each aggregate to compute the decay rates, as explained

in the following. We obtain the following 3-level rate equations,

$$\frac{dP_0(t)}{dt} = -(R_C + R_B)P_0(t) + (\langle R\rangle_C + \langle\gamma\rangle_C)P_C(t) + (\langle R\rangle_B + \langle\gamma\rangle_B)P_B(t) + \kappa P_B(t) \ , \\ + \kappa_{NR}[P_C(t) + P_B(t)] \tag{7.19a}$$

$$\frac{dP_C(t)}{dt} = R_C P_0(t) - (\langle R\rangle_C + \langle\gamma\rangle_C)P_C(t) + K_{B,C}P_B(t) - K_{C,B}P_C(t) - \kappa_{NR}P_C(t) \ , \tag{7.19b}$$

$$\frac{dP_B(t)}{dt} = R_B P_0(t) - (\langle R\rangle_B + \langle\gamma\rangle_B)P_B(t) + K_{C,B}P_C(t) - K_{B,C}P_B(t) - \kappa P_B(t) \\ - \kappa_{NR}P_B(t) \ , \tag{7.19c}$$

where $P_0(t)$, $P_C(t)$ and $P_B(t)$ are the populations of the ground state, the cylinder and the baseplate, respectively. $R_C = \sum_{n\in C} R_n$ and $R_B = \sum_{n\in B} R_n$ are the total absorption rates of the cylinder and the baseplate, respectively. $(\langle R\rangle_C + \langle\gamma\rangle_C)$ and $(\langle R\rangle_B + \langle\gamma\rangle_B)$ are the thermal-averaged emission rates, given by

$$\langle R\rangle_{C,B} + \langle\gamma\rangle_{C,B} = \sum_{n\in C,B} (R_n + \Gamma_n/\hbar)p_n \tag{7.20}$$

of the cylinder (C) and the baseplate (B) with the Boltzmann weights within each aggregate

$$p_n = \frac{e^{-E_n/(k_B T)}}{\sum_{m\in C,B} e^{-E_m/(k_B T)}} \ , \tag{7.21}$$

$K_{C,B}$, $K_{B,C}$ are donor-acceptor rates computed from Eq. (7.18) using the Lorentzian lineshapes as in Eq. (7.14).

The collective Förster energy transfer between two aggregates often exhibits simple scaling laws as a function of distance, site and orientation. Using the generalized MC-FRET, we analyzed the scaling laws for interwire energy transfer [136]. This approach can be applied to other geometries and was recently adopted for the chlorosome lamellae [137, 138]. The reported results on energy transfer can be understood in this framework.

We numerically solve Eqs. (7.19) at the steady-state to obtain the number of excitations trapped in the RCs per unit time,

$$I_{RCs} = \kappa P_B^{SS} \ . \tag{7.22}$$

We also compute the internal efficiency as the ratio between the excitations trapped in the RC per unit time and the excitations absorbed per unit

time [16],

$$\eta_{in} = \frac{\kappa P_B^{SS}}{(R_C + R_B) P_0^{SS}} \ . \tag{7.23}$$

7.3.3 Thermal equilibrium among all the aggregates

If the transfer rate between the aggregates is very fast, we can make a further approximation and assume that all the aggregates are at thermal equilibrium between one another. In such case, let us recall the rate equation for the population of the ground state, Eq. (7.6a)

$$\begin{aligned} \frac{dP_0(t)}{dt} = &- \sum_n R_n P_0(t) + \sum_n R_n P_n(t) \\ &+ \sum_n \frac{\Gamma_n}{\hbar} P_n(t) + \sum_n \kappa_{NR} P_n(t) + \sum_{n \in B} \kappa P_n(t) \, , \end{aligned} \tag{7.24}$$

where P_0 is the population of the ground state and P_n is the population of the n-th excitonic eigenstate.

Then, let us assume that the whole single-excitation subspace is at thermal equilibrium with a temperature $T = 300$ K. This approximation is reasonable in the case where the thermalization process among all the aggregates (between cylinders, or between cylinders and the baseplate) happens faster than the superradiant radiative decay of the cylinders. In this case, we define the population in the excited subspace of the whole system at time t as

$$P_e(t) = \sum_{n=1}^{N} P_n(t) \, , \tag{7.25}$$

so that the trace preservation condition can be written as

$$P_0(t) + P_e(t) = 1 \, , \tag{7.26}$$

and, crucially, we assume that

$$P_n(t) = P_e(t) p_n \quad \text{with} \quad p_n = \frac{e^{-E_n/(k_B T)}}{\sum_m e^{-E_m/(k_B T)}} \ . \tag{7.27}$$

By substituting (7.27) into (7.24) we have

$$\begin{aligned}\frac{dP_0(t)}{dt} = &-\left(\sum_n R_n\right) P_0(t) + \left(\sum_n R_n p_n\right) P_e(t) \\ &+ \left(\sum_n \frac{\Gamma_n}{\hbar} p_n\right) P_e(t) + \kappa_{NR}\left(\sum_n p_n\right) P_e(t) \\ &+ \kappa\left(\sum_{n\in B} p_n\right) P_e(t)\,. \end{aligned} \tag{7.28}$$

Eq. (7.28) can be expressed in terms of the thermal averages of the parameters,

$$\langle R\rangle = \sum_n R_n p_n\ , \qquad \langle\gamma\rangle = \sum_n \frac{\Gamma_n}{\hbar} p_n\ , \tag{7.29}$$

noting that $\sum_n p_n = 1$, defining the fraction of the excited population on the baseplate $p_B = \sum_{n\in B} p_n$, and by defining the total absorption rate as $R_{TOT} = \sum_n R_n$ we get

$$\frac{dP_0(t)}{dt} = -R_{TOT}P_0(t) + \left(\langle R\rangle + \langle\gamma\rangle + \kappa_{NR} + \kappa p_B\right) P_e(t)\,. \tag{7.30}$$

The current trapped at the steady state is obtained by using Eq. (7.26):

$$I_{RCs} = \kappa p_B P_e^{SS} = \frac{\kappa p_B R_{TOT}}{R_{TOT} + \langle R\rangle + \langle\gamma\rangle + \kappa_{NR} + \kappa p_B}\,, \tag{7.31}$$

while the internal efficiency is

$$\eta_{in} = \frac{\kappa p_B P_e^{SS}}{R_{TOT} P_0^{SS}} = \frac{\kappa p_B}{\langle R\rangle + \langle\gamma\rangle + \kappa_{NR} + \kappa p_B}\ . \tag{7.32}$$

Here, P_e^{SS} represents the total excitonic population in the system at the steady state, under natural sunlight illumination, assuming thermal equilibrium in the whole system and accounting for radiative and non-radiative recombination. This method only requires the knowledge of the radiative and non-radiative decay rates of the eigenstates and of their energies.

Note that, since the baseplate is well gapped below the cylinder, we have $p_B \approx 1$. Moreover, for $\kappa_{NR} = 1\ \mathrm{ns}^{-1}$, we also typically have $\langle R\rangle + \langle\gamma\rangle \ll \kappa_{NR}$. Therefore, the internal efficiency has the approximate expression:

$$\eta_{in} \approx \frac{\kappa}{\kappa_{NR} + \kappa}\ . \tag{7.33}$$

7.4 Results and discussions

7.4.1 Exciton energy transfer in GSB light-harvesting systems

In this section the main results of this study are presented comparing the natural structure with the light-harvesting systems obtained by modifying the orientation of the dipoles in the cylindrical aggregates.

First we consider a single-wall nanotube coupled to a baseplate where the excitation can be trapped with a trapping rate k_{FMO}. For the single-wall nanotubes, we consider three different types of cylindrical aggregates (MT, PD and RD, see Sec. 7.2). All single-wall cylinders are composed of 6000 BChl molecules and they are 821.7 Å long. The baseplate coupled to the cylindrical structures is composed of 2184 BChl molecules and has an area of 550.8×2739.1 Å^2. In addition to the single-wall nanotubes, we also consider the full model of the GSB photosynthetic antenna (chlorosome) composed of 132840 BChl molecules distributed among three MT adjacent concentric cylinders (four wall each), see Sec. 7.2. Each concentric cylinder includes 44280 BChl molecules, and the baseplate for the whole chlorosome is composed of 3350 molecules and with an area of 1145.7×3075.3 Å^2, see Table B.2 in section B.2 of the Appendix B where a more detailed explanation of the geometrical features of the cylindrical aggregates and baseplate is given.

For each light-harvesting complex we computed the trapped current (Fig. (7.6) and Fig. (7.7) panel (A)) and the internal efficiency (Fig. (7.6) and Fig. (7.7) panel (B)). The external efficiency has been computed for the entire chlorosome coupled to a baseplate (Fig. 7.7 panel C), and for all the other single-cylinder models, see section B.1 of the Appendix B.

In Fig. (7.6), the trapped current and the internal efficiency have been computed using the three different approaches described in Sec. 7.3 (full rate equations, partially thermalized rate equations, and fully thermalized rate equations) as a function of the k_{FMO} trapping rate for the single-wall cylindrical models (MT, PD and RD) coupled to a dimeric baseplate. Circular open symbols stand for the full rate equations model (see Eqs. (7.15), (7.16) in Sec. 7.3) dashed line for the partially thermalized model (Eqs. (7.22) and (7.23) in Sec. 7.3.2) and the continuous line is given by Eqs. (7.31) and (7.32) in Sec. 7.3.3, referring to the fully thermalized model. Note that the full rate equations give results in very good agreement with the partially

thermalized rate equations for the three different cylindrical structures. On the other hand, the fully thermalized rate equations overestimate the efficiencies and trapped current and their result is independent of the specific kind of cylinder considered (MT, PD, RD), see Eq. (7.33). The MT model has the largest values of trapped current and internal efficiency. We also note that the results for the MT model of the internal efficiency, see (Fig. (7.6) panel (B), obtained from the full rate equations and the partially thermalized rate equations, are close to the results obtained with the fully thermalized rate equations. For this reason, for the whole chlorosome built with the MT cylindrical structures, we use only the fully thermalized rate equations.

Fig. (7.7) shows the trapped current (panel A), the internal efficiency (panel B) and the external efficiency (panel C) as a function of the k_{FMO} trapping rate for the entire chlorosome obtained by using the fully thermalized model. One of the most interesting results is that the trapped current per RC (see panel A), which is of the order of ~ 1 ms^{-1} in the realistic range of values for k_{FMO}, matches the closure rate range of the RCs, see yellow box in Fig. (7.7). This suggests that natural complexes may tend to optimize the number of excitations which arrive on the RC in order to match its operational time. Indeed, a lower number of excitations per second arriving on the RC would leave the RC in the open state for longer times, thus decreasing the rate of charge separation, while a larger number of excitation per second would not be used, since the RC could be in the closed state. Panel B shows the internal efficiency that can reach values between $70 - 85\%$ for the entire chlorosome for 0.023 ps$^{-1} < k_{FMO} < 0.044$ ps^{-1}, the typical range of FMO (see the yellow window). Note that this value of internal efficiency is in good agreement with Refs. [18, 36, 37]. On the other hand, the external efficiency (see panel C) has a value close to $\sim 1\%$ in agreement with our theoretical prediction, see also section B.1 of the Appendix B.

7.4.2 Study of the relationship between geometry and efficient energy transfer

In order to explain the better efficiency of natural structures (MT model with a single-wall cylinder and the entire chlorosome) to transfer the excitation to the RCs with respect to the other single-wall cylinder models (RD and PD), we now analyze the dependence of the efficiency on the orientation of the TDMs in the cylinder and the coupling strength between different cylinder

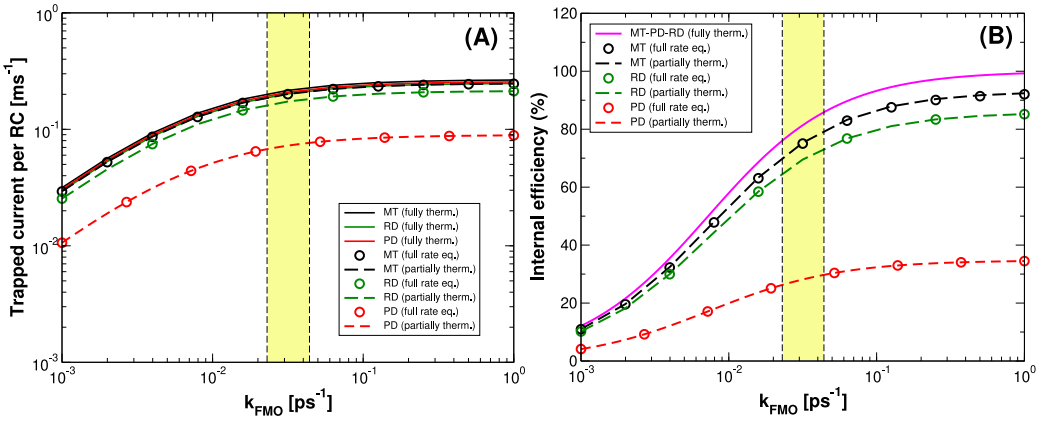

Figure 7.6: *Trapped current and internal efficiency vs. transfer rate k_{FMO} from baseplate to RCs for single-cylinder models.* Trapped current per RC (panel A) and internal efficiency (panel B) for the single-cylinder models (MT, PD, RD coupled to the dimeric baseplate) comprising 6000 BChl c in the cylinder and 2184 BChl a in the baseplate. More details about the dimensions of the systems can be found in Table B.2 of the Appendix B. Black, green and red dashed lines have been obtained assuming thermalization in each aggregate and solving Eq. (7.19) in MT, RD and PD models, respectively. Open circles represents the results obtained by solving the full rate equations given in Eq. (7.6). Continuous lines represent the trapped current and internal efficiency assuming thermalization among all aggregates, obtained from Eq. (7.24). According to Eq. (7.33) the internal efficiency has a universal expression for all the models. The yellow box between the two vertical dashed lines represents the regime in which FMO complexes typically work ($0.023\ \text{ps}^{-1} < k_{FMO} < 0.044\ \text{ps}^{-1}$). Trapped current and internal efficiency for the RD model have been computed averaging over 10 realizations of random dipole orientations.

models and the baseplate. In Fig. (7.8) (panels (A-B)) the trapped current and the internal efficiency are computed for a single cylindrical aggregate containing 6000 BChl c coupled to a dimeric baseplate with 2184 BChl a as a function of the TDMs orientation with respect to the cylinder main axis, given by the β angle, see panel D of Fig. (7.8). For $\beta = 0$ we have the PD model, for $\beta = 55°$ we have the MT model [13,14,28,62], for $\beta = \pi/2$ we have the TD model (tangent dipoles) discussed in Ref. [13]. Panels (A-B) show that among all the possible orientations of the TDMs, for $\beta = 55°$, which is

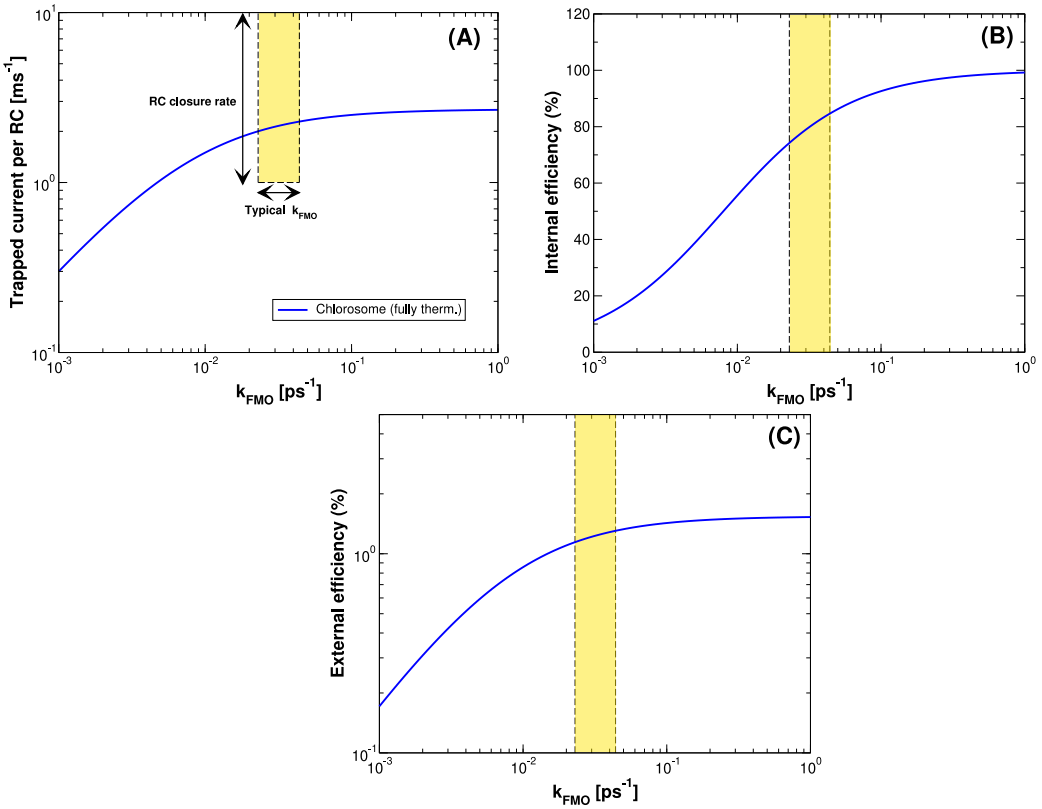

Figure 7.7: *Trapped current, internal and external efficiency vs. transfer rate k_{FMO} from baseplate to RCs for the chlorosome coupled to a dimeric baseplate.* Trapped current per RC (panel A), internal efficiency (panel B) and external efficiency (panel C) for the entire chlorosome coupled to a dimeric baseplate computed assuming thermalizazion among all the aggregates. Both the trapped current and the efficiency have been obtained by solving the rate equation system shown in Eq. (7.24) at the steady state. The system contains 132840 BChl *c* molecules distributed among three MT adjacent concentric cylinders, each including 44280 BChl molecules, on a baseplate composed of 3350 BChl *a* molecules and with an area of 1145.7×3075.3 Å^2. See Table B.2 in section B.2 of the Appendix B for more details about the geometry. The yellow box in panels (A-C) between the two vertical dashed lines represents the regime in which FMO complexes typically work (0.023 ps$^{-1} < k_{FMO} < 0.044$ ps^{-1}). Only for panel A the height of the yellow box represents the range where the RCs closure rate is typically found, which is between 1 and 10 ms^{-1} [40, 41].

the angle found for the MT model (see the red dashed line), the two figures of merit reach the largest values. We also included the RD model (see the gray area between the horizontal black dashed lines), which has large values of both trapped current and internal efficiency, but always smaller than the MT model.

A possible explanation for the higher efficiencies of the natural model (MT) can be found analyzing the MC-FRET transfer rates, see Sec. 7.3.2: $K_{C,B}$ from cylinder to baseplate and $K_{B,C}$ from baseplate to cylinder. Panel C in Fig. (7.8) shows the MC-FRET rates $K_{C,B}$ and $K_{B,C}$ (black and magenta curves respectively) given by Eq. (7.18) and the thermal-averaged emission rate from the cylinder $\langle R \rangle_C + \langle \gamma \rangle_C$ (green curve), see Eq. (7.20) used in Eq. (7.19) as a function of β angle. From panel C of Fig. (7.8) we can see that the MC-FRET rate from cylinder to baseplate $K_{C,B}$ is faster than the backward rate and the thermal-averaged emission rate, ensuring most of the excitation in the cylinder is funneled to the baseplate. $K_{C,B}$ has the same behavior as the trapped current and the internal efficiency, reaching the largest values for $\beta = 55°$, which is about 15 ns^{-1} in agreement with Ref. [18]. Once the excitation reaches the baseplate, it is transferred to the RCs through the FMO complexes by the average FMO trapping rate κ (see the horizontal yellow window), that typically ranges from 3.17 to 6 ns^{-1} in GSB light-harvesting aggregates. Other radiative and non-radiative processes are present in these systems (see the continuous green curve and the blue dashed line respectively), but for the MT model ($\beta = 55°$) these quantities are more than one order of magnitude less than the MC-FRET rate from cylinder to baseplate.

These foundings explain that only specific geometries can exploit an efficient exciton energy transfer under natural sunlight even in presence of thermal dephasing comparable to room temperature energy and confirm that natural models are the only ones capable to present a geometrical arrangement of TDMs such that both the trapped current and the internal efficiency are maximized with respect to the other mathematical models. See also section B.4 of the Appendix B, where the results for another natural model, the wild type (WT), has been provided and compared to the MT model. The values of the trapped current and internal efficiency found for the WT are close to the ones found for the MT model and higher than all the other mathematical models.

The origin of such a fast MC-FRET rate $K_{C,B}$ in the MT model cylinder

is investigated by comparing the spectral properties of the different models (MT, PD and RD) involved in the calculation of $K_{C,B}$. MC-FRET rates describe the incoherent excitation energy transfer from a donor to an acceptor unit. In our case the cylinder plays the role of the donor, while the baseplate is the acceptor unit. As already demonstrated in section B.3 of the Appendix B, the MC-FRET rate $K_{C,B}$ is strictly related to the Förster rates computed between all the possible pairs of eigenstates of cylinder and baseplate, weighted on the Boltzmann factor for the donor unit (the cylinder). Förster rates given in Eq. (7.14) depends on the squared coupling strength between the TDMs associated to the eigenstates of the donor and acceptor units. In Fig. (7.9) the MC-FRET rates $K_{m,BPL} = \sum_{n \in BPL} p_m K_{nm}$ between each eigenstate of the cylinder, indicated by the index m, and all the eigenstates of the baseplate is shown for MT, PD and RD models (panels (A-C)) as a function of the dipole strength and the eigenvalues of the cylinder (see Eq. (B.13) in section B.3 of the Appendix B). The most relevant terms that mainly contribute to the MC-FRET rate $K_{C,B} = \sum_{m \in C} K_{m,BPL}$ arise from eigenstates in the energy window between the lowest eigenvalue of the cylinder E_1 and $E_1 + k_B T$ ($T = 300$ K), as dictated by the Boltzmann factor shown in Eq. (7.18), see the gray window in panels (A-C) between the two dashed lines. Panel A shows that for the MT model the states with the largest MC-FRET rate lie in the lowest part of the spectrum within the gray area. These states dominate the total rate $K_{C,B}$, resulting in an overall fast MC-FRET from the cylinder to the baseplate. Note that not only some superradiant states have a large MC-FRET but also some subradiant states. Indeed for such closeby aggregates it is not the dipole moment of the eigenstates which determined the efficiency of the energy transfer. On the other hand, for the PD model (see panel B) the eigenstates with the highest MC-FRET are far from the gray area. As a consequence, for the PD model MC-FRET is significantly lower than in the MT model. Note that for the PD model the $K_{m,BPL}$ rates are three orders of magnitude lower than the ones found for the MT model. Finally for the RD model (panel C) a few eigenstates included in the gray area can still show $K_{m,BPL}$ rate comparable to those ones found for the MT model, however the trapped current and the efficiency are worse (see panels (A-B) in Fig. (7.8)).

7.4.3 How static disorder affects exciton energy transfer

Considering the effect of disorder to model the environment is an important issue in light-harvesting complexes. Here we propose a more realistic study of the energy transfer in the single cylindrical aggregates (MT, PD and RD) by adding static disorder. Static disorder is modeled as space-dependent and time-independent fluctuations of the site energies, keeping the couplings between the molecules constant. This approach has been widely used in literature [13, 14, 18, 26, 102, 139]. The fluctuations which occur on a time scale much larger than the time scale of the dynamics are usually described as static disorder. Specifically, we consider energy fluctuations that are uniformly distributed around the excitation energy of the molecules e_0, between $e_0 - W/2$ and $e_0 + W/2$, where W represents the disorder strength . In this study the trapped current and internal efficiency are computed as a function of static disorder for the three single cylindrical aggregates (MT-PD-RD models) by solving the rate equations given in Eq. (7.19) and assuming thermal equilibrium within each aggregate, see Fig. (7.10). Static disorder affects both BChl *a* in the baseplate and BChl *c* in the cylindrical aggregates and the values of current and internal efficiency have been computed averaging over 100 realizations of static disorder for MT and PD models and 10 realizations of disorder and random orientations of TDMs for the RD model respectively. Fig. (7.10) shows the trapped current (panel A) and internal efficiency (panel B) as a function of the disorder strength for the single cylinder models (MT, PD and RD) comprising 6000 BChl *c* coupled to a dimeric baseplate with 2184 BChl *a*. The main results found in Fig. (7.10) demonstrate that all the models (MT,PD and RD) are robust to static disorder, showing constant values of both trapped current and internal efficiency up to a disorder strength W close to 10^3 cm^{-1}. For larger values of W both figures of merit in MT and RD models start to drop, while for the PD model they increase, reaching a common value for all the models. The yellow window between the two black dashed lines represents the realistic values of static disorder found in the literature [18, 25, 37, 107, 140] for GSB light-harvesting complexes ((1014 cm^{-1} $< W <$ 1368 cm^{-1})).

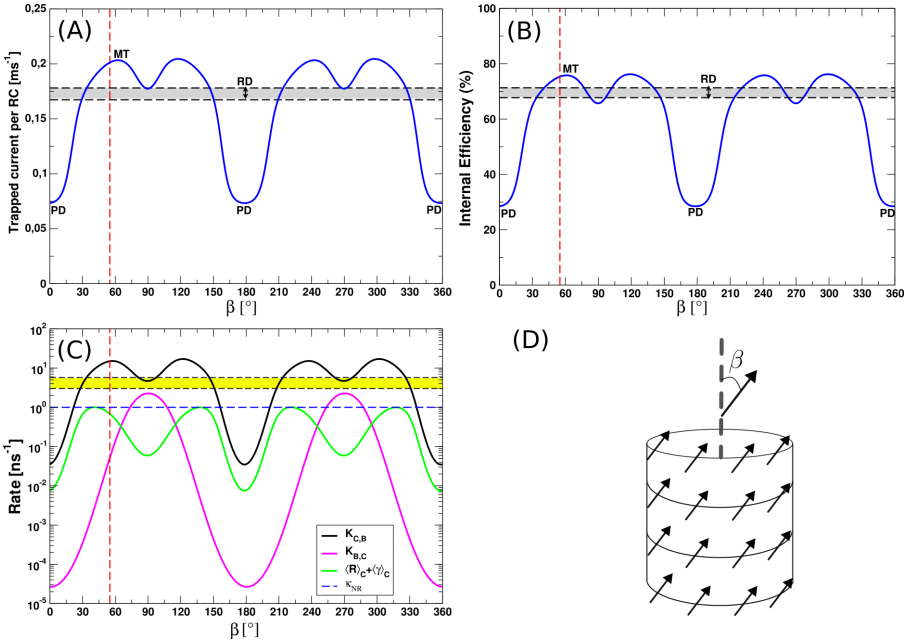

Figure 7.8: *Study of the relationship between trapped current and internal efficiency in single-wall aggregates and the orientation of TDMs.* Panels (A-B) show the trapped current and the internal efficiency as a function of the β angle of each TDM and the main axis of the cylindrical aggregate. Each model contains 6000 BChl *c* molecules in the cylinder and 2184 BChl *a* molecules in the baseplate. The results have been obtained by assuming thermalization inside each aggregate, see Eqs. (7.22) and (7.23). The red dashed line represents $\beta = 55°$, the typical angle found for the MT model. The gray window between the two black dashed lines represents the interval for the trapped current and efficiency computed for the RD model and averaging over 10 realizations for random dipole orientations. The two black dashed lines in panels (A-B) represent the average value of trapped current and internal efficiency ± one standard deviation. Panel (C): the rates used in Eq. (7.19) have been shown as a function of β angle. The black and magenta curves are the MC-FRET rates from cylinder to baseplate and viceversa, respectively. The green curve is the radiative decay rate from the cylinder, accounting for both fluorescence and stimulated emission due to sunlight. The blue dashed line represents the non-radiative decay rate κ_{NR}. Finally the yellow window between the black dashed lines represents the average trapping rate from baseplate to RCs $\kappa = 0.138 \cdot k_{FMO}$ that ranges from $\sim 3.17 - 6$ ns^{-1}. Panel (D): the orientation of the TDMs in a cylindrical structure is represented. β is the angle between each TDM and the main axis of the cylinder. The positions of the TDM are the same used for the MT model, but we vary continuously the β angle and we keep α, the alternating angle of each dipole with respect to the tangent plane of the cylinder, equal to zero, see Ref. [13] for more details about the geometry.

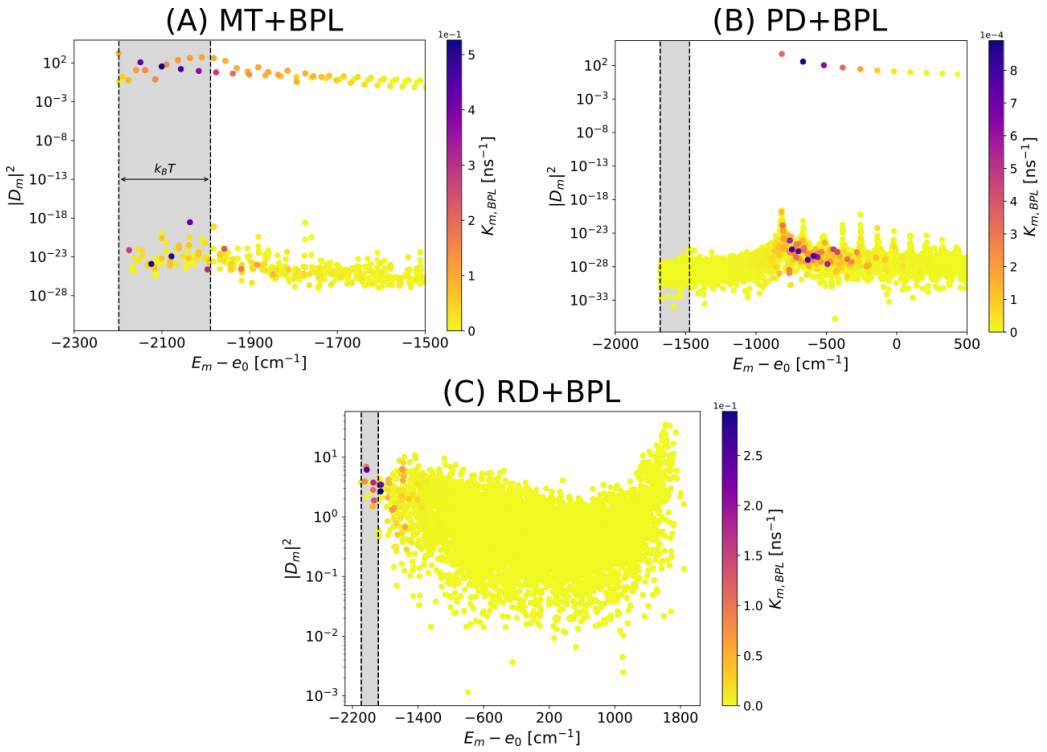

Figure 7.9: *Transfer rates $K_{m,BPL}$ between each eigenstate of the cylindrical models and baseplate.* Panels (A-C): transfer rates computed between each single eigenstate of the cylinder and all the eigenstates of the baseplate for MT and PD and RD models coupled to a dimeric baseplate. The rates $K_{m,BPL} = \sum_{n \in BPL} p_m K_{nm}$ are represented as a function of the dipole strength $|D_m|^2$ and the eigenvalues $E_m - e_0$ of the cylinder (see Eq. (B.13) in section B.3 of the Appendix B). Note that the dipole strength has been represented in logarithmic scale. The system contains 6000 BChl *c* molecules in the cylinder and 2184 BChl *a* molecules in the baseplate. The indices m and n refers to the eigenstates of the cylinder and baseplate respectively, while e_0 is the excitation energy of BChl *c*. The gray area between the two dashed lines represents the energy region between the lowest eigenvalue E_1 of the cylinder and $E_1 + k_BT$ computed at room temperature ($T = 300$ K). Panels (A-B): $K_{m,BPL}$ rates for MT and PD models, respectively. In these cases only the lowest portion of the spectrum, where the SRSs and the most relevant rates are present, is represented. Here the maximal dipole strength reaches 1760 and 2638 for MT and PD, respectively. Panel (C): $K_{m,BPL}$ rates for a single realization of random dipoles. In this case the whole spectrum has been represented. For RD model the maximal value of the dipole strength is about ~ 50.

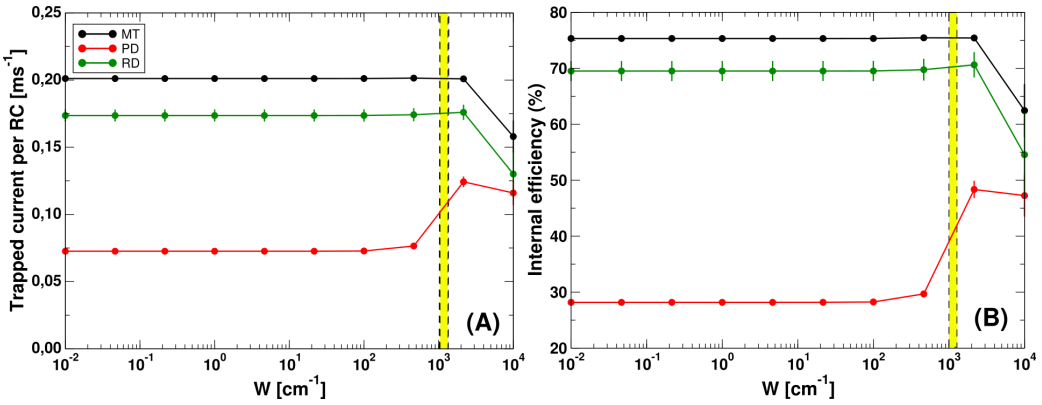

Figure 7.10: *Static disorder in single cylindrical complexes coupled to a dimeric baseplate: trapped current and internal efficiency.* Panels (A-B): trapped current per RC and internal efficiency as a function of static disorder strength W for all the single cylinder models MT, PD and RD comprising 6000 BChl *c* coupled to a dimeric baseplate with 2184 BChl *a*. In all panels all the simulations have been run by assuming thermalization inside each aggregate. Eq. (7.22) and (7.23) in the main text have been used to compute respectively the trapped current per RC and the internal efficiency. Numerical results have been obtained by averaging over 100 realizations for MT and PD models, while for the RD model 10×10 realizations have been done by changing both the randomness and the disorder strength. The yellow window between the two dashed vertical lines represent the typical disorder strength found in literature for GSB light-harvesting systems ($1014\ \text{cm}^{-1} < W < 1368\ \text{cm}^{-1}$) [18, 25, 37, 107, 140].

7.5 Conclusions

In this chapter we have studied the excitation energy transfer process in the entire light-harvesting apparatus of GSB, comprising more that 100000 BChl molecules distributed in the chlorosome and in the baseplate, from solar light absorption to the trapping of excitation in the RCs. Sunlight is modeled through its black body spectrum, taking into account the Earth-Sun distance. Also the coupling to room temperature thermal bath in presence of static disorder has been taken into account. We have developed three rate equations approaches in order to describe the process of the energy transfer: full rate equations model, with the highest computational costs, partially thermalized and fully thermalized models. The partially thermalized model requires less numerical efforts and it gives results in agreement with the full rate equation approach.

The chlorosome has been modeled as three adjacent concentric cylindrical aggregates coupled to a dimeric baseplate. The trapped current per RC and the internal efficiency have been chosen as the two main figures of merit and we have demonstrated that for the chlorosome coupled to the dimeric baseplate the trapped current matches the RC closure rate, while the internal efficiency is about $\sim 80\%$. In order to investigate the high efficiency of natural systems, we have considered smaller systems composed of a single wall cylindrical aggregate coupled to a baseplate: the MT model, used to build up the entire chlorosome, and other mathematical models, obtained by changing the β angle of each TDM with respect to the main axis of the cylinder. In particular we focused our study on two mathematical models: the RD model, where all the TDMs have random orientation in the space, and the PD model, where all the TDMs are parallel to the cylinder axis ($\beta = 0°$). The main foundings presented in this paper confirm that natural models show the largest values of trapped current and internal efficiency and their behavior is strictly related to their geometry. In fact, natural models (single cylinder MT model and the entire chlorosome coupled to the dimeric baseplate) are characterized by the typical orientation of their TDMs with respect to the cylinder axis ($\beta = 55°$), that ensures a fast MC-FRET from the cylinder to the baseplate, faster than all the other radiative and non-radiative processes. Our results demonstrate the non trivial interplay of geometry and functionality in realistic light-harvesting systems, showing that the specific symmetry present in natural complexes is optimal for energy

transfer. Proving the sensibility of energy transfer on the specific dipole disposition and orientation, our analysis will inspire the design of artificial light-harvesting systems.

Chapter 8

Modeling the excitation dynamics in isolated chromatophores of *Rhodobacter sphaeroides*

Following the results presented in the previous chapter, here a different approach has been developed in order to provide a possible explanation of the excitation energy transfer even in Purple bacteria light-harvesting complexes. The entire dynamics of the excitation, from sunlight absorption in BChl molecules to charge separation in the RC, has been modeled using the network-based theory, a powerful tool for addressing the main topic of this thesis: finding a possible explanation of the relationship between geometry and functionality. This study not only provides a deep insight into the exciton dynamics of PB antennae from a new point of view, but it also drives a novel proposal for achieving lasing under natural sunlight fully exploiting the capability of natural antennae to light-harvest and funnel the incoming solar radiation within the framework of the APACE project. Hence, in this chapter, we are going to characterize the properties of the natural chromatophore of Rhodobacter sphaeroides as a function of two parameters: first the solar irradiance, and second the rate at which reaction centers re-open. The characterization consists in the evaluation of four properties of the chromatophore: the charge separation quantum yield (number of charge separation per photons absorbed), the fluorescence quantum yield (number of fluorescence emissions per

photons absorbed), the proportion of open and closed RC and the factor by which the antenna increases the rate of excitation of the reaction centers (enhancement factor). This predictions will be carried out using two distinct models: a stochastic model providing an exact solution to the master equation of the system using the Gillespie algorithm and a deterministic model relying on mean-field approaches and rate-equations.

8.1 Biological background

8.1.1 Basic principles of reaction center structure and function

The initial stage of photosynthesis starts with the interception of sunlight photons by photosynthetic pigments, mainly chlorophyll. The initial excitation is transferred to a special chlorophyll pair, which then undergo charge separation, giving its electron to a Quinone, driving the quinone cycle producing the proton gradient responsible for the production of adenosine triphosphate (ATP) by ATP synthases.

In the photosynthetic purple bacteria *Rhodobacter sphaeroides*, the organelle responsible for this part of the photosynthetic function is a network of interconnected vesicles called chromatophores. Chromatophore vesicles are composed of a phospholipid bilayer membrane packed with transmembrane protein complexes. The interior of the vesicle correspond to the periplasm of the bacteria, and the exterior, to the cytoplasm. The integral protein complexes present in the chromatophore belong to one of the 5 following types.

- **Reaction centers (RC)**, which are protein complexes containing the special pair of bacteriochlorophyll(BChl) A molecules in which the charge separation happens, driving the quinone cycle.
- **Light-harvesting 2 (LH2) antenna complexes**, which are the main component of the membrane, whose role is to capture light through photosynthetic pigments, BChls *a* and carotenoids.
- **Light-harvesting 1 (LH1) antenna complexes**, special antenna complexes surrounding the RC. Beside performing the same function

as LH2 complexes, they also channel excitation captured by LH2 to the RC.

- **Cytochrome $\mathbf{bc_1}$ complexes**, another type of protein complexes involved in the generation of the proton gradient.
- **ATP synthases**, the protein complexes responsible for the production of ATP.

Typically, an incident photon is absorbed by a BChl molecule within one of the many LH2 complexes of the chromatophore, and the resulting excitation is coherently shared among its BChl a molecules in the form of an exciton. The exciton is transferred to a neighbor antenna complex by incoherent multi-chromophoric transfer rate and eventually reaches a LH1 antenna which in turn transfers the excitation to the RC. In the RC, the excitation reaches the reduced special BChl pair ($P \rightarrow P^*$), which can then transfer one electron to a downstream acceptor ($P^*A \rightarrow P^+A^-$): this process is known as charge separation. The electron transfer chain is composed of a specific sequence of successive acceptors: a BChl molecule, bacteriopheophytin, a static quinone referred to as Q_A and a dynamic quinone referred to as Q_B [19]. Acceptors can accept one electron at a time, except of Q_B which can accept two. Each time Q_B accepts an electron, it also binds a proton from the cytoplasm

$$Q_B \xrightarrow{e^-} Q_B^- \xrightarrow{H^+_{cyto}} Q_BH \xrightarrow{e^-} Q_B^-H \xrightarrow{H^+_{cyto}} Q_BH_2 \ . \tag{8.1}$$

Once the special pair has lost its electron (P^+), it can no longer be excited or undergo charge separation (it cannot lose another electron). The reaction center with this oxidized special pair is referred to as closed RC, as opposed with the open RC where P is reduced. This distinction is very important as both states have different properties: closed RCs cannot undergo charge separation and have different absorption, dissipation and electron transfer dynamics. To go back from closed to open, the special pair must receive an electron form a protein called cytochrome c, a soluble electron carrier. The reduced cytochrome first binds the RC, then transfer its electron to the special pair [42]

$$c^-P^+ \rightarrow cP \ . \tag{8.2}$$

The RC is then back to its open state.

8.1.2 The quinone cycle

Incident sunlight photons (ν) captured by antenna complexes drive the production of ATP through a photochemical process called the quinone cycle.

Two successive charge separation events allow for the double reduction of a quinone (Q) into quinol (QH_2) and the uptake of two protons from the cytoplasm. Each time, the special pair gets back its electron from a soluble cytochrome c

$$2\nu + Q + 2H^+_{cyto} + 2c^- \xrightarrow{\text{RC}} QH_2 + 2c \ . \tag{8.3}$$

The cytochrome bc_1 complex then transfers back the electrons from the quinol to two soluble cytochrome c. This process is accompanied by the uptake of two more protons from the cytoplasm and the release of four protons into the periplasm

$$QH_2 + 2H^+_{cyto} + 2c \xrightarrow{\text{cyt bc}_1\text{ complex}} Q + 4H^+_{peri} + 2c^- \ . \tag{8.4}$$

The 4 periplasmic protons are eventually translocated to the cytoplasm through the ATP synthase, driving the production of 1 ATP molecule from 1 ADP and one inorganic phosphate (P_i)

$$ADP + P_i + 4H^+_{peri} \xrightarrow{\text{ATP synthase}} ATP + 4H^+_{cyto} \ , \tag{8.5}$$

which completes the quinone cycle.

8.1.3 Motivation for a new model

Why should we model the excitation dynamics of a chromatophore? *Rhodobacter sphaeroides* is a model organism whose photosynthetic apparatus, the spherical vesicular chromatophore, have been extensively studied and characterized in the literature, see Refs. [141–143], and also in this thesis, see Chapt. 2. While such works usually focus on the fundamental properties of the biological system, our hope here is to build a model which would give us insights on how we can use chromatophore for bioengineering applications. One case for such application is the use of the chromatophore as a photon antenna concentrating light for lasing applications, in the scope of the APACE project.

To this end, we are interested in the ability of the chromatophore to efficiently gather and concentrate solar energy. When a photon is absorbed by the chromatophore, the excitation can follow different pathways: it can be lost through radiative or non-radiative decay, or it can be funneled to other complexes before such losses occur. The efficiency of the chromatophore it is related to the charge separation quantum yield η_{cs},which represents the proportion of absorbed photons which end up triggering charge separation, and to the fluorescence quantum yield η_f, which is the probability that an absorbed photon triggers fluorescence. Another interesting quantity is the enhancement factor of excitations at the RC, representing how much the antenna system contributes to the excitation of the RC. It is defined as the ratio between the total RC excitation frequency within the antenna and the RC excitation solely from direct absorption.

Since the properties of the chromatophore strictly depends on the state of its RCs (open or closed), here we want to predict the proportion of open and closed RC, depending on the conditions (solar irradiance and RC closure time) to which the chromatophore is exposed.

8.2 Detailed Kinetic model for the natural chromatophore

The natural chromatophore is modeled as a graph where each node corresponds to a LH2 antenna complex (LH2), a LH1 antenna complex (LH1) or a reaction center (RC) and edges associate only nearest-neighbor nodes, see Fig. (8.1) panel (A). The structure of the graph is based on the chromatophore structure determined by Valzelli et al. [14], form which we determine node positions from the center of mass of the BChl molecules arrangements, and define edges between nearest-neighbor nodes.

Nodes are modeled as two level systems being either in a basal or excited state, see Fig. (8.1) panels (B-C). Any node i can receive excitation by absorbing an incident photon from sunlight with a rate k_{ai} proportional to the solar irradiance Φ as

$$k_{ai}(\Phi) = \Phi \beta N_{BChl,i} \ , \tag{8.6}$$

where $\beta = 1.25 \times 10^{-11}$ ps^{-1} is the rate at which a single BChl molecule absorbs under natural sunlight (1 sun), see Refs. [19, 43] and calculations

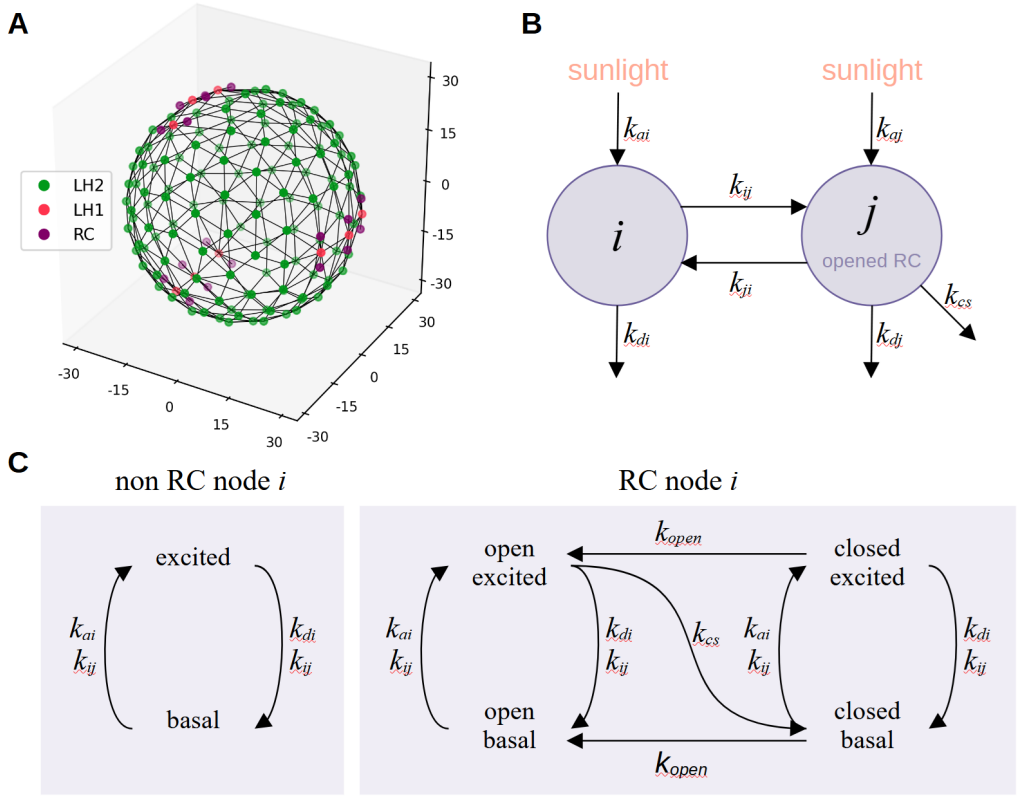

Figure 8.1: *Excitation dynamics on the natural chromatophore of R. sphaeroides.* Panel (A): graph of natural chromatophore antenna complexes and RC based on Ref. [14]. Each node represents an aggregate of BChl *a* molecules. Green dots indicate LH2 complexes, red dots represent s-shaped LH1 complexes, and purple dots correspond to the RCs. Nodes are placed in the center of mass of each aggregate. Panel (B): excitation dynamics between two nearest-neighbor nodes i and j, where node j is an open RC. As explained in in the main text, k_{ai} and k_{aj} are the absorption rates from sunlight, k_{di} and k_{dj} are dissipation rates, k_{ij} and k_{ji} are excitation transfer rates, and k_{cs} is the charge separation rate. Panel (C): two-level excitation dynamics for RC and non RC nodes.

Node type	k_a (ps^{-1})	k_d (ps^{-1})	p_f
LH2	3.375×10^{-10}	0.00101	0.0986
LH1	7.0×10^{-10}	0.00146	0.0814
RC (open)	5.0×10^{-11}	0.000335	0.18
RC (closed)	5.0×10^{-11}	(1/30)	0.00181

Table 8.1: *Absorption and dissipation rates and fluorescence probabilities for each type of node.* The absorption rates under 1 sun k_a are determined according to Eq. (8.6) and assuming 56 BChls for s-shaped LH1 [27], 27 Bchls for LH2 [144] and 4 and 2 Bchl per RC in the open and closed state respectively [145]. For the dissipation rates k_d, accounting for both radiative and non-radiative dissipation, as well as for the probability of fluorescence in LH2, LH1 and open RC, we use the values from Monshouwer et al. [10]. For the closed RC, we use the dissipation rate from Ref. [143], assuming the same radiative rate of the open RC.

direction	rate	note
LH2→LH2	(1/10) ps^{-1}	[146]
LH2→LH1	(1/10) ps^{-1}	s-shaped [27]
LH1→LH2	(1/50) ps^{-1}	s-shaped (*)
LH1→LH1	(1/20) ps^{-1}	closed ring [146]
LH1→RC (open)	(1/20) ps^{-1}	s-shaped [27]
LH1→RC (closed)	(1/200) ps^{-1}	s-shaped (**)
RC (open) →LH1	(1/8) ps^{-1}	s-shaped [27]
RC (closed) →LH1	(1/10) ps^{-1}	s-shaped (**)

Table 8.2: *Excitation transfer rates.* Multi-chromophoric transfer rates between LH2, LH1, and RC complexes. Columns indicate, respectively: (1) direction of the exciton flow; (2) corresponding transfer rate; (3) LH1 type (s-shaped or closed-ring) and literature sources. All the rates, but not the ones indicated by the symbols (*) and (**), have been taken from the literature, as indicated in the third column. The transfer rate from LH1 to LH2, see (*) has been computed by generalized MC-FRET approach already shown in Eq. (7.18) of Chapter 7, assuming thermalization in each aggregate and detailed balance. Bloch-Redfield approach has been used to compute the transfer rates between closed RC and LH1, finding good agreement with the data present in the literature [147], see (**).

in section 5.2.2 in Chapt. 5, and $N_{BChl,i}$ the number of BChl molecules in the node i, which depend on the type of node, see values reported in Tab. (8.1). The excitation in the node i can be lost by dissipation at a rate k_d, with a certain probability p_{fi} of being radiative (fluorescence), depending on the node type, or transferred to a non-excited neighbor node j with a rate k_{ij}, which depend on the donor and acceptor node types, see Tab. (8.2). Excited RC nodes can additionally undergo charge separation, losing their excitation in the process with a rate $k_{cs} = 1/3$ ps^{-1} [27]. Upon charge separation, a RC switches from an opened to a closed conformation, where charge separation is impossible due to the oxidation of the special pair. After some time, the special pair receives an electron from a reduced cytochrome and switches back to open state, with a rate k_{open}. The reopening of RC after charge separation requires a full turn of the photosynthetic quinone cycle. We will use $k_{open} = 1$ ms^{-1} from Ref. [143].

8.2.1 Observables of the model

The behavior of the chromatophore under specific conditions is a direct consequence of the open/closed state of its reaction centers, which influence the kinetics of sunlight absorption, excitation transfer, dissipation and charge separation. Thus, a key output of our model will be the number of closed reaction center per chromatophore N_{closed}.

Two other outputs will be the charge separation and fluorescence quantum yields, η_{cs} and η_f, which correspond to the probabilities that a photon absorbed on the chromatophore ends up driving charge separation at a reaction center or dissipated as fluorescence, respectively. The charge separation quantum yield directly measures the photosynthetic efficiency of the system, while the fluorescence quantum yield corresponds to a typical experimental observable and serves as a useful benchmark for model validation.

The last output of the model is the RC excitation enhancement factor F_{rc}, the factor by which the antenna complexes increases the rate of excitation of the reaction centers. It can be defined as the ratio of the total rate of excitation of the RC and the rate of direct photon absorption by the RC. This quantity measures the contribution of antenna complexes to the efficiency of the system, which is particularly relevant in an engineering context.

8.3 Exact stochastic simulations

Let us define x the excitation state of the whole chromatophore, where x_i is the excitation state of the node i. Since we consider a two level system, we have

$$x_i = \begin{cases} 1 & \text{if node } i \text{ is excited} \\ 0 & \text{if it is in the ground state.} \end{cases} \tag{8.7}$$

The open/closed state of each node of the chromatophore is represented in a vector ω where

$$\omega_i = \begin{cases} 1 & \text{if node } i \text{ is an open RC} \\ 0 & \text{otherwise (closed or not a RC).} \end{cases} \tag{8.8}$$

Now, we can define each state as a function of ω and Φ, as absorption, dissipation and excitation transfer events involving RC nodes have rates which depend on whether the it is open or closed: $k_{ai}(\Phi, \omega_i)$, $k_{di}(\omega_i)$ and $k_{ij}(\omega_i, \omega_j)$. Let us consider an initial state where all the system is in the ground state and all RC are open (i.e. a chromatophore in dark conditions). Now we want to simulate the evolution of this system in time according to the kinetic parameters defined in the previous section. This can be achieved using the Gillespie algorithm [148], which allow to generate one possible trajectory of the system according to its master equation, one reaction at a time. At each iteration, we determine which reaction must happen next as well as the associated time step. First we need to determine the propensities a_μ associated with each possible event μ. For absorption, dissipation, charge separation, excitation transfer and RC re-opening, respectively, propensities are defined as

$$a_{ai} = (1 - x_i) k_{ai}(\Phi, \omega_i) \ , \tag{8.9a}$$

$$a_{di} = x_i k_{di}(\omega_i) \ , \tag{8.9b}$$

$$a_{cs,i} = x_i \omega_i k_{cs} \ , \tag{8.9c}$$

$$a_{ij} = x_i (1 - x_j) k_{ij}(\omega_i, \omega_j) \ , \tag{8.9d}$$

$$a_{\text{open}} = (1 - \omega_i) k_{\text{open}} \ . \tag{8.9e}$$

Given the sum of all propensities

$$a_{\text{tot}} = \sum_\mu a \ , \tag{8.10}$$

we define the probability to chose a given reaction μ as

$$P(\mu) = \frac{a_\mu}{a_{\text{tot}}} \tag{8.11}$$

and draw the time step τ according to an exponential distribution

$$\tau \sim \text{Exp}\left(\frac{1}{a_{\text{tot}}}\right) \ , \tag{8.12}$$

as we assume reaction are poissonian events.

During a simulation, the total number of events occurring in the chromatophore in the $[0, t]$ time interval is determined. Specifically, one obtains

- the total number of photon absorbed by the chromatophore $N_a(t)$,
- the total number of charge separation events $N_{cs}(t)$,
- the total number of fluorescence emission events $N_f(t)$, which is obtained from the total number of dissipation events in each type of node multiplied by the corresponding fluorescence probability, given in Tab. (8.1),
- the total number of excitations received by the RC $N_{t,RC}(t)$, and the total number of photons absorbed by the RC $N_{a,RC}(t)$.

From these event counts, one can estimate the steady state value for three of the four observables of the model (charge separation quantum yield η_{cs}, fluorescence quantum yield η_f and excitation enhancement factor F_{rc}) by using a value of t large enough:

$$\eta_{cs} = \lim_{t\to\infty} \frac{N_{cs}(t)}{N_a(t)} \ , \tag{8.13a}$$

$$\eta_f = \lim_{t\to\infty} \frac{N_f(t)}{N_a(t)} \ , \tag{8.13b}$$

$$F_{rc} = \lim_{t\to\infty} \frac{N_{t,RC}(t)}{N_{a,RC}(t)} \ . \tag{8.13c}$$

$$\tag{8.13d}$$

By keeping track, at each RC opening and closure events μ on the $[0, t]$ interval, of the number of closed RC $N_{closed}(\mu)$ and time elapsed since the

last opening/closing event (or simulation start) τ_μ, one also estimate the average and standard error of the number of closed RC at steady sate

$$\langle N_{closed} \rangle = \frac{\sum_\mu \tau_\mu N_{closed}(\mu)}{\sum_\mu \tau_\mu} \ , \tag{8.14a}$$

$$\sigma_{N_{closed}} = \sqrt{\frac{\sum_\mu \tau_\mu \left(N_{closed}(\mu) - \langle N_{closed} \rangle \right)^2}{\sum_\mu \tau_\mu}} \ . \tag{8.14b}$$

8.4 Deterministic rate-equation approximation

8.4.1 Excitation diffusion on a chromatophore with fixed open/closed RC

Let us consider a chromatophore where the state of reaction centers is fixed. Open RCs stay open and closed RCs stay closed. On such a system, assuming there is at most a single excitation on the chromatophore at any time, we can actually model excitation transfer as a continuous diffusive process. Considering the excitation sources (absorption) and sinks (dissipation and charge separation) in each node, we can model the whole process as a linear reaction-diffusion system. Once more, we have $x = (x_0, \ldots, x_{n-1})$ be the excitation state of the chromatophore, except this time x_i is the excitation density in the node i. The dynamics of x, for a given solar irradiance Φ and fixed RCs configuration ω can be described with a set of rate equations as

$$\begin{aligned} \frac{dx_i(\Phi,\omega)}{dt} =& k_{ai}(\Phi,\omega_i) - (k_{di}(\omega_i) + \omega_i k_{cs}) x_i \\ &+ sum_{j \in \mathcal{N}(i)} k_{ji}(\omega_i,\omega_j) x_j - k_{ij}(\omega_i,\omega_j) x_i \ , \end{aligned} \tag{8.15}$$

where $\mathcal{N}(i)$ is the set of nearest-neighbors of node i. By solving $dx/dt = 0$, we obtain x^s, the steady state value of x.

From this steady state of density of excitation, all the global event currents for the corresponding fixed chromatophore can be derived. Let an event μ (i.e. absorption, charge separation, fluorescence, ...), its steady state global current in a chromatophore with a fixed open/closed configuration ω under solar irradiance Φ is termed $I_\mu^{\text{fixed}}(\Phi,\omega)$. Typically, such currents do not depend on the exact configuration of ω but rather on the number of closed RC $N_{closed} = ||\omega||^2$. Additionally, for a chromatophore with

fixed ω, currents are proportional to the solar irradiance. As a consequence, one can define

$$I_{\mu}^{\text{fixed}}(\Phi, N_{\text{closed}}) = \Phi I_{\mu 0}^{\text{fixed}}(N_{\text{closed}}) \ , \tag{8.16}$$

where $I_{\mu 0}^{\text{fixed}}$ is the corresponding current under natural sunlight (1 sun).

Using this approach, we define the global currents under 1 sun for charge separation (cs), fluorescence (f) and excitation transfer from LH1 to RC (t) from the corresponding steady state of excitation density under 1 sun x^{s0}

$$I_{cs0}^{\text{fixed}}(N_{closed}) \simeq \sum_{i \in \text{RC}} \omega_i k_{cs} x_i^{s0}(\omega) \quad \text{with } ||\omega||^2 = N_{closed} \ , \tag{8.17a}$$

$$I_{f0}^{\text{fixed}}(N_{closed}) \simeq \sum_{i} p_{fi} k_{di}(\omega_i) x_i^{s0}(\omega) \quad \text{with } ||\omega||^2 = N_{closed} \ , \tag{8.17b}$$

$$I_{t0}^{\text{fixed}}(N_{closed}) \simeq \sum_{i \in \text{RC}} \sum_{j \in \mathcal{N}(i)} k_{ji}(\omega_i) x_j^{s0}(\omega) \quad \text{with } ||\omega||^2 = N_{closed} \ , \tag{8.17c}$$

$$\tag{8.17d}$$

as well as global absorption currents for the whole chromatophore (a) and for the RC only (a, rc), which do not depend on the excitation state

$$\begin{aligned} I_{a0}^{\text{fixed}}(N_{closed}) = {} & N_{\text{LH2}} \ k_{a,\text{LH2}}(1 \text{ sun}) \\ & + N_{\text{LH1}} \ k_{a,\text{LH1}}(1 \text{ sun}) \\ & + I_{a,rc0}^{\text{fixed}}(N_{closed}) \ , \end{aligned} \tag{8.18a}$$

$$\begin{aligned} I_{a,rc0}^{\text{fixed}}(N_{closed}) = {} & N_{closed} \ k_{a,\text{RC}_{\text{closed}}}(1 \text{ sun}) \\ & + (N_{\text{RC}} - N_{closed}) \ k_{a,\text{RC}_{\text{open}}}(1 \text{ sun}) \ . \end{aligned} \tag{8.18b}$$

Global currents determined from simulations are only defined for discrete integer values of N_{closed}. For the charge separation current under one sun, a continuous analytical form (required for the next parts of the model) can be approximated using a logarithmic function fit

$$I_{cs0}^{\text{fixed}}(N_{closed}) \simeq a \ln(b(N_{closed} - 18) + 1) \ , \tag{8.19}$$

where a and b are the fit parameters, see Fig. (C.1) in the Appendix C. For other event currents, one can simply rely on linear interpolation

$$\begin{aligned} I_{\mu 0}^{\text{fixed}}(N_{closed}) \simeq {} & I_{\mu 0}^{\text{fixed}}(\lfloor N_{closed} \rfloor) + \\ & \left(I_{\mu 0}^{\text{fixed}}(\lfloor N_{closed} \rfloor + 1) - I_{\mu 0}^{\text{fixed}}(\lfloor N_{closed} \rfloor)\right) \\ & (N_{closed} - \lfloor N_{closed} \rfloor) \, , \end{aligned} \tag{8.20}$$

where $\lfloor N_{closed} \rfloor$ is the floor function that returns the closest integer inferior to the real number N_{closed}.

8.4.2 Dynamics of N_{closed} in a chromatophore with RC opening/closure

Now, let us re-introduce the opening and closing of the RC in the model: the dynamics of opening and closing of RCs for a given solar irradiance Φ is ruled by a simple rate equation

$$\frac{dN_{closed}}{dt}(\Phi) = \Phi I_{cs0}^{\text{fixed}}(N_{closed}) - k_{open} N_{closed} \ . \tag{8.21}$$

Taking advantage of the continuous analytical extrapolation of $I_{cs0}^{\text{fixed}}(N_{closed})$ defined in Eq.(8.19), one can obtain an analytical solution to the steady state value of $N_{closed}(\Phi)$, as

$$N_{closed}(\Phi) = \frac{-ab\Phi W\left(\frac{k_{open} e^{\frac{k_{open}(18b+1)}{ab\Phi}}}{ab\Phi}\right) + k_{open}(18b+1)}{bk_{open}} \ , \tag{8.22}$$

where W is the Lambert W function, and a and b are the fit coefficient of Eq. (8.19).

It is now possible derive the global current of any event μ for this chromatophore with dynamic RC opening/closing as a function of the solar irradiance Φ, as

$$I_{\mu}(\Phi) = \Phi I_{\mu 0}^{\text{fixed}}(N_{\text{closed}}(\Phi)) \ . \tag{8.23}$$

Using these global currents, we can define the three other observables of the model as

$$\eta_{cs}(\Phi) = \frac{I_{cs}(\Phi)}{I_a(\Phi)} \ , \tag{8.24a}$$

$$\eta_{f}(\Phi) = \frac{I_{f}(\Phi)}{I_a(\Phi)} \ , \tag{8.24b}$$

$$F_{rc}(\Phi) = \frac{I_{t,\text{RC}}(\Phi) + I_{a,\text{RC}}(\Phi)}{I_{a,\text{RC}}(\Phi)} \ . \tag{8.24c}$$

8.5 Results and discussions

The chromatophore of *Rhodobacter sphaeroides* has been characterized under increasing values of solar irradiance and closure rate of the RCs, through

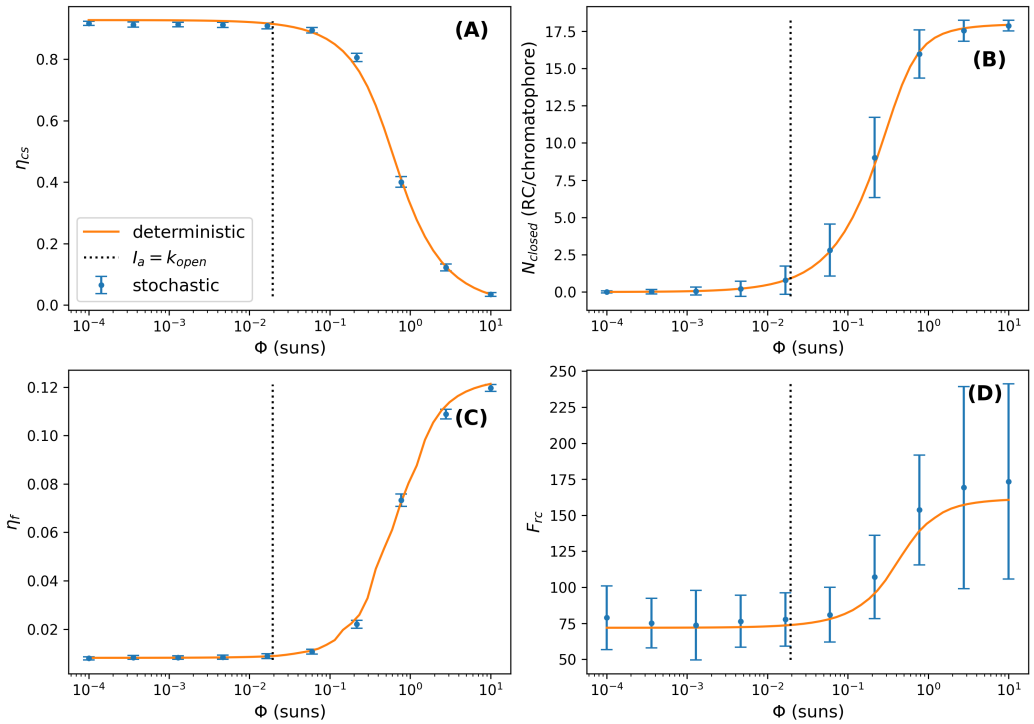

Figure 8.2: *Steady state properties of the natural chromatophore as a function of solar irradiance.* Panel (A): charge separation quantum yield η_{cs}. Panel (B): number of closed RCs N_{closed}. Panel (C): fluorescence quantum yield η_{cs}. Panel (D): RC excitation enhancement factor F_{rc}. Blue points with error bars represent average ± standard error of values computed with the stochastic method described in Sec. 8.3, while plain orange lines are computed with the deterministic model, see Eq. (8.24). For stochastic simulations, results are averaged over 50 simulation repetitions, each ran until 1000 photon absorption events occurred. The vertical dashed line marks the sunlight intensity for which the global rate of photon absorption of the chromatophore matches the rate of RC re-opening.

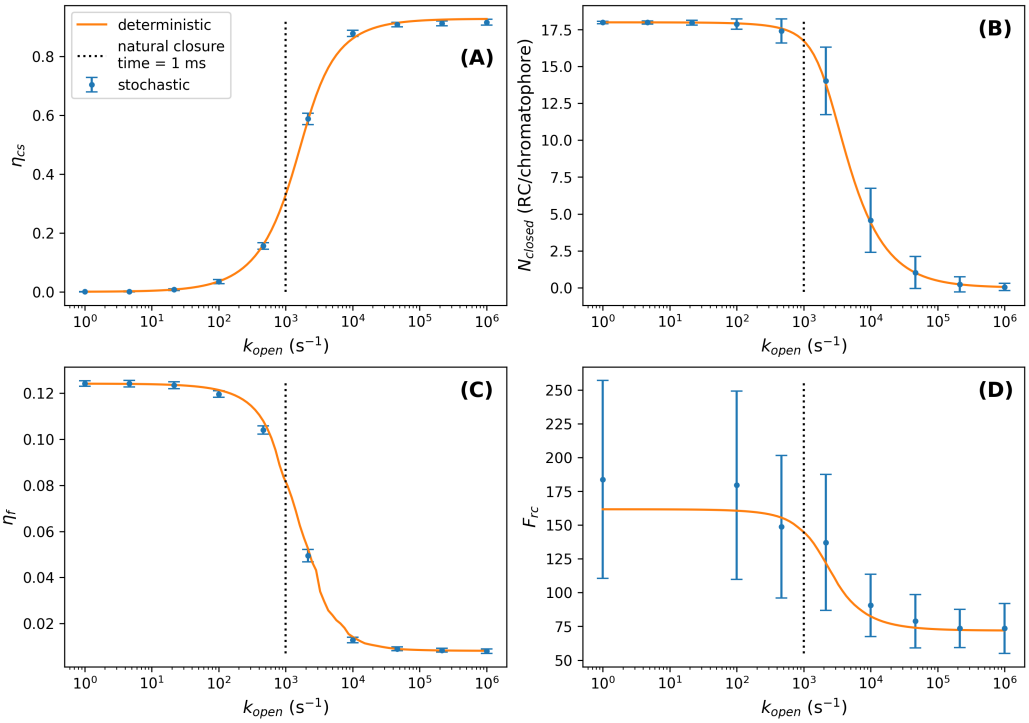

Figure 8.3: *Steady state properties of the natural chromatophore under 1 sun as a function of the RC re-opening rate* k_{open}. Panel (A): charge separation quantum yield η_{cs}. Panel (B): Number of closed RC N_{closed}. Panel (C): fluorescence quantum yield η_{cs}. Panel (D): RC excitation enhancement factor F_{rc}. Blue points with error bars represent average ± standard error of values computed with the stochastic method described in Sec. 8.3, while plain orange lines are computed with the deterministic model, see Eq. (8.24). For stochastic simulations, results are averaged over 50 simulation repetitions, each ran until 1000 photon absorption events occurred. The vertical dashed line marks the natural value of k_{open}.

quantification of the fluorescence and charge separation quantum yields, the quantity of closed RC and the RC excitation enhancement factor, see results in Figs. (8.2) and (8.3). Results were obtained using both the stochastic and deterministic methods, showing good agreement overall, aside from a slight underestimation of the RC excitation enhancement factor. The deterministic model has been parameterized after numerical estimations of the global event rates as functions of the number of closed RC, as showed in Appendix C (Figure C.1).

In Fig. (8.2) steady state values of the fluorescence and charge separation quantum yields, η_{cs} and η_f, the number of closed RC per chromatophore N_{closed} and the RC excitation enhancement factor F_{rc} have been determined as a function of the solar irradiance Φ with both the stochastic and deterministic approaches. As Φ increases, the delay between two subsequent photon absorption events decreases with respect to the RC closure time, causing the average number of closed RC at the steady state to increase from 0 to 18, see panel (B) in Fig. (8.2). As a matter of fact, the number of closed RC starts to increase dramatically after the frequency of photon absorption exceeds the rate of RC reopening (vertical dashed lines). Under low light conditions, when all RC are open, the charge separation quantum yield reached 0.927, a high value which is comparable to the one determined by Sener et al. [141]. This value drops down to 0 as solar irradiance increases, due to RC being closed, see panel (A) in Fig. (8.2). The fluorescence quantum yield, however, increases from 0.0082 to 0.12 with solar irradiance, see panel (C) in Fig. (8.2). Since closed RC does no undergo charge separation, the excitation has higher chanced to exit the RC and end up being dissipated under higher illumination conditions. It should also be noted that the profile of the fluorescence quantum yield as a function of the proportion of closed RC (see Fig. (C.2) in Appendix C) obtained with the model shows a qualitatively similar trend to the one measured experimentally by Comayras et al. [142].

Regarding the contribution of the antenna complexes to photosynthetic process, panel D of Fig. (8.2) shows that under low light conditions, LH1 and LH2 increase the number of excitations reaching the RC by a factor of 71.9. This factor increases with solar irradiance, which can be explained by the higher frequency of excitation transfer between LH1 and the RC in the closed state caused by the absence of charge separation. This is consistent with the increased lifetime of the excitation on the chromatophore reported by Fassioli et al. [143].

In a context of engineering, one might be interesting in changing the photochemical properties of the chromatophore. One way to achieve this is to use compounds which blocks the Quinone cycle: inhibitors. Depending on where this inhibition takes place, one might expect either an under-production of reduced cytochrome, causing the RC closure time to increase, or an accumulation of electrons in the RCs, which could shorten the closure time. To better understand the possible effects of inhibition, we thus studied the properties of the chromatophore, η_{cs}, η_f, N_{closed} and F_{rc} as a function of the RC re-opening rate k_{open} (inverse of the closure time), under a solar irradiance on 1 sun, see Fig. (8.3). The higher k_{open} is, the faster closed RC re-open, the higher is the proportion of open RC, the higher the charge separation quantum yield is, see panels (A-B) in Fig. (8.3). Naturally, it is the opposite for the fluorescence quantum yield, which decrease as k_{open} increases, due to open RC consuming the excitations in the charge separation process, see panel (C) in Fig. (8.3). Same goes for the RC excitation enhancement factor which decreases with increasing k_{open}, see panel (D) in Fig. (8.3), probably due to the higher lifetime of the excitation on the chromatophore when RC are closed, according to Ref. [143]. Overall, k_{open} and solar irradiance have antagonistic effects on the system.

8.6 Conclusions and future perspectives

So far, our results show good agreement with the literature. We successfully predicted the characteristically high charge separation quantum yield of the chromatophore under low light. Our predictions regarding fluorescence quantum yield are also consistent with previous works. We additionally characterized the effect of the closure time on the system, which is an important parameters in the engineering context as it could be fine-tuned for specific applications using inhibition.

Of coursed, there is still room for a wide range of future developments and improvements for the model. Implementing long range excitation transfer in the model, instead of the fixed nearest neighbor cutoff based interaction which is considered at the moment, should allow for a more precise and realistic evaluation of the four observables of the model, and would thus be one of the principal improvements. Besides, for now, we only consider solar irradiance as light source input parameter. In the future, we will extend this study using also artificial light sources in order to have a model more

easily comparable to experimental data. Also, here, we only consider a single chromatophore structure. It might be interesting in the future to investigate different chromatophore geometries (e.g. changing the ratio of LH2/LH1). Finally, inhibition can be used to alter some properties of the chromatophore, which is a key aspect in engineering this system. Specifically, inhibition of the quinone cycle, typically targeting the RC or the cytochrome bc_1 complex, might impact the RC closure time of the reaction center which, as we have seen, is determined by the global excitation transfer properties. Future developments of the model will thus include the detailed modeling of the quinone cycle in order to predict the exact closure time as a function of light intensity, inhibitor type and concentration, and other parameters.

Chapter 9

Conclusions

In this thesis we have analyzed how the architecture of a complex system made of a huge number of constituents can affect its functionality. In particular, in our study we focused on the light-harvesting systems found in GSB and PB antennae, which are among the most efficient aggregates of BChl molecules capable of performing photosynthesis with high internal efficiency even under low light conditions. In the literature there is evidence that their behavior is strictly related to the geometry of the BChl molecules in the antenna complexes, in particular the position and the TDM orientation. This relationship remains an open question in the field of quantum biology. Therefore, motivated by previous findings, this thesis aimed to provide a possible explanation for this phenomenon.

In this work we demonstrated that the high internal efficiency found in GSB and PB complexes arises from the emergence of cooperative behaviors. In particular, we investigated the coherent emission of radiation from PB and GSB antenna complexes, under the assumption that a single photon has already been absorbed by a single BChl molecule. Our findings showed that such systems can support a few red-shifted eigenstates characterized by a fast radiative decay rate (superradiant), which is enhanced with respect to that of a single emitter. This phenomenon, also called 'single-photon superadiance', has been investigated by using a non-hermitian Hamiltonian approach and it has been found not only in smaller portions of the antennae, but also in the entire light-harvesting complexes comprising up to 10^5 emitters. Furthermore, we found that the superradiant decay rate is robust even in presence of static and thermal noise comparable to room temperature energy. This property is typical of natural systems, as we demonstrated

that mathematical models exhibit significantly lower efficiency.

Another crucial aspect explored in this thesis is how cooperativity can influence the energy transfer process, from absorption to charge separation in the RCs. We addressed this issue with two different approaches. For the GSB light-harvesting apparatus we modeled the entire process of excitation energy transfer by using incoherent rate equations for the populations of the system, accounting for the weak interaction of our aggregates with sunlight and a thermal bath, while for the PB antennae we developed a theoretical model based on the network-theory. Our results showed that the emergence of superradiance ensures a fast incoherent energy transfer from a donor to an acceptor unit before radiative and non radiative losses occur. For GSB we have found an internal efficiency close to $\sim 80\%$, proving that almost all the absorbed excitation is funneled to the RCs for charge separation, while the results for PB antennae have shown a charge separation quantum yield close to $\sim 90\%$, comparable to the literature.

Finding new strategies for light-harvesting and clean energy production is a recent goal of quantum biology. Nowadays the study is not limited to understanding natural processes, but also extends to the development of quantum devices able to mimic the interesting and efficient behavior of such systems. Within this framework, this thesis also offers a brief explanation of a possible application of the unique properties exhibited by natural light-harvesting antennae. Within this context, the main goal of the APACE project is to turn the incoherent solar radiation into a coherent laser beam by using light-harvesting systems from natural and artificial antennae for absorption and funneling of the excitation to a lasing medium. In Ref. [46] there is evidence that the lasing threshold can be significantly reduced, allowing the active medium to achieve population inversion even under natural sunlight illumination.

9.1 Summary of contributions

This section summarizes the main contributions from each chapter.

Chapter 2. In this chapter the geometrical structure of PB and GSB light-harvesting systems has been explained. In particular, three complexes has been considered as representative of the GSB: a single-wall cylinder, four

concentric cylinders and three adjacent concentric cylinders. The first two configurations represent smaller portion of the antenna, while the third one, also referred to as the chlorosome, is representative of natural models. It reaches a length of 150 nm containing up to 10^5 BChls *c*. For the PB antennae we considered two models: an s-shaped LH1 complex with two RCs at its core surrounded by 10 LH2 ring (B800 + B850), which represent a portion of the antenna complex, and the entire light-harvesting unit, known as the chromatophore, which has a diameter of 60 nm and includes more that 4000 BChls *a*.

Chapter 3. In this chapter the study of spontaneous emission from an ensemble of emitters in single excitation regime has been addressed. The emergence of single-photon superradiance has been investigated in both GSB and PB light-harvesting systems made of BChl molecules by using a non-hermitian Hamiltonian approach, valid beyond the small-volume limit. Two approximations have been considered: the hermitian Hamiltonian and the Frenkel dipole-dipole interaction, valid when resonances do not overlap and within the small-volume limit. Our findings revealed that superradiance is still present in the entire light-harvesting complexes of PB and GSB, and not only in smaller subunits, as already demonstrated in the literature. Furthermore, for systems extending beyonda the small-volume limit, such as for the chlorosome of GSB and for aggregates of PB chromatophores, the non-hermitian Hamiltonian formalism represents the only approach to describe superradiance.

Chapter 4. Considering the effect of disorder and thermal noise is an important issue in biological systems. Here due to the large size of our systems we implemented a simplified yet valid model to take these effects into account. Assuming our systems are in canonical equilibrium with a thermal bath, we have computed the thermal coherence length, that measures how much a single excitation is shared coherently among the molecules of the aggregates. In addition, static disorder has been modeled as site-energy fluctuations. The main findings of this chapter have shown that superradiance and thermal coherence length can be sustained in PB and GSB antennae even in presence of static disorder and thermal noise comparable to room temperature energy. This demonstrated that quantum coherence in natural light-harvesting aggregates can persist under ambient conditions.

Chapter 5. In this chapter the absorption and emission properties of both single emitters and entire aggregates have been investigated. After a preliminary discussion on the solar irradiance, here modeled through the black body radiation theory, the theoretical framework of J- and H-aggregates has been introduced. Finally the comparison with our theoretical model and experimental absorption and emission spectra has been shown. A good agreement has been found between experimental and numerical results, confirming the validity of the non-hermitian Hamiltonian approach for these systems.

Chapter 6. Modeling the interaction with a thermal bath, treated as an independent bath of harmonic oscillators, is an important aspect to consider when studying excitation energy transfer in light-harvesting systems. Assuming that the emitters are weakly coupled to a thermal bath, here we have provided a complete derivation of the master equation in the Lindblad form for the reduced density matrix. Finally the detailed-balance thermal rates between the eigenstates of the system have been computed, assuming a linear spectral density to model the system–bath interaction. These results served as the starting point for the next chapter, where the entire process of energy transfer is described.

Chapter 7. In this chapter the entire process of the exciton energy transfer in the entire light-harvesting apparatus of GSB, from sunlight absorption to exciton trapping in the reaction centers, has been considered. The energy transfer has been analyzed using the radiative non-hermitian Hamiltonian and solving the rate equations for the populations. Sunlight pumping has been modeled through black-body radiation, while the presence of a thermal bath has been considered as an ensemble of independent harmonic oscillator. Cylindrical structures typical of GSB antenna complexes, and the dimeric baseplate comparable to natural size have been considered. Our analysis has shown that under natural sunlight, the number of excitations reaching the RC per unit time matches the RC closure rate and the internal efficiency shows values close to $\sim 80\%$. We have also considered mathematical models where the orientation of the dipoles does not reflect the natural one and we have demonstrated that the light-harvesting efficiency is lower than in the natural structure.

Chapter 8. Here we have provided a different approach of the excitation energy transfer in PB light-harvesting complexes. The entire dynamics of the excitation has been modeled using the network-based theory. In this chapter, we have characterized the properties of the natural chromatophore as a function of two parameters: first the solar irradiance, and second the rate at which reaction centers re-open. Two different models have been implemented: a stochastic model providing an exact solution to the master equation of the system using the Gillespie algorithm and a deterministic model relying on mean-field approaches and rate-equations. Our findings have revealed that out model successfully predicted the high charge separation quantum yield of the chromatophore under low light.

9.2 Limits of validity of the models presented in this thesis

Even though the approaches developed and used in this thesis have been validated and supported by comparisons between the obtained numerical results and the data coming from literature and experiments, in this section a critical discussion regarding the approximations and their limits of validity of our theoretical models is provided.

- **Modeling of BChl molecules.** In this thesis a strong approximation in the modeling of the BChl molecules is the treatment of each molecule as a two-level system with an associated transition dipole moment. As detailed in chapter 5, while the broad absorption spectrum of BChls exhibits multiple transitions, specifically Q_y, Q_x and Soret band, the Q_y is the dominant contribution to the spectrum in the low-frequency range. By isolating this transition, we can effectively capture the optical properties of the BChl molecules without introducing significant discrepancies with respect to the experimental data of the absorption and emission spectra, see Fig. 5.2 and calculations provided in chapter 5. However, including other electronic transitions would be interesting for understanding how this effect could modify the spectroscopic properties of the aggregates. Moreover, a more sophisticated model that accounts for vibronic levels and inter-system crossing from singlet to triplet states could represent a future perspective for providing a better description of the system.

- **Validity of the non-hermitian Hamiltonian model.** Open quantum systems are nowadays at the center of many research fields in physics, in a typical situation a discrete quantum system is coupled to an external environment characterized by a continuum of states. Elimination of the continuum of the EMF leads to an effective non-hermitian Hamiltonian that describes the interaction of the system with the radiative field. This approach has been shown to be a very effective tool, offering several advantages: it allows to compute the whole time evolution of the relevant subsystem and to analyze the effects of interference between discrete states and the continuum, such as superradiance or Fano resonances. However the problem of its validity is often overlooked. A study conducted in Ref. [149] shows that the non-hermitian approach is valid when the energy dependence of the coupling to the external environments is sufficiently smooth in the energy range spanned by the eigenstates of the network. Note that, in the limit of a single excitation in the system and zero temperature in the photon bath, the non-hermitian Hamiltonian description is equivalent to the standard master equation in Lindblad form, obtained under the Born-Markov secular approximation. Nevertheless, the non-hermitian Hamiltonian approach is computationally much more efficient because one has to integrate only N equations while, with the master equation approach, one has $\mathrm{O}(N^2\ )$ equations to deal with.

- **Relationship between cooperativity and system length.** In chapter 3 and chapter 4 a study of the emergence of superradiance and thermal coherence length in large molecular systems has been conducted using a non-hermitian Hamiltonian approach to model the light-matter coupling. A key result is that superradiance scales with the system size in the small volume regime ($L < \lambda_0$). Nevertheless, we demonstrated that such behavior cannot be sustained for indefinitely length aggregates. As the system size increases beyond a fraction of λ_0, superradiance tends to saturate and the cooperative response is lost. In this framework another parameter has been considered: the thermal coherence length, which quantifies the spatial extent over which a single excitation is coherently spread across the aggregate in presence of a canonical bath and static disorder. The results provided in chapter 4 show that the saturation of both superradiance and thermal coherence

length in PB and GSB (see Figs. 4.2 and 4.3) defines an upper bound to the length of the aggregates. When the system size is comparable with λ_0, cooperativity tends to saturate due the effects of the coupling to the continuum of the EMF and to the presence of static and thermal noise, well captured by the thermal coherence length, which becomes the most relevant parameter for describing the cooperative effects in such systems.

- **Modeling of thermal bath in the master equation.** In this thesis the dynamics of the system coupled to a thermal bath has been derived in the Lindblad approach, under the assumptions of a weak system-bath interaction, markovian and secular approximation. Under these assumptions the coherences are decoupled from the populations of the system and decay fast with respect to the system timescales. This approach allows to derive incoherent rate equations for the populations of the system, thereby significantly reducing numerical costs. In this framework the internal efficiency for large molecular light-harvesting complexes containing up to 10^5 BChl molecules has been computed, finding results comparable to experimental data, thereby validating the robustness of the underlying approximations for large-scale molecular systems. However, as previously discussed in chapter 4 and chapter 7, in literature more sophisticated techniques have been developed to model the system-bath interaction. Some are numerically exact, meaning that given sufficient computational resources, they will converge to the correct dynamics. These techniques include path integral [150], hierarchical equations of motion [151] and density matrix renormalization group methods [152]. Recently, relying on the process tensor approach, the automated compression of environments algorithm (ACE), widely discussed in Ref. [153], has emerged as a powerful tool for simulating open quantum systems coupled to arbitrary environments. By reducing the large number of environmental degrees of freedom to those which are most relevant, ACE fully accounts for non-markovian effects, system–environment correlations and non-gaussian baths.

  Additionally, assuming a second-order perturbative approach to describe the weak system-bath interaction is fundamental to derive the Lindblad master equation. This approximation can be valid when the coupling between system and environment is weak or when internal

system couplings are strong. However, in the opposite or intermediate regimes this approach fails and the polaron transformation becomes important, see Refs. [154–157]. In this formalism, the electronic system + phonon bath Hamiltonian is transformed into a new frame (polaron frame) where electronic couplings are renormalized and fluctuate due to the interaction with the vibrational modes. Under certain conditions, the energy scale of the electronic coupling fluctuations induced by the displaced vibrations is small in comparison to all other energy scales in the system and, therefore, such fluctuations can be treated as a perturbation. Standard projection operator techniques can then be used to derive a second-order master equation that captures non-markovian and non-equilibrium bath effects in the intermediate regime.

- **Regime of validity of the environments independence in the master equation.** To model the dynamics of light-harvesting complexes coupled to more environments, the isolated action of each bath has been represented by markovian liouvillian super-operators within the quantum master equations framework in Lindblad form. In this approach the photon and phonon baths and the excitation-trapping sinks are modeled independently in the master equation, under the assumption that they influence the system additively, while neglecting their mutual interaction. Specifically, in Ref. [158] the authors investigated the regime of validity of such approximation for natural light-harvesting complexes, finding that the additive approximation is valid when the strength of the energy fluctuations produced by the phonon bath is small compared to the bandwidth of the continuum of EMF and sink. Excitonic transport in natural light-harvesting complexes happens through two different ways: (1) by recombination and photon emission and (2) by trapping and charge separation in reaction centers. As for the electromagnetic environment, its bandwidth is clearly very large since the photon can have any energy, moreover thermal fluctuations (~ 200 cm^{-1}) are only a tiny fraction of the excitation energy of the single molecule ($\sim 10^4$ cm^{-1}) and they are comparable with the system bandwidth. For this reason, even if a more quantitative analysis should be carried out, the widespread use of the independence hypothesis is supported. Regarding exciton loss by trapping in a reaction center, due to the complexity of the actual physical processes

involved, the validity of the wide-band approximation should be evaluated specifically for each biological system.

In this thesis we also model the space-dependent static disorder, which affects the excitation energies of the BChl molecules. Within this additive framework, the effect of static disorder and the coupling with different environments (EMF, thermal bath, trapping to the RC) are treated indipendently. Specifically, the non-hermitian Hamiltonian approach used to describe the coupling to the EMF is derived under the assumption of uniform excitation energy. However, in presence of static disorder, we include energy fluctuations accounting for the local-environment. Given that the range of disorder is much smaller than the energy bandwidth of the EMF field, see Ref. [149], static disorder does not affect the radiative decay rate to the continuum of EMF. In this regard, it is worth noting that Ref. [159] provides a more accurate description of light-matter interaction, showing a proof of principle of how excitation energy detuning can influence the coupling to the EMF in dimeric systems with different optical transitions.

- **Limitations and validity of the MC-FRET approach.** In this work the incoherent multi-chromophoric energy transfer from a donor to an acceptor molecular aggregate mediated by the thermal bath has been extensively employed in chapter 7 to model the energy transfer process between different molecular complexes. This theoretical framework, widely used in Refs. [15, 34, 35], relies on two fundamental assumptions: (1) the system-bath interaction is weak with respect to intermolecular coupling within each aggregate and (2) a markovian canonical thermal bath ensures that the donor reaches the thermal equilibrium. However, such a simplified treatment of the thermal bath may represent a limitation in the calculation of energy transfer rates. As a future perspective, it would be highly valuable to investigate how a more sophisticated description of the bath affects these rates. To advance our understanding, using a more modern approach relying on polaron theory that accurately captures the strong coupling of each monomer to a vibrational phonon bath could be interesting. This model allows not only to capture the change of energy transfer due to temperature effects, but also to describe the impact of the environment on the delocalization of electronic states within the aggregates.

Despite these approximations, the main results shown in this thesis, specifically the emergence of cooperative effects and the study of the excitation energy transfer, align closely with experimental data. In chapter 5 a comparison between experimental and numerical emission and absorption spectra obtained with the radiative non-hermitian Hamiltonian is provided, finding good agreement. Furthermore, in chapter 7 a study of the energy transfer efficiency in GSB light-harvesting systems has been pursued, matching the internal efficiency typically found in the literature. These findings support the validity of our theoretical approach; however the previously discussed limitations must be carefully considered when extending the analysis to larger systems or more sophisticated environments.

9.3 Directions for future work

In this section future research avenues have been discussed. Specifically, we focus on two main research lines with the overall aim of finding evidences of efficient energy transfer from natural or artificial antennae to other molecular aggregates, such as lasing units within the scope of the APACE project.

- The emergence of superradiance is a widely studied topic within the framework of quantum biology, both experimentally and theoretically. Here we have performed simulations on the entire light-harvesting complexes of GSB and PB with a non-hermitian Hamiltonian approach, valid beyond the small-volume limit. We have already started collaborations with research groups at LENS and CNR of Florence, at CNR of Bari and University of Parma in order to give experimental evidence of superradiance in the antennae of GSB and PB complexes, using spectroscopic methods. In particular, we plan to characterize the size dependence of the optical response determining the radiative decay widths obtained through time resolved fluorescence spectroscopy and the quantum yield obtained from spectrofluorimetric measurements conducted at different temperatures (from 77 K to room temperature). Within the scope of the APACE project, we aim to further extend this study, both experimentally and theoretically, to artificial antennae, such as C8S3 nanotubes, which are among the best candidates as energy donors in hybrid systems.

- As a future outlook, the study of the excitation energy transfer in PB antennae through the network theory will be extended implementing long-range in the network-based model. In addition, we aim to optimize the antenna geometry to enhance both absorption and excitation energy transfer processes. To achieve this goal, we plan to model the inhibition of the RCs in order to enable direct excitation transfer from the antenna to the lasing medium, thereby preventing charge separation. Similarly, a study can be conducted on the light-harvesting apparatus of GSB, where reaction centers (RCs) can be replaced by lasing units to achieve lasing under natural sunlight.

Appendix A

A.1 Inverse-Mollweide projection

We use the inverse-Mollweide projection [83] to map planar regions to spherical patches. The Mollweide projection from a sphere onto a plane is an area-preserving projection that generates the familiar rendering of the Earth globe where circles of latitude are mapped onto parallel lines on the plane. In order to model the PB chromatophore of radius R, see Sec. 2.1.2 in the main text, we use the following mapping:

$$\beta = \arcsin\left(\frac{x}{\sqrt{2}(R+\Delta z)}\right) , \tag{A.1a}$$

$$\xi = \frac{\pi y}{2\sqrt{2}(R+\Delta z)\cos\beta} , \tag{A.1b}$$

$$\theta = \arcsin\left(\frac{\sin 2\beta + 2\beta}{\pi}\right) , \tag{A.1c}$$

$$\begin{cases} x' = (R+\Delta z)\cos\theta\cos\xi \\ y' = (R+\Delta z)\cos\theta\sin\xi \\ z' = (R+\Delta z)\sin\theta , \end{cases} \tag{A.2}$$

where x and y are the in-plane coordinates of chlorophyll molecule positions, Δz is the vertical shift of the molecules with respect to the plane, ξ and θ are respectively the longitude and the latitude angles and x', y' and z' are the Cartesian coordinates on the sphere.

Panel A of Fig. (A.1) shows the projection of a light-harvesting system comprising 2 RCs and a s-shaped LHI surrounded by 10 LHII complexes B850

and B800 on a spherical cap. As expected, the absorption spectrum of the projection on the sphere does not differ significantly from that of the planar region, even though small variations that concerns both the positions of the eigenmodes in the energy spectrum and the decay widths can be observed, see Fig. (A.1 B).

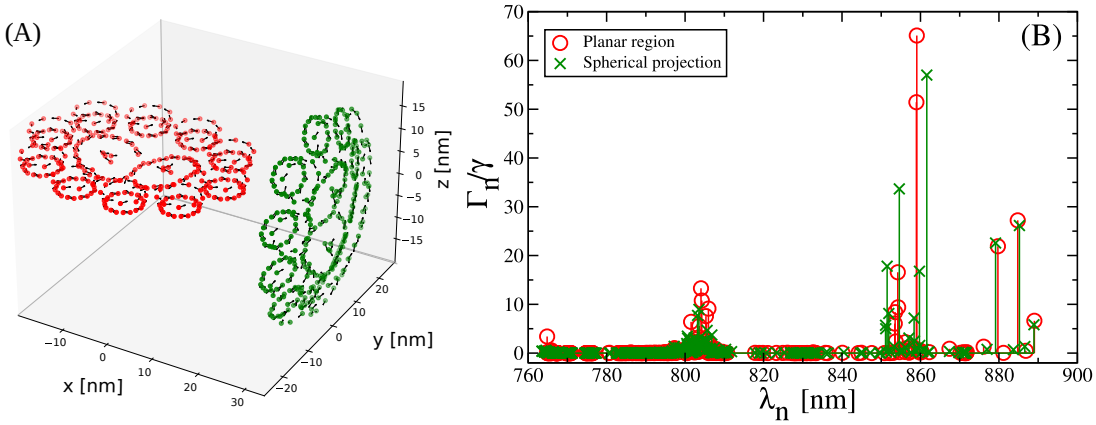

Figure A.1: *Inverse-Mollweide projection.* Panel (A): Comparison between planar region and spherical area preserving mapping of the PB complex A, see main text, on a spherical cap with $R = 6$ nm. The projection has been obtained by using the inverse Mollweide projection defined in Eq. (A.1-A.2). Panel (B) represents the radiative decay width as a function of the wavelength computed by using the full radiative Hamiltonian in Eq. (3.1) for both the systems on planar region (red circles) and on a spherical cap (green crosses).

A.2 Radiative Hamiltonian parameters

In our model each molecule is represented as a two-level system with an excitation energy e_0 and a transition dipole moment (TDM) $\vec{\mu_0}$. Specifically, we set the excitation energy e_0 in cm^{-1}, corresponding to a transition wavelentgth $\lambda_0 = 1/e_0 \times 10^7$ nm, so that the wave vector is $k_0 = 2\pi e_0 \times 10^{-8}$ Å^{-1}. Finally if $\vec{\mu_0}$ is expressed in debye and the corresponding squared transition dipole moment $|\mu_0|^2$ in Å^3 cm^{-1} (for the conversion, see [111]), we can define the radiative decay rate of each molecule $\gamma = 4|\mu_0|^2 k_0^3/3$, corresponding to the radiative lifetime τ_γ (for the conversion, see [160]).

The parameters of the photosynthetic antennae considered here have been taken from literature [13, 16, 46, 79, 161, 162]. They are shown in details respectively in Tab. (A.1) and Tab. (A.2). Moreover the N-N couplings between dipoles on adjacent sub-units have been shown in Tab. (A.3) for both PB and GSB complexes.

Site energy	$e_0 = 15390$ cm^{-1}
Transition wavelength	$\lambda_0 \sim 650$ nm
Wave vector	$k_0 = 9.670 \cdot 10^{-4}$ Å^{-1}
Dipole moment	$\lvert\vec{\mu_0}\rvert = \sqrt{30}$ D so that $\lvert\vec{\mu_0}\rvert^2 = 151024$ Å^3 cm^{-1}
Decay rate	$\gamma = 1.821 \cdot 10^{-4}$ cm^{-1}
Radiative lifetime	$\tau_\gamma = 21.15$ ns
N-N couplings	$\Omega_1 = 618$ cm^{-1}
	$\Omega_2 = 248$ cm^{-1}

Table A.1: Parameters for the **Green sulfur bacteria** photosynthetic antenna. In GSB all the molecules have the same excitation energy e_0, while their transition dipole moments have the same magnitude but different orientations in the space. Finally Ω_1 and Ω_2 are respectively the azimuthal and vertical N-N couplings in GSB complex A.

Subunit	**Site energy** [cm^{-1}]	**N-N coupling** [cm^{-1}]
LHI B875	12121	alt. 300 - 233
LHII B850	alt. 12458 - 12654	alt. 363 - 320
LHII B800	12564	/
RC	P1 12180	(P1-P2) 500
		(P1-B1) -50
		(P1-B2) -60
	P2 12080	(P2-B2) -50
		(P2-B1) -60
	B1 12500	
	B2 12530	
$\lvert\vec{\mu_0}\rvert$	10.151 D	
$\overline{e}_0$	12500 cm^{-1}	

Table A.2: Parameters for the **Purple bacteria**. The table shows the site energies and the nearest-neighbour couplings in each subunits of Purple bacteria light-harvesting complex. The site energies are set to match the main fluorescence peaks at 800 nm (B800), 850 nm (B850) and 875 nm (LHI). P1, P2 and B1 and B2 represent the four pigments found in each RC. The two strongly-coupled monomers, indicated by P1 and P2, form the special pair, while the other two, B1 and B2, are the accessory pigments in the RC. In the PB antenna, molecules belonging to different subunits have different excitation energies and the nearest-neighbour (N-N) couplings are given in [27] and also used in [46] and [16]. In the LHI and LH2 B850 complexes alternating (alt.) N-N couplings have been used and the excitation energies of the Bchl molecules in the LH2 B850 system are chosen in alternation, as well. Furthermore the intensity of the transition dipole moment $|\vec{\mu_0}|$ and the average excitation energy $\overline{e}_0$ computed as the weighted average of the excitation energies of each sub-unit are shown.

A.3 Regime of validity of the Hamiltonian models

In this section a deeper study of the three Hamiltonian models used in the main text has been addressed (see discussion in Chapt. 3 in the main text). In particular here we have studied the regime of validity of three Hamiltonian models (DH, HH and NHH) and we have compared our results of the

Complex	**N-N coupling** Ω [cm$^-$1]	**Distance** d $[nm]$
GSB complex B	16	2.1
PB complex B	80	2.2

Table A.3: N-N couplings in PB and GSB complexes. N-N couplings Ω and distances d between N-N dipoles belonging to adjacent sub-units in GSB and PB complexes are computed by using the HH model and the parameters shown in Tab. (A.1) and (A.2). For GSB complex B the N-N coupling between dipoles on consecutive cylinders has been considered, while for PB complex B the N-N coupling between dipoles belonging to adjacent LH2 systems is shown.

dipole strength and radiative decay width obtained diagonalizing the three Hamiltonian models with the expectation value of the non-hermitian part of the full Hamiltonian (NHH), according to the perturbation theory.

As already described in the main text, the perturbed Hamiltonian is given by the NHH model and it reads:

$$\hat{H}_{NHH} = \sum_{i=1}^{N} e_0 |i\rangle\langle i| + \sum_{i\neq j} \Delta_{ij} |i\rangle\langle j| - \frac{\mathrm{i}}{2} \sum_{i,j=1}^{N} Q_{ij} |i\rangle\langle j| \,, \tag{A.3}$$

where $e_0 = \hbar\omega_0$ is the excitation energy of the single emitter, while Δ_{ij} and Q_{ij} are the out-of diagonal terms with $Q_{ij} \ll \Delta_{ij}$.

The diagonal part of Δ_{ij} and Q_{ij} are given by:

$$\Delta_{jj} = 0 \,, \qquad Q_{jj} = \frac{4}{3}\mu^2 k_0^3 = \gamma \,, \tag{A.4}$$

where γ is the radiative decay width associated to each emitter.

The non-hermitian Hamiltonian gives complex eigenvalues $\varepsilon_n = \mathrm{E}_n - \mathrm{i}\frac{\Gamma_n}{2}$ where $\Gamma_n/\hbar$ is the radiative decay rate of the n^{th} eigenstate in s^{-1}.

In our systems the out-of diagonal term Q_{ij} can be treated as a perturbation, since $Q_{ij} \ll \Delta_{ij}$. Let us define the unperturbed Hamiltonian, which coincides with the hermitian part of the NHH shown in Eq. (A.3) and reads:

$$\hat{H}_{HH} = \sum_{i=1}^{N} e_0 |i\rangle\langle i| + \sum_{i\neq j} \Delta_{ij} |i\rangle\langle j| \,, \tag{A.5}$$

whose unperturbed eigenvalues and eigenstates are E_n^0 and $|E_n^0\rangle$, respectively. [1]

[1]Note that only in this section we introduce this notation to indicate eigenvalues and

According to the non-degenerate perturbation theory, the first-order energy shifts [2], which are the expectation values of the perturbation Hamiltonian Q_{ij} while the system is in the unperturbed eigenstate $|E_n^0\rangle$, have been computed and compared to the radiative decay widths obtained by diagonalizing the full non-hermitian Hamiltonian.

Fig. A.2 shows the maximal dipole strength obtained diagonalizing the DH (black circles) and HH (red squares) models and the maximal decay width (blue stars) obtained with the NHH model as a function of the length of the MT cylinder rescaled over λ_0 (see Tab. 5.1 for the value of λ_0 for BChl *c*). Finally the first-order energy shifts $\langle E_n^0|Q|E_n^0\rangle/\gamma$ (magenta diamonds) computed with the perturbation theory are compared with the previous results. In all models we added a source of static disorder ($W = 1$ cm^{-1}, a single realization), such that degeneracies have been broken while superradiance is preserved. The geometrical model that we consider is the single-wall MT cylinder with 6 TDMs on each ring with a length L that goes from 74.7 to 8291.7 Å.

In Fig. A.2 the maximal dipole strength computed with the DH and HH models increases linearly with the length of the system (see black circles and red squares in Fig. A.2), while the radiative decay width (see blue stars) tends to saturate. Finally a comparison with the perturbation theory is provided. Since the imaginary part Q_{ij} is a small perturbation of the non-hermitian Hamiltonian, the first-order energy shifts have been computed as the expectation value of Q_{ij} with the unperturbed eigenstates $|E_n^0\rangle$ of the hermitian Hamiltonian given by Eq. (A.5). The results show that the maximal value of $\langle E_n^0|Q|E_n^0\rangle/\gamma$ (see magenta diamonds in Fig. A.2) is in agreement with all the other three methods (DH, HH, NHH) when $L < \lambda_0$. When the system size increases the dipole strength description is no longer valid, while the perturbation approach is still in agreement with the NHH model, showing a tendency of the superradiant decay width to saturate with

eigenstates of the unperturbed Hamiltonian (HH), while in the main text we use E_n and $|E_n\rangle$. The reason of this choice is to distinguish clearly between the eigenstates and eigenvalues of the perturbed and unperturbed Hamiltonians.

[2]Note that here we use the non-degenerate perturbation theory to compute the energy-shift. This approach is valid only when the eigenstates of the unperturbed system are non-degenerate. In this case the unperturbed system shows degeneracies that have been broken by adding static disorder $W = 1$ cm^{-1}. Such value of static disorder does not affect the spectrum and does not destroy superradiance, but it is enough to remove the degeneracy.

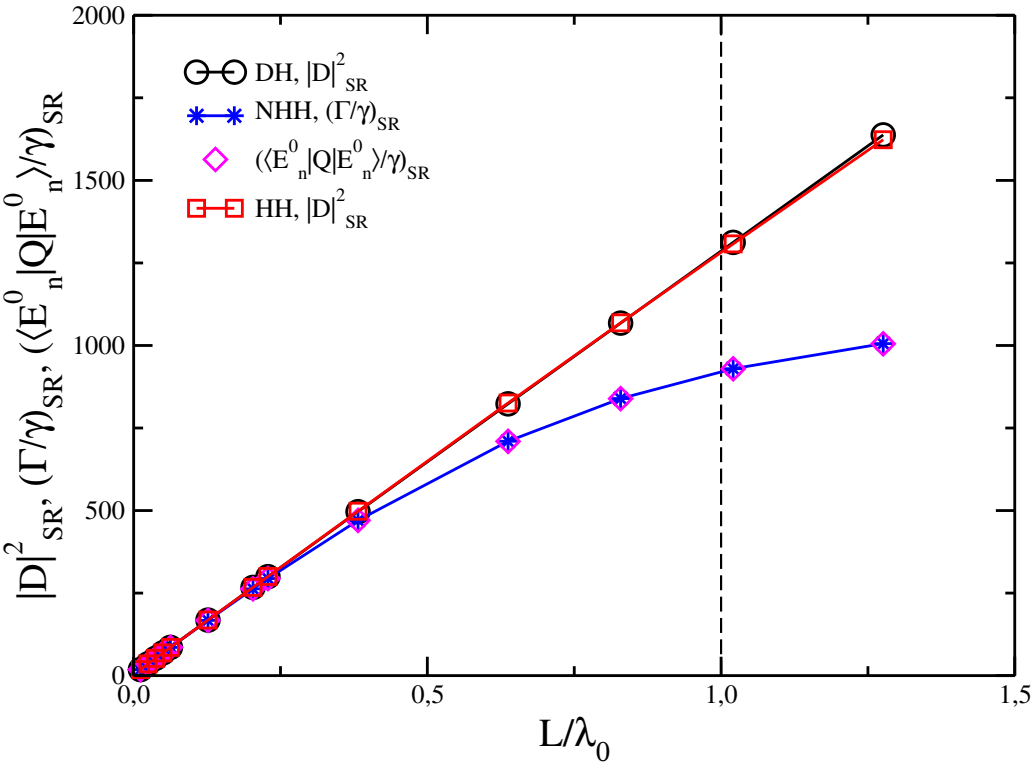

Figure A.2: *Regime of validity of the three hamiltonian models and comparison with the perturbation theory approach in a single wall MT cylinder.* Maximal dipole strength obtained by diagonalizing the DH (black cirlces) and HH (red squares) models and the maximal decay width (blue stars) obtained with the NHH model as a function of the length of the MT cylinder rescaled over λ_0. The first-order energy shifts $\langle E^0_n|Q|E^0_n\rangle/\gamma$ (magenta diamonds) computed with the perturbation theory is shown. The geometrical model considered is the single wall MT cylinder with 6 TDMs on each ring with a length $74.7 \leq L \leq 8291.7$ Å. The total number of TDMs goes from 60 to 60000 for the longest cylinder that we consider here. The vertical dashed line ($L = \lambda_0$) stands for a cylinder length comparable to the excitation wavelength of the single emitter. In all models a source of static disorder ($W = 1\text{cm}^{-1}$, a single realization) has been added in order to break the degeneracies in the unperturbed system, without changing the spectral properties of the system and the superradiance response.

the length of the cylinder.

From our analysis, we can conclude that all the models (dipole strength

computed with DH and HH, radiative decay width computed with NHH and perturbative approach) are in good agreement when the system size is small compared to the transition wavelength of the single emitter λ_0. When the system size becomes comparable to λ_0 and the small volume approximation starts to fail, the dipole strengths computed with the DH and HH Hamiltonians are no longer good approximations to describe superradiance, but only the NHH model and the perturbative approach are still valid ($\Gamma_{SR} < \delta$, where δ is the mean energy level spacing). As already proved in Chapt. 3, if we consider larger aggregates, such as the entire chlorosome, also the perturbation approach fails, because resonances start to overlap ($\Gamma_{SR} > \delta$) and the NHH becomes the only model that can describe superradiance.

It is known that disorder and thermal noise induce localization of the excitation. For one-dimensional systems the most relevant parameter is the localization length, instead of the system length L, and the small-volume limit refers to the regime in which the localization length is smaller than λ_0, regardless of the system size L. If we assume a disorder strength that induces a localization length smaller than λ_0, for one-dimensional systems the three Hamiltonian models give always good agreement. In three-dimensional systems, however, due to the stronger influence of long-range interactions, the behavior is not so trivial. Therefore, in this case the system size has been taken as the upper bound for the localization length.

A.4 Cooperativity in GSB antenna

In this section we consider GSB complexes A, B and C, see Sec. 3.2.1 in the main text, with a length $L = 82.17$ nm, corresponding to 100 rings for each cylindrical structure. Panels A, B and C of Fig. (A.3) show the energy spectra computed respectively for a single cylinder (A, in green colour), four concentric cylinders (B, in red colour) and three adjacent cylinders with four concentric rolls each (C, in blue colour). Here the three Hamiltonian models are compared: NHH (in dark colours), HH (in medium shade of colours) and DH (in light colours). For complex A all the models we considered (NHH, HH and DH) give a good description of superradiance, for complex B the DH model is no longer valid, while HH and NHH model are in agreement even if small deviations can be observed, finally for complex C the NHH model differs from the HH model only in the most superradiant states, with a 20% difference, much smaller than what happens for larger system sizes. This should be compared with Fig. (3.1), where the larger system size is shown and where the differences between the HH and NHH model are much larger (close to 60% for complex C) and involve a much larger number of states. For this reason to study the robustness of cooperative effects to disorder and noise for this system size (100 rings) we used the HH model, see discussion in Sec. 3.2.1.

In panel D of Fig. (A.3), it is shown that for complexes A and B the non-hermitian part of the Hamiltonian can be considered perturbatively, while for complexes C only for the most superradiant states the resonances overlap. Again this should be compared with panel (D) of Fig. (3.1) where for larger system sizes it is shown that the decay widths of a much larger number of states overlap.

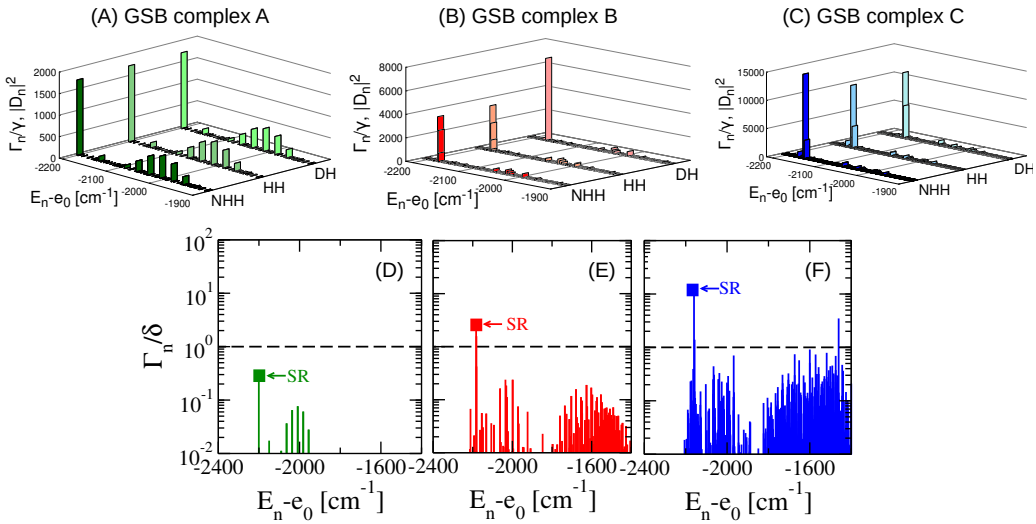

Figure A.3: *Superradiant states in Green sulfur Bacteria Antennae.* Complexes A (single cylinder in green colour), B (four concentric cylinders in red colour), C (three adjacent concentric cylinders in blue colour) are shown in the respective panels (Panels A, B, C). Three different Hamiltonian models are compared for each model using different shades of colour (NHH: non-hermitian Hamiltonian Eq. (3.1, in dark colours), HH: hermitian Hamiltonian Eq. (3.5, in medium shade of colours), DH: Dipole Hamiltonian Eq. (3.8, in light colours). The squared dipole strength $|\mathrm{D}_n|^2$, see Eq. (3.7), is shown for the HH and DH models, while the radiative decay width Γ_n/γ is shown for the NHH model as a function of the energy $E_n - e_0$. Panels (A-C) show only the lowest part of the energy spectrum where the most superradiant states are located. Results are computed by using a fixed length $L = 82.17$ nm for each aggregate, which corresponds to 100 rings for each cylinder. (D-F) These panels show the ratio between the decay width Γ_n obtained by diagonalizing the full radiative Hamiltonian (NHH model) in Eq. (3.1) and the mean level spacing δ as a function of the energy $E_n - e_0$ for complexes A (in dark green colour), B (in dark red colour), C (in dark blue colour) with a fixed length $L = 82.17$ nm. The mean level spacing δ is computed as the ratio between the energy spectral width and the total number of eigenmodes. Green, red and blue squares indicate the positions in the energy spectra of the most superradiant state for each complex. The horizontal dashed line represents the value of the ratio ($\Gamma_n/\delta = 1$) above which resonances overlap.

A.5 Probability distribution of the most superradiant states

Knowing the cooperativity of the antenna complexes can be useful for understanding the initial state to study the energy transfer within these aggregates. Indeed under light illumination, superradiant states are the most excited ones and so they determine the correct initial conditions for the energy transfer. To address this issue, here we consider the probability distribution over the sites of the superradiant states both in the GSB and in the PB antenna.

A.5.1 Most superradiant state in the GSB antenna

Here we consider GSB complex B with four concentric cylinders, comprising 180 rings. Fig. (A.4) shows how the three most superradiant eigenmodes are delocalized on the four concentric cylinders.

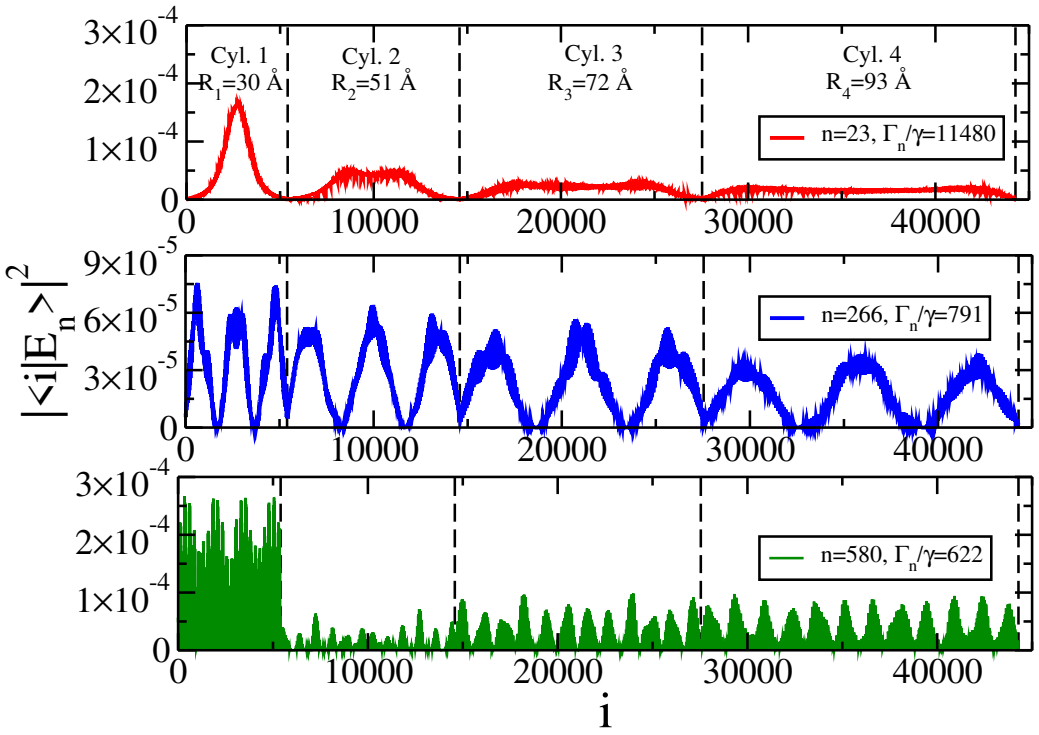

Figure A.4: *Delocalization of the superradiant states in complex B of GSB.* The probability $|\langle i|E_n\rangle|^2$ of the three most superradiant eigenmodes to be on the i^{th} site of the aggregate is shown. The most superradiant states are respectively the 23^{rd} excited state (red continuous line), the 266^{th} exc. state (blue continuous line) and the 580^{th} exc. state (green continuous line). Here we consider an aggregate with four concentric cylinders (GSB complex B) made of 180 rings with a length $L = 148.57$ nm. The vertical black dashed lines define the end of an inner cylinder and the beginning of an outer one. The eigenstates of the system $\langle i|E_n\rangle$ are computed by using the radiative Hamiltonian in Eq. (3.1).

A.5.2 Most superradiant state in the PB antenna

Fig. (A.5) and Fig. (A.6) represent respectively the energy spectra of complexes A (red colour) and B (blue colour) of PB antennae, showing the comparison between the three models we used: NHH (square symbols), HH (circle symbols) and DH (cross symbols). The decay width, computed using the NHH model, and the squared dipole strength, computed using both the HH and DH models, are shown as functions of the wavelength in these figures. The most superradiant states at approximately 800, 860, and 880 nm are indicated by black arrows.

Fig. (A.7) and Fig. (A.8) show the probability of the most superradiant eigenstates being delocalized across the sites of the system. Fig. (A.7) refers to PB complex A, while Fig. (A.8) to PB complex B. Each panel in both figures represents the projection of one of the most superradiant states, identified by black arrows in their respective energy spectra. These figures reveal that in both complexes, superradiant states at 800 nm are primarily delocalized over the sites of the LHII B800 rings, those at 860 nm are delocalized over the LHII B850 rings, and finally, superradiant states at around 880 nm are delocalized over the LHI system.

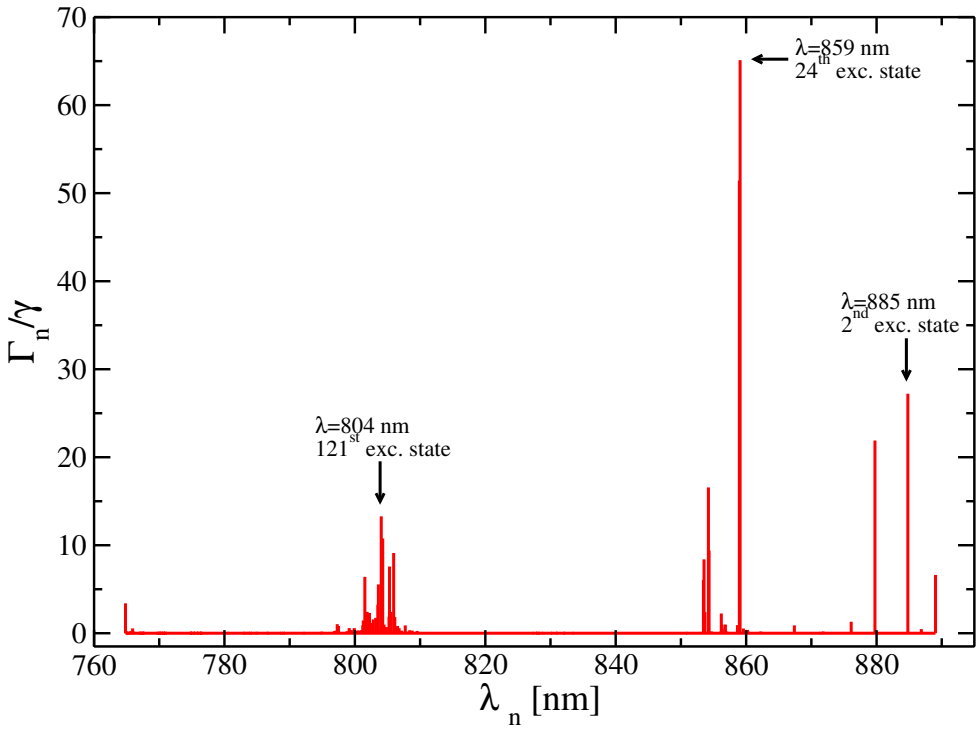

Figure A.5: *Cooperativity and superradiance in PB light-harvesting systems (complex A).* Energy spectrum of the light-harvesting system found in Purple bacteria with $N = 334$ Bchls formed by a s-shaped LHI complex (B875) with 2 RCs surrounded by 10 LHII rings (B850 and B800) (see panel (A) of Fig. (2.2)). Radiative decay width calculated with the NHH model as a function of the wavelength. The square dipole strengths computed by using DH and HH models are not shown since they give similar results. Black arrows indicate the positions in the energy spectrum of the most superradiant eigenstates which are delocalized on the subunits of the light-harvesting complex here considered, see Fig. (A.7).

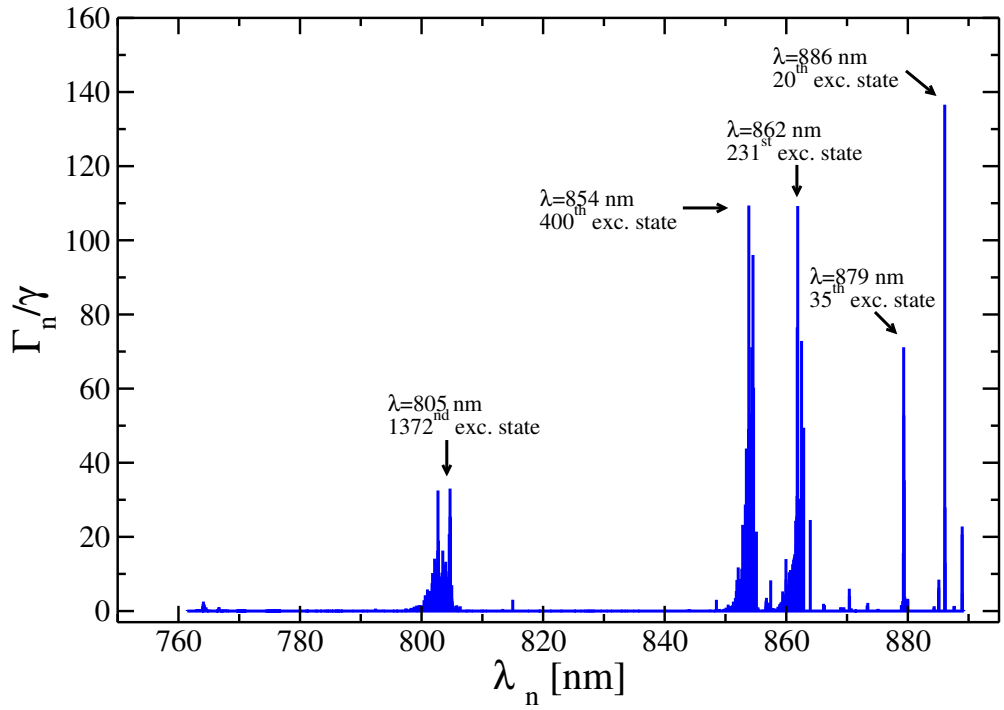

Figure A.6: *Cooperativity and superradiance in PB chromatophore (complex B).* Energy spectrum of the chromatophore of Purple bacteria with $N = 4113$ Bchls (see panel (B) of Fig. (2.2)). Radiative decay width calculated with the NHH model as a function of the wavelength. The square dipole strengths computed by using DH and HH models are not shown since they give similar results. Black arrows indicates the positions in the energy spectrum of the most superradiant eigenstates which are delocalized on the subunits of the light-harvesting complex here considered, see Fig. (A.8).

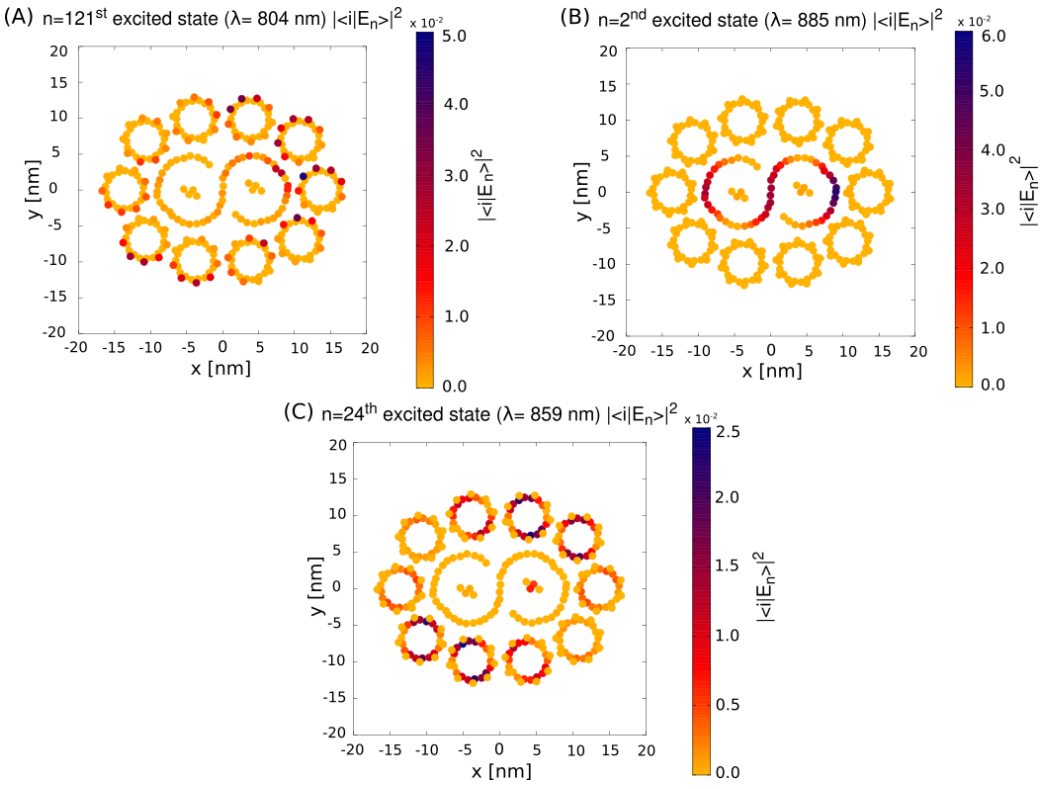

Figure A.7: *Delocalization of superradiant eigenmodes in complex A of PB.* (Panels A-C) delocalization of the most superradiant eigenstates on the sites of the system. $|\langle i|E_n\rangle|^2$ is the probability of the n^{th} eigenstate to be delocalized on the i^{th} site. The eigenstates of the system are computed by diagonalizing only the hermitian part of the full radiative Hamiltonian described in Eq. (3.1). See Fig. (A.5) to read the positions in the energy spectrum of the most superradiant states. The colorbar on the right represents the values of the probability of the n^{th} eigenmode to be projected on a site.

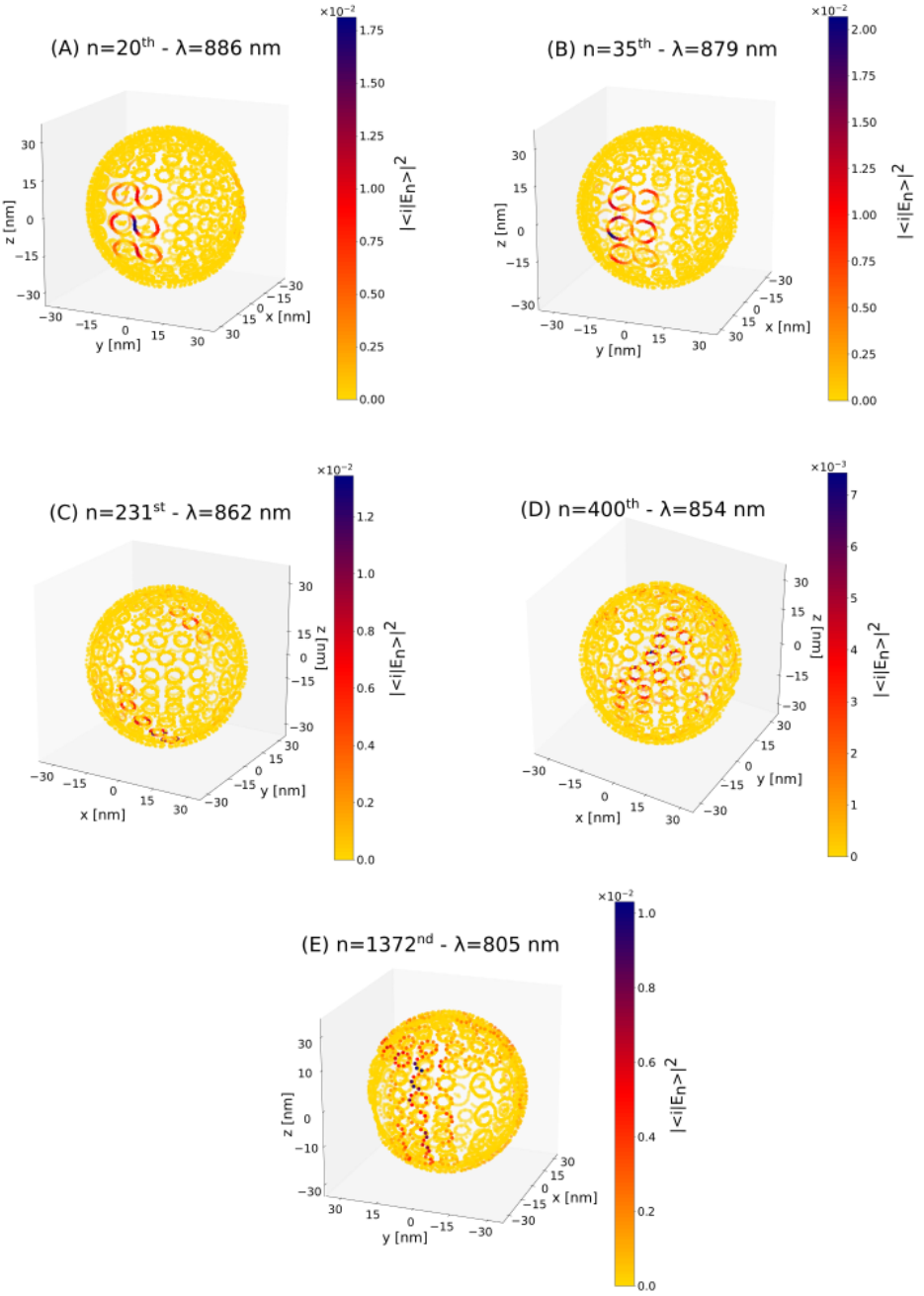

Figure A.8: *Delocalization of superradiant eigenmodes in complex B of PB.* (Panels A-E) probability of the superradiant eigenstates $|\langle i|E_n\rangle|^2$ to be projected on the sites. The eigenstates of the system are computed by diagonalizing only the hermitian part of the full radiative Hamiltonian described in Eq. (3.1). The colorbar on the right represents the values of the probability of the n^{th} eigenmode to be projected on a site. See Fig. (A.6) to read the positions in the energy spectrum of the most superradiant states.

A.6 PB chromatophore structure

Here we consider a different model for PB chromatophore. A vesicle (PB complex B) where all the LHII rings are randomly rotated around the axis joining the center of the chromatophore with the center of each LHII ring is studied. Fig. (A.9) shows the comparison between the energy spectra computed for a chromatophore with randomly rotated LHII rings (magenta stars) and without rotations (blue diamonds) as a function of the wavelength. Results are obtained by using the DH model (which is valid for the PB chromatophore). It can be observed that the differences between the two cases are not very large. For this reason we did not implement random rotations of the LHII complex in the PB chromatophore model considered in the main text.

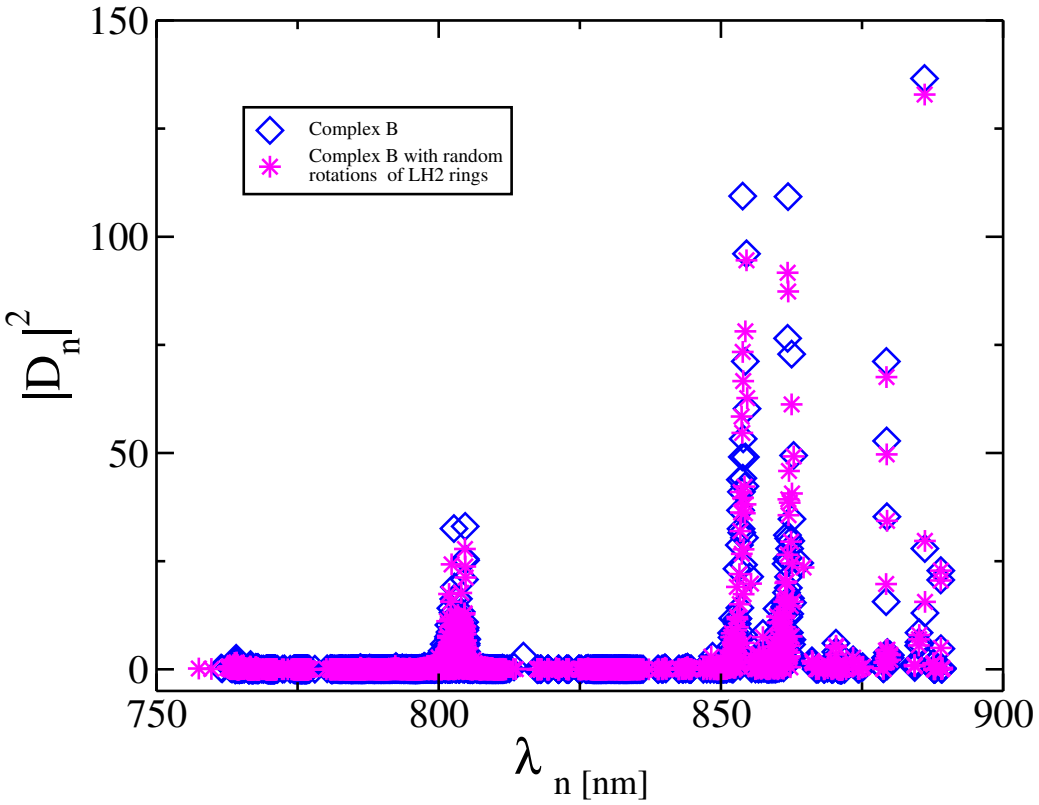

Figure A.9: *Random rotations of LHII light-harvesting systems in the chromatophore of PB.* Comparison between the energy spectra computed for the chromatohore shown in the text (blue diamond) and the chromatophore with LHII rings rotated around the axis joining the origin of the vesicle and the center of the ring by a random angle (magenta stars). The dipole strength as a function of the wavelength have been computed with the DH model shown in Eq. (3.8).

A.7 Robustness of superradiance with respect to random dipole orientation

The main purpose of this thesis was to study cooperative effects at large scale, for realistic photosynthetic antennae sizes. Our findings reveal that as the portion of the antenna analyzed is increased, also the cooperative effects are enhanced. To show that this is not a trivial effect, we here consider how cooperativity is affected when the dipole orientation are partially randomized. For this reason we compare the results shown in Chap. 3 for the PB and GSB complexes with these new models. For the GSB antenna, a system with four concentric cylinders with 100 rings is considered. All the dipoles have the same positions as the complex B presented in Sec. 2.1.1. The dipole orientation is randomized in all cylinders but one (the one with radius of 7.2 nm which is the closest in diameter to GSB complex A). On the other hand, for the PB antenna we consider a system where all dipoles have the same positions as in the chromatophore presented in Sec. 2.1.2, nevertheless the dipole orientation are randomized for all molecules except the molecules belonging to a single LHI + 2RCs complex (which have been chosen at random among the 9 LHI+RC complexes present on the chromatophore).

Fig. (A.10) shows the dipole strength as a function of the energy computed with the HH model for both PB and GSB complexes. For both models the comparison between the randomized system and the realistic complexes (GSB complex B and PB complex B) shows that the presence of randomized dipoles strongly decreases superradiance. Nevertheless, we can observe that superradiance in random complexes is not completely suppressed. Indeed, superradiant states survive and are characterized by dipole strengths comparable with those found in the portion of the antenna whose dipoles have not been randomized. Probably this is due to the fact that the coupling between different sub-units in the GSB and PB antennae are not very strong. Indeed, in general surrounding an ordered structure, which presents superradiance, with dipoles having random orientation could easily quench superradiance.

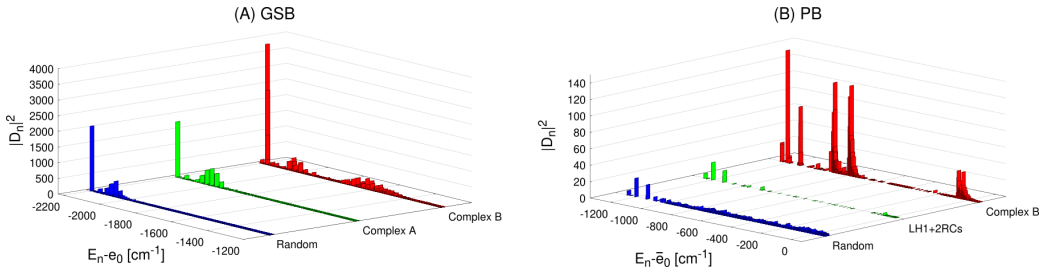

Figure A.10: *GSB and PB spectra: the effect of randomness on superradiance.* The squared dipole strength as a function of the energy computed with the HH model is represented in both panels A and B. (A) GSB complex with a fixed length $L = 82.17$ nm, corresponding to 100 rings. GSB complex B (in red colour) comprises four concentric cylinders, while GSB complex A (in green colour) is made of a single wall. In both of them the dipoles orientations are defined in the main text, see Sec. 2.1.1. GSB random dipoles (in blue colour) have the same structure as in the GSB complex B, but with random orientation except for the the 3^{rd} cylinder with radius $R = 7.2$ nm. (B) PB complex spectra are shown. PB complex B (in red colour) represents the chromatophore described in Sec. 2.1.2, while PB LHI + 2RCs (in green colour) comprises a single s-shaped LHI with two RCs projected on a spherical cap. Finally, PB random dipoles (in blue colour) represent the chromatophore, where all dipoles have random orientations, except those belonging to a single LHI + 2RCs.

A.8 Analysis of the three Hamiltonian models

In this section we analyze in more detail the difference between the three Hamiltonian models considered to study the photosynthetic antennae. In particular, the average coupling in all the complexes (GSB complexes A,B,C and PB complexes A,B) analyzed in Chapt. 2 for the three different Hamiltonian models is studied. The average coupling $\langle J \rangle$ has been computed in the following way:

$$\langle J \rangle = \frac{1}{N} \sum_{i=1}^{N} \sqrt{\sum_{j \neq i} |H_{i,j}|^2}, \tag{A.6}$$

where N is the system size, while $H_{i,j}$ is the Hamiltonian matrix element $H_{i,j} = \langle i | \, H \, | j \rangle$.

		NHH [cm^{-1}]	HH [cm^{-1}]	DH [cm^{-1}]
GSB	complex A	981.08233	981.08233	981.04971
	complex B	982.53042	982.53042	981.04971
	complex C	982.53956	982.53956	982.49831
PB	complex A	394.31019	394.30997	394.30079
	complex B	393.40191	393.40191	393.39299

Table A.4: Average couplings $\langle J \rangle$ (see Eq. A.6) obtained with the three Hamiltonian models (NHH, HH and DH) for all the complexes we consider in Chapt. 2 (GSB complexes A, B, C with length L=150 nm and PB complexes A, B).

Tab. (A.4) shows that the coupling are almost identical. Also the spectral widths and the lowest excitonic energy obtained with the three different Hamiltonian models for all the complexes considered are almost identical, see Tab. (A.5).

The reason for these results is explained here below.

- NHH and HH differ only by the non-hermitian part in the Hamiltonian. Its contribution is very small, of the order of 10^{-4} cm^{-1}, see [13], while the hermitian part gives a maximal contribution of about 600 cm^{-1}.

- The DH and the other models have similar couplings since the maximal system size considered, which is about 150 nm, is smaller than the tran-

		$E_{max} - E_{min}$ [cm^{-1}]			$E_{min} - e_0$ [cm^{-1}]		
		NHH	HH	DH	NHH	HH	DH
GSB	complex A	3663.92	3663.92	3661.67	-2207.69	-2207.69	-2205.47
	complex B	3681.73	3668.2	3667.95	-2216.46	-2210.87	-2210.64
	complex C	3668.41	3668.41	3667.99	-2211.08	-2211.08	-2210.68
PB	complex A	1826.67	1826.67	1826.61	-1252.79	-1252.79	-1252.71
	complex B	1886.7	1886.7	1886.7	-1254.88	-1254.88	-1254.88

Table A.5: Spectral width $E_{max} - E_{min}$ and red-shifted GS energy $E_{min} - e_0$ computed with the NHH, HH and DH models for each complex here considered (GSB complexes A, B, C with length L=150 nm and PB complexes A, B). e_0 represents the excitation energy of the single molecule.

sition wavelength λ_0, which is 650 nm. Thus, so as far as the couplings are concerned, the small volume limit is a good approximation.

Nevertheless the differences we have found between the three Hamiltonian models regard the lifetime of the eigenstates (decay widths) and not their spectral width. These are not simply due to the coupling strengths but they depend on how the dipole strength is redistributed among the eigenstates. This redistribution is very sensitive to the overlap of the eigenstates decay widths (resonance overlap criterion). This is explained in the text, see Fig. (3.1) (panels D,E,F), Fig. (3.3) (panels: C,D) and Fig. (A.3) (panels: D,E,F).

Appendix B

B.1 External efficiency of the GSB light-harvesting complex

Here we compute the external efficiency for the entire light-harvesting complex of GSB, comprising the chlorosome and the baseplate. Chlorosomes contain mainly BChl *c*, while the baseplate is formed by BChl *a* molecules. We assume that the photons flux on Earth from sunlight is

$$I_{Sun} = \int_{\lambda_i}^{\lambda_f} d\lambda\, \Phi(\lambda)\, \frac{\lambda}{hc} = 1.75 \cdot 10^{21}\ \mathrm{s}^{-1}\mathrm{m}^{-2}\ , \tag{B.1}$$

obtained by integration of the solar irradiance given in Fig. (5.2) from $\lambda_i = 280$ nm to $\lambda_f = 4000$ nm and in agreement with the results provided in Ref. 19. Using the results found in the previous sections, the total absorption rate in the GSB light-harvesting system is computed. The total absorption rate in the chlorosome and in the baseplate is given respectively by:

- $N_{chl} = 132840$ BChl *c* and $N^c_{abs} = 132840 \cdot 8.6 = 1184299\ \mathrm{s}^{-1}$,
- $N_{BPL} = 3350$ BChl *a* and $N^a_{abs} = 3350 \cdot 12.5 = 41875\ \mathrm{s}^{-1}$,

where 3350 and 132840 are the total number of BChl molecules in the baseplate and in the chlorosome respectively. If we assume the baseplate area $A_{BPL} = 3.5 \cdot 10^{-14}\ \mathrm{m}^2$, the absorption rate per unit area in the GSB reads:

$$I_{abs} = \frac{N^c_{abs} + N^a_{abs}}{A_{BPL}} = 3.4 \cdot 10^{19}\ \mathrm{s}^{-1}\mathrm{m}^{-2}. \tag{B.2}$$

Finally the absorption efficiency for the GSB can be estimated as:

$$\eta_{abs} = \frac{I_{abs}}{I_{Sun}} = 1.9\%\ . \tag{B.3}$$

For light-harvesting complexes three main quantities have been determined: the internal efficiency $\eta_{int} = \frac{I_{RCs}}{I_{abs}}$, the external efficiency $\eta_{ext} = \frac{I_{RCs}}{I_{Sun}}$ and the absorption efficiency η_{abs} defined above in Eq. (B.3). In our theoretical model we have found values of the internal efficiency between $70\% < \eta_{int} < 85\%$ for the chlorosome, close to the values found in literature [16]. Assuming the absorption efficiency is about $\sim 1.9\%$ for the chlorosome, the external efficiency has been determined by

$$\eta_{ext} = \eta_{abs} \times \eta_{int} \tag{B.4}$$

and we found values between $1.3 - 1.6\%$.

These calculations represent an approximate estimate of the external efficiency in the GSB antenna complexes in good agreement with the numerical results found by using the rate equations approach. Fig. (B.1) shows the external efficiency obtained by using Eq. (7.17) in the main text as a function of the k_{FMO} trapping rate for the chlorosome (see the blue continuous line). The results show that the theoretical prediction given above is in agreement with numerical simulations, considering realistic values for the k_{FMO} trapping rate represented in the yellow window in Fig. (B.1). Fig. (B.1) also shows the external efficiency computed by numerical simulations for all the three single cylinder models (MT, PD and RD) coupled to the baseplate. Here systems formed by a single cylindrical aggregate with 6000 BChl *c* and a length of 821.7 Å and a dimeric baseplate with 2184 BChl *a* and an area of 2739.1×550.8 Å^2 have been considered. For single cylinder aggregates lower values of the external efficiency have been found. Also these numerical results can be compared to the theoretical prediction presented in Tab. (B.1), where a calculation of the external efficiency in the systems formed by a single cylindrical aggregate has been done following the same approach used for the chlorosome.

The total absorption rate in the cylinders and in the baseplate are given respectively by:

- $N^c_{abs} = 51600$ s^{-1},
- $N^a_{abs} = 27300$ s^{-1}.

The absorption rate per unit area in all the models (MT, PD and RD) is given by Eq. (B.2) and reads $I_{abs} = 5.26 \cdot 10^{13}$ s^{-1}m^{-2}, while the absorption

efficiency is around $\eta_{abs} \approx 0.3\%$ for MT, PD and RD models. The following table shows the external efficiency calculated for the systems comprising a single cylinder and a baseplate.

Model	**Int. Efficiency**	**Ext. Efficiency**
MT + BPL	$70\% - 80\%$	$0.21\% - 0.24\%$
PD + BPL	$25\% - 30\%$	$0.08\% - 0.09\%$
RD + BPL	$65\% - 73\%$	0.2%

Table B.1: Internal and external efficiencies computed for the single cylindrical models (MT, PD and RD) with 6000 BChl *c* and a length of 821.7 Å placed above a dimeric baseplate with with 2184 BChl *a* and an area of 2739.1×550.8 Å^2. The internal efficiency has been taken from Fig. 7.6 in the main text assuming $0.023\ \text{ps}^{-1} < k_{FMO} < 0.044\ \text{ps}^{-1}$, while the external efficiency has been computed following Eq. (B.4).

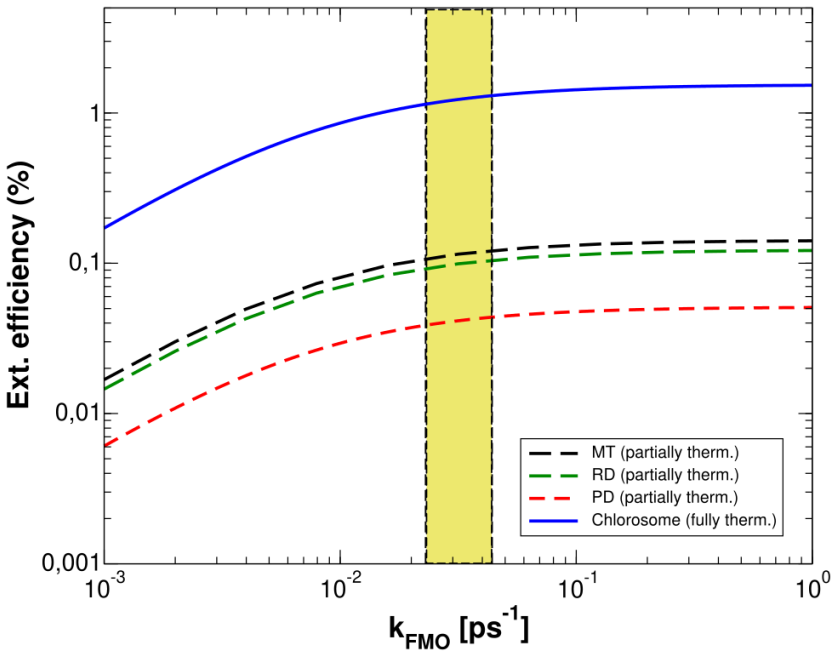

Figure B.1: *External efficiency in the chlorosome and in the single cylinder models coupled to a dimeric baseplate.* The figure shows the external efficiency as a function of the k_{FMO} trapping rate for different systems: the chlorosome and single cylinder models (MT-PD-RD) coupled to a baseplate. The results for the entire chlorosome (blue continuous line) have been obtained by assuming thermalization among all the aggregates, while for the single cylinders model the partially thermalized rate equations approach has been used (see the black, red and green dashed lines). For the RD model an average over 10 realizations of random TDMs orientations has been computed. The yellow window represents the typical range for k_{FMO} trapping rate.

B.2 Table of the models

Here a table comprising all the models taken into account in Chapt. 7 is given. Tab. (B.2) contains the total number of molecules and the dimensions for both cylindrical aggregates and baseplate.

MODEL	CYLINDER PARAMETERS	BASEPLATE PARAMETERS
MT/PD/RD + BPL	N_{TOT}=6000 L_{cyl}=821.7 Å	N_{TOT}=2184 N_Z=91 L_Z=2739.1 Å N_X=12 L_X=550.8 Å
WT + BPL	N_{TOT}=6000 L_{cyl}=618,75 Å	N_{TOT}=1608 N_Z=67 L_Z= 2016.7 Å N_X=12 L_X= 550.8 Å
CHLOROSOME + BPL	N_{TOT}=132840 L_{cyl}=1485.7 Å	N_{TOT}=3350 N_Z=67 L_Z=3075.3 Å N_X=25 L_X=1147.5 Å

Table B.2: *Cylinder and dimeric baseplate parameters.* The table shows the sizes and the total number of BChl molecules in each aggregate (single cylinder models (MT, PD, RD and WT) and the entire chlorosome coupled to a baseplate). N_{TOT} is the total number of molecules in the cylinder or baseplate. L_{cyl} refers to the cylinders length, while L_z and L_x are respectively the length and the width of the dimeric baseplate. N_z and N_x represent the number of dimers of the baseplate along the x and z directions. For the baseplate the total number of BChl molecules is given by $N_{TOT} = 2 \times N_x \times N_z$. Ref. 18 has been taken into account to determine the relative dimensions between cylindrical aggregates and the dimeric baseplate.

B.3 Multichromophoric transfer rates MC-FRET

In this section a deeper study of the MC-FRET is given. MC-FRET has already been used in literature to model the incoherent energy transfer between different aggregates [17,34,35] and it is computed by using the Förster rate K_{nm} defined in Eq. (7.14) in Chapt. 7. K_{nm} depends mainly on two quantities: the overlap between the emission spectrum of the donor and the absorption spectrum of the acceptor, and the coupling strength between the eigenstates of the two aggregates. The former depends on the parameter Γ_ϕ.

An aggregate absorption spectrum is given by [44, 125, 126]:

$$A(E) \propto \sum_n \mu^2 |D_n|^2 A_n(E) \ , \tag{B.5}$$

where $|D_n|^2$ and $A_n(E)$ are, respectively, the dipole strength and the normalized lineshape for each n eigenstate.

The emission spectrum, on the other hand, is

$$F(E) \propto \sum_m \mu^2 |D_m|^2 F_m(E) \ , \tag{B.6}$$

where the emission lineshapes are multiplied by the thermal populations p_m, see Eq. (7.21) in the main text, namely

$$F_m(E) = p_m A_m(E). \tag{B.7}$$

For high temperature and short bath correlation time [34, 44], we can neglect the phonon-induced Stokes and anti-Stokes shifts and approximate all the absorption lines as Lorentzians

$$A_n(E) = \frac{2\Gamma_\phi}{\Gamma_\phi^2 + (E - E_n)^2} \tag{B.8}$$

peaked at the eigenstate energy E_n and with a dephasing-induced linewidth Γ_ϕ. Note that the normalization condition gives $\int_{-\infty}^{+\infty} A_n(E) dE = 2\pi$.

Fig. (B.2) shows the overlap between the emission and absorption spectra of MT, PD and RD cylinders and baseplate respectively, assuming a Lorentzian linewidth of 500 cm^{-1} for both cylinders and baseplate spectra. The choice of the linewidth for the emission and absorption spectra is consistent with experimental data. See Ref. [14] for a more detailed comparison between experimental and numerical spectra in GSB antenna complexes, where a similar linewidth has been used.

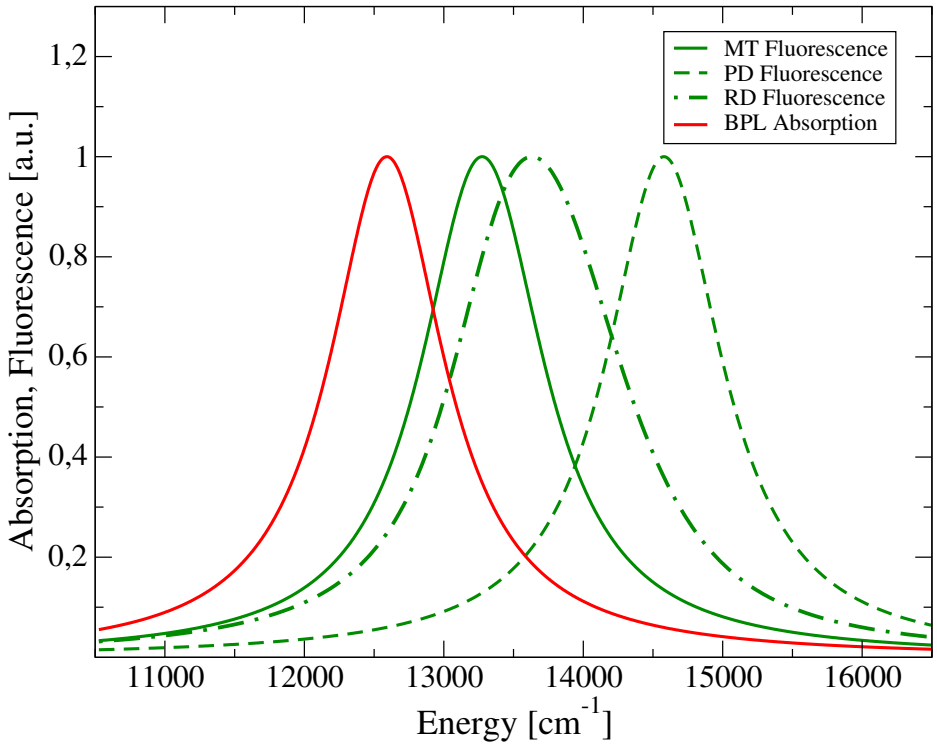

Figure B.2: *emission and absorption spectra in MT, PD, RD cylinders and baseplate.* Normalized emission spectra for the donor aggregates in green color, see Eq. (B.6). Continuous line for the MT model, dashed line for the PD model and dashed-dotted line for the RD model. The red continuous line represents the absorption spectrum of the baseplate, see Eq. (B.5). Here a Lorentzian lineshape with linewidth of 500 cm^{-1} has been considered for all the models.

Furthermore the couplings $\Omega_{n,m}$ between cylinder and baseplate eigenstates are studied. If $\hat{H}_{DH}$ is the Hamiltonian of the entire system (cylinder + baseplate) written on the site basis, see Chapt. 3, the coupling strength between the m^{th} eigenstate of the cylinder $|E_m\rangle$ and the n^{th} eigenstate of the baseplate $|E_n\rangle$ reads:

$$\Omega_{n,m} = \langle E_m | \hat{H}_{DH} | E_n \rangle = \sum_{i \in C, j \in B} C_m^*(i) C_n(j) H_{DH}(i,j) \ , \tag{B.9}$$

where $C_m(i)$ and $C_n(j)$ are the projections of the eigenstates on the sites basis, while $H_{DH}(i,j)$ is the coupling computed with the Frenkel Hamiltonian between sites i and j belonging respectively to the cylinder and baseplate.

Finally, the following calculations justify the choice of the parameter $\Gamma_\phi = 1000\ \mathrm{cm}^{-1}$, where $\Gamma_\phi/\hbar$ is the dephasing rate, in Eq. (7.14) in the main text as the sum of the absorption and emission spectra linewidths.

The MC-FRET rate is usually expressed as

$$K_{D,A} = \sum_{m\in D}\sum_{n\in A} \frac{|\Omega_{n,m}|^2}{2\pi\hbar} \int_{-\infty}^{+\infty} F_m(E)A_n(E)dE = \sum_{m\in D}\sum_{n\in A} p_m\, K_{n,m}\ , \quad \text{(B.10)}$$

where $\Omega_{n,m} = \langle E_m|H_{DH}|E_n\rangle$ is the Hamiltonian matrix element between the m donor eigenstate and the m acceptor eigenstate computed in Eq. (B.9).

Under the assumption made before for the absorption and emission lineshapes, the overlap integral in equation (B.10) is analytically computed. If Γ_d and Γ_a are the linewidths for the donor and acceptor aggregates respectively, the overlap integral reads

$$\int_{-\infty}^{+\infty} F_m(E)A_n(E)dE = p_m \int_{-\infty}^{+\infty} \frac{4\Gamma_d\Gamma_a}{[\Gamma_d^2 + (E-E_m)^2][\Gamma_a^2 + (E-E_n)^2]} dE\ . \quad \text{(B.11)}$$

The integral in Eq. (B.11) can be solved using Jordan's lemma and the final expression is as follows:

$$\int_{-\infty}^{+\infty} F_m(E)A_n(E)dE = p_m \frac{4\pi(\Gamma_d+\Gamma_a)}{(\Gamma_d+\Gamma_a)^2 + (E_m-E_n)^2}\ . \quad \text{(B.12)}$$

Eq. (B.12) shows that the overlap integral of the two Lorentzian functions with Γ_d and Γ_a linewidths is still a Lorentzian function peaked at $E_n - E_m$ and with a total dephasing-induced linewidth which is the sum of Γ_d and Γ_a.

Therefore, if $\Gamma_\phi = \Gamma_a + \Gamma_d$, we can express the MC-FRET rate in equation (B.10) as

$$K_{D,A} = \sum_{m\in D}\sum_{n\in A} p_m K_{n,m}\ , \quad \text{(B.13)}$$

where the transfer rates between a m donor eigenstate and a n acceptor eigenstate are

$$K_{n,m} = \frac{|\langle E_m|H_{DH}|E_n\rangle|^2}{\hbar} \cdot \frac{2\Gamma_\phi}{\Gamma_\phi^2 + (E_m-E_n)^2}\ . \quad \text{(B.14)}$$

Note that these rates are symmetric, $K_{n,m} = K_{m,n}$, causing Eq. (B.14) to break detailed balance. Since in the GSB aggregates that we consider

here usually the donor and acceptor eigenvalues are not resonant, we correct these rates by using Eq. (B.14) only for energetically downward transitions, otherwise taking $K_{n,m} = K_{m,n}e^{-(E_n-E_m)/k_BT}$. This method has already been used in Refs. 15, 16 in order to describe excitation energy transfer in Purple bacteria light-harvesting aggregates. In the main text (see Eq. (7.14)) the transfer rates $K_{n,m}$ have been given by adding this correction. As a consequence, if both donor and acceptor aggregates are made of one molecule, the MC-FRET gives forward and backward rates which are detailed balance.

B.4 Comparison between MT and WT models

GSB light-harvesting systems studied in the main text belong to the family of the mutant type model, obtained by genetic modifications of the system found in nature, which is the wild type model (WT). Experimental studies reveal that the WT chlorosomes are much more heterogeneous than chlorosomes from the MT model, furthermore the half-band width of the Q_y absorption maximum of the BChl *c* aggregates is largest for WT chlorosomes isolated from cells grown at low light intensity and it is also much broader than for chlorosomes of the MT model [28, 62].

In this section we propose a comparison between the mutant type (MT) and the wild type (WT) models for the GSB light-harvesting single-wall nanotubes. The geometry of the WT and MT models has been determined starting from the 2-dimensional Bravais lattice and wrapping it up according to two different rolling vectors, which are mutually perpendicular, see Ref. 62 for a description of the Bravais lattice. The result is that in the MT model BChls are organized into equal, horizontal and coaxial rings, while in the WT model BChls are organized into vertical chains, originating a helical structure. A brief explanation of the geometry of the WT model is provided in Fig. (B.3), while a wider explanation of the geometry of all the single-walled models can be found in Ref. [13]. Here we compare the trapped current and internal efficiency for both MT and WT models, computed by using the partially thermalized rate equations approach described in Sec. 7.3.2 in the main text. Fig. (B.4) shows the trapped current (panel A) and the internal efficiency (panel B) as a function of the FMO trapping rate. Our foundings demonstrate that MT and WT models have a similar behavior: both of them show a trapped current between $1 - 3 \times 10^{-1}$ ms^{-1} and an internal efficiency between $70 - 80\%$, see the yellow box that represents the typical FMO trapping rate range. These results confirm that the realistic models (both WT and MT) exploit excitation energy transfer efficiently and they are able to funnel almost all the absorbed excitation to the RCs with higher performance than the other mathematical models.

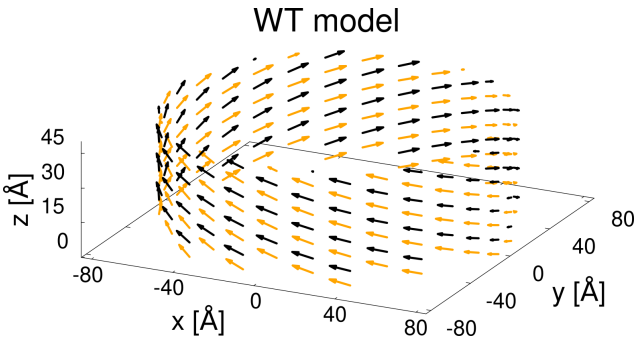

Figure B.3: *Geometry of the wild type (WT) model.* The figure represents a section of the wild type antenna complex. Positions and orientations of the TDMs associated to each BChl *c* molecule are represented by orange and black arrows. For the sake of clarity we show only 30 dipoles per ring instead of 60 as we considered in this paper. Moreover the distances along the z-axis are enhanced by a factor of 5 with respect to the distances on the $x - y$ axes. The WT model can be thought as organized into vertical chains to originate a helical structure. Also in the WT model there is the alternation $\pm 4°$ between consecutive dipoles on the same chain, here represented by the alternation between black and orange arrows. For more details about the structure of the WT model see Ref. [13].

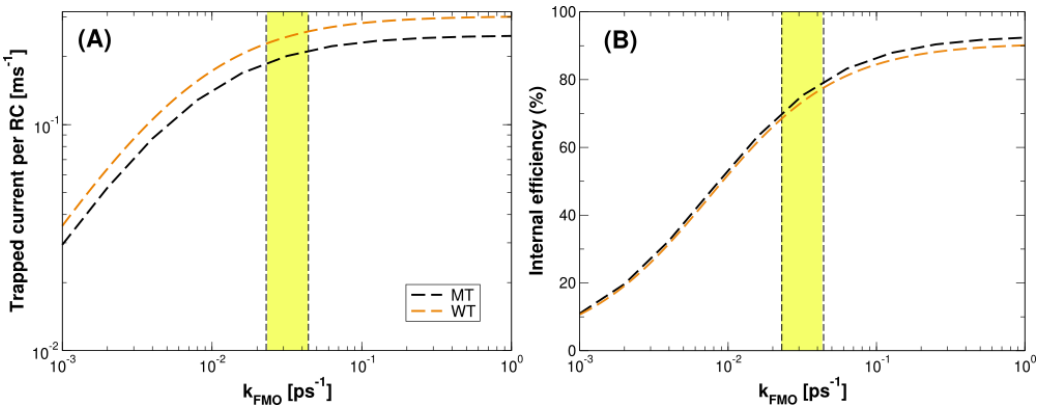

Figure B.4: *Comparison between WT and MT models.* Trapped current (panel A) and internal efficiency (panel B) as a function of the k_{FMO} trapping rate for MT and WT models coupled to a dimeric baseplate. The results have been obtained with the partially thermalized model using Eqs. (7.22) and (7.23) for the trapped current and the internal efficiency, respectively. For the MT model we consider a cylinder made of 6000 BChl *c* molecules and a dimeric baseplate containing 2184 BChl *a* molecules. For the WT model a cylinder with 6000 BChl *c* molecules and a dimeric baseplate containing 1608 BChl *a* molecules have been considered. More details about the size of the aggregates and the number of BChl molecules are provided in Tab. (B.2). The yellow window between the two dashed lines represent the region where the k_{FMO} trapping rate typically works in GSB species.

Appendix C

C.1 Global currents under 1 sun used for the deterministic model

As explained in Chapt. 8, the deterministic model relies on the evaluation of the global event currents under one sun in chromatophores with a fixed number of closed RC. This requires to solve the reaction-diffusion rate equations describing the dynamics of excitation on the chromatophore, see Eq.(8.15), and to compute global event currents form the steady state distribution of excitation in each node, see Eq. (8.17d). The currents obtained for N_{closed} ranging from 0 to 18 (all RC closed) are shown in Fig. (C.1). Additionally, panel (A) shows the logarithm function fit (Eq. (8.19)) on the global charge separation current. The absorption current shown in panel C uses a plain line as it does not depend on steady-state simulations (see Eq. (8.18b)).

C.2 Relation between fluorescence quantum yield and number of closed RC

Fig. (C.2) shows the quantum yield as a function of the number of closed RC. This plot is interesting as it allows a comparison with the experimental data from Ref. [142]. It is realized using the same data as for Fig. (8.2).

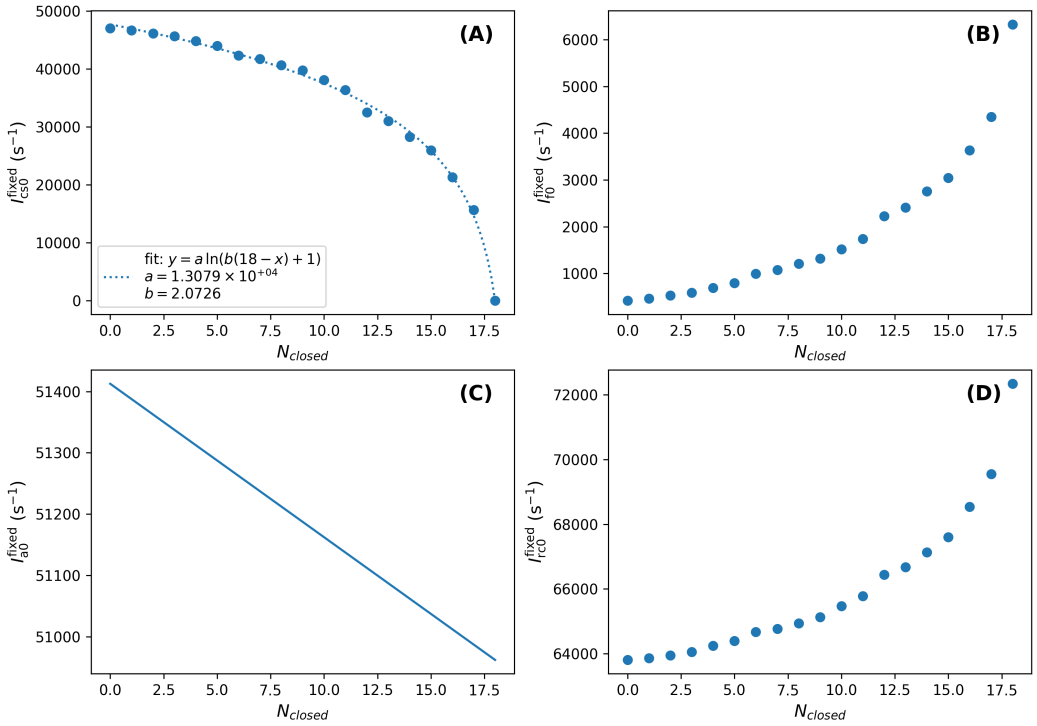

Figure C.1: *Global steady-state currents for the natural chromatophore with fixed open/closed RC under 1 sun as a function of the number of closed RC.* Considering a natural chromatophore under 1 sun, the quantity of excitation in each node at steady state is determined using the rate equation model for the dynamics of excitation on the chromatophore (Eq. (8.15)) for N_{closed} ranging from 0 to 18. Global event currents under one sun are computed from the corresponding steady states (as defined in Eq. (8.17d and 8.18b)). Panel (A): global current of charge separation. The dashed line shows the logarithm function fit (Eq. 8.19). Panel (B): global current of fluorescence. Panel (C): global current of absorption (steady-state independent). Panel (D): global current of excitation transfer to the reaction centers.

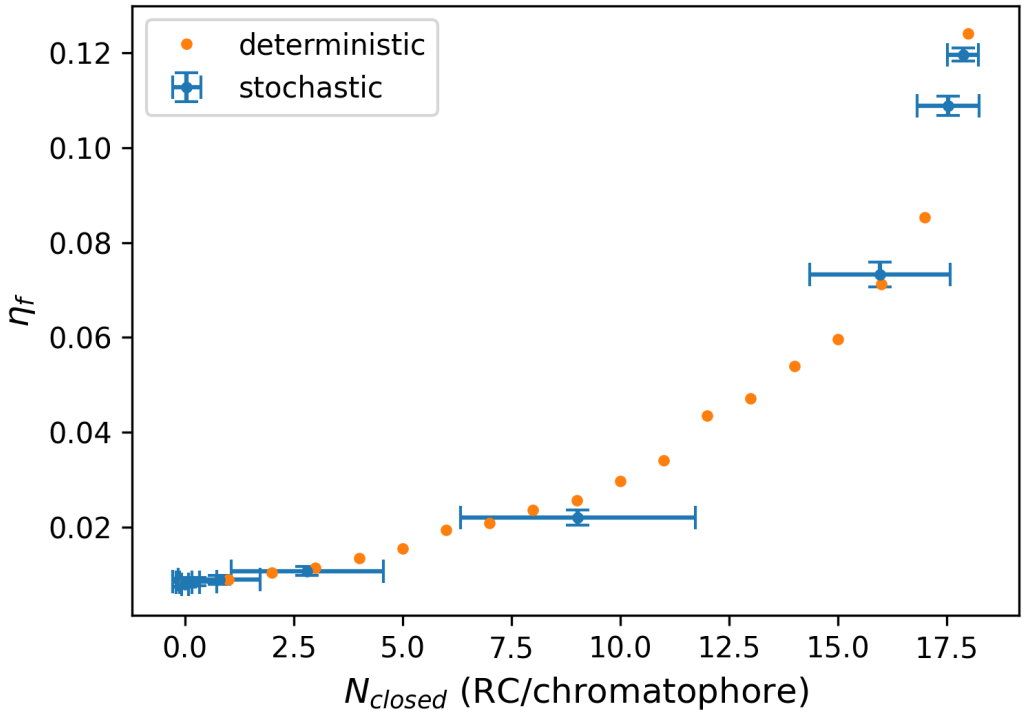

Figure C.2: *Steady state fluorescence quantum yield as a function of the number of closed RC.* Values are computed with both the stochastic model (blue) and the deterministic one (orange). The plot uses the exact same simulation data as in Fig. (8.2): 50 simulations for increasing value of solar irradiance, each ran until 1000 photons are absorbed. Points represent average values from the simulations, while error bars represent the corresponding standard deviations. Horizontal error bars represent the standard deviation of steady state N_{closed} obtained for the increasing values of solar irradiance (same as the vertical error bars in Fig. (8.2) panel (B)) while vertical error bars are the standard-deviation on the fluorescence quantum yield (same as the vertical error bars in Fig. (8.2) panel (C)). Deterministic values computed from the same data as those plotted in Fig. (C.1).

Appendix D

D.1 Derivation of the non-hermitian Hamiltonian

The problem of an ensemble of emitters coupled to the modes of the electromagnetic field is considered. The field is considered as coming from a black body at a finite temperature, which is a rough model for sunlight. A master equation is derived that is valid both for aggregates smaller than the transition wavelength and larger than that, reproducing previous results [163]. When the black-body temperature is vanishing, the master equation models cooperative radiative decay and reduces to the effective non-hermitian Hamiltonian widely used in quantum optics.

D.2 Hamiltonian and master equation for the whole system

Let us consider an aggregate of N two-level systems all having the same excitation energy ω_0. Below we refer to the two-level systems as "sites". In these calculations we use natural units so that $\hbar = 1$. The aggregate is assumed to interact with the radiation emitted by a black body at temperature T_S. The full Hamiltonian is written as

$$\hat{H} = \hat{H}_S + \hat{H}_B + \hat{H}_I \,. \tag{D.1}$$

Here the site Hamiltonian is

$$\hat{H}_S = \frac{\omega_0}{2} \sum_{j=1}^{N} \hat{\sigma}_j^z \,, \tag{D.2}$$

with $\hat{\sigma}_j^z$ being the z Pauli matrix for the j-th site. The black body Hamiltonian is

$$\hat{H}_B = \sum_{\vec{k},\lambda} \omega_k \hat{b}^\dagger_{\vec{k},\lambda} \hat{b}_{\vec{k},\lambda} \tag{D.3}$$

where the summation runs over the modes $\vec{k}$ and the polarizations $\lambda = 1, 2$ of the field, the dispersion relation is $\omega_k = ck$ and the creation/annihilations operators follow the commutation rules $[\hat{b}_{\vec{k},\lambda}, \hat{b}^\dagger_{\vec{k}',\lambda'}] = \delta_{\vec{k},\vec{k}'}\delta_{\lambda,\lambda'}$. Finally, the interaction Hamiltonian is

$$\hat{H}_I = -\sum_{j=1}^{N} \hat{\vec{D}}_j \cdot \hat{\vec{E}}(\vec{r}_j) \ , \tag{D.4}$$

where

$$\hat{\vec{D}}_j = \vec{d}_j(\hat{\sigma}_j^+ + \hat{\sigma}_j^-) \tag{D.5}$$

is the dipole operator on the j-th site, $\vec{d}_j$ is the transition dipole moment of the same site, $\hat{\sigma}_j^\pm = (\hat{\sigma}_j^x \pm i\hat{\sigma}_j^y)/2$ and

$$\hat{\vec{E}}(\vec{r}_j) = i \sum_{\vec{k},\lambda} \sqrt{\frac{2\pi\omega_k}{V}} \vec{e}_{\vec{k},\lambda} \left[e^{i\vec{k}\cdot\vec{r}_j} \hat{b}_{\vec{k},\lambda} - e^{-i\vec{k}\cdot\vec{r}_j} \hat{b}^\dagger_{\vec{k},\lambda} \right] \tag{D.6}$$

is the electric field in the position $\vec{r}_j$, with $\vec{e}_{\vec{k},\lambda}$ being a unit vector which specifies the polarization.

The dynamics of the full system is described by the Liouville master equation which, in the interaction picture, reads [128]

$$\frac{d\hat{\rho}(t)}{dt} = -i \left[\hat{H}_I(t), \hat{\rho}(t) \right] \ , \tag{D.7}$$

where $\hat{\rho}(t)$ is the density matrix in the interaction picture and it is related to the density matrix in the Schrödinger picture $\hat{\rho}$ by

$$\hat{\rho}(t) = e^{i(\hat{H}_S + \hat{H}_B)t} \, \hat{\rho} \, e^{-i(\hat{H}_S + \hat{H}_B)t} \, . \tag{D.8}$$

Note that also the density matrix $\hat{\rho}$ in the Schrödinger picture is time-dependent. Here we choose to write explcitly the dependence on time just for the operators representend in the interaction picture, to distinguish them to their respective Schrödinger representation.

The interaction Hamiltonian in the interaction picture can be factorized as

$$\hat{H}_I(t) = \sum_{\omega=\pm\omega_0} \sum_{j=1}^{N} e^{-i\omega t} \hat{A}_j(\omega) \otimes \hat{B}_j(t) = \sum_{\omega=\pm\omega_0} \sum_{j=1}^{N} e^{+i\omega t} \hat{A}_j^\dagger(\omega) \otimes \hat{B}_j(t) \tag{D.9a}$$

where $\hat{A}_j(\omega)$ are operators acting on the system,

$$\hat{A}_j(\omega_0) = \hat{\sigma}_j^- \,, \qquad \hat{A}_j(-\omega_0) = \hat{A}_j^\dagger(\omega_0) = \hat{\sigma}_j^+ \tag{D.10}$$

and $\hat{B}_j(t)$ are hermitian operators acting only on the black body, given by

$$\hat{B}_j(t) = i \sum_{\vec{k},\lambda} \sqrt{\frac{2\pi\omega_k}{V}} \left(\vec{d}_j \cdot \vec{e}_{\vec{k},\lambda}\right) \left[e^{i(\vec{k}\cdot\vec{r}_j - \omega_k t)} \hat{b}_{\vec{k},\lambda} - e^{-i(\vec{k}\cdot\vec{r}_j - \omega_k t)} \hat{b}_{\vec{k},\lambda}^\dagger\right] . \tag{D.11}$$

Eq. (D.7) can be integrated from 0 to t to obtain

$$\hat{\rho}(t) = \hat{\rho}(0) - i \int_0^t dt' \left[\hat{H}_I(t'), \hat{\rho}(t')\right] \tag{D.12}$$

which, substituted back into (D.7), gives the integro-differential equation

$$\frac{d\hat{\rho}(t)}{dt} = -i \left[\hat{H}_I(t), \hat{\rho}(0)\right] - \int_0^t dt' \left[\hat{H}_I(t), \left[\hat{H}_I(t'), \hat{\rho}(t')\right]\right] . \tag{D.13}$$

Born-Markov and secular approximations are performed on Eq. (D.13) in order to get a master equation in the Lindblad form. See the discussion in Chapt. 6 for a more detailed explanation and derivation of the master equation in Lindblad form:

$$\frac{d\hat{\rho}_S(t)}{dt} = \sum_{\omega=\pm\omega_0} \sum_{i,j} \Gamma_{ij}(\omega) \left[\hat{A}_j(\omega)\hat{\rho}_S(t)\hat{A}_i^\dagger(\omega) - \hat{A}_i^\dagger(\omega)\hat{A}_j(\omega)\hat{\rho}_S(t)\right] + \text{h.c.} \,, \tag{D.14}$$

where

$$\Gamma_{ij}(\omega) = \int_0^\infty d\tau \, e^{i\omega\tau} \left\langle \hat{B}_i(\tau)\hat{B}_j(0)\right\rangle_B . \tag{D.15}$$

D.3 Explicit calculation of the rates

Now we proceed to write explicitly the rates $\Gamma_{ij}(\omega)$. By substituting the expressions (D.11) into (D.15) we have

$$\begin{aligned}\Gamma_{ij}(\omega) = \int_0^\infty d\tau\, e^{i\omega\tau} \sum_{\vec{k},\lambda,\vec{k}',\lambda'} \frac{2\pi\sqrt{\omega_k\omega_{k'}}}{V} \left(\vec{d}_i\cdot\vec{e}_{\vec{k},\lambda}\right)\left(\vec{d}_j\cdot\vec{e}_{\vec{k}',\lambda'}\right)\Big[e^{i(\vec{k}\cdot\vec{r}_i-\vec{k}'\cdot\vec{r}_j-\omega_k\tau)}\left\langle \hat{b}_{\vec{k},\lambda}\hat{b}^\dagger_{\vec{k}',\lambda'}\right\rangle_B \\ - e^{i(\vec{k}\cdot\vec{r}_i+\vec{k}'\cdot\vec{r}_j-\omega_k\tau)}\left\langle \hat{b}_{\vec{k},\lambda}\hat{b}_{\vec{k}',\lambda'}\right\rangle_B + e^{-i(\vec{k}\cdot\vec{r}_i-\vec{k}'\cdot\vec{r}_j-\omega_k\tau)}\left\langle \hat{b}^\dagger_{\vec{k},\lambda}\hat{b}_{\vec{k}',\lambda'}\right\rangle_B \\ -e^{-i(\vec{k}\cdot\vec{r}_i+\vec{k}'\cdot\vec{r}_j-\omega_k\tau)}\left\langle \hat{b}^\dagger_{\vec{k},\lambda}\hat{b}^\dagger_{\vec{k}',\lambda'}\right\rangle_B\Big]. \end{aligned} \tag{D.16}$$

Now we assume that the black body is at thermal equilibrium, i.e.

$$\hat{\rho}_B = \frac{e^{-\beta\hat{H}_B}}{\mathrm{tr}_B\left\{e^{-\beta\hat{H}_B}\right\}}\,, \tag{D.17}$$

where $\beta = 1/(k_BT)$ is the inverse temperature. In this case one can show that the correlators in (D.16) are

$$\left\langle \hat{b}_{\vec{k},\lambda}\hat{b}_{\vec{k}',\lambda'}\right\rangle_B = 0 \tag{D.18a}$$

$$\left\langle \hat{b}^\dagger_{\vec{k},\lambda}\hat{b}^\dagger_{\vec{k}',\lambda'}\right\rangle_B = 0 \tag{D.18b}$$

$$\left\langle \hat{b}_{\vec{k},\lambda}\hat{b}^\dagger_{\vec{k}',\lambda'}\right\rangle_B = \delta_{\vec{k},\vec{k}'}\delta_{\lambda,\lambda'}\left(1+N(\omega_k)\right) \tag{D.18c}$$

$$\left\langle \hat{b}^\dagger_{\vec{k},\lambda}\hat{b}_{\vec{k}',\lambda'}\right\rangle_B = \delta_{\vec{k},\vec{k}'}\delta_{\lambda,\lambda'}N(\omega_k) \tag{D.18d}$$

where we have defined the Bose-Einstein function

$$N(\omega_k) = \frac{1}{e^{\beta\omega_k}-1}\,. \tag{D.19}$$

Thus, defining $\vec{r}_{ij} = \vec{r}_i - \vec{r}_j$, Eq. (6.23) can be written as

$$\begin{aligned}\Gamma_{ij}(\omega) = \int_0^\infty d\tau\, e^{i\omega\tau} \sum_{\vec{k},\lambda} \frac{2\pi\omega_k}{V} \left(\vec{d}_i\cdot\vec{e}_{\vec{k},\lambda}\right)\left(\vec{d}_j\cdot\vec{e}_{\vec{k},\lambda}\right) \\ \left[e^{i(\vec{k}\cdot\vec{r}_{ij}-\omega_k\tau)}\left(1+N(\omega_k)\right) + e^{-i(\vec{k}\cdot\vec{r}_{ij}-\omega_k\tau)}N(\omega_k)\right].\end{aligned} \tag{D.20}$$

As regards the sum over $\vec{k}$, we take the continuum limit

$$\frac{1}{V}\sum_{\vec{k}} \to \frac{1}{(2\pi)^3}\int d\vec{k} = \frac{1}{(2\pi c)^3}\int d\Omega \int_0^\infty d\omega_k\,\omega_k^2\,. \tag{D.21}$$

Now, if we assume that the dipoles have all the same magnitude μ but different orientation, namely $\vec{d}_j = \mu\,\hat{p}_j$, and defining the function

$$F_{ij}(x) = \frac{1}{4\pi}\sum_{\lambda}\int_0^{2\pi} d\phi \int_{-1}^{1} d(\cos\theta)\left(\hat{p}_i\cdot\vec{e}_{\vec{k},\lambda}\right)\left(\hat{p}_j\cdot\vec{e}_{\vec{k},\lambda}\right)e^{ix\cos\theta}\ , \quad \text{(D.22)}$$

choosing a frame where the z axis has the same direction as $\vec{r}_{ij}$, we have

$$\Gamma_{ij}(\omega) = \int_0^{\infty} d\tau\, e^{i\omega\tau}\int_0^{\infty} d\omega_k \frac{\mu^2\omega_k^3}{\pi c^3}\left[e^{-i\omega_k\tau}F_{ij}(kr_{ij})\,(1+N(\omega_k)) + e^{i\omega_k\tau}F_{ij}(-kr_{ij})N(\omega_k)\right]. \quad \text{(D.23)}$$

Now we perform the integral over τ using the relation

$$\int_0^{\infty} d\tau\, e^{i\omega\tau} = \pi\delta(\omega) + i\mathrm{P}\frac{1}{\omega}\ , \quad \text{(D.24)}$$

where $\delta(x)$ is the Dirac delta and P is the Cauchy principal value. So, we can split the rates into their real and an imaginary parts,

$$\Gamma_{ij}(\omega) = \frac{1}{2}\gamma_{ij}(\omega) + iS_{ij}(\omega) \quad \text{(D.25)}$$

which are, respectively,

$$\gamma_{ij}(\omega) = \int_0^{\infty} d\omega_k \frac{2\mu^2\omega_k^3}{c^3}\left[\delta(\omega-\omega_k)F_{ij}(kr_{ij})\,(1+N(\omega_k)) + \delta(\omega+\omega_k)F_{ij}(-kr_{ij})N(\omega_k)\right]\ , \quad \text{(D.26)}$$

$$S_{ij}(\omega) = \mathrm{P}\int_0^{\infty} d\omega_k \frac{\mu^2\omega_k^3}{\pi c^3}\left[\frac{F_{ij}(kr_{ij})\,(1+N(\omega_k))}{\omega-\omega_k} + \frac{F_{ij}(-kr_{ij})N(\omega_k)}{\omega+\omega_k}\right]. \quad \text{(D.27)}$$

D.3.1 Real Part

Let us start from the real part (D.26). The two integrals are easily performed, taking into account that the only possible values of ω are $\pm\omega_0$. By defining $k_0 = \omega_0/c$ we get

$$\gamma_{ij}(\omega) = \frac{2\mu^2\omega_0^3}{c^3}\left[\delta_{\omega,\omega_0}F_{ij}(k_0r_{ij})\,(1+N(\omega_0)) + \delta_{\omega,-\omega_0}F_{ij}(-k_0r_{ij})N(\omega_0)\right]. \quad \text{(D.28)}$$

To have the explicit dependence of $\gamma_{ij}(\omega)$ on the parameters, let us evaluate $F_{ij}(x)$. First of all, let us compute the sum over λ in (D.22), writing the three cartesian component of each vector $\alpha, \beta = 1, 2, 3$:

$$\sum_{\lambda} \left(\hat{p}_i \cdot \vec{e}_{\vec{k},\lambda}\right) \left(\hat{p}_j \cdot \vec{e}_{\vec{k},\lambda}\right) = \sum_{\lambda} \sum_{\alpha,\beta=1}^{3} p_i^{\alpha} p_j^{\beta} e_{\lambda}^{\alpha} e_{\lambda}^{\beta} \,. \tag{D.29}$$

Here, since the two polarizations $\lambda = 1, 2$ and the propagation unit vector $\hat{k}$ form an orthonormal basis, $\left\{\vec{e}_1, \vec{e}_2, \hat{k}\right\}$, we have

$$\sum_{\lambda=1,2} e_{\lambda}^{\alpha} e_{\lambda}^{\beta} = \delta^{\alpha\beta} - \frac{k^{\alpha} k^{\beta}}{k^2} \,, \tag{D.30}$$

so that we obtain

$$\sum_{\lambda} \left(\hat{p}_i \cdot \vec{e}_{\vec{k},\lambda}\right) \left(\hat{p}_j \cdot \vec{e}_{\vec{k},\lambda}\right) = \hat{p}_i \cdot \hat{p}_j - \left(\hat{p}_i \cdot \hat{k}\right) \left(\hat{p}_j \cdot \hat{k}\right) \,. \tag{D.31}$$

Then, we split $F_{ij}(x)$ into two integrals:

$$\begin{aligned} F_{ij}(x) =& \frac{1}{4\pi} \left(\hat{p}_i \cdot \hat{p}_i\right) \int_0^{2\pi} d\phi \int_{-1}^{1} d(\cos\theta) e^{ix\cos\theta} \\ & - \frac{1}{4\pi} \int_0^{2\pi} d\phi \int_{-1}^{1} d(\cos\theta) \left(\hat{p}_i \cdot \hat{k}\right) \left(\hat{p}_j \cdot \hat{k}\right) e^{ix\cos\theta} \,. \end{aligned} \tag{D.32}$$

The first integral can be easily performed and it has the value

$$\int_0^{2\pi} d\phi \int_{-1}^{1} d(\cos\theta) e^{ix\cos\theta} = 4\pi \frac{\sin x}{x} \,. \tag{D.33}$$

As regards the second integral, we have to expand the scalar products. Since we are working in spherical coordinates, we can expand the unit vector $\hat{k}$ over the cartesian components $\hat{k} = \cos\phi \sin\theta \, \hat{x} + \sin\phi \sin\theta \, \hat{y} + \cos\theta \, \hat{z}$, and this helps us write the scalar products

$$\begin{aligned} & \left(\hat{p}_i \cdot \hat{k}\right) \left(\hat{p}_j \cdot \hat{k}\right) = p_i^x p_j^x \cos^2\phi \sin^2\theta + p_i^y p_j^y \sin^2\phi \sin^2\theta + p_i^z p_j^z \cos^2\theta \\ & + \left(p_i^x p_j^y + p_i^y p_j^x\right) \cos\phi \sin\phi \sin^2\theta + \left(p_i^x p_j^z + p_i^z p_j^x\right) \cos\phi \sin\theta \cos\theta \\ & + \left(p_i^y p_j^z + p_i^z p_j^y\right) \sin\phi \sin\theta \cos\theta \,, \end{aligned} \tag{D.34}$$

so that, if we can compute the integral over ϕ, we have only 2 nonvanishing terms,

$$\begin{aligned}\int_0^{2\pi} d\phi \left(\hat{p}_i \cdot \hat{k}\right)\left(\hat{p}_j \cdot \hat{k}\right) =& \pi \left(p_i^x p_j^x + p_i^y p_j^y\right) \sin^2\theta + 2\pi p_i^z p_j^z \cos^2\theta \\ =& \pi \left(\hat{p}_i \cdot \hat{p}_j\right)\left(1-\cos^2\theta\right) + \pi \left(\hat{p}_i \cdot \hat{r}_{ij}\right)\left(\hat{p}_j \cdot \hat{r}_{ij}\right)\left(3\cos^2\theta - 1\right) \ ,\end{aligned} \tag{D.35}$$

where we used the fact that the unit vector $\hat{r}_{ij}$ is along the z axis. So, we have only 2 integrals over θ to perform:

$$\int_{-1}^{1} d\left(\cos\theta\right) e^{ix\cos\theta} = 2\frac{\sin x}{x} \ , \tag{D.36a}$$

$$\begin{aligned}\int_{-1}^{1} d(\cos\theta)\cos^2\theta\, e^{ix\cos\theta} &= -\frac{\partial^2}{\partial x^2}\int_{-1}^{1} d\left(\cos\theta\right) e^{ix\cos\theta} = -2\frac{\partial^2}{\partial x^2}\left(\frac{\sin x}{x}\right) \\ &= 2\frac{\sin x}{x} + 4\frac{\cos x}{x^2} - 4\frac{\sin x}{x^3} \ ,\end{aligned} \tag{D.36b}$$

from which

$$\pi\int_{-1}^{1} d(\cos\theta)\ \left(1-\cos^2\theta\right) e^{ix\cos\theta} = 4\pi\left(-\frac{\cos x}{x^2} + \frac{\sin x}{x^3}\right) \ , \tag{D.37}$$

$$\pi\int_{-1}^{1} d(\cos\theta)\ \left(3\cos^2\theta - 1\right) e^{ix\cos\theta} = 4\pi\left(\frac{\sin x}{x} + 3\frac{\cos x}{x^2} - 3\frac{\sin x}{x^3}\right) . \tag{D.38}$$

Summing up all the similar terms, we finally have

$$\begin{aligned}F_{ij}(x) = &\left[\frac{\sin x}{x} + \frac{\cos x}{x^2} - \frac{\sin x}{x^3}\right]\left(\hat{p}_i \cdot \hat{p}_j\right) \\ &+ \left[-\frac{\sin x}{x} - 3\frac{\cos x}{x^2} + 3\frac{\sin x}{x^3}\right]\left(\hat{p}_i \cdot \hat{r}_{ij}\right)\left(\hat{p}_j \cdot \hat{r}_{ij}\right) \ .\end{aligned} \tag{D.39}$$

Note that $F_{ij}(x)$ is an even function of x which, in our case, gives the useful equality $F_{ij}(-k_0 r_{ij}) = F_{ij}(k_0 r_{ij})$. Moreover, one can see that $F_{ji}(x) = F_{ij}(x)$, which implies that both the matrices $\gamma_{ij}(\omega)$ and $S_{ij}(\omega)$ are symmetric. As regards the diagonal terms ($i = j$) we can analytically extend the function to $x = 0$ thanks to the limit

$$\lim_{x\to 0} F_{ii}(x) = \frac{2}{3} \, . \tag{D.40}$$

Let us write the real parts of the rates as

$$\gamma_{ij}(\omega) = \frac{3\gamma}{2} F_{ij}(k_0 r_{ij}) \left[\delta_{\omega,\omega_0} \left(1 + N(\omega_0)\right) + \delta_{\omega,-\omega_0} N(\omega_0)\right] ,$$

where we have defined the diagonal decay rates

$$\gamma = \frac{4}{3}\mu^2 \frac{\omega_0^3}{c^3} . \tag{D.41}$$

Now let us compute the contribution of the real parts computed above to the master equation. Since $\gamma_{ji}(\omega) = \gamma_{ij}(\omega)$ we have

$$\begin{aligned}\left[\frac{d\hat{\rho}_S(t)}{dt}\right]_{real} &= \sum_{\omega=\pm\omega_0} \sum_{i,j} \frac{1}{2}\gamma_{ij}(\omega) \left[\hat{A}_j(\omega)\hat{\rho}_S(t)\hat{A}_i^\dagger(\omega) - \hat{A}_i^\dagger(\omega)\hat{A}_j(\omega)\hat{\rho}_S(t)\right] + \text{h.c.} \\ &= \sum_{\omega=\pm\omega_0} \sum_{i,j} \gamma_{ij}(\omega) \left[\hat{A}_j(\omega)\hat{\rho}_S(t)\hat{A}_i^\dagger(\omega) - \frac{1}{2}\left\{\hat{A}_i^\dagger(\omega)\hat{A}_j(\omega), \hat{\rho}_S(t)\right\}\right] ,\end{aligned} \tag{D.42}$$

where $\{\cdot,\cdot\}$ denotes the anti-commutator and, taking $A_j(\omega)$ from (D.10), we have

$$\begin{aligned}\left[\frac{d\hat{\rho}_S(t)}{dt}\right]_{real} =& \sum_{i,j} \gamma_{ij} \left(1 + N(\omega_0)\right) \left[\hat{\sigma}_j^- \hat{\rho}_S(t) \hat{\sigma}_i^+ - \frac{1}{2}\left\{\hat{\sigma}_i^+ \hat{\sigma}_j^-, \hat{\rho}_S(t)\right\}\right] \\ &+ \sum_{i,j} \gamma_{ij} N(\omega_0) \left[\hat{\sigma}_j^+ \hat{\rho}_S(t) \hat{\sigma}_i^- - \frac{1}{2}\left\{\hat{\sigma}_i^- \hat{\sigma}_j^+, \hat{\rho}_S(t)\right\}\right] ,\end{aligned} \tag{D.43}$$

which is clearly written in the Lindblad form [128] and where we have defined the coefficients

$$\gamma_{ij} = \frac{\gamma_{ij}(\omega_0)}{1 + N(\omega_0)} = \frac{\gamma_{ij}(-\omega_0)}{N(\omega_0)} = \frac{3}{2}\gamma F_{ij}(k_0 r_{ij}) . \tag{D.44}$$

D.3.2 Imaginary Part (Lamb Shift)

Let us now focus on the imaginary part contribution to the master equation. Thanks to the symmetry $S_{ji}(\omega) = S_{ij}(\omega)$ we have

$$\begin{aligned}\left[\frac{d\hat{\rho}_S(t)}{dt}\right]_{imag} =& i \sum_{\omega=\pm\omega_0} \sum_{i,j} S_{ij}(\omega) \left[\hat{A}_j(\omega)\hat{\rho}_S(t)\hat{A}_i^\dagger(\omega) - \hat{A}_i^\dagger(\omega)\hat{A}_j(\omega)\hat{\rho}_S(t)\right] + \text{h.c.} \\ =& -i \sum_{\omega=\pm\omega_0} \sum_{i,j} S_{ij}(\omega) \left[\hat{A}_i^\dagger(\omega)\hat{A}_j(\omega), \hat{\rho}_S(t)\right] = -i\left[\hat{H}_{LS}, \hat{\rho}_S(t)\right] ,\end{aligned} \tag{D.45}$$

where we have defined the Lamb shift Hamiltonian using (D.10)

$$\hat{H}_{LS} = \sum_{\omega=\pm\omega_0} \sum_{i,j} S_{ij}(\omega)\hat{A}_i^\dagger(\omega)\hat{A}_j(\omega) = \sum_{i,j} \left[S_{ij}(\omega_0)\hat{\sigma}_i^+\hat{\sigma}_j^- + S_{ij}(-\omega_0)\hat{\sigma}_j^-\hat{\sigma}_i^+\right] . \tag{D.46}$$

Let us start by separating the diagonal terms of $\hat{H}_{LS}$ from the off-diagonal ones. Thanks to the Pauli matrices commutation rules $\left[\hat{\sigma}_i^+, \hat{\sigma}_j^-\right] = \delta_{ij}\hat{\sigma}_z$ we have

$$\hat{H}_{LS} = \sum_i \left[S_{ii}(\omega_0)\hat{\sigma}_i^+\hat{\sigma}_i^- + S_{ii}(-\omega_0)\hat{\sigma}_i^-\hat{\sigma}_i^+\right] + \sum_{\substack{i,j \\ i\neq j}} \Delta_{ij}\hat{\sigma}_i^+\hat{\sigma}_j^- \ , \tag{D.47}$$

where we have defined the coupling terms

$$\Delta_{ij} = S_{ij}(\omega_0) + S_{ij}(-\omega_0) . \tag{D.48}$$

To make the evaluation of the coupling terms easier, let us first rewrite $S_{ij}(\omega_0)$ by separating the terms depending on the black body temperature ($N(\omega_k)$) from the ones which are independent of it. That means

$$S_{ij}(\omega_0) = \frac{\mu^2}{\pi c^3}\mathrm{P}\int_0^\infty d\omega_k \frac{\omega_k^3}{\omega_0-\omega_k}F_{ij}(kr_{ij}) + \frac{\mu^2}{\pi c^3}\mathrm{P}\int_0^\infty d\omega_k \frac{2\omega_0\omega_k^3 N(\omega_k)}{\omega_0^2-\omega_k^2}F_{ij}(kr_{ij}) . \tag{D.49}$$

To compute Δ_{ij} we need $S_{ij}(-\omega_0)$. Now, if we replace ω_0 with $-\omega_0$ in the previous expression, by performing the change of variable $\omega_k \to (-\omega_k)$ in the first integral, we have

$$S_{ij}(-\omega_0) = \frac{\mu^2}{\pi c^3}\mathrm{P}\int_{-\infty}^0 d\omega_k \frac{\omega_k^3}{\omega_0-\omega_k}F_{ij}(kr_{ij}) - \frac{\mu^2}{\pi c^3}\mathrm{P}\int_0^\infty d\omega_k \frac{2\omega_0\omega_k^3 N(\omega_k)}{\omega_0^2-\omega_k^2}F_{ij}(kr_{ij}) . \tag{D.50}$$

Therefore, if we sum $S_{ij}(\omega_0) + S_{ij}(-\omega_0)$, the terms depending on the black body temperature cancel and the first integral is extended through the whole real axis, i.e.

$$\Delta_{ij} = \frac{\mu^2}{\pi c^3}\mathrm{P}\int_{-\infty}^\infty d\omega_k \frac{\omega_k^3}{\omega_0-\omega_k}F_{ij}(kr_{ij}) . \tag{D.51}$$

Before evaluating the above integral, let us change the integration variable to $x = \omega_k r_{ij}/c$ and define the parameter $x_0 = \omega_0 r_{ij}/c$, so that we have

$$\Delta_{ij} = \frac{\mu^2}{\pi r_{ij}^3}\mathrm{P}\int_{-\infty}^\infty dx \frac{x^3}{x_0-x}F_{ij}(x) . \tag{D.52}$$

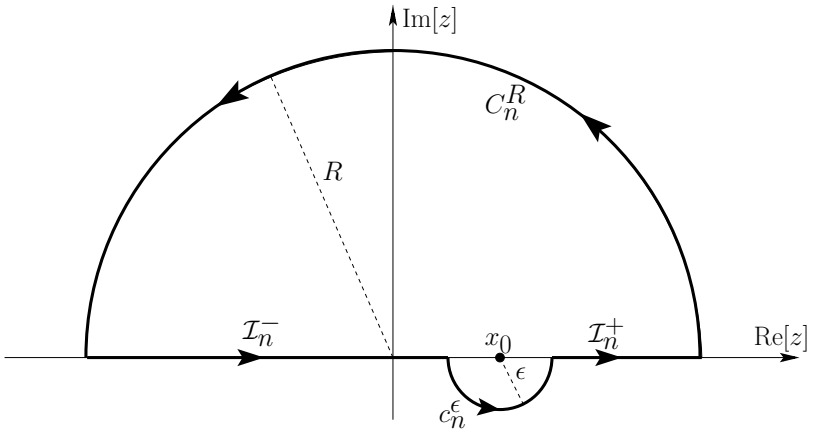

Figure D.1: Path of the contour integral $\mathcal{Y}_n$ (D.56) in the complex plane.

By expanding $F_{ij}(x)$ using (D.39) we have

$$\begin{aligned}\Delta_{ij} =&\frac{\mu^2}{\pi r_{ij}^3}\left[-\left(\hat{p}_i\cdot\hat{p}_j\right)+3\left(\hat{p}_i\cdot\hat{r}_{ij}\right)\left(\hat{p}_j\cdot\hat{r}_{ij}\right)\right]I_0+\\ &+\frac{\mu^2}{\pi r_{ij}^3}\left[\left(\hat{p}_i\cdot\hat{p}_j\right)-3\left(\hat{p}_i\cdot\hat{r}_{ij}\right)\left(\hat{p}_j\cdot\hat{r}_{ij}\right)\right]I_1+\\ &+\frac{\mu^2}{\pi r_{ij}^3}\left[\left(\hat{p}_i\cdot\hat{p}_j\right)-\left(\hat{p}_i\cdot\hat{r}_{ij}\right)\left(\hat{p}_j\cdot\hat{r}_{ij}\right)\right]I_2\ ,\end{aligned} \tag{D.53}$$

where the three real integrals I_0,I_1 and I_2 can be all related to one complex integral

$$I_0=\mathrm{Im}\left(\mathcal{I}_0\right)\ ,\quad I_1=\mathrm{Re}\left(\mathcal{I}_1\right)\ ,\quad I_2=\mathrm{Im}\left(\mathcal{I}_2\right) \tag{D.54}$$

which is

$$\mathcal{I}_n=\mathrm{P}\int_{-\infty}^{\infty}dx\frac{x^n\,e^{ix}}{x_0-x}\,. \tag{D.55}$$

To compute $\mathcal{I}_n$ let us consider the contour integral

$$\mathcal{Y}_n=\oint_C dz\frac{z^n\,e^{iz}}{x_0-z}\ , \tag{D.56}$$

where C here is the closed curve shown as a solid line in Fig. D.1.

As one can see from Fig. D.1, the path C has been chosen so that we can split $\mathcal{Y}_n$ into four terms,

$$\mathcal{Y}_n=\mathcal{I}_n^-+c_n^\epsilon+\mathcal{I}_n^++C_n^R\,. \tag{D.57}$$

If we take the limit $R \to \infty$, then $C_n^R \to 0$ thanks to Jordan's Lemma. Moreover, $\mathcal{Y}_n$ can be computed by means of the residue theorem and has the value

$$\mathcal{Y}_n = 2\pi i \mathrm{Res}\left[\frac{z^n\, e^{iz}}{x_0 - z}\right]_{z=x_0} = -2\pi i x_0^n e^{ix_0}\,. \tag{D.58}$$

So, if we take the limit $\epsilon \to 0$ we have

$$\begin{aligned}\mathcal{I}_n^- + \mathcal{I}_n^+ &= \lim_{\epsilon\to 0}\left[\int_{-\infty}^{x_0-\epsilon} dx \frac{x^n\, e^{ix}}{x_0 - x} + \int_{x_0+\epsilon}^{\infty} dx \frac{x^n\, e^{ix}}{x_0 - x}\right] = \mathrm{P}\int_{-\infty}^{\infty} dx \frac{x^n\, e^{ix}}{x_0 - x} = \mathcal{I}_n \\ &= \mathcal{Y}_n - \lim_{\epsilon\to 0} c_n^\epsilon\,.\end{aligned} \tag{D.59}$$

We can compute c_n^ϵ explicitly by choosing the parametrization $z = x_0 + \epsilon e^{i\theta}$ for $\theta \in [-\pi, 0]$, thus having

$$c_n^\epsilon = \int_{-\pi}^{0} \left(i\epsilon e^{i\theta}\right) d\theta \frac{x_0^n e^{ix_0}}{-\epsilon e^{i\theta}} + o(\epsilon) = -i\pi x_0^n e^{ix_0} + o(\epsilon)\,. \tag{D.60}$$

Substituting (D.58) and (D.60) into (D.59) we finally have

$$\mathcal{I}_n = -i\pi x_0^n e^{ix_0}\,. \tag{D.61}$$

Now we can put $\mathcal{I}_n$ into (D.54) to compute the explicit expression of Δ_{ij}, which is

$$\begin{aligned}\Delta_{ij} = &-\frac{\mu^2}{r_{ij}^3}\left[-\left(\hat{p}_i\cdot\hat{p}_j\right) + 3\left(\hat{p}_i\cdot\hat{r}_{ij}\right)\left(\hat{p}_j\cdot\hat{r}_{ij}\right)\right]\cos x_0 \\ &+\frac{\mu^2}{\pi r_{ij}^3}\left[\left(\hat{p}_i\cdot\hat{p}_j\right) - 3\left(\hat{p}_i\cdot\hat{r}_{ij}\right)\left(\hat{p}_j\cdot\hat{r}_{ij}\right)\right] x_0 \sin x_0 \\ &-\frac{\mu^2}{\pi r_{ij}^3}\left[\left(\hat{p}_i\cdot\hat{p}_j\right) - \left(\hat{p}_i\cdot\hat{r}_{ij}\right)\left(\hat{p}_j\cdot\hat{r}_{ij}\right)\right] x_0^2 \cos x_0\ ,\end{aligned} \tag{D.62}$$

where we can define $x_{ij} = x_0 = k_0 r_{ij}$ and rearrange it to

$$\begin{aligned}\Delta_{ij} = &\frac{3\gamma}{4}\left[-\frac{\cos x_{ij}}{k_0 r_{ij}} + \frac{\sin x_{ij}}{x_{ij}^2} + \frac{\cos x_{ij}}{x_{ij}^3}\right]\left(\hat{p}_i\cdot\hat{p}_j\right) \\ &+\frac{3\gamma}{4}\left[\frac{\cos x_{ij}}{k_0 r_{ij}} - 3\frac{\sin x_{ij}}{x_{ij}^2} - 3\frac{\cos x_{ij}}{x_{ij}^3}\right]\left(\hat{p}_i\cdot\hat{r}_{ij}\right)\left(\hat{p}_j\cdot\hat{r}_{ij}\right)\ .\end{aligned} \tag{D.63}$$

As regards the diagonal terms ($i = j$) of $\hat{H}_{LS}$, they produce a correction to the site energy (changing it to a "dressed" energy) which is independent of the site itself, but it diverges. The renormalization of the dressed energy is not treated here, though.

D.3.3 Final expression

Let us now re-write the master equation that we derived. In the Schrödinger picture we have

$$\begin{aligned}\frac{d\hat{\rho}_S}{dt} =& - i \left[\hat{H}_S + \hat{H}_{LS}, \hat{\rho}_S\right] + \sum_{i,j} \gamma_{ij} \left(1 + N(\omega_0)\right) \left[\hat{\sigma}_j^- \hat{\rho}_S \hat{\sigma}_i^+ - \frac{1}{2} \left\{\hat{\sigma}_i^+ \hat{\sigma}_j^-, \hat{\rho}_S\right\}\right] \\ &+ \sum_{i,j} \gamma_{ij} N(\omega_0) \left[\hat{\sigma}_j^+ \hat{\rho}_S \hat{\sigma}_i^- - \frac{1}{2} \left\{\hat{\sigma}_i^- \hat{\sigma}_j^+, \hat{\rho}_S\right\}\right] \ , \end{aligned} \tag{D.64}$$

were $N(\omega_0)$ is the Bose-Einstein function and, defining the parameters $x_{ij} = \omega_0 r_{ij}/c$ and $\gamma = \frac{4}{3}\mu^2 \frac{\omega_0^3}{c^3}$ we have

$$\begin{aligned}\gamma_{ij} =& \frac{3\gamma}{2} \left[\frac{\sin x_{ij}}{x_{ij}} + \frac{\cos x_{ij}}{x_{ij}^2} - \frac{\sin x_{ij}}{x_{ij}^3}\right] (\hat{p}_i \cdot \hat{p}_j) + \\ &+ \frac{3\gamma}{2} \left[-\frac{\sin x_{ij}}{x_{ij}} - 3\frac{\cos x_{ij}}{x_{ij}^2} + 3\frac{\sin x_{ij}}{x_{ij}^3}\right] (\hat{p}_i \cdot \hat{r}_{ij}) (\hat{p}_j \cdot \hat{r}_{ij}) \ . \end{aligned} \tag{D.65}$$

As regards the Hamiltonian term, subtracting the terms proportional to the identity, we have

$$\hat{H}_S + \hat{H}_{LS} = \frac{\overline{\omega_0}}{2} \sum_i \hat{\sigma}_i^z + \sum_{\substack{i,j \\ i \neq j}} \Delta_{ij} \hat{\sigma}_i^+ \hat{\sigma}_j^- \ , \tag{D.66}$$

where the dressed site energy is obtained from (D.47)

$$\overline{\omega_0} = \omega_0 + \frac{4\mu^2 \omega_0}{\pi c^3} \mathrm{P} \int_0^\infty d\omega_k \frac{\omega_k^3 \mathrm{ctanh} \frac{\beta\omega_k}{2}}{\omega_0^2 - \omega_k^2} \tag{D.67}$$

and the coupling terms Δ_{ij} are given by (D.63). The dressed energy is divergent, but equal for all levels and therefore it can be neglected.

D.4 Single excitation approximation and effective non-hermitian Hamiltonian

Let us consider only a subset of the full many-body basis: the state $|0\rangle$, where all the sites are in the ground state, and the single-excitation states $|j\rangle = \hat{\sigma}_j^+ |0\rangle$. Here we proceed to write the master equation neglecting the

contribution of the states having more than one excitation, and this is equivalent to replacing $\hat{\sigma}_j^+$ with $|j\rangle\langle 0|$ and $\hat{\sigma}_j^-$ with $|0\rangle\langle j|$ into (D.64). If now we call $\hat{\rho} = \hat{\rho}_S$ the density matrix of the aggregate, we have

$$\frac{d\hat{\rho}}{dt} \simeq -i\left[\hat{H}_S + \hat{H}_{LS}, \hat{\rho}\right] + \sum_{i,j}\gamma_{ij}\left(1+N(\omega_0)\right)\left[\rho_{ji}\,|0\rangle\langle 0| - \frac{1}{2}\left\{|i\rangle\langle j|, \hat{\rho}\right\}\right] + \sum_{i,j}\gamma_{ij}N(\omega_0)\left[\rho_{00}\,|j\rangle\langle i| - \frac{1}{2}\delta_{ij}\left\{|0\rangle\langle 0|, \hat{\rho}\right\}\right], \tag{D.68}$$

with the Hamiltonian

$$\hat{H}_S + \hat{H}_{LS} \simeq \overline{\omega_0}\sum_i |i\rangle\langle i| + \sum_{\substack{i,j\\ i\neq j}}\Delta_{ij}\,|i\rangle\langle j|\,. \tag{D.69}$$

Now, let us consider the particular case where there exist a common eigenbasis $|\alpha\rangle$ for both $\left(\hat{H}_S + \hat{H}_{LS}\right)$ and $\sum_{i,j}\gamma_{ij}\,|i\rangle\langle j|$ such that

$$\langle\alpha|\,\hat{H}_S + \hat{H}_{LS}\,|\beta\rangle = E_\alpha\delta_{\alpha\beta}\,, \tag{D.70}$$

$$\langle\alpha|\left(\sum_{i,j}\gamma_{ij}\,|i\rangle\langle j|\right)|\beta\rangle = \gamma_\alpha\delta_{\alpha\beta}\,. \tag{D.71}$$

We can then write (D.68) on such basis and have

$$\frac{d\hat{\rho}}{dt} \simeq -i\sum_\alpha E_\alpha\left[|\alpha\rangle\langle\alpha|, \hat{\rho}\right] + \sum_\alpha\gamma_\alpha\left(1+N(\omega_0)\right)\left[\rho_{\alpha\alpha}\,|0\rangle\langle 0| - \frac{1}{2}\left\{|\alpha\rangle\langle\alpha|, \hat{\rho}\right\}\right] + \sum_\alpha\gamma_\alpha N(\omega_0)\left[\rho_{00}\,|\alpha\rangle\langle\alpha| - \frac{1}{2}\left\{|0\rangle\langle 0|, \hat{\rho}\right\}\right]. \tag{D.72}$$

D.4.1 Radiative non-Hermitian Hamiltonian at zero temperature

At zero temperature, the occupation number of photons is $N(\omega_0) = 0$, so that the single-excitation master equation (D.68) simplifies to

$$\frac{d\hat{\rho}}{dt} \simeq -i\left[\hat{H}_S + \hat{H}_{LS}, \hat{\rho}\right] + \sum_{i,j}\gamma_{ij}\left[\rho_{ji}\,|0\rangle\langle 0| - \frac{1}{2}\left\{|i\rangle\langle j|, \hat{\rho}\right\}\right], \tag{D.73}$$

that can be also written as

$$\frac{d\hat{\rho}}{dt} \simeq -i\left(\hat{\mathcal{H}}\hat{\rho} - \hat{\rho}\hat{\mathcal{H}}^\dagger\right) + \sum_{i,j}\gamma_{ij}\rho_{ji}\,|0\rangle\langle 0|\,, \tag{D.74}$$

where we have defined the effective non-Hermitian Hamiltonian

$$\begin{aligned}\hat{\mathcal{H}} &= \hat{H}_S + \hat{H}_{LS} - \frac{i}{2}\sum_{i,j}\gamma_{ij}\left|i\right\rangle\left\langle j\right| \\ &= \sum_j\left(\omega_0 - \frac{i\gamma}{2}\right)\left|j\right\rangle\left\langle j\right| + \sum_{\substack{i,j \\ i\neq j}}\left(\Delta_{ij} - \frac{i}{2}\gamma_{ij}\right)\left|i\right\rangle\left\langle j\right| \ , \end{aligned} \tag{D.75}$$

with the hermitian elements Δ_{ij} given by Eq. (D.63) and the non-hermitian ones, γ_{ij}, by Eq. (D.65). Such Hamiltonian is called *radiative Hamiltonian* since it models the coupling and the losses induced in the system due to the interaction with the collective emitted field.

As one can see, the evolution of an initial excitation in Eq. (D.74) is uniquely determined by $\hat{\mathcal{H}}$, since the last term in Eq. (D.74) (sometimes called "quantum jump term") simply accounts for the refilling of $|0\rangle$ due to the loss of excitation. Therefore, an analysis of the complex spectrum of $\hat{\mathcal{H}}$ allows to completely characterize the features of the system coupled to the decay channels of the vacuum electromagnetic field. Following this approach, in Chapt. 3 we start our analysis precisely from the radiative hamiltonian, $\hat{\mathcal{H}}$.

Appendix E

Publications

This research activity has led to several publications in international journals and conferences. These are summarized below.[1]

International Journals

1. **A. Valzelli**, A. Boschetti, F. Mattiotti, A. Kargol, C. Green, F. Borgonovi, G. L. Celardo. "Large scale simulations of photosynthetic antenna systems: interplay of cooperativity and disorder", *J. Phys. Chem. B* 2024, 128, 40, 9643–9655 [10.1021/acs.jpcb.4c02406]

2. M. Gullì, **A. Valzelli**, F. Mattiotti, M. Angeli, F. Borgonovi, G. L. Celardo. "Macroscopic coherence as an emergent property in molecular nanotubes", *New J. Phys.* 2019, 21, 013019 [10.1088/1367-2630/aaf01a]

To be submitted

1. **A. Valzelli**, F. Mattiotti, J. Cao, G. L. Celardo. "Relation between structure and functionality in photosynthetic antenna complex of green sulfur bacteria: efficiency under natural sunlight pumping", available as a pre-print on arXiv [https://arxiv.org/abs/2510.19453]

Conferences, Workshops and PhD Schools

1. 13-18/07/2025 Firenze, 'StatPhys29', oral contribution.

[1] The author's bibliometric indices are the following: H-index = 2, total number of citations = 27 (source: Google Scholar on Month 10, 2025).

2. 09-13/06/2025 Napoli, 'Biological Physics and Statistical Mechanics: from molecules to cells and beyond', oral contribution.

3. 29-30/10/2024 Sorbonne Université & L'Institut des Nanosciences Paris, 'Polaron Day Paris 2024', oral contribution.

4. 28/08-07/09/2023 IMT School for Advanced Studies Lucca, SIFS PhD School 2023.

5. 04-08/11/2019 Centro Internacional de Ciencias A.C. Cuernavaca (Mexico), 'Non-Hermitian Quantum Systems', oral contribution.

6. 27-31/10/2019 Benemérita Universidad Autonoma de Puebla (Mexico), 'QuEBS: Quantum Effects in Biological Systems', Second best poster award: 'Macroscopic coherence as an emergent property in molecular nanotubes' .

Technical Reports

1. F. S. Lozano-Negro, A. Sherniyozov, M. Kueblboeck, **A. Valzelli**, J. Wiercinski, A. Haque, D. Busko, F. Martelli, A. Boschetti, B. S. Richards, H. Fattahi, E. M. Gauger, G. L. Celardo. "Unconcentrated bio-inspired solar lasing based on natural and artificial light-harvesting antennae", internal report.

Bibliography

[1] J. McFadden and J. Al-Khalili, "The origins of quantum biology," *Proceedings of the Royal Society A*, vol. 474, no. 2220, p. 20180674, 2018.

[2] J. Cao, R. J. Cogdell, D. F. Coker, H.-G. Duan, J. Hauer, U. Kleinekathöfer, T. L. C. Jansen, T. Mančal, R. J. D. Miller, J. P. Ogilvie, V. I. Prokhorenko, T. Renger, H.-S. Tan, R. Tempelaar, M. Thorwart, E. Thyrhaug, S. Westenhoff, and D. Zigmantas, "Quantum biology revisited," *Science Advances*, vol. 6, no. 14, p. eaaz4888, 2020.

[3] G. Celardo, M. Angeli, T. Craddock, and P. Kurian, "On the existence of superradiant excitonic states in microtubules," *New Journal of Physics*, vol. 21, no. 2, p. 023005, 2019.

[4] E. M. Gauger, E. Rieper, J. J. Morton, S. C. Benjamin, and V. Vedral, "Sustained quantum coherence and entanglement in the avian compass," *Phys. Rev. Lett.*, vol. 106, no. 4, p. 040503, 2011.

[5] L. Turin, "A spectroscopic mechanism for primary olfactory reception," *Chemical senses*, vol. 21, no. 6, pp. 773–791, 1996.

[6] T. Ritz, P. Thalau, J. B. Phillips, R. Wiltschko, and W. Wiltschko, "Resonance effects indicate a radical-pair mechanism for avian magnetic compass," *Nature*, vol. 429, no. 6988, pp. 177–180, 2004.

[7] E. Collini, C. Y. Wong, K. E. Wilk, P. M. Curmi, P. Brumer, and G. D. Scholes, "Coherently wired light-harvesting in photosynthetic marine algae at ambient temperature," *Nature*, vol. 463, no. 7281, pp. 644–647, 2010.

[8] H. Lee, Y.-C. Cheng, and G. R. Fleming, "Coherence dynamics in photosynthesis: protein protection of excitonic coherence," *Science*, vol. 316, no. 5830, pp. 1462–1465, 2007.

[9] G. S. Engel, T. R. Calhoun, E. L. Read, T.-K. Ahn, T. Mančal, Y.-C. Cheng, R. E. Blankenship, and G. R. Fleming, "Evidence for wavelike energy transfer

through quantum coherence in photosynthetic systems," *Nature*, vol. 446, no. 7137, pp. 782–786, 2007.

[10] R. Monshouwer, M. Abrahamsson, F. van Mourik, and R. van Grondelle, "Superradiance and exciton delocalization in bacterial photosynthetic light-harvesting systems," *The Journal of Physical Chemistry B*, vol. 101, no. 37, pp. 7241–7248, 1997.

[11] E. J. Dodson, N. Werren, Y. Paltiel, E. M. Gauger, and N. Keren, "Large-scale fret simulations reveal the control parameters of phycobilisome light-harvesting complexes," *Journal of The Royal Society Interface*, vol. 19, no. 196, p. 20220580, 2022.

[12] H. Schoffman, W. M. Brown, Y. Paltiel, N. Keren, and E. M. Gauger, "Structure-based hamiltonian model for isia uncovers a highly robust pigment–protein complex," *Journal of The Royal Society Interface*, vol. 17, no. 169, p. 20200399, 2020.

[13] M. Gullì, A. Valzelli, F. Mattiotti, M. Angeli, F. Borgonovi, and G. L. Celardo, "Macroscopic coherence as an emergent property in molecular nanotubes," *New Journal of Physics*, vol. 21, no. 1, p. 013019, 2019.

[14] A. Valzelli, A. Boschetti, F. Mattiotti, A. Kargol, C. Green, F. Borgonovi, and G. L. Celardo, "Large scale simulations of photosynthetic antenna systems: interplay of cooperativity and disorder," *The Journal of Physical Chemistry B*, vol. 128, no. 40, pp. 9643–9655, 2024.

[15] S. Baghbanzadeh and I. Kassal, "Geometry, supertransfer, and optimality in the light harvesting of purple bacteria," *The Journal of Physical Chemistry Letters*, vol. 7, no. 19, pp. 3804–3811, 2016.

[16] ——, "Distinguishing the roles of energy funnelling and delocalization in photosynthetic light harvesting," *Phys. Chem. Chem. Phys.*, vol. 18, no. 10, pp. 7459–7467, 2016.

[17] J. Strümpfer, M. Sener, and K. Schulten, "How quantum coherence assists photosynthetic light-harvesting," *The journal of physical chemistry letters*, vol. 3, no. 4, pp. 536–542, 2012.

[18] J. Huh, S. K. Saikin, J. C. Brookes, S. Valleau, T. Fujita, and A. Aspuru-Guzik, "Atomistic study of energy funneling in the light-harvesting complex of green sulfur bacteria," *Journal of the American Chemical Society*, vol. 136, no. 5, pp. 2048–2057, 2014.

[19] R. E. Blankenship, *Molecular mechanisms of photosynthesis*. John Wiley & Sons, 2021.

[20] R. G. Saer and R. E. Blankenship, "Light harvesting in phototrophic bacteria: structure and function," *Biochemical Journal*, vol. 474, no. 13, pp. 2107–2131, 2017.

[21] Z. Eltsova, M. Bolshakov, and A. Tsygankov, "Effect of light intensity and various organic acids on the growth of rhodobacter sphaeroides lhii-deficient mutant in a turbidostat culture," *Photosynthesis research*, vol. 130, pp. 307–316, 2016.

[22] A. G. M. Chew, N.-U. Frigaard, and D. A. Bryant, "Bacteriochlorophyllide c c-82 and c-121 methyltransferases are essential for adaptation to low light in chlorobaculum tepidum," *Journal of bacteriology*, vol. 189, no. 17, pp. 6176–6184, 2007.

[23] J. M. Linnanto and J. E. Korppi-Tommola, "Exciton description of chlorosome to baseplate excitation energy transfer in filamentous anoxygenic phototrophs and green sulfur bacteria," *The Journal of Physical Chemistry B*, vol. 117, no. 38, pp. 11 144–11 161, 2013.

[24] T. Malina, R. Koehorst, D. Bína, J. Pšenčík, and H. van Amerongen, "Superradiance of bacteriochlorophyll c aggregates in chlorosomes of green photosynthetic bacteria," *Scientific reports*, vol. 11, no. 1, p. 8354, 2021.

[25] R. A. Molina, E. Benito-Matias, A. D. Somoza, L. Chen, and Y. Zhao, "Superradiance at the localization-delocalization crossover in tubular chlorosomes," *Physical Review E*, vol. 93, no. 2, p. 022414, 2016.

[26] T. Fujita, J. Huh, S. K. Saikin, J. C. Brookes, and A. Aspuru-Guzik, "Theoretical characterization of excitation energy transfer in chlorosome light-harvesting antennae from green sulfur bacteria," *Photosynthesis research*, vol. 120, pp. 273–289, 2014.

[27] M. K. Şener, J. D. Olsen, C. N. Hunter, and K. Schulten, "Atomic-level structural and functional model of a bacterial photosynthetic membrane vesicle," *Proceedings of the National Academy of Sciences*, vol. 104, no. 40, pp. 15 723–15 728, 2007.

[28] S. Ganapathy, G. T. Oostergetel, P. K. Wawrzyniak, M. Reus, A. Gomez Maqueo Chew, F. Buda, E. J. Boekema, D. A. Bryant, A. R. Holzwarth, and H. J. De Groot, "Alternating syn-anti bacteriochlorophylls form concentric

helical nanotubes in chlorosomes," *Proceedings of the National Academy of Sciences*, vol. 106, no. 21, pp. 8525–8530, 2009.

[29] C. M. Borrego, J. B. Arellano, C. A. Abella, T. Gillbro, and J. Garcia-Gil, "The molar extinction coefficient of bacteriochlorophyll e and the pigment stoichiometry in chlorobium phaeobacteroides," *Photosynthesis research*, vol. 60, pp. 257–264, 1999.

[30] J. S. Connolly, E. B. Samuel, and A. F. Janzen, "Effects of solvent on the fluorescence properties of bacteriochlorophyll a," *Photochemistry and photobiology*, vol. 36, no. 5, pp. 565–574, 1982.

[31] J. Pšenčík, S. J. Butcher, and R. Tuma, "Chlorosomes: structure, function and assembly," *The structural basis of biological energy generation*, pp. 77–109, 2014.

[32] R. Stanier and J. Smith, "The chlorophylls of green bacteria," *Biochimica et biophysica acta*, vol. 41, no. 3, pp. 478–484, 1960.

[33] Y. Fedotova and J. Zeilstra-Ryalls, "Analysis of the role of prra, ppsr, and fnrl in intracytoplasmic membrane differentiation of rhodobacter sphaeroides 2.4. 1 using transmission electron microscopy," *Photosynthesis research*, vol. 119, no. 3, pp. 283–290, 2014.

[34] L. Cleary and J. Cao, "Optimal thermal bath for robust excitation energy transfer in disordered light-harvesting complex 2 of purple bacteria," *New J. Phys.*, vol. 15, no. 12, p. 125030, 2013.

[35] J. Ma and J. Cao, "Förster resonance energy transfer, absorption and emission spectra in multichromophoric systems. i. full cumulant expansions and system-bath entanglement," *J. Chem. Phys.*, vol. 142, no. 9, p. 094106, 2015.

[36] J.-H. Chen, H. Wu, C. Xu, X.-C. Liu, Z. Huang, S. Chang, W. Wang, G. Han, T. Kuang, J.-R. Shen *et al.*, "Architecture of the photosynthetic complex from a green sulfur bacterium," *Science*, vol. 370, no. 6519, p. eabb6350, 2020.

[37] J. Dostál, J. Pšenčík, and D. Zigmantas, "In situ mapping of the energy flow through the entire photosynthetic apparatus," *Nature Chemistry*, vol. 8, no. 7, pp. 705–710, 2016.

[38] J. Martiskainen, J. Linnanto, R. Kananavičius, V. Lehtovuori, and J. Korppi-Tommola, "Excitation energy transfer in isolated chlorosomes from chloroflexus aurantiacus," *Chemical Physics Letters*, vol. 477, no. 1-3, pp. 216–220, 2009.

[39] J. Martiskainen, J. Linnanto, V. Aumanen, P. Myllyperkiö, and J. Korppi-Tommola, "Excitation energy transfer in isolated chlorosomes from chlorobaculum tepidum and prosthecochloris aestuarii," *Photochemistry and photobiology*, vol. 88, no. 3, pp. 675–683, 2012.

[40] G. Hauska, T. Schoedl, H. Remigy, and G. Tsiotis, "The reaction center of green sulfur bacteria," *Biochim. Biophys. Acta*, vol. 1507, no. 1-3, pp. 260–277, 2001.

[41] A. Van Der Est, C. Hager-Braun, W. Leibl, G. Hauska, and D. Stehlik, "Transient electron paramagnetic resonance spectroscopy on green-sulfur bacteria and heliobacteria at two microwave frequencies," *Biochimica et Biophysica Acta (BBA)-Bioenergetics*, vol. 1409, no. 2, pp. 87–98, 1998.

[42] E. Abresch, M. Paddock, M. Villalobos, and M. Okamura, "Interaction between cytochrome c(2) and the photosynthetic reaction center from rhodobacter sphaeroides: Role of interprotein hydrogen bonds in binding and electron transfer," *Biochemistry*, vol. 47, pp. 13 318–25, 12 2008.

[43] A. Valzelli, F. Mattiotti, J. Cao, and G. L. Celardo, "Relation between structure and functionality in photosynthetic antenna complex of green sulfur bacteria: efficiency under natural sunlight pumping," 2025. [Online]. Available: http://arxiv.org/abs/2510.19453

[44] F. Mattiotti, M. Sarovar, G. G. Giusteri, F. Borgonovi, and G. L. Celardo, "Efficient light harvesting and photon sensing via engineered cooperative effects," *New Journal of Physics*, vol. 24, no. 1, p. 013027, 2022.

[45] K. Woronowicz, S. Ahmed, A. A. Biradar, A. V. Biradar, D. P. Birnie, T. Asefa, and R. A. Niederman, "Near-ir absorbing solar cell sensitized with bacterial photosynthetic membranes," *Photochemistry and photobiology*, vol. 88, no. 6, pp. 1467–1472, 2012.

[46] F. Mattiotti, W. M. Brown, N. Piovella, S. Olivares, E. M. Gauger, and G. L. Celardo, "Bio-inspired natural sunlight-pumped lasers," *New Journal of Physics*, vol. 23, no. 10, p. 103015, 2021.

[47] J. Sławski, J. Maciejewski, R. Szukiewicz, K. Gieczewska, and J. Grzyb, "Quantum dots assembled with photosynthetic antennae on a carbon nanotube platform: A nanohybrid for the enhancement of light energy harvesting," *ACS omega*, vol. 8, no. 44, pp. 41 991–42 003, 2023.

[48] A. Damjanović, T. Ritz, and K. Schulten, "Excitation energy trapping by the reaction center of rhodobacter sphaeroides," *International Journal of Quantum Chemistry*, vol. 77, no. 1, pp. 139–151, 2000.

[49] N. P. Sawaya, J. Huh, T. Fujita, S. K. Saikin, and A. Aspuru-Guzik, "Fast delocalization leads to robust long-range excitonic transfer in a large quantum chlorosome model," *Nano Letters*, vol. 15, no. 3, pp. 1722–1729, 2015.

[50] J. T. Beatty, J. Overmann, M. T. Lince, A. K. Manske, A. S. Lang, R. E. Blankenship, C. L. Van Dover, T. A. Martinson, and F. G. Plumley, "An obligately photosynthetic bacterial anaerobe from a deep-sea hydrothermal vent," *Proc. Natl. Acad. Sci. U.S.A.*, vol. 102, no. 26, pp. 9306–9310, 2005.

[51] X. Hu, T. Ritz, A. Damjanović, and K. Schulten, "Pigment organization and transfer of electronic excitation in the photosynthetic unit of purple bacteria," *J. Phys. Chem. B*, vol. 101, no. 19, pp. 3854–3871, 1997.

[52] X. Hu, A. Damjanović, T. Ritz, and K. Schulten, "Architecture and mechanism of the light-harvesting apparatus of purple bacteria," *Proc. Natl. Acad. Sci. U.S.A.*, vol. 95, no. 11, pp. 5935–5941, 1998.

[53] G. Panitchayangkoon, D. Hayes, K. A. Fransted, J. R. Caram, E. Harel, J. Wen, R. E. Blankenship, and G. S. Engel, "Long-lived quantum coherence in photosynthetic complexes at physiological temperature," *Proc. Natl. Acad. Sci. U.S.A.*, vol. 107, no. 29, pp. 12 766–12 770, 2010.

[54] J. Grad, G. Hernandez, and S. Mukamel, "Radiative decay and energy transfer in molecular aggregates: the role of intermolecular dephasing," *Physical Review A*, vol. 37, no. 10, p. 3835, 1988.

[55] F. C. Spano and S. Mukamel, "Superradiance in molecular aggregates," *J. Chem. Phys.*, vol. 91, no. 2, pp. 683–700, 1989.

[56] G. L. Celardo, F. Borgonovi, M. Merkli, V. I. Tsifrinovich, and G. P. Berman, "Superradiance transition in photosynthetic light-harvesting complexes," *J. Phys. Chem. C*, vol. 116, no. 42, pp. 22 105–22 111, 2012.

[57] D. Ferrari, G. Celardo, G. P. Berman, R. Sayre, and F. Borgonovi, "Quantum biological switch based on superradiance transitions," *J. Phys. Chem. C*, vol. 118, no. 1, pp. 20–26, 2014.

[58] P. Qian, M. Z. Papiz, P. J. Jackson, A. A. Brindley, I. W. Ng, J. D. Olsen, M. J. Dickman, P. A. Bullough, and C. N. Hunter, "Three-dimensional structure of the rhodobacter sphaeroides rc-lh1-pufx complex: dimerization and

quinone channels promoted by pufx," *Biochemistry*, vol. 52, no. 43, pp. 7575–7585, 2013.

[59] M. Koolhaas, R. Frese, G. Fowler, T. Bibby, S. Georgakopoulou, G. Van der Zwan, C. Hunter, and R. Van Grondelle, "Identification of the upper exciton component of the b850 bacteriochlorophylls of the lh2 antenna complex, using a b800-free mutant of rhodobacter sphaeroides," *Biochemistry*, vol. 37, no. 14, pp. 4693–4698, 1998.

[60] X. Hu, T. Ritz, A. Damjanović, F. Autenrieth, and K. Schulten, "Photosynthetic apparatus of purple bacteria," *Q. Rev. Biophys.*, vol. 35, no. 1, pp. 1–62, 2002.

[61] G. S. Orf and R. E. Blankenship, "Chlorosome antenna complexes from green photosynthetic bacteria," *Photosynthesis research*, vol. 116, pp. 315–331, 2013.

[62] L. M. Günther, M. Jendrny, E. A. Bloemsma, M. Tank, G. T. Oostergetel, D. A. Bryant, J. Knoester, and J. Köhler, "Structure of light-harvesting aggregates in individual chlorosomes," *The Journal of Physical Chemistry B*, vol. 120, no. 24, pp. 5367–5376, 2016.

[63] J. M. Linnanto and J. E. Korppi-Tommola, "Investigation on chlorosomal antenna geometries: tube, lamella and spiral-type self-aggregates," *Photosynthesis research*, vol. 96, pp. 227–245, 2008.

[64] M. Ø. Pedersen, J. Linnanto, N.-U. Frigaard, N. C. Nielsen, and M. Miller, "A model of the protein–pigment baseplate complex in chlorosomes of photosynthetic green bacteria," *Photosynthesis research*, vol. 104, pp. 233–243, 2010.

[65] N.-U. Frigaard and D. A. Bryant, "Chlorosomes: antenna organelles in photosynthetic green bacteria," in *Complex intracellular structures in prokaryotes*. Springer, 2006, pp. 79–114.

[66] G. T. Oostergetel, M. Reus, A. G. M. Chew, D. A. Bryant, E. J. Boekema, and A. R. Holzwarth, "Long-range organization of bacteriochlorophyll in chlorosomes of chlorobium tepidum investigated by cryo-electron microscopy," *FEBS letters*, vol. 581, no. 28, pp. 5435–5439, 2007.

[67] J. Pšenčík, T. Ikonen, P. Laurinmäki, M. Merckel, S. Butcher, R. Serimaa, and R. Tuma, "Lamellar organization of pigments in chlorosomes, the light harvesting complexes of green photosynthetic bacteria," *Biophysical journal*, vol. 87, no. 2, pp. 1165–1172, 2004.

[68] J. Pšenčík, J. B. Arellano, T. P. Ikonen, C. M. Borrego, P. A. Laurinmäki, S. J. Butcher, R. E. Serimaa, and R. Tuma, "Internal structure of chlorosomes from brown-colored chlorobium species and the role of carotenoids in their assembly," *Biophysical journal*, vol. 91, no. 4, pp. 1433–1440, 2006.

[69] J. Psencík, A. M. Collins, L. Liljeroos, M. Torkkeli, P. Laurinmäki, H. M. Ansink, T. P. Ikonen, R. E. Serimaa, R. E. Blankenship, R. Tuma *et al.*, "Structure of chlorosomes from the green filamentous bacterium chloroflexus aurantiacus," *Journal of bacteriology*, vol. 191, no. 21, pp. 6701–6708, 2009.

[70] M. F. Hohmann-Marriott, R. E. Blankenship, and R. W. Roberson, "The ultrastructure of chlorobium tepidum chlorosomes revealed by electron microscopy," *Photosynthesis research*, vol. 86, pp. 145–154, 2005.

[71] G. T. Oostergetel, H. Van Amerongen, and E. J. Boekema, "The chlorosome: a prototype for efficient light harvesting in photosynthesis," *Photosynthesis research*, vol. 104, pp. 245–255, 2010.

[72] L. A. Staehelin, J. R. Golecki, R. C. Fuller, and G. Drews, "Visualization of the supramolecular architecture of chlorosomes (chlorobium type vesicles) in freeze-fractured cells of chloroflexus aurantiacus," *Archives of Microbiology*, vol. 119, pp. 269–277, 1978.

[73] L. A. Staehelin, J. R. Golecki, and G. Drews, "Supramolecular organization of chlorosomes (chlorobium vesicles) and of their membrane attachment sites in chlorobium limicola," *Biochimica et Biophysica Acta (BBA)-Bioenergetics*, vol. 589, no. 1, pp. 30–45, 1980.

[74] G. Cohen-Bazire, N. Pfennig, and R. Kunisawa, "The fine structure of green bacteria," *The Journal of cell biology*, vol. 22, no. 1, pp. 207–225, 1964.

[75] S. K. Saikin, Y. Khin, J. Huh, M. Hannout, Y. Wang, F. Zare, A. Aspuru-Guzik, and J. K.-H. Tang, "Chromatic acclimation and population dynamics of green sulfur bacteria grown with spectrally tailored light," *Scientific Reports*, vol. 4, no. 1, pp. 1–8, 2014.

[76] V. Eric, X. Li, L. Dsouza, S. K. Frehan, A. Huijser, A. R. Holzwarth, F. Buda, G. A. Sevink, H. J. De Groot, and T. L. Jansen, "Manifestation of hydrogen bonding and exciton delocalization on the absorption and two-dimensional electronic spectra of chlorosomes," *The Journal of Physical Chemistry B*, vol. 127, no. 5, pp. 1097–1109, 2023.

[77] V. Eric, J. L. Castro, X. Li, L. Dsouza, S. K. Frehan, A. Huijser, A. R. Holzwarth, F. Buda, G. A. Sevink, H. J. de Groot *et al.*, "Ultrafast anisotropy

decay reveals structure and energy transfer in supramolecular aggregates," *The Journal of Physical Chemistry B*, vol. 127, no. 34, pp. 7487–7496, 2023.

[78] J. Linnanto, J. Korppi-Tommola, and V. Helenius, "Electronic states, absorption spectrum and circular dichroism spectrum of the photosynthetic bacterial lh2 antenna of rhodopseudomonas a cidophila as predicted by exciton theory and semiempirical calculations," *The Journal of Physical Chemistry B*, vol. 103, no. 41, pp. 8739–8750, 1999.

[79] J. Strümpfer and K. Schulten, "Excited state dynamics in photosynthetic reaction center and light harvesting complex 1," *The Journal of chemical physics*, vol. 137, no. 6, p. 065101, 2012.

[80] H. Michel and J. Deisenhofer, "Relevance of the photosynthetic reaction center from purple bacteria to the structure of photosystem ii," *Biochemistry*, vol. 27, no. 1, pp. 1–7, 1988.

[81] Chromatophore total area: $A_{tot} = 4\pi R^2 = 1.13 \cdot 10^4$ nm^2. Empty spherical cap at the south pole: $A_{emp} = 39.17$ nm^2. Total area occupied by LHI+RCs complexes: $A_{LHI+RC} = 1.413 \cdot 10^3$ nm^2. Total area occupied by LHII complexes: $A_{LHII} = 2.89 \cdot 10^3$ nm^2. Area occupied by photosynthetic complexes: $S_{Bchl} = A_{LHII} + A_{LHI+RC} = 4.303 \cdot 10^3$ nm^2. Available spherical area: $S_{av} = A_{tot} - A_{emp} = 1.126 \cdot 10^4$ nm^2. Ratio between the amount of surface occupied by photosynthetic complexes and the available spherical area: $\frac{S_{Bchl}}{S_{av}} = 0.38$.

[82] M. Lapaine, "Mollweide map projection," *KoG*, vol. 15, no. 15., pp. 7–16, 2011.

[83] J. P. Snyder, *Map projections–A working manual*. US Government Printing Office, 1987, vol. 1395.

[84] F. Mattiotti, "Cooperative effects in quantum systems: Superradiance and long-range interactions," PhD thesis, University of Notre Dame, 2021, dOI: 10.7274/k0698626w08. [Online]. Available: https://curate.nd.edu/articles/thesis/Cooperative_Effects_in_Quantum_Systems_Superradiance_and_Long-Range_Interactions/24820755

[85] E. Akkermans, A. Gero, and R. Kaiser, "Photon localization and dicke superradiance in atomic gases," *Physical review letters*, vol. 101, no. 10, p. 103602, 2008.

[86] M. Gross and S. Haroche, "Superradiance: An essay on the theory of collective spontaneous emission," *Physics reports*, vol. 93, no. 5, pp. 301–396, 1982.

[87] G. Celardo, N. Auerbach, F. Izrailev, and V. Zelevinsky, "Distribution of resonance widths and dynamics of continuum coupling," *Physical review letters*, vol. 106, no. 4, p. 042501, 2011.

[88] $\sum_{n=1}^{N} |\vec{D}_n|^2 = \sum_{n=1}^{N} \vec{D}_n \cdot \vec{D}_n^{\dagger} = \sum_{n=1}^{N} \left[\sum_i C_n(i)\hat{\mu}_i \cdot \sum_j C_n^*(j)\hat{\mu}_j\right] = \sum_{n=1}^{N} \sum_{i,j} \langle i|E_n\rangle \langle E_n|j\rangle \, \hat{\mu}_i \cdot \hat{\mu}_j = \sum_i |\hat{\mu}_i|^2 = N.$

[89] G. Rainò, M. A. Becker, M. I. Bodnarchuk, R. F. Mahrt, M. V. Kovalenko, and T. Stöferle, "Superfluorescence from lead halide perovskite quantum dot superlattices," *Nature*, vol. 563, no. 7733, pp. 671–675, 2018.

[90] M. O. Scully and A. A. Svidzinsky, "The super of superradiance," *Science*, vol. 325, no. 5947, pp. 1510–1511, 2009.

[91] F. C. Spano, "The spectral signatures of frenkel polarons in h-and j-aggregates," *Accounts of chemical research*, vol. 43, no. 3, pp. 429–439, 2010.

[92] C. Bradac, M. T. Johnsson, M. v. Breugel, B. Q. Baragiola, R. Martin, M. L. Juan, G. K. Brennen, and T. Volz, "Room-temperature spontaneous superradiance from single diamond nanocrystals," *Nature communications*, vol. 8, no. 1, p. 1205, 2017.

[93] T. Bienaimé, R. Bachelard, N. Piovella, and R. Kaiser, "Cooperativity in light scattering by cold atoms," *Fortschritte der Physik*, vol. 61, no. 2-3, pp. 377–392, 2013.

[94] M. Scheibner, T. Schmidt, L. Worschech, A. Forchel, G. Bacher, T. Passow, and D. Hommel, "Superradiance of quantum dots," *Nature Physics*, vol. 3, no. 2, pp. 106–110, 2007.

[95] S. Doria, T. S. Sinclair, N. D. Klein, D. I. Bennett, C. Chuang, F. S. Freyria, C. P. Steiner, P. Foggi, K. A. Nelson, J. Cao *et al.*, "Photochemical control of exciton superradiance in light-harvesting nanotubes," *ACS nano*, vol. 12, no. 5, pp. 4556–4564, 2018.

[96] V. May and O. Kühn, *Charge and energy transfer dynamics in molecular systems*. John Wiley & Sons, 2023.

[97] private communication by Prof. M. Trotta group (CNR Bari).

[98] P. Qian, D. J. Swainsbury, T. I. Croll, P. Castro-Hartmann, G. Divitini, K. Sader, and C. N. Hunter, "Cryo-em structure of the rhodobacter sphaeroides light-harvesting 2 complex at 2.1 å," *Biochemistry*, vol. 60, no. 44, pp. 3302–3314, 2021.

[99] A. Mattioni, F. Caycedo-Soler, S. F. Huelga, and M. B. Plenio, "Design principles for long-range energy transfer at room temperature," *Physical Review X*, vol. 11, no. 4, p. 041003, 2021.

[100] F. Caruso, A. W. Chin, A. Datta, S. F. Huelga, and M. B. Plenio, "Entanglement and entangling power of the dynamics in light-harvesting complexes," *Physical Review A*, vol. 81, no. 6, p. 062346, 2010.

[101] A. Ishizaki and G. R. Fleming, "Theoretical examination of quantum coherence in a photosynthetic system at physiological temperature," *Proceedings of the National Academy of Sciences*, vol. 106, no. 41, pp. 17 255–17 260, 2009.

[102] G. L. Celardo, G. G. Giusteri, and F. Borgonovi, "Cooperative robustness to static disorder: Superradiance and localization in a nanoscale ring to model light-harvesting systems found in nature," *Physical Review B*, vol. 90, no. 7, p. 075113, 2014.

[103] C. Olbrich, J. Liebers, and U. Kleinekathöfer, "Modeling of light-harvesting in purple bacteria using a time-dependent hamiltonian approach," *physica status solidi (b)*, vol. 248, no. 2, pp. 393–398, 2011.

[104] L. Varvelo, J. K. Lynd, B. Citty, O. Kühn, and D. I. Raccah, "Formally exact simulations of mesoscale exciton diffusion in a light-harvesting 2 antenna nanoarray," *The Journal of Physical Chemistry Letters*, vol. 14, no. 12, pp. 3077–3083, 2023.

[105] A. Damjanović, I. Kosztin, U. Kleinekathöfer, and K. Schulten, "Excitons in a photosynthetic light-harvesting system: a combined molecular dynamics, quantum chemistry, and polaron model study," *Physical Review E*, vol. 65, no. 3, p. 031919, 2002.

[106] J. Strümpfer and K. Schulten, "Light harvesting complex ii b850 excitation dynamics," *The Journal of chemical physics*, vol. 131, no. 22, p. 225101, 2009.

[107] J. Dostal, T. Mancal, R.-n. Augulis, F. Vacha, J. Psencik, and D. Zigmantas, "Two-dimensional electronic spectroscopy reveals ultrafast energy diffusion

in chlorosomes," *Journal of the American Chemical Society*, vol. 134, no. 28, pp. 11 611–11 617, 2012.

[108] P. W. Anderson, "Absence of diffusion in certain random lattices," *Physical review*, vol. 109, no. 5, p. 1492, 1958.

[109] J. Olšina, A. G. Dijkstra, C. Wang, and J. Cao, "Can natural sunlight induce coherent exciton dynamics?" *arXiv preprint arXiv:1408.5385*, 2014.

[110] P. Würfel and U. Würfel, *Physics of solar cells: from basic principles to advanced concepts*. John Wiley & Sons, 2016.

[111] Let us recall that, in Gaussian units, the unit dipole-dipole interaction energy is $[E] = [\mu]^2[d]^{-3}$, where $[\mu]$ is the unit dipole and $[d]$ the unit distance. We express the dipoles in D (debye), the distance in Å and the energy in cm^{-1} units (applying the standard conversion $[E]/(hc)$, with h being the Planck constant and c the speed of light), so that $[\mu]^2/(hc) = \mathrm{cm}^{-1}\mathrm{Å}^3$. Now, from the definition $1\ \mathrm{D} = 10^{-18}\ \mathrm{cm}^{5/2}\ \mathrm{g}^{1/2}\ \mathrm{s}^{-1}$ we have $1\ \mathrm{D}^2 = 10^{-12}\ \mathrm{cm}^2\ \mathrm{g}\ \mathrm{s}^{-2}\ \mathrm{Å}^3$. Recalling the Planck constant $h = 6.626 \cdot 10^{-27}\ \mathrm{cm}^2\ \mathrm{g}\ \mathrm{s}^{-1}$ and the speed of light $c = 2.998 \cdot 10^{10}\ \mathrm{cm}\ \mathrm{s}^{-1}$, we have $1\ \mathrm{D}^2/(hc) = 5034\ \mathrm{cm}^{-1}\ \mathrm{Å}^3$. So, a transition dipole $\mu = \sqrt{30}$ D results in $|\mu|^2 = 30 \times 5034\ \mathrm{cm}^{-1}\ \mathrm{Å}^3 = 151\,020\ \mathrm{cm}^{-1}\ \mathrm{Å}^3$. Note that in these calculations we write explicitly where the energy is divided by hc for clarity, while in the main text we always assume implicitly that any energy is divided by hc.

[112] M. Kasha, "Energy transfer mechanisms and the molecular exciton model for molecular aggregates," *Radiation research*, vol. 20, no. 1, pp. 55–70, 1963.

[113] N. J. Hestand and F. C. Spano, "Expanded theory of h-and j-molecular aggregates: the effects of vibronic coupling and intermolecular charge transfer," *Chemical reviews*, vol. 118, no. 15, pp. 7069–7163, 2018.

[114] E. G. McRae and M. Kasha, "Enhancement of phosphorescence ability upon aggregation of dye molecules," *The Journal of Chemical Physics*, vol. 28, no. 4, pp. 721–722, 1958.

[115] M. Anzola, F. Di Maiolo, and A. Painelli, "Optical spectra of molecular aggregates and crystals: testing approximation schemes," *Physical Chemistry Chemical Physics*, vol. 21, no. 36, pp. 19 816–19 824, 2019.

[116] S. Sengupta and F. Würthner, "Chlorophyll j-aggregates: from bioinspired dye stacks to nanotubes, liquid crystals, and biosupramolecular electronics," *Accounts of chemical research*, vol. 46, no. 11, pp. 2498–2512, 2013.

[117] C. Didraga and J. Knoester, "Chiral exciton wave functions in cylindrical j aggregates," *The Journal of chemical physics*, vol. 121, no. 2, pp. 946–959, 2004.

[118] S. Lampoura, C. Spitz, S. Dähne, J. Knoester, and K. Duppen, "The optical dynamics of excitons in cylindrical j-aggregates," *The Journal of Physical Chemistry B*, vol. 106, no. 12, pp. 3103–3111, 2002.

[119] F. S. Freyria, J. M. Cordero, J. R. Caram, S. Doria, A. Dodin, Y. Chen, A. P. Willard, and M. G. Bawendi, "Near-infrared quantum dot emission enhanced by stabilized self-assembled j-aggregate antennas," *Nano letters*, vol. 17, no. 12, pp. 7665–7674, 2017.

[120] A. P. Deshmukh, W. Zheng, C. Chuang, A. D. Bailey, J. A. Williams, E. M. Sletten, E. H. Egelman, and J. R. Caram, "Near-atomic-resolution structure of j-aggregated helical light-harvesting nanotubes," *Nature chemistry*, vol. 16, no. 5, pp. 800–808, 2024.

[121] N. R. Reddy, M. Aubin, A. Kushima, and J. Fang, "Fluorescent h-aggregate vesicles and tubes of a cyanine dye and their potential as light-harvesting antennae," *The Journal of Physical Chemistry B*, vol. 125, no. 28, pp. 7911–7918, 2021.

[122] H. Yao, T. Isohashi, and K. Kimura, "Electrolyte-induced mesoscopic aggregation of thiacarbocyanine dye in aqueous solution: counterion size specificity," *The Journal of Physical Chemistry B*, vol. 111, no. 25, pp. 7176–7183, 2007.

[123] J. R. Caram, S. Doria, D. M. Eisele, F. S. Freyria, T. S. Sinclair, P. Rebentrost, S. Lloyd, and M. G. Bawendi, "Room-temperature micron-scale exciton migration in a stabilized emissive molecular aggregate," *Nano letters*, vol. 16, no. 11, pp. 6808–6815, 2016.

[124] S. Doria, M. Di Donato, R. Borrelli, M. F. Gelin, J. Caram, M. Pagliai, P. Foggi, and A. Lapini, "Vibronic coherences in light harvesting nanotubes: unravelling the role of dark states," *Journal of Materials Chemistry C*, vol. 10, no. 18, pp. 7216–7226, 2022.

[125] N. Babcock, G. Montes-Cabrera, K. Oberhofer, M. Chergui, G. Celardo, and P. Kurian, "Ultraviolet superradiance from mega-networks of tryptophan in biological architectures," *The Journal of Physical Chemistry B*, 2024.

[126] T. Renger and R. A. Marcus, "On the relation of protein dynamics and exciton relaxation in pigment–protein complexes: An estimation of the spectral

density and a theory for the calculation of optical spectra," *The Journal of chemical physics*, vol. 116, no. 22, pp. 9997–10 019, 2002.

[127] private communication by Prof. F. Terenziani group (University of Parma).

[128] H.-P. Breuer and F. Petruccione, *The theory of open quantum systems*. OUP Oxford, 2002.

[129] M. Schlosshauer, *Decoherence and the quantum-to-classical transition*. Springer, 2007.

[130] M. Rätsep, Z.-L. Cai, J. R. Reimers, and A. Freiberg, "Demonstration and interpretation of significant asymmetry in the low-resolution and high-resolution qy fluorescence and absorption spectra of bacteriochlorophyll a," *The Journal of Chemical Physics*, vol. 134, no. 2, 2011.

[131] M. Mohseni, P. Rebentrost, S. Lloyd, and A. Aspuru-Guzik, "Environment-assisted quantum walks in energy transfer of photosynthetic complexes," *J. Chem. Phys*, vol. 129, no. 17, p. 174106, 2008.

[132] J. Moix, J. Wu, P. Huo, D. Coker, and J. Cao, "Efficient energy transfer in light-harvesting systems, iii: The influence of the eighth bacteriochlorophyll on the dynamics and efficiency in fmo," *J. Phys. Chem. Lett.*, vol. 2, no. 24, pp. 3045–3052, 2011.

[133] D. Bína, Z. Gardian, F. Vácha, and R. Litvín, "Native fmo-reaction center supercomplex in green sulfur bacteria: an electron microscopy study," *Photosynth Res*, vol. 128, no. 1, pp. 93–102, 2016.

[134] J. Wen, H. Zhang, M. L. Gross, and R. E. Blankenship, "Membrane orientation of the fmo antenna protein from chlorobaculum tepidum as determined by mass spectrometry-based footprinting," *Proc. Natl. Acad. Sci.*, vol. 106, no. 15, pp. 6134–6139, 2009.

[135] J. M. Moix, Y. Zhao, and J. Cao, "Equilibrium-reduced density matrix formulation: Influence of noise, disorder, and temperature on localization in excitonic systems," *Physical Review B—Condensed Matter and Materials Physics*, vol. 85, no. 11, p. 115412, 2012.

[136] C. Chuang, J. Knoester, and J. Cao, "Scaling relations and optimization of excitonic energy transfer rates between one-dimensional molecular aggregates," *The Journal of Physical Chemistry B*, vol. 118, no. 28, pp. 7827–7834, 2014.

[137] K. Zhong, H. L. Nguyen, T. N. Do, H.-S. Tan, J. Knoester, and T. L. Jansen, "An efficient time-domain implementation of the multichromophoric förster resonant energy transfer method," *The Journal of Chemical Physics*, vol. 158, no. 6, 2023.

[138] A. S. Bondarenko, J. Knoester, and T. L. Jansen, "Comparison of methods to study excitation energy transfer in molecular multichromophoric systems," *Chemical Physics*, vol. 529, p. 110478, 2020.

[139] A. Klinger, D. Lindorfer, F. Müh, and T. Renger, "Living on the edge: light-harvesting efficiency and photoprotection in the core of green sulfur bacteria," *Physical Chemistry Chemical Physics*, vol. 25, no. 28, pp. 18 698–18 710, 2023.

[140] J. Pšenčík, T. Polívka, P. Němec, J. Dian, J. Kudrna, P. Malỳ, and J. Hála, "Fast energy transfer and exciton dynamics in chlorosomes of the green sulfur bacterium chlorobium tepidum," *The Journal of Physical Chemistry A*, vol. 102, no. 23, pp. 4392–4398, 1998.

[141] M. Sener, J. Strumpfer, A. Singharoy, C. N. Hunter, and K. Schulten, "Overall energy conversion efficiency of a photosynthetic vesicle," *Elife*, vol. 5, p. e09541, 2016.

[142] F. Comayras, C. Jungas, and J. Lavergne, "Functional consequences of the organization of the photosynthetic apparatus of *Rhodobacter sphaeroides*," *The journal of biological chemistry*, vol. 280, no. 12, 2005.

[143] F. Fassioli, A. Olaya-Castro, S. Scheuring, J. N. Sturgis, and N. F. Johnson, "Energy transfer in light-adapted photosynthetic membranes: from active to saturated photosynthesis," *Biophysical journal*, vol. 97, no. 9, pp. 2464–2473, 2009.

[144] W. Kühlbrandt, "Structure and function of bacterial light-harvesting complexes," *Structure*, vol. 3, no. 6, pp. 521–525, Jun. 1995. [Online]. Available: https://www.sciencedirect.com/science/article/pii/S0969212601001848

[145] S. Lin, P. R. Jaschke, H. Wang, M. Paddock, A. Tufts, J. P. Allen, F. I. Rosell, A. G. Mauk, N. W. Woodbury, and J. T. Beatty, "Electron transfer in the rhodobacter sphaeroides reaction center assembled with zinc bacteriochlorophyll," *Proceedings of the National Academy of Sciences*, vol. 106, no. 21, pp. 8537–8542, 2009. [Online]. Available: https://www.pnas.org/doi/abs/10.1073/pnas.0812719106

[146] T. Ritz, S. Park, and K. Schulten, "Kinetics of Excitation Migration and Trapping in the Photosynthetic Unit of Purple Bacteria," *The Journal of Physical Chemistry B*, vol. 105, no. 34, pp. 8259–8267, Aug. 2001, publisher: American Chemical Society. [Online]. Available: https://doi.org/10.1021/jp011032r

[147] F. Ma, Y. Kimura, X.-H. Zhao, Y.-S. Wu, P. Wang, L.-M. Fu, Z.-Y. Wang, and J.-P. Zhang, "Excitation dynamics of two spectral forms of the core complexes from photosynthetic bacterium thermochromatium tepidum," *Biophysical journal*, vol. 95, no. 7, pp. 3349–3357, 2008.

[148] D. T. Gillespie, "Exact stochastic simulation of coupled chemical reactions," *The Journal of Physical Chemistry*, vol. 81, no. 25, pp. 2340–2361, 1977.

[149] G. G. Giusteri, F. Mattiotti, and G. L. Celardo, "Non-hermitian hamiltonian approach to quantum transport in disordered networks with sinks: Validity and effectiveness," *Physical Review B*, vol. 91, no. 9, p. 094301, 2015.

[150] N. Makri and D. E. Makarov, "Tensor propagator for iterative quantum time evolution of reduced density matrices. ii. numerical methodology," *The Journal of chemical physics*, vol. 102, no. 11, pp. 4611–4618, 1995.

[151] M. Tanaka and Y. Tanimura, "Multistate electron transfer dynamics in the condensed phase: Exact calculations from the reduced hierarchy equations of motion approach," *The Journal of chemical physics*, vol. 132, no. 21, 2010.

[152] J. Prior, A. W. Chin, S. F. Huelga, and M. B. Plenio, "Efficient simulation of strong system-environment interactions," *Physical review letters*, vol. 105, no. 5, p. 050404, 2010.

[153] M. Cygorek, M. Cosacchi, A. Vagov, V. M. Axt, B. W. Lovett, J. Keeling, and E. M. Gauger, "Simulation of open quantum systems by automated compression of arbitrary environments," *Nature Physics*, vol. 18, no. 6, pp. 662–668, 2022.

[154] F. A. Pollock, D. P. McCutcheon, B. W. Lovett, E. M. Gauger, and A. Nazir, "A multi-site variational master equation approach to dissipative energy transfer," *New Journal of Physics*, vol. 15, no. 7, p. 075018, 2013.

[155] A. Kolli, A. Nazir, and A. Olaya-Castro, "Electronic excitation dynamics in multichromophoric systems described via a polaron-representation master equation," *The Journal of chemical physics*, vol. 135, no. 15, 2011.

[156] P. Banerjee, A. Burgess, J. Wiercinski, M. Cygorek, and E. M. Gauger, "Optical signatures of coherence in molecular dimers," *The Journal of Chemical Physics*, vol. 163, no. 20, 2025.

[157] J. Wiercinski, M. Cygorek, and E. M. Gauger, "Role of polaron dressing in superradiant emission dynamics," *Physical Review Research*, vol. 6, no. 3, p. 033231, 2024.

[158] G. G. Giusteri, F. Recrosi, G. Schaller, and G. L. Celardo, "Interplay of different environments in open quantum systems: Breakdown of the additive approximation," *Physical Review E*, vol. 96, no. 1, p. 012113, 2017.

[159] V. N. Shatokhin, M. Walschaers, F. Schlawin, and A. Buchleitner, "Coherence turned on by incoherent light," *New J. Phys.*, vol. 20, no. 11, p. 113040, 2018.

[160] The lifetime related to an energy width γ is defined as $\tau_\gamma = \hbar/\gamma$. Note that we implicitly divide each energy by hc (with h being the Planck constant and c the speed of light), so that $[\gamma]/(hc) = [\text{cm}]^{-1}$. Therefore, the unit time is $[\tau_\gamma] = \frac{h}{2\pi[\gamma]} = \left(2\pi c[\text{cm}]^{-1}\right)^{-1}$, where $c = 2.998 \cdot 10^{-2}$ cm ps^{-1}. Thus, given a width in $[\text{cm}]^{-1}$ units, its lifetime is obtained by multiplying the width by $2\pi c = 0.1884$ cm ps^{-1} and taking the reciprocal of the result.

[161] V. Prokhorenko, D. Steensgaard, and A. Holzwarth, "Exciton dynamics in the chlorosomal antennae of the green bacteria chloroflexus aurantiacus and chlorobium tepidum," *Biophysical journal*, vol. 79, no. 4, pp. 2105–2120, 2000.

[162] ——, "Exciton theory for supramolecular chlorosomal aggregates: 1. aggregate size dependence of the linear spectra," *Biophysical journal*, vol. 85, no. 5, pp. 3173–3186, 2003.

[163] R. H. Lehmberg, "Radiation from an n-atom system. i. general formalism," *Phys. Rev. A*, vol. 2, pp. 883–888, Sep 1970.